Computational Studies of Microporous Materials.

The Royal Institution of Great Britain.
Davy Faraday Laboratory,
London.

Department of Chemistry,
University College London,
London.

Ashley R. George

Thesis submitted for the degree of Ph.D.
University of London.
December 1993

ProQuest Number: 10106850

All rights reserved

INFORMATION TO ALL USERS
The quality of this reproduction is dependent upon the quality of the copy submitted.

In the unlikely event that the author did not send a complete manuscript
and there are missing pages, these will be noted. Also, if material had to be removed,
a note will indicate the deletion.

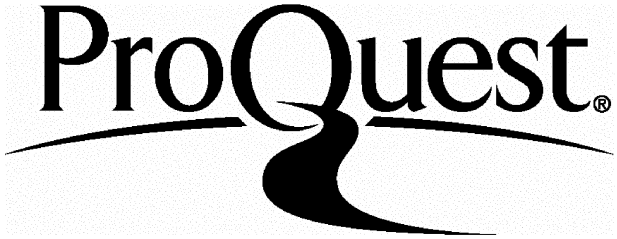

ProQuest 10106850

Published by ProQuest LLC(2016). Copyright of the Dissertation is held by the Author.

All rights reserved.
This work is protected against unauthorized copying under Title 17, United States Code.
Microform Edition © ProQuest LLC.

ProQuest LLC
789 East Eisenhower Parkway
P.O. Box 1346
Ann Arbor, MI 48106-1346

In memory of my father

A.W.E. George.

Acknowledgements.

First and foremost I would like to thank my supervisors Prof. C. R. A. Catlow, and Prof. Sir J. M. Thomas for fruitful discussions and advice concerning the work contained within this thesis.

I am would also thank SERC and the RI for the financial support for the duration of my thesis.

I would also like to thank the following for their valuable contributions which helped this project come to a successful conclusion. Dr. R.G. Bell for general assistance and for some of the potentials embodied within this thesis; Dr. J.D. Gale for his help with "GULP" and other such topics; A. Dornford-Smith, D. Lewis, Dr. T.S. Bush and Dr. S. Carling for useful discussions long into the night and all at the RI for making the last three years highly enjoyable.

A special thank-you to S.E. Appleton for her support and help in the final preparations of this thesis. Last but not least, I would like to thank my mother for her patience and total support throughout my education.

Abstract.

The use of computational modelling is becoming evermore prominent in the area of solid state chemistry and indeed with the continuing advances in computational power, it is possible to investigate the interesting and demanding areas associated with heterogeneous catalysis.

In the first half of this thesis, it is shown how a range of contemporary computational techniques, (including Molecular Dynamics and *ab-initio* calculations), can be used to explain in detail the structural and mechanistic features associated with a complex catalytic process, the cyclotrimerisation of acetylene to benzene in the presence of Nickel substituted zeolite-Y. In such a process, the ligand itself plays a vital role in extracting the cation into a more accessible site and then, via electrostatic and short-range forces, the acetylene molecules react in a manner that is significantly different from the classical Diels-Alder type of concerted ring formation.

In the latter half of this thesis, we study several problems in solid state chemistry prior to their experimental investigation. In particular, solid solutions of GeO_2/SiO_2 polymorphs, with similar structures to several zeolites are predicted to be stable. In addition, the details of the phase transition of GeO_2 α-quartz to the more stable rutile structure have been modelled successfully.

Finally, computational modelling has been applied to the investigation of a new member of the Clathrasil family, Octadecasil. This structure was found to be stable without the presence of extraframework ions. This line of investigation was continued with the study of the energetics of exchange with various ions, which allows us to evaluate the potential of this structure for use as an ion-exchange material.

Table of contents.

Chapter 1.

Chapter 2.

Chapter 3.

Chapter 4.

Chapter 5.

Chapter 6.

Chapter 7.

Chapter 8.

Appendix.

List of Tables.

List of Figures.

Chapter 1.

Chapter 2.

Chapter 3.

Chapter 4.

Chapter 5.

Chapter 6.

Chapter 7.

Appendix.

Chapter 1

Introduction.

1.1 General Overview.

In this thesis we investigate by computational methods new aspects of the solid state chemistry of micro-crystalline solids and catalysts.

The background lies in the wide range of experimental work reported in recent years regarding mono-phasic uniform heterogeneous catalysts. Catalysts play a major rôle in the evolution of new processes, including those which are inherently clean[1], the pressure for the development of which is increased by the environmental awareness underlying society today. A good example is the Mobil-Badger process whereby the acid zeolite H^+-ZSM-5 is used to produce ethylbenzene, an intermediate in the production of polystyrene, from benzene and ethene, rather than by using the environmentally harmful and chemically less selective catalyst, aluminium trichloride in a Friedel-Crafts type reaction. Economic as well as social issues contribute to the interest in catalysis today: by 2000 AD it is estimated that 6 billion pounds worth of catalysts will be consumed annually. Table 1.1.1 reports some of the commercially significant reactions[2] as well as a number of potential reaction which could become commercially viable, but are only at a laboratory scale at present. In this as in other science based industries research is at a premium and as with any rapidly expanding field new techniques either experimental, such as Quick EXAFS[3,4], SEXAFS[5,6] and quasi-inelastic neutron scattering[7] or computational methodologies[8,9] are being used.

Table 1.1.1 : A selection of important reactions catalysed by uniform heterogeneous catalysis.[10]

Reaction	*Catalyst*	*Uses*
Hydrocarbon cracking	H-La-Y	C
Friedel-Crafts reactions	H-ZSM-5, H-Y	C
Isomerisation of ethylbenzene and disproportionation of toluene to form para-xylene	H-ZSM-5	C
Conversion of methanol to gasoline	H-ZSM-5	C
Conversion of methanol to light alkenes	SAPO-34, Ni-SAPO-34	PC
Skeletal rearrangement of paraffins and alkenes.	H-Y, H-La-T	LS
Formation of ethers and esters	Acidic clay. H-ZSM-5	PC
Alkylation of phenol with methanol	SAPO-5, 11, 34	LS
Synthesis of methyltertbutylether(MTBE) from 2-methylpropene and methanol	Acidic clay	PC
Acetalisation of aldehydes	H-ZSM-5	LS
Synthesis of methylamines	H-Rho, H-ZSM-5	LS
Addition of CO to methanol to form acetic acid	Rh-X, Y	LS
Synthesis of hydroquinone from phenol and H_2O_2	Ti-Silicalite	C
Synthesis of propene oxide from propene and H_2O_2	Ti-Silicalite	PC
Isomerisation reactions of aliphatic compounds	Na-B-ZSM-5	LS
NO-N_2 + O_2	Cu-ZSM-5, Ni-Y	LS
Hydrogenation and dehydrogenation	Me-ZSM-5	LS
Oligomerisation of light alkenes	Ni-ZSM-5, Ni/Zn-ZSM-5 SAPO-11, MeAPO-11	LS
Benzene + N_2O - phenol	Fe-ZSM-5	LS
C_2H_2 - benzene	Ni-Y	LS
Cyclar process: light alkanes - aromatics.	Me-ZSM-5	C

C= commercial: PC = potentially commercial

LS= laboratory scale.

The study of catalysts in action poses several problems, particularly for heterogeneous catalysts where the operating conditions, are such as to preclude investigation by many techniques and where low levels of ill defined surface sites may be crucial. Therefore it is not surprising that the understanding of the mechanism of homogenous catalysts far exceeds the knowledge of the mechanisms of heterogeneous catalysis. The study and use of crystalline catalysts is predominantly due to the surface area being at a maximum and a greater concentration of active sites than for an amorphous solid; a crystalline solid also has a defined periodic structure which perhaps contains within it the active site; such a structure can be refined by X-ray or neutron diffraction techniques.

Zeolites are the archetypal uniform heterogeneous catalysts; they are microcrystalline aluminosilicalites, usually with an idealised stoichiometry of $H_xSi_mO_{2m}.Al_nO_{2n}M_y$ (m/n = 2→20,000, m>60 and x+y=n), where M is a singly charged cation although it is possible to substitute in more ionic cations, i.e. Ni^{2+} or Cr^{3+}. These cations are easily exchanged and it is indeed this ion-exchange capacity that has provided one of the more profitable aspects of the zeolite field, for instance their use in detergents.[11] Zeolites are sometimes termed molecular sieves which is due to their hydrophilic nature in the presence of cations and the subsequent ability to separate water from apolar liquids.[12]. This ability to sieve molecular heterogeneous phases has long been exploited in the area of gas separation[13], whereby a dehydrated zeolite with the appropriate size and/or shape differences between the crystal aperture and the adsorbate molecule is used. For example, at temperatures of around -183°C, zeolite-A adsorbs oxygen freely whilst nitrogen is not adsorbed over long periods of time.

Where the cations are replaced by protons, the host zeolite becomes acidic in nature, which coupled with the open and well defined structures, makes zeolites suitable as shape selective solid acid catalysts[14]. In such a process, the shape or molecular dimensions of the zeolite allows only part of the reacting molecules to pass through the catalyst pores, or in product selectivity, only products with the correct

dimensions can diffuse out of the pores; thus the final reaction is determined by the zeolite pore shape.

Zeolites are microcrystalline as the individual particles are normally smaller than 50μm; depending on particle size usually around 90% or more of the accessible surface area is internal because of the extensive 3-dimensional network of pores and channels that exist in many zeolites. The common factor in many solid state catalysts is that they possess a high concentration of accessible "surface" OH functional groups from which, depending upon the Brønsted acidity of the system, protons can be detached. Indeed, it is the ability to produce these relatively free protons that holds the key to a solid catalysts performance and in some degree it is possible to vary all three factors - the number of OH groups per unit area, the degree of accessibility and the strength of proton attachment. Solid state catalyst precursors, are generally found in all areas of science and zeolites have much in common to enzyme catalysts[15,16] such as Carbonic Anhydrase in the hydration of CO_2 or Lysozyme. Therefore, much work so far has been into the variation of the above three proton related variables to yield a stable, yet effective solid state catalyst regarding which the variability of the zeolite family has proved an important.

The first reported zeolite was the mineral, stilbite, which was discovered in 1756 by the Swedish mineralogist Cronstedt[17],. Since then many natural and synthetic zeolites have been discovered[18]. The crucial point is that molecules may be absorbed in the zeolite cages and pores can diffuse unhindered in and out of the crystals; indeed, the name "zeolites" reflects this property stemming from ζειυ (to boil) and λιθσς (stone). These solid catalysts are usually made up of tetrahedral building units, although trigonal bi-pyramidal and octahedral units although not common are known and it is the way in which these units are combined together which makes the different voids and cavities. Figure 1.1.1 depicts a TO_4^{4-} unit and several possible combinations of such building units to form larger more complex structures.

Figure 1.1.1 : The TO_4^{4-} building unit and some of the more complex resulting structures.

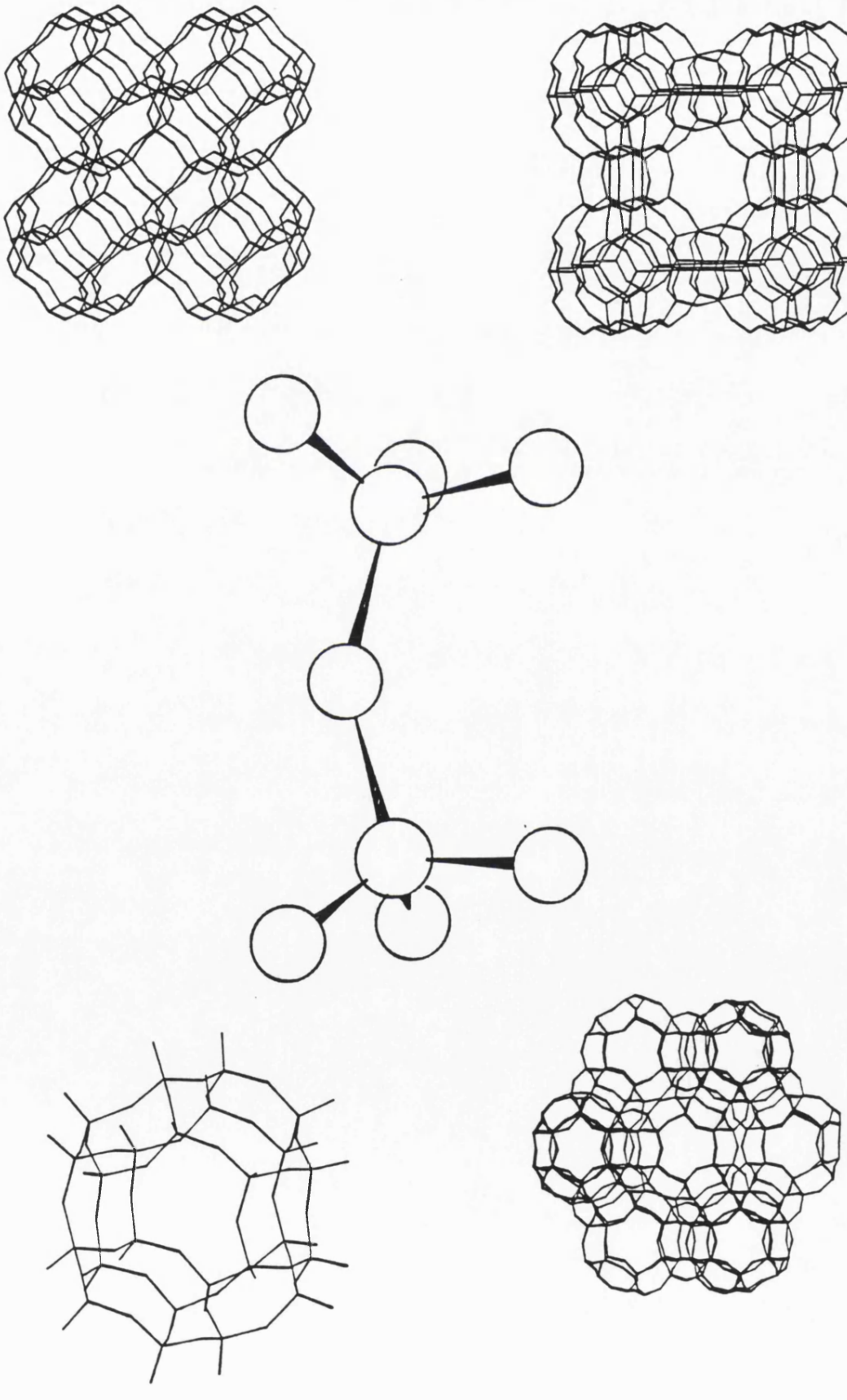

These low density microporous structures are metastable with respect to more dense close packed structures for example the tetrahedrally co-ordinated α-quartz structure[19] in the case of a SiO_2 or rutile[20], which is an octahedrally co-ordinated structure adopted by GeO_2, (as well as the quartz structure). Figure 1.1.2 depicts the two contrasting types of crystal structure, that of α-quartz, and below the more complex and structurally interesting metastable states of Mordenite[21], Silicalite-I[22], and Zeolite-Y[23]; the tetrahedral building units are described as solid polygons, with the T atom defined at the centre and the oxygen ions at the apices.

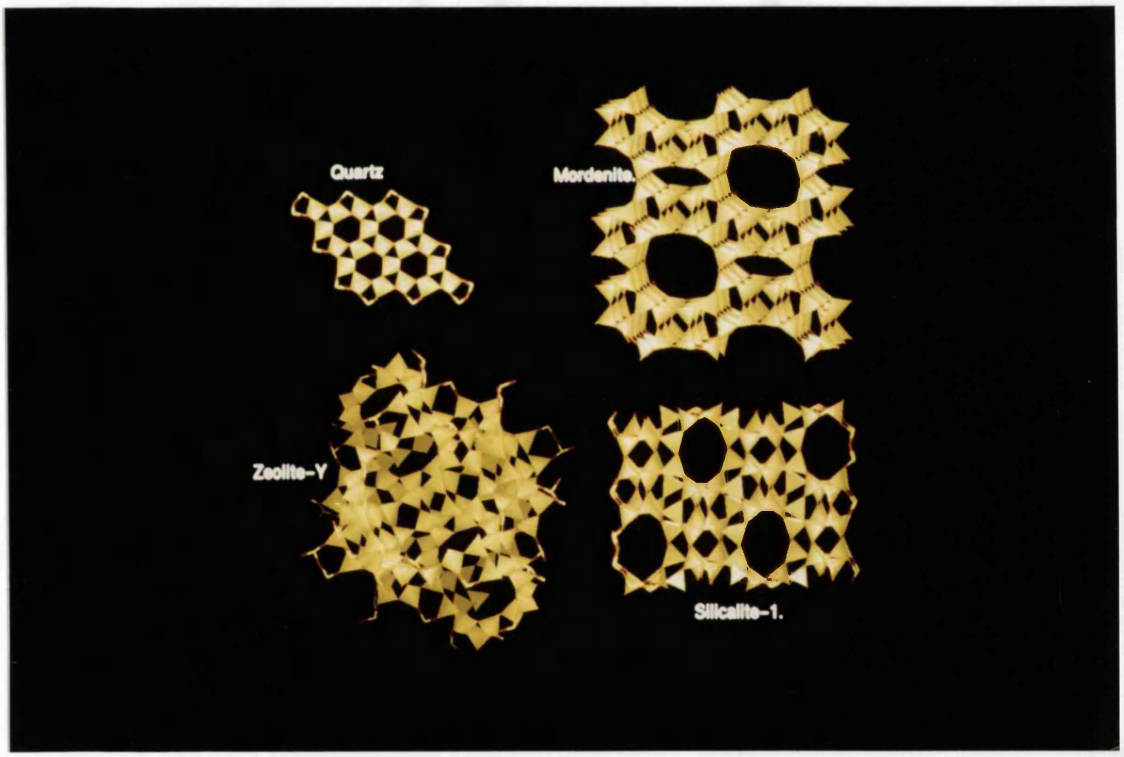

Figure 1.1.2 : A polygon description of the most dense structure, α-quartz above and below, the less dense Mordenite, Silicalite-I and Zeolite-Y topologies.

The structures shown here are only a few of many microporous topologies and indeed, recently large pore size structures have been synthesised; firstly with Cloverite[24] a Gallophosphate with a pore dimension of 13.2Å and more recently a large meso-pore[25], which has a reported pore size in-excess of 25Å, (although this structure does seem to lack well defined order along the *c* axis.) Figure 1.1.3 summaries the pore size and it's corresponding structure and also includes the date on which this structure was reported in the open literature.

This brief overview demonstrates how the field of solid state catalysis is rapidly expanding, as are the numbers and sizes of structures investigated, yet the discovery of new reactions or catalytic processes remains very much a "hit and miss" affair and thus computational chemistry is being increasing used to probe the details of the structure, properties an reactions and indeed to explore new and more innovative reactions prior to an experimental investigation.

Figure 1.1.3 : A selection of the larger pore structures and the date on which they appeared in the literature.

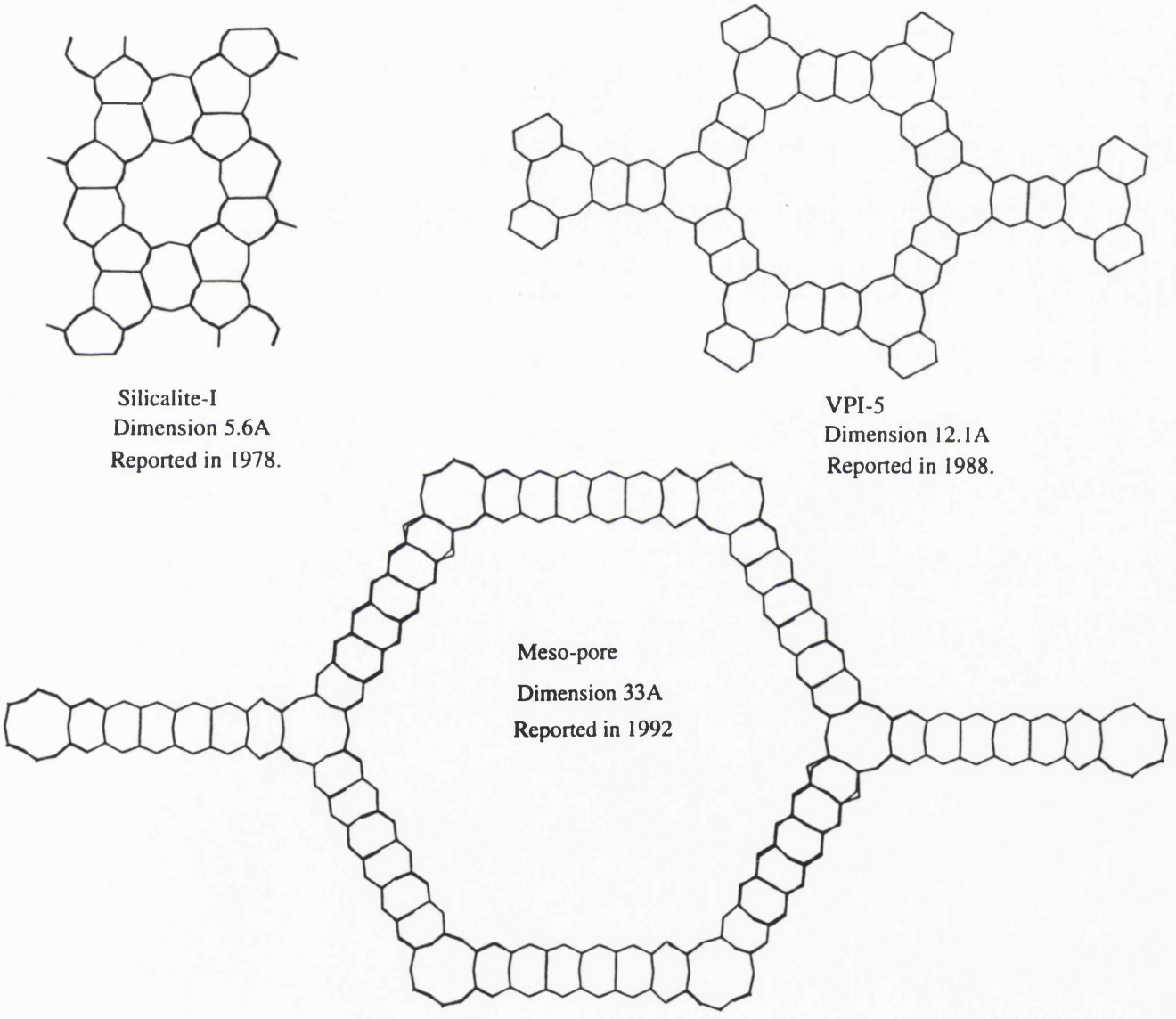

1.2 Scope of this thesis.

The introduction of aluminium into a zeolite framework causes several problems in modelling, first of all, in most structure refinements no explicit aluminium atom positions are given only positions of T atoms that could be partially occupied by aluminium. Thus in the structural investigation of Ni-Na-Zeolite-Y, reported in chapter 3, a number of different models were proposed for the possible different aluminium environments and the effect that such spatial arrangements have on the lattice perturbations. This investigation was extended to include calculation of the IR. spectra and the way in which different models could be combined to represent the experimental IR. spectra, in which many possible aluminium distributions are represented. These studies employed interatomic potentials techniques to calculate atomic positions within the zeolite framework, although most calculations employed static energy minimisation techniques, and so the resulting structures are appropriate to zero Kelvin (neglecting zero point effects). However, use of the Molecular Dynamics, MD, technique allows thermal effects to be included and in chapter 3.3, MD has been successfully applied in the investigation of a cation substituted zeolite at finite temperatures.

In chapter 4, we present a comprehensive step by step investigation of a complex catalytic cycle, that of the cyclotrimerisation of acetylene to form benzene in the presence of Ni-Zeolite-Y. In this catalytic system, which has been extensively studied by XRD[26] and EXAFS[27], the nickel cations migrated out of a very stable double hexagonal prism and into the large ligand-accessible supercage, following which the acetylene molecules undergo a relatively clean trimerisation to benzene, during which the cations are reduced to Ni^{+} and then once the reaction is completed are oxidised back to the Ni^{2+}. If the catalyst is subsequently dehydrated, the cations migrate back into the prism site, also termed the S_1 site.

The predictive capacity of computational chemistry is illustrated by the investigation of Ge containing zeolite lattices, which as discussed in chapter 5, form

stable solid solutions. Indeed using computational techniques, it has been possible to investigate the phase change from the α-quartz to the rutile structure as a function of Ge mole fraction contained in the zeolite framework. The properties of the intermediate structures, (IR. spectra and XRD) patterns have been calculated.

In chapter 6, we investigate docking small flexible molecules into large macrostructures where we overcome the problems of multiple minima by using a blend of Molecular Dynamics, Monte Carlo and lattice energy minimisation. This type of approach is particularly useful in acquiring an insight into the potential use of a particular zeolite structure to separate out different isomers or even enantiomers, for which purpose zeolites have been used for a number of years.[28] A typical example which reflects this property is firstly the Parex process[29] which exploits zeolite-X or Y as sorbates in the separation of aromatic C_8 isomers; while a good examples of a catalytic shape selective separation is provided by the isomerisation of metaxylene to paraxylene by ZSM-5[30]. Yet little is known concerning the detailed behaviour of sorbants in these materials. In the present investigation, we docked n-alkanes and 1-n-alkenes into two very different pore shape structures. We also investigate the successive loading of methane molecules into several structures and study structures and energies as a function of loading.

Zeolite synthesis has for the majority of time been based upon techniques using aqueous gel environments[31]. However, recently Bibby *et al*[32] have used an F^- gel based synthesis to great effect on a new group of interesting structures. One such structure is Octadecasil[33], a purely siliceous clathrasil, which has an F^- anion trapped inside a double four-ring cage; in chapter 7 we investigate this system via classical as well as *ab-initio* simulations. Indeed, the calculations have been extended to include potential ion-exchanged materials, as well as framework only, aluminated and protonated structures. This chapter uses most of the computational techniques currently being applied and represents a change of direction for theoretical chemistry, whereby a number of different techniques are applied to a system of interest and not a number of different systems applied to a technique of interest.

1.3 References.

1 Thomas J.M.; *Sci. Am.*, **4**, 112, (1992).

2 John C.S.; Clark D.M.; Maxwell I.E., in "*Perspectives in catalysis: a chemistry for the 21st century monograph*"; eds. Thomas J.M.; Zamaraev K.I.; Blackwell Scientific, Oxford, (1992).

3 Sankar G.; Wright P.A.; Natarajan S.; Thomas J.M.; Greaves G.N.; Dent A.J.; Dobson B.R.; Ramsdale C.A.; Jones R.H.; *J. Phys. Chem.*, **97**, 9550, (1993).

4 Clausen B.S.; Grabuek L.; Steffensen G.; Hansen P.L. Topsoe H.; *Catal. Lett.*; **1**, 23, (1993).

5 Solomon J.L.; Madix R.J.; Stohr J.; *Surface Science*, **12**, 255, (1991).

6 Xu H.; Uvdul P.; Friend C.M.; Stohr J.; *Surface Science*; **1** 599, (1993).

7 Kneller G.R.; Dosher W.; Settles M.; Cusack S.; Smith J.C.; *J. Chem. Phys.*, **12**, 8864, (1992).

8 Jones R.H.; Chen J.; Thomas J.M.; George A.R.; Hursthouse M.; Xu R.; Li S.; Lu Y.; Yang G.; *Materials*, **4**, 808, (1992).

9 Shannon M.D.; Casci J.L.; Cox P.A.; Andrews S.J.; *Nature*, **353**, 6343, (1991).

10 Thomas J.M.; Chen J.; George A.R.; *Chemistry in Britain*, **28**, 991, (1992).

11 Moscou L. in "*Introduction to zeolite science and practice.*", van Bekkum H.; Flanigen E.M.; Jansen J.C. eds.; *Stud. Surf. Sci. Catal.*, **58**, 1, (1991).

12 Mc.Bain J.W., "*The sorption of gases and vapours by solids*", Rutledge and sons. London, (1932).

13 Breck D.W.; "*Zeolite Molecular Sieves*", J. Wiley & Sons, N.York, 663, (1984).

14 Barthameuf D.; Derouane E.G.; Holderich W.F.; NATO Asi Series B, **221**, Plenum Press. N.York,, 319, (1990).

15 Eigen M.; *Angew. Chem. Int. Edn. Engl.*, **3**, 1, (1964).

16 Williams R.J.P.; *Pure appl. Chem.*, **54**, 1889, (1982).

17 Cronstedt A.F.; *Akad. Handl. Stockholm.* **18**, 120, (1756).

18 Meier W.M.; Olson D.H.; "*Atlas os zeolite structure types*", Butterworths, London, (1992).

19 Wyckoff, "*Crystal Structures*", **1**, 312, Interscience, Wiley & Sons, N. York, (1965).

20 Wyckoff, "*Crystal Structures*", **1**, 251, Interscience, Wiley & Sons, N. York, (1965).

21 Meier W.M.; *Z. Kristallogr*, **115**, 439, (1961).

22 Flanigen E.M.; Bennett J.M.; Grose R.W.; Cohr J.P.; Patton R.L.; Kirchner R.M.; Smith J.V.; *Nature*, **271**, 512, (1978).

23 Costenoble M.L.; Morlier J.W.; Uytterhoven , *J.C.S. Farad. Trans.*, **72**, 1877, (1976).

24 Eastermann M.; McCusker L.B.; Baerkocher C.H.; Merrouche A.; *Nature*, **352**, 320, (1991).

25 Kresge C.T.; Leonowicz M.E.; Roth W.J.; Vortuli J.C.; Beck J.S.; *Nature*, **359**, 710, (1992).

26 Thomas J.M.; *Angew. Chem. Adv. Mater.*, **101**, 1105, (1989).

27 Couves J.W. et al.; *Adv. Mater.*, **2**, 181, (1990).

28 Newsam J.M.; "*Solid state Chemistry Vol. 2: Compounds*"; Cheetham A.K.; Day P. eds; Oxford University Press; (1990).

29 Ruthven D.M.; "*Principles of Absorption and Adsorption Process*"; Wiley-Interscience, New York, (1984).

30 Chen N.Y.; Gorring R.L.; Ireland H.R.R.; *Oil Gas J.*; **75**, 165, (1977).

31 Occelli M.L.; Robson H.E.; "*Zeolite Synthesis*"; ACS Symposium Series **398**, (1989).

32 Bibby D.M.; Dale M.P.; *Nature*, **317**, 157, (1985).

33 Caullet P.; Guth J.L.; Hazm J.; Lamblin J.M.; Geis H.; *Eur. J. Solid State Inorg. Chem.*, **28**, 345, (1991).

Chapter 2.

Methodology.

2.0 Introduction.

The field of computational chemistry has emerged from the early theoretical beginnings of the 1930's and 1940's. Many techniques employ interatomic potentials from which predictions of structures, energies and dynamics may be made using a variety of simulation formulations. Landmarks in the field were the work of Alder *et al*[1] who first derived the methodology of Molecular Dynamics and the work of Metropolis *et al*[2] who formulated the Monte Carlo Importance Sampling Algorithm. These methodologies all work within the Born-Oppenheimer approximation[3], that is the electronic distributions follow instantaneously the nuclear motion. Indeed, this approximation is implicit in approaches in which the forces acting between the atoms are described by interatomic potentials. However, with the continuing advances in computer architecture and "raw" processing power, it is becoming increasing possible to use first principles *ab-initio,* techniques for large systems. Indeed, with the emergence of the Car-Parrinello technique[4], it is now possible to remove the Born-Oppenheimer approximation and to follow simultaneously both nuclear and electronic motions.

This chapter presents a brief outline of the techniques used in this work and serves as a methodological base, upon which much of the work presented within this thesis builds.

2.1 Inter-atomic Forces.

Interatomic potentials describe in analytical and numerical terms the total energy of an arrangement of atoms as a function of their nuclear co-ordinates. The functional forms can range from the simple harmonic form to Morse functions[5], Lennard-Jones[6,7] and Buckingham[8] functions to name but a few. Transferability between different systems is clearly most desirable for a set of potential parameters.

The types of potential model may be broken down into two broad categories. First are molecular mechanics forcefields in which the energy is given as a function of bond lengths, angles, torsional planes and other cross-terms which are described explicitly for the particular system and therefore an appropriate different potential form exists for each system. The second approach focuses on atoms or ions rather than bonds and is particularly useful for extended solids where bonds are not specifically defined, although the potential contains two-body and if necessary three-body terms. Born model potentials for ionic solids provide the best example of this latter category. An important distinction is that the Born model and related potentials have a uniquely defined zero for all systems. This is in stark contrast to a Molecular Mechanics approach where the absolute energy of a molecule or system has no intrinsic meaning, because each forcefield has a different zero energy point for each molecule and thus energetic comparisons can be made only between different conformations of each molecule. In the sections which follow we concentrate first on Born model potentials which are more appropriate for the simulation studies on solids reported later in this thesis and then on molecular mechanics forcefields which are needed for modelling molecular conformations.

2.1.1 Potential Functions in Born Model Potentials.

As previously discussed potentials comprise a long range Coulombic interaction and short range two-body and higher order terms. The summation of the interactions between all atoms in the system gives the potential energy of the system.

$$E_{Total} = \sum_{i}\left(\sum_{j,i\neq j} f\{Coulombic(i,j)\} + \sum_{j,i\neq j} f\{Two-body(i,j)\} + \sum_{l,j\neq i,j\neq(i,j)} f\{Three-body(i,j,l)\} \right) \quad (2.1.1)$$

The first term is the Coulombic term corresponding to the electrostatic interaction between each particle. This includes contributions from monopole-monopole, monopole-dipole, dipole-dipole and higher order terms, though most of the calculations presented here only consider the monopole-monopole Coulombic contribution. The second term contains the two-body interactions, which include Pauli repulsion between neighbours and van der Waals attraction. Next is a three-body term which depends on the deviation of the bond angle from an equilibrium value, (e.g. the bending of an O-Si-O bond in a tetrahedral group.) Higher order terms are not generally included in this type of potential model.

Into the general equation, (2.1.1), we can substitute specific functional forms, which are used to represent some of the interatomic interactions. In this thesis a widely used expression will be :-

$$E_{Total} = \sum_{i}\left(\sum_{j,j\neq i} \frac{q_i q_j}{r_{ij}} + \sum_{j,j\neq i}\left[A_{ij} \exp\left\{\frac{-r_{ij}}{\rho_{ij}}\right\} - \frac{C_{ij}}{r_{ij}^6}\right] + \sum_{l,j\neq i,l\neq(i,j)} k_{ijl}\left[\theta_{ijl} - \theta_{ijl}^{o}\right]^2 \right) \quad (2.1.2)$$

q_i = Charge on atom i.

r_{ij} = Distance between atoms i and j.

A_{ij} ρ_{ij} C_{ij} = Parameters of the Buckingham or '6-exp' function.

θ_{ijl} = Angle between bonds ij and il. θ_{ijl}^{o} denotes the equilibrium angle.

k_{ijl} = Three-body force constant.

The Coulombic interaction corresponds to the interaction between the point charges on each atom and does not contain any of the higher electrostatic terms, such as the monopole-monopole and dipole-dipole interactions, (although a representation of polarisability can be included via the Shell model methodology, discussed in section 2.1.2.) Simple point charge models are currently being superseded by a more detailed treatment of the electrostatic terms using Distributed Multipole Analysis[9]. In this technique, a spherical harmonic expansion of the electrostatic potential around each atom is used. The program DMAREL[10], which is currently under development will incorporate this approach in a lattice simulation code. However, for the systems examined in this thesis, models which assign point charges to atom centres are acceptable.

Due to the long range nature of the electrostatic terms, $E_{Coulombic} \propto \frac{1}{r}$, the summation of these terms converges very slowly in real space. However, several approaches are available to overcome this problem. The Ewald[11,12] technique sums the electrostatic interactions in both real and reciprocal space, which leads to much more rapid convergence, than by a direct real space summation. The Coulombic term of the potential then takes the form : -

$$E_{Coulombic} = \frac{1}{2}\sum_{i=1}^{N}\sum_{j=1}^{N} q_i q_j F(\mathbf{r}_{ij}) \qquad (2.1.3)$$

where F is given by:

$$F(\mathbf{r}_{ij}) = \frac{2}{\pi \upsilon}\sum_{\mathbf{h}}^{N}{}' \frac{1}{|\mathbf{h}|^2}\exp\left[-\frac{\pi^2|\mathbf{h}|^2}{\eta^2}\right]\cos(2\pi \mathbf{h}.\mathbf{r}_{ij}) + \sum_{\mathbf{l}} \frac{erfc(\eta|\mathbf{r}_{ij}+\mathbf{l}|)}{|\mathbf{r}_{ij}+\mathbf{l}|} - \frac{2\eta}{\sqrt{\pi}}\delta_{ij}\delta_{|\mathbf{l}|0} \qquad (2.1.4)$$

with

N = Number of ions per unit cell.

υ = Unit cell volume.

$\mathbf{h}$ = Reciprocal lattice vector.

$\mathbf{l}$ = Direct lattice vector.

$erfc$ = Complementary error function $\frac{2}{\sqrt{\pi}}\int_{y}^{\infty}\exp(-t^2)\partial t$.

$\sum'$ = Sum over non-centrosymmetric lattice vectors.

The value η of which optimises the convergence of both summations is given by[13], $\sqrt[6]{N}\frac{\sqrt{\pi}}{\sqrt[3]{\upsilon}}$. The cut-off value for the direct lattice sum is given by $\frac{\sqrt{\log C}}{\eta}$, the cut-off value for the reciprocal lattice sum by $\frac{\eta\sqrt{\log C}}{\pi}$. C is the Madelung sum accuracy which usually has a value of around 10^6.

The two-body short range potential can use Lennard-Jones, Buckingham or other functional forms. Analytical expressions are desirable because continuous derivatives of the functional form are required for the calculation of some properties. In polar crystals such as silicates, the Buckingham term is generally favoured and indeed was incorporated in equation (2.1.2); it comprises of a Born type repulsion term and an r^{-6} attractive term. The r^{-6} term should not necessarily be identified with the dispersive attraction between non-bonded atoms; it may include other attractive forces such as partial covalent bonding.

The three-body bond-bending term is harmonic about the equilibrium angle, θ^{o}_{ijl}, defined between bonds ij and il. Functional forms are available for anharmonic bond bending terms, though these tend to be used for more anisotropic systems and have an associated increase in computational cost due to the evaluation of a more complex functional form.

The energies acquired from such calculations can be compared, via a thermodynamic cycle to experimental heats of formation or other enthalpy measurements which is in contrast to the results of Molecular Mechanics studies where the calculated energy has no absolute significance; it simply gives the energy relative to the equilibrium configuration of the molecule.

2.1.2 Shell Model Treatment of Polarisation.

As discussed in the previous sections, it is possible to include a representation of ionic polarisation by the Shell model[14]. The polarizable atoms consist of a charged point mass, usually termed the core and a massless isotropically charged shell, the two being connected by an harmonic spring, so that the self energy of the polarised atom is given by $E_{Self} = \frac{1}{2} k_{shell} x^2$, where x is the core-shell displacement as schematically represented in figure 2.1.1.

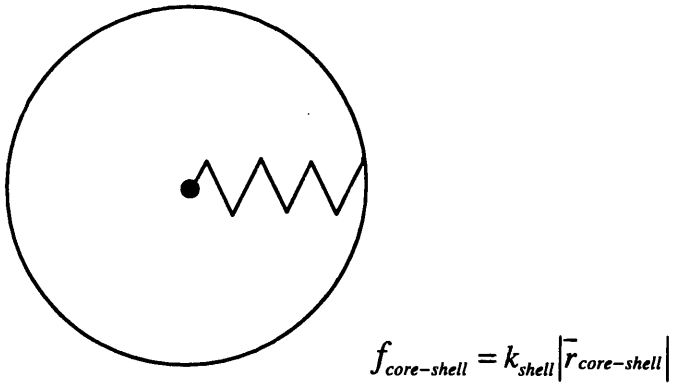

Figure 2.1.1 : Diagrammatic representation of the Shell model. (Note the shell is in fact a point entity).

More complex models have been developed such as the spherical Gaussian charge distribution of Iishi *et al.*[15], or the elliptical deformable shell models[16]. A crucial feature of all models is that the short-range interaction with other ions is only calculated via the shells, which allows coupling of the short range interactions and the polarisation term.

A shell model is used, when the electronic polarizability of the free ion is significant and hence significant deformations of the electron clouds may occur. The electronic polarizability, α, can be related to the charge on the shell, q_{shell}, and to the force constant, k_{shell}, via the relationship, (2.1.5).

$$\alpha = \frac{(q_{shell})^2}{k_{shell}} \qquad (2.1.5)$$

The use of massless shells has other far reaching implications, in particular it cannot straightforwardly be implemented in the Molecular Dynamics, methodology, as the Born-Oppenheimer approximation requires that shells are always in full equilibrium with respect to the cores. However, recent work of Gillan *et al*[17] has realised the possibility of Shell model MD either by performing shell equilibration each time step, or by using a small mass for the shells.

2.1.3 Molecular Mechanics: A Forcefield Type of Approach.

Molecular mechanics, as noted above starts from the specification of bonds, bond angles, torsional angles, etc. within the system and to which all the potential energy functions are related. Indeed, the potentials typically have simple analytical terms that provide an energetic penalty for deviations from the associated equilibrium values, together with terms for the long range Coulombic and classical van der Waals non-bonding interactions. Parameters are normally obtained by empirically fitting to known molecular properties and as such, the forcefield interpolates and extrapolates from the experimental data of the small set of molecules which are used in the parameterisation, to a larger set of related molecules and structures. There is no general forcefield suitable for every interaction. Indeed, forcefields are usually developed for specific types of molecules and their use with other systems will often yield poor results, as they are being employed beyond the original range of molecular parameters for which they were developed.

There are now several standard forcefields, each considered suitable for a certain area of molecular modelling; examples are MM2[18], AMBER[19] or CFF91[20,21]. The AMBER forcefield was parameterised against a number of compounds related to proteins and nucleic acids and hence is widely applied in biological modelling. Other more general forcefields such as MM2, require many experimental observables for the parameterisation and as such can restrict the applicability and transferability of the forcefield. However, with the emergence of reliable *ab-initio* calculations with large basis sets, a more rigorous methodology for the generation of the parameters is available. *Ab-initio* calculations can provide information about a molecule including energies and dipole moments for equilibrium geometries and force constants for vibrations. The forcefield is fitted to *ab-initio* data generated from many distorted structures of several model compounds for each functional group as in CFF91. Correction factors are sometimes required because of the known limitations of *ab-initio* calculations. The Hartree-Fock force constants for bond stretching, are

consistently about 10-20% too large due to the inadequate dissociation behaviour of the Hartree-Fock wave function[22].

The functional form used to describe each term varies between the different forcefields. For example, MM2 has both a quadratic and a cubic stretch term representing the variations in bond length, whereas AMBER only a quadratic stretch and CFF91 has both a Morse and harmonic functional form. AMBER, (Assisted Model Building and Energy Refinement), is one of the oldest and simplest forcefields, since it neglects the formulation and representation of cross terms. It comprises the following terms :-

$$E_{Total} = \sum_{b} k_b (b - b^o)^2 + \sum_{\theta} H_\theta (\theta - \theta^o)^2 + \sum_{\varphi} \frac{V_n}{2}\left(1 + Cos\{n\varphi - \varphi^o\}\right) + \sum_{i} \sum_{j,j>i} \left(\frac{A_{ij}}{r_{ij}^{12}} - \frac{B_{ij}}{r_{ij}^{6}} \right) + \sum_{i} \sum_{j,j>i} \frac{q_i q_j}{r_{ij}} \qquad (2.1.6)$$

b, b^o = Bond length, equilibrium bond length.

k_b = Bond length force constant.

H_θ = Bond angle force constant.

θ, θ^o = Bond angle, equilibrium bond angle of atoms geminal to each other.

V_n = Torsional force constant

φ, φ^o = Torsion and equilibrium angle of atoms vicinal to each other.

n = Periodicity of the torsional bond.

A_{ij}, B_{ij} = Terms relating to the van der Waals non-bonded interaction.

q_i = The effective charge on atom i.

Despite the wide variation in the details of the different forcefields, it is possible to represent the general features graphically as shown in figure 2.1.2.

Figure 2.1.2 : Graphic illustration of functional terms in a Molecular Mechanics type forcefield.

1. 2.

3. 4.

+ $\sum$ Cross terms which represent coupling between deformations of internal coordinates.

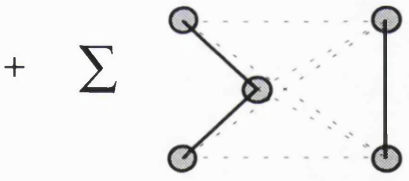

5.

1. 1-2 bond stretching term.
2. Bond angle deformation of atoms geminal to each other.
3. Torsion angle deformations of atoms vicinal to each other.
4. Out of planes or improper torsion angles, associated with maintaining the planarity of planar atoms.
5. Non-bonded van der Waals and Coulombic interactions.

The associated problem of evaluation and slowly convergent nature of the Coulombic interaction has been discussed in the previous section. The Molecular Mechanics methodology due to the definition of specific bonds and chemical interactions is more suited to molecular based systems and less to extended solids. However, the combination of these methodologies is needed when one considers molecules within extended solids.

2.2 Energy Minimisation.

The previous section focused on the representation of the potential energy surface and the different ways in which it can be approximated. The technique of energy minimisation relates to static information about the system (and thus strictly to the system at zero Kelvin) and essentially consists of exploring the potential energy surface to locate configurations of minimum energy. This involves finding a point in configurational space where the force on each atom is zero, that is where :-

$$\frac{\partial V}{\partial r_i} = 0 \ : \ V = \text{Potential Energy, } r_i \ = \text{co-ordinate system.} \qquad (2.2.1)$$

Minimisation procedures evidently require first an equation describing the energy of the system as a function of its co-ordinates. Iterative numerical procedures are then used to search for the minimum; these normally involve calculation of the derivative of the energy with respect to atomic co-ordinates.

Several algorithms are available. These include Steepest descent[23], Conjugate Gradients[24] and the Newton-Raphson method[25,26]. The outline of each methodology is briefly described below:-

Steepest Descent: in this minimisation algorithm, the vector of variables x whose value is $x_{(k+1)}$ for the $(k+1)^{th}$ iteration are directly related to the previous values determined for the $(k)^{th}$ iteration.

$$\vec{x}_{(k+1)} = \vec{x}_{(k)} - \alpha_k \left(\frac{\partial E}{\partial x} \right)_{(k)} \qquad (2.2.2)$$

Where α_k is a numerical constant chosen for each iteration in order to increase the efficiency of the procedure.

Conjugate Gradients: the algorithm, as the name suggests, uses information derived from the previous values of the gradients to speed up the optimisation. The equation can be formulated as follows :-

$$\vec{x}_{(k+1)} = \vec{x}_{(k)} + \alpha_k \vec{S}_{(k)} \tag{2.2.3}$$

where α_k is a variable numerical constant.

$$\vec{S}_{(k)} = -\vec{g}_{(k-1)} + \beta_k \vec{S}_{(k-1)} \tag{2.2.4}$$

and

$$\beta_k = \frac{\vec{g}^T_{(k-1)} \cdot \vec{g}_{(k-1)}}{\vec{g}^T_{(k-2)} \cdot \vec{g}_{(k-2)}} \tag{2.2.5}$$

$\vec{g}_{(k)}$ are vectors whose components are derivatives with respect to individual co-ordinates, $\frac{\partial E}{\partial x}$ and the indice ^{T} indicates the transpose of the vector.

Newton-Raphson: in this formulation the rate of convergence is increased by knowledge of the second derivatives and the minimisation direction proceeds according to :-

$$\vec{x}_{(k+1)} = \vec{x}_{(k)} - \vec{H}_{(k)} \cdot \vec{g}_{(k)} \ , \tag{2.2.6}$$

where $\vec{g}_{(k)}$ is as previously defined and $\vec{H}_{(k)}$ is the inverse of the second derivative matrix, $W_{ij} = \frac{\partial^2 E}{\partial x_i \partial x_j}$. In the implementation of this algorithm the $\vec{H}_{(k)}$ matrix is not recalculated every iteration, but instead, is updated via algorithms such as the Davidson-Fletcher-Powell algorithm and typically the $\vec{H}_{(k)}$ is recalculated every 10-20 iterations.

Each algorithm has advantages and disadvantages: the steepest descent and Conjugate Gradient methods only use the first derivatives, hence less memory is needed but they require a larger number of iterations; whilst Newton-Raphson methods use the information on second derivatives in the Hessian Matrix, $\vec{H}_{(k)}$, (which as noted, is the inverse of the second derivative matrix), as a method of reducing the number of iterations but at the expense of an increased memory requirement. The minimisation algorithm is chosen to match the nature and size of the system, although the use of one algorithm in the early stages of minimisation, followed by a switch to another near completion is common.

In modelling solids, we must of course describe the periodicity, which is achieved using Periodic Boundary Conditions, (PBC), and ensures the removal of the problems associated with edge effects. An excellent review of the theory and application of such procedures can be found in Allen and Tildesley[27]. In carrying out minimisation on solids it is necessary to decide whether the dimensions of the box, (which is repeated periodically) should be varied, i.e. whether to use "constant volume minimisation" or minimisation to constant pressure. When minimising to constant volume, the repeating box, i.e. unit cell vectors, are held fixed and only the internal degrees of freedom allowed to vary. In a constant pressure minimisation, the cell dimension and angles as well as the internal co-ordinates are allowed to vary until zero force is achieved.

Several codes are available, for performing energy minimisation routinely using the techniques and algorithms described above. DISCOVER[28] (developed and distributed by Biosym Technologies) was used to perform energy minimisation using the molecular mechanics type methodologies and both THBREL[29,30] and GULP[31] were employed for the lattice energy minimisation and subsequent calculation of dielectric and elastic constants for the solid state calculations in which PBC's were required. The solid state lattice energy minimisation codes, THBREL and GULP use a variety of user accessible minimisation algorithms and potential models, together

with a Shell model methodology. They also embody an Ewald summation to perform the long-range Coulombic summations. GULP is particularly useful in performing minimisation of more complex systems as it permits the optimisation of certain parameters whilst others are held constant. Section 5.2 exploits this particular feature for the computational modelling of the phase change from the α-quartz to the rutile structure in pure GeO_2.

2.3 Defect Simulations.

In many systems of experimental interest, defects play a vital role; these include point defects, line defects (e.g. dislocations) and planar defects (e.g. shear planes). However, the simulation techniques for the solid state systems, so far described invoke the use of PBC techniques, which require a repeating unit cell and are thus at first sight unsuitable for the simulation of defective systems. Several techniques have emerged for the simulation of defects and the accurate treatment of the lattice relaxation around the defective species, whether a substitutional interstitial or vacancy defect. First, the supercell technique developed by Leslie *et al*[32] in which the defect is surrounded by a suitable size region of perfect structure after which the PBC technique is invoked. This in effect repeats the defect but at distances and concentrations for which interactions are considered unimportant. The technique requires large computational resources due to the effective size of the periodic box and this box size requirement is substantially increased if the defect is charged, due to the long range nature of Coulombic forces.

The alternative and more traditional approach to defect simulations is to use an infinite dilution technique, based on the Mott-Littleton approximation[33], developed by Lidiard *et al*[34] and coded by Norgett[35]. In this technique a defect is introduced into a crystal, which extends to infinity, although only a certain proportion is represented explicitly. This method is based on a two region strategy with the crystal surrounding the defect being divided into two regions as depicted in figure 2.3.1.

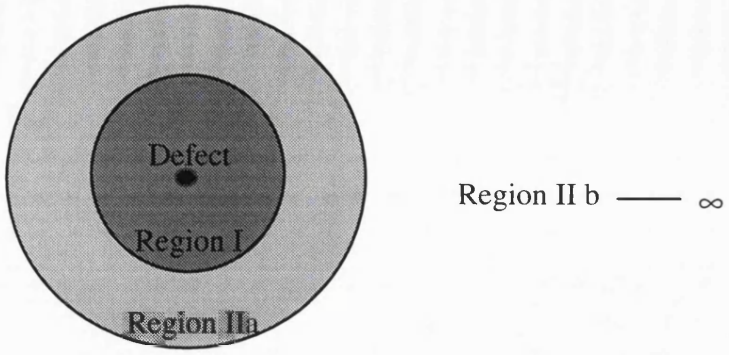

Figure 2.3.1 : Illustrates the two region strategy for defect calculation.

Region I is treated atomistically, since the forces exerted by the defect on this part of the surrounding lattice are strong. All the internal co-ordinates of region I ions are adjusted until the minimum energy configuration around the defect is achieved. The algorithms used for this procedure are typically the ones used for the energy minimisation procedures described above, although slight differences do exist[36]; the Newton-Raphson is again one of the most effective algorithms. The size of region I may have a marked effect on the calculated defect energy and thus the region's size is adjusted until little variation in the energy is observed with increase in the region size; a region I size of 150-300 particles is usually suitable for "convergence" . For region IIb, which extends to infinity, the crystal is assumed to respond as a dielectric continuum only to the net charge on the defect. This is an acceptable approximation since the forces are relatively weak and the responds to them may be treated by methods based on continuum theories. In the interface region, region IIa, the Mott-Littleton approximation is performed explicitly to calculate the displacements, as a sum of those due to all the charge defects in region I and for the explicit calculation of the I-IIa interaction.

The energy of the system can be represented as the sum of the different regions:-

$$E_{Total} = E_1(\vec{x},\vec{\varsigma}) + E_2(\vec{x},\vec{\varsigma}) + E_3(\vec{\varsigma}) \qquad (2.3.1)$$

where $E_1(\vec{x})$ = Energy of region I.

$E_3(\vec{\varsigma})$ = Energy of region IIb.

$E_2(\vec{x},\vec{\varsigma})$ = Interaction energy of region I and IIb.

With $\vec{x}$ being independent co-ordinates of region I and $\vec{\varsigma}$ being independent co-ordinates of region II. $E_3(\vec{\varsigma})$ is assumed to be a quadratic function of $\vec{\varsigma}$. Hence the region extending to infinity is treated by a continuum approximation.

$$E_3(\vec{\varsigma}) = \frac{1}{2}\vec{\varsigma}.\vec{A}.\vec{\varsigma} \quad \Rightarrow \frac{\partial E}{\partial \vec{\varsigma}} = \left.\frac{\partial E_2(\vec{x},\vec{\varsigma})}{\partial \vec{\varsigma}}\right|_{\vec{\varsigma}=\vec{\varsigma}_e} + \vec{A}.\vec{\varsigma} \ , \qquad (2.3.2)$$

where $\vec{\varsigma}_e$ are the equilibrium values for $\vec{\varsigma}$ corresponding to the relaxed value of $\vec{x}$. Hence an alternative form of the total energy can be derived which is independent of region IIb and only involves summation over pairs of ions in region I together with the interaction of I and IIa.

$$E_{Total} = E_1(\vec{x}) + E_2(\vec{x},\vec{\varsigma}) - \frac{1}{2}\left.\frac{\partial E_2(\vec{x},\vec{\varsigma})}{\partial \vec{\varsigma}}\right|_{\vec{\varsigma}=\vec{\varsigma}_e} .\vec{\varsigma}_e \qquad (2.3.4)$$

The code CASCADE[37], based on the above methodology, with Newton-Raphson minimisation, has been applied to the simulation of the defective systems described in chapter 3.1 and chapter 7.1.

2.4 Lattice Dynamics.

The previous simulation techniques described above are all concerned with the minimum energy configuration of a static system and as noted, strictly represent the structure at zero degrees Kelvin. "Static" models of course exclude any explicit description of thermal effects. However, we may calculate thermodynamic properties by calculating vibrational frequencies in periodic structures, using methods pioneered by Born and Huang[38]. The major underlying assumption of the approach is the quasi-harmonic approximation, which assumes that the vibrational modes in a solid are comprised of harmonic oscillators, whose temperature dependence can be fully accounted for by the temperature variation of the cell volume. The methodology will be briefly outlined below, more detailed discussions are available[39] elsewhere. From the calculation of vibrational frequencies we may calculate the entropy, free energy, heat capacity and the thermal expansion coefficient.

2.4.1 Derivation of Phonon Frequencies.

The potential of a system of N coupled with oscillators, for small harmonic oscillations, is given by equation 2.4.1.

$$V = \frac{1}{2}\sum_{j=1}^{N}\sum_{k=1}^{N}\vec{\mathbf{q}}_j^{T}\mathbf{V}_{jk}\vec{\mathbf{q}}_k \qquad (2.4.1)$$

$\vec{\mathbf{q}}_k$ = The mass weighted displacement vectors from the equilibrium position of k with mass m_k.

$$\vec{\mathbf{q}}_j \equiv \sqrt{m_j}\begin{bmatrix}\Delta x_j\\ \Delta y_j\\ \Delta z_j\end{bmatrix}$$

$\vec{\mathbf{q}}_j^{T}$ = The transpose matrix of $\vec{\mathbf{q}}_j$.

$\mathbf{V}_{jk}$ = The force constant matrix.

The kinetic energy is given by equation 2.4.2,

$$T = \frac{1}{2}\sum_{j=1}^{N}\mathbf{p}_j^{T}\mathbf{p}_j \text{ where } \mathbf{p}_j \equiv \sqrt{m_j}\begin{bmatrix}\Delta\dot{x}_j\\ \Delta\dot{y}_j\\ \Delta\dot{z}_j\end{bmatrix} = \dot{\mathbf{q}}_j \qquad (2.4.2)$$

$\mathbf{p}_j$ is the mass weighted momentum vector of the j^{th} oscillator. The $\dot{\mathbf{q}}$ notation represents differentiation with respect to time. From equations 2.4.1 and 2.4.2, the Lagrangian, $L \equiv T - V$, the equation of motion can be solved :-

$$m\frac{\partial^2\vec{\mu}}{\partial t^2} = \frac{\partial V}{\partial\vec{\mu}} \text{ where } \vec{\mu} \text{ relates to displacements of the species } i \text{ or } j.$$

which in this case can be rewritten as :-

$$\frac{\partial\left(\frac{\partial L}{\partial \mathbf{p}_j}\right)}{\partial t} = \frac{\partial L}{\partial \vec{\mathbf{q}}_j} \tag{2.4.3}$$

The above formulation is applicable to both the rigid ion and shell models. In the case of the shell model, we have the added condition that, $\frac{\partial V}{\partial \vec{\omega}} = 0$ where $\vec{\omega}$ is the massless shell displacement corresponding to zero net force on the shells. The detailed solution of the equations of motion will not be reported here, but can be found in reference[40], although an example of the solution to a one-dimensional system composed on two different atoms is examined.

A chain containing two different types of atoms, (M_1, the mass of the heavier atom and M_2, the mass of the lighter) is connected by a spring with a force constant K, as depicted in figure 2.4.1.

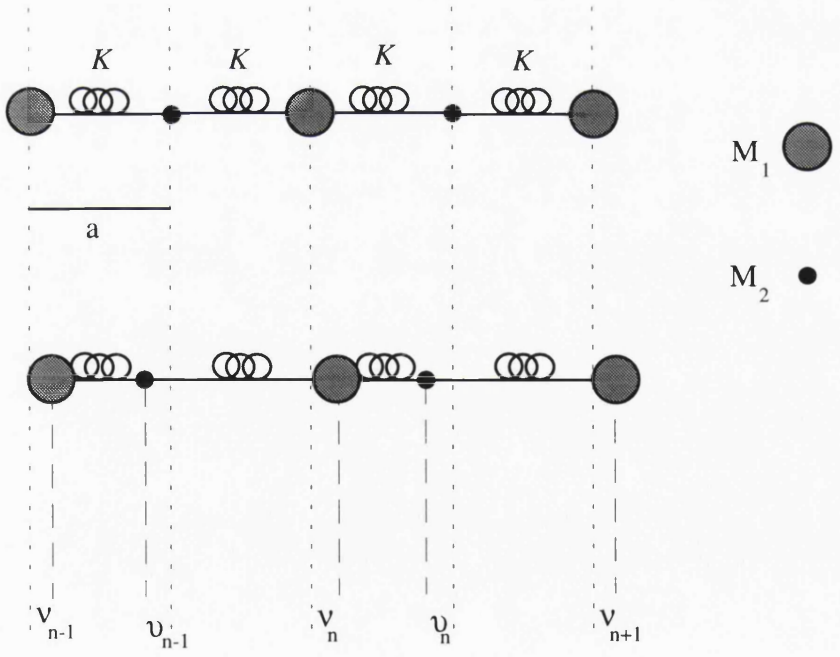

Figure 2.4.1 : A schematic diagram of a one-dimensional chain comprising of two different types of atoms.

Thus the potential energy of the system is given by :-

$$V=\sum_{n=1}^{N}\frac{K}{2}(\upsilon_n-\nu_n)^2+\frac{K}{2}(\nu_n-\upsilon_{n+1})^2 \qquad (2.4.4)$$

By differentiating equation 2.4.4 with respect to μ_n and υ_n, two equations of motion for μ_n and υ_n, are obtained and by substituting in the expressions ;

$$\upsilon_n=\upsilon\exp(i(2nka-\omega t)) \qquad (2.4.5)$$

$$\nu_n=\nu\exp(i((2n+1)ka-\omega t)) \qquad (2.4.6)$$

into the previous equations, the results are : -

$$-M_2\omega^2\upsilon=a(\nu(e^{ika}+e^{-ika})-2\upsilon) \qquad (2.4.7)$$

$$-M_1\omega^2\nu=a(\upsilon(e^{ika}+e^{-ika})-2\nu) \qquad (2.4.8)$$

These equations can be expressed in matrix form and by finding the determinate one can obtain the dispersion relation for the diatomic chain, which is : -

$$\omega^2=K\left(\frac{M_1+M_2}{M_1M_2}\right)\pm\left[\left(\frac{M_1+M_2}{M_1M_2}\right)-\left(\frac{2(1-\cos\{ka\})}{M_1M_2}\right)\right]^{\frac{1}{2}} \qquad (2.4.9)$$

There are two possible solution for a given value of K and such solutions are termed the optic or acoustic vibration mode in the dispersion curves. However, wave propagation in a complex solid is not solely via one-dimensional longitudinal motion, but rather via three different mutually perpendicular directions, one longitudinal and two transverse vibrations. Hence the theory of the one-dimensional model can be extended to that of real crystals with a few exceptions. The model must deal with transverse as well as longitudinal modes and the number of branches in the dispersion

curve is proportional to the number of degrees of freedom per unit cell. In general for a given value of K there are 3 acoustic branches and $3N-3$ optic modes, where N is the number of atoms in the unit cell. If the potential energy function contains a term relating to the electrostatic interactions, then further splitting occurs due to the long-range nature of this type of interaction.

The following is an example of a specific solution[41] for a model of a diatomic, cubic alkali-halide crystal having only a simple Coulombic interaction and nearest neighbour short range forces which for a wave vector at the zero boundary solution gives :-

$$\mu\ddot{w}_{LO} + Sw_{LO} = Ze\beta_{LO}P = -\frac{8\pi}{3}\frac{Z^2e^2}{\upsilon_a}w_{LO} \qquad (2.4.10)$$

$$\mu\ddot{w}_{TO} + Sw_{TO} = Ze\beta_{TO}P = \frac{4\pi}{3}\frac{Z^2e^2}{\upsilon_a}w_{TO} \qquad (2.4.11)$$

LO = Refers to the Longitudinal Optical mode.

TO = Refers to the Transversal Optical mode.

μ = Reduced mass.

w = Relative displacement of two ions.

S = Force constant derived from the short range potential.

Z = Charge on the ions.

P = Polarisation.

υ_a = Volume per oscillator.

$$\text{and } \beta_{LO} = -\frac{8\pi}{3} \; ; \; \beta_{TO} = \frac{4\pi}{3} \; ; \; P = \frac{Zew}{\upsilon_a}$$

Thus the expressions relating to the frequencies ω are :-

$$\mu\omega_{LO}^2 = S + \frac{8\pi Z^2e^2}{3\upsilon_a} \qquad (2.4.12)$$

$$\mu\omega_{TO}^2 = S - \frac{4\pi Z^2e^2}{3\upsilon_a} \qquad (2.4.13)$$

From the brief outline above, it is clearly possible to calculate all the vibrational frequencies in the crystal and at any point within the Brillouin zone. However, it is the post processing of these results which yields the required thermodynamic functions. An example is the heat capacity of the solid, which is given by, $C_v = k\sum_i^m \frac{(x^2 e^x)}{e^x - 1}$ with m = the total number of phonon frequencies and $x = \frac{h\omega_i}{kT}$. Such an equation involves the sum over all frequencies whilst the calculation of other properties only specific vibrational modes.

2.4.2 Group Theoretical Projection Methods.

From the large number of phonon frequencies, at all the points within the irreducible Brillouin zone, it is necessary to obtain only these frequencies and corresponding intensities that are either Infrared, (IR.), or, Raman active. For both Raman scattering and IR. absorption, the wavelength of the incidental beam is very long compared to the dimensions of the unit cell resulting in the wave vector, k, of the beam being very short with respect to the dimensions of the Brillouin zone. So only phonons near the centre of the Brillouin cell, k=0, are involved in these processes. This is called the k=0 approximation. However, longitudinal modes are inactive[42] to IR. and Raman excitation. Thus, the number of possible phonon modes which would be visible in either the IR. or Raman technique is greatly reduced. Group theoretical projection methods[43], described below, are used to separate out the IR. active, Raman active and inactive modes from the phonon modes of the primitive unit cell.

A vibration can in general be mapped either onto itself, commuted into its opposite or mapped via a linear combination with its partner (if it is a member of a degenerate pair or triplet), by various symmetry operations. These transpositions are those of the irreducible representations (or symmetry species) of the point group, appropriate to the structure. The number of vibrations in the crystal which relate to a certain symmetry species of the point group may be determined by factor group analysis, (FGA). Tables for 230 species and the associated FGA are available[44]. The resulting use of group theory which is described in detail in many texts[45], allows character tables for the relevant point groups to be constructed and also information concerning the activity of the modes in the IR. and Raman spectroscopy. A vibrational mode is IR. active for symmetry species pertaining to the translation T_x, T_y and/or T_z and Raman active for symmetry species which relate to the components of the polarisability tensor. These translation and components of the polarisability tensor are listed in the character tables of the relevant symmetry groups[46]. The

number of the calculated bands is usually larger than the number of bands observed, due mainly to the overlapping of many bands contained within the experimental spectra. In general, the total number of stretching modes including symmetric and asymmetric vibrations is equal to the number of bonds per unit cell.

Once one has derived the active modes, a vibrational density of states can also be derived and using the method of Kleinman and Spitzer[47] line intensities may be calculated. Infrared line intensities are calculated from the change in dipole moment that is caused by the vibrational displacements of ionic charges and Raman intensities are calculated using isotropic bond polarisabilities derived from atomic displacements. This thesis does not consider the calculated Raman spectra, as the codes available at the present time, do not allow optical relaxation (i.e. shell relaxation within the Shell model methodology) for the atoms displaced at the appropriate vectors. However, we report extensive studies of the infrared line intensities. These require the definition of an effective charge tensor for every atom *i*, although a more general form more widely used is given in equation (2.4.14) from reference [48] :-

$$I_k = \left| \sum_i q_i \bar{\mathbf{u}}_{ki} \right|^2 \qquad (2.4.14)$$

I_k = Infrared line intensity of mode *k*.

$\bar{\mathbf{u}}_{ki}$ = Displacement vector of atom *i* of mode *k*.

q_i = Charge on atom *i*.

Spectra calculated by the above method will have zero line width and to assist comparison to experiment, these calculated lines are each convoluted with a Gaussian line shape of half width $10cm^{-1}$. This half width was chosen to keep most of the calculated peaks discreet, a larger line width would have a "blurring" effect on the spectra and thus hide some less intense peaks. However, line widths of up to 75 cm^{-1} have been observed[49] and used in theoretical calculations[50], but because of our

interest in specific modes a moderate line width is taken, which remains constant with wavenumber.

An alternative approach to the calculation of IR. spectra has recently been reported by Demontis *et al*[51]. In this work, a Molecular Dynamics simulation (see chapter 2.5.1) is performed at an ambient temperature and the vibrational frequencies are calculated from the Fourier transform of the velocity auto-correlation function of the atoms involved in the simulation. The advantage of this approach is that the full anharmonicity of the potential energy surface can be examined, because the atoms are in motion and can sample the potential energy surface without constraints. In contrast, the atoms in the lattice dynamics are an assembly of harmonic oscillators at specific lattice sites. However, the Molecular Dynamics approach does not require the Group theoretical projection methods since only accessible conformational space is sampled due to Newton's Law of Motion being solved explicitly.

The work contained within this thesis used the codes, THBPHON[52] to perform the vibrational frequency calculations for the energetically minimised structures and INTEN[53], to perform the Group theoretical analysis and the corresponding intensity calculations.

2.5 Dynamical Motion.

The methodology outlined in the previous sections, provides a way of computing a potential energy surface around the minimum energy surface, from which a lattice dynamical analysis may follow. Indeed with such an approach, one can investigate many chemical phenomena relating to the *static* system and to properties depending on harmonic motions around a minimum. However, the explicit inclusion of temperature effects is of major interest and is possible via two predominant methodologies. The Monte Carlo, MC, method which randomly moves atoms in such a way as to generate an ensemble of configurations within the possible configurational space available; the resulting ensemble corresponds to a specific temperature. It should be noted that MC does not yield any information regarding the time evolution of the system and as such can only show equilibrium, time-averaged properties. In contrast, the Molecular Dynamics, MD, technique which iteratively solves the classical equations of motion for a system, yields the time evolution of the system which is consistent with the interatomic potentials representing the potential energy surface. Both methodologies will be subsequently discussed in detail, but it is worth emphasising fundamental differences between the two techniques.

The solution for the equations of motion of a system gives the *time evolution* of the molecular motions and can be used to study time dependent properties such as diffusion coefficients[54], protein-drug interactions[55], etc. However, this time dependence which is the technique's strength, is also a weakness, as the length of time that can be practically simulated is of the order of 10^{-12} to 10^{-9} seconds, i.e. picosecond to nanosecond time scales. Hence, chemical phenomena which happen on longer time scales are unlikely to be observed in an MD simulation (e.g. interconversion between the chair and boat conformers of cyclohexane observed by NMR.). The Monte Carlo method, however, is not restricted by such problems; moreover, algorithms have been developed since its conception in 1956, to allow the creation and destruction of particles within the system[56], i.e. the chemical potential is

fixed while the number of molecules fluctuates. The MC algorithm is particularly well suited to the simulation of all the accessible conformational space available to a system and can for example reliably simulate the conformational interconversion of cyclohexane. The primary drawback to MC is that the iterative conformations do not represent a time dependent trajectory.

In work of Leggetter and Tildesley[57], MC was found to be more efficient than MD in the simulation of thermodynamic properties. Thus when one is proposing to model the dynamical nature of a system, it is important to consider what properties are required and choose a simulation technique best suited to that task.

2.5.1 Molecular Dynamics, MD.

As noted above, Molecular Dynamics allows a system to evolve in time, by solving, in an iterative manner, the classical equation of motion using interatomic potentials to represent the forces within the system. The force, F_i on atom i can be evaluated directly from the first derivative of the potential energy, V, with respect to the co-ordinates, r, and can then be implemented in Newton's Second Law :-

$$F_i = m_i a_i \tag{2.5.1}$$

which becomes :

$$-\frac{\partial V}{\partial r_i} = m_i \frac{\partial^2 r_i}{\partial t_i^2} \tag{2.5.2}$$

Closed analytical solutions can only be found for one or two independent particles and the solution of larger systems requires numerical methods. The kinetic energy, K, is defined in terms of the velocities, $\vec{v}$:-

$$K = \frac{1}{2} m_i \vec{v}_i^2 = \frac{1}{2} m_i \left(\frac{\partial \vec{r}_i}{\partial t} \right)^2 \tag{2.5.3}$$

The total energy of the system can be represented as a sum of the kinetic energy, K and the potential energy, V:-

$$H(r,\rho) = K(\rho) + V(r) \tag{2.5.4}$$

H = The classical Hamiltonian.

r = Set of co-ordinates.

ρ = Momentum of atoms.

The motion of the particle *i* can be expressed as a standard Taylor series :-

$$\vec{\mathbf{r}}(t+\Delta t)=\vec{\mathbf{r}}(t)+\frac{\partial\vec{\mathbf{r}}}{\partial t}\Delta t+\frac{\partial^2\vec{\mathbf{r}}}{\partial t^2}\frac{\Delta t^2}{2}+\ldots\ldots \qquad (2.5.5)$$

To evaluate such an expression, we must know the position, $\vec{\mathbf{r}}(t)$, the velocity, $\frac{\partial\vec{\mathbf{r}}}{\partial t}$, and the acceleration, $\frac{\partial^2\vec{\mathbf{r}}}{\partial t^2}$ and perhaps an approximation to the higher order terms, although these can sometimes be evaluated directly, depending on the methodology, as in for example, Fifth order Gear corrector algorithms[58,59]. However, much simpler algorithms, such as those first described by Verlet[60], are usually used. In the so called Verlet leap frog algorithm we write :-

$$\vec{\mathbf{r}}(t+\Delta t)=\vec{\mathbf{r}}(t)+\vec{\mathbf{V}}_{ave}\Delta t \qquad (2.5.6)$$

where it is assumed that the velocity is changing linearly during Δt. Thus, the average velocity can be equated to the instantaneous velocity at $\frac{\Delta t}{2}$.

$$\vec{\mathbf{V}}_{ave}=\vec{\mathbf{V}}\left(t+\frac{\Delta t}{2}\right) \qquad (2.5.7)$$

Combination of these equations gives :-

$$\vec{\mathbf{r}}(t+\Delta t)=\vec{\mathbf{r}}(t)+\vec{\mathbf{V}}\left(t+\frac{\Delta t}{2}\right)\Delta t \qquad (2.5.8)$$

This is termed the leap frog method because the velocity is out of step with the position by half a time step. Indeed, a key point in the Verlet algorithm is that the

integration time step, Δt, is required to be small, usually $\approx 10^{-15}$ seconds (i.e. femtoseconds, fs), in order to keep the linear approximation in the velocity valid. After solution of equation 2.5.5, the original co-ordinates are substituted with the new ones, the velocities are updated and the acceleration is corrected by calculating the gradients with the new co-ordinates.

Before the iterative process can be started, initial velocities are required. These may be chosen in a variety of ways but are commonly chosen to satisfy the Maxwell Boltzmann equation :-

$$P(v)\partial v = \left(\frac{m}{2\pi kT}\right)^{\frac{3}{2}} e^{\frac{-mv^2}{2kT}} 4\pi v^2 \partial v \qquad (2.5.9)$$

$P(v)$ = The probability of velocity v

m = Mass of particle.

v = Velocity of particle.

T = Temperature.

k = Boltzmann constant.

An initial velocity is usually ascribed to each particle in the system, with a Boltzmann weighted distribution. Once the system is in motion, the temperature is directly related to the kinetic energy, K by :-

$$K = \frac{3}{2}kT \qquad (2.5.10)$$

An expression for the temperature, T, in terms of velocity can be derived :-

$$T = \frac{mv^2}{3k} \qquad (2.5.11)$$

Indeed, using the above classical theory with a suitable iterative algorithm, which is an approximation to the Taylor expansion series, one can calculate the time evolution of the system.

MD calculations use a number of standard ensembles, in particular the following :-

Constant number of particles; constant energy; constant volume; NVE;

The Microcanonical ensemble.

Constant number of particles; constant temperature; constant volume; NVT;

The Canonical ensemble.

Constant number of particles; constant temperature; constant pressure; NPT.

Several codes are readily available which perform MD with a given set of interatomic potentials and a given ensemble. The codes employed for the MD work contained with in this thesis are firstly: DISCOVER, which embodies the molecular mechanics forcefield approach to interatomic potentials and the Verlet algorithm; secondly, FUNGUS[61] which again is based on the Verlet algorithm approximation to the Taylor expansion but uses the short range Born model atomic potential and is particularly suited to solid state simulation, due to the provision of Ewald summation for the Coulombic interactions and thirdly PENICILLIN[62], which uses a fifth order Gear predictor corrector algorithm instead of the Verlet leap frog algorithm.

2.5.2 Monte Carlo Sampling.

The Monte Carlo method, as the name suggests involves the use of random numbers which are employed in such a way, as to search the configurational space of a system so as to generate ensembles which are consistent with a given thermal energy. The methodology was first derived in 1949 by Metropolis *et al*[63], with their proposal of the Importance Sampling Algorithm[64]. Perhaps the earliest documented use of random sampling was that of Comte De Buffon who investigated the probability of a needle intersecting a line[65]. Since then, the range of possible sampling algorithms has expanded rapidly to include very complex algorithms such as the Grand Canonical ensemble[66], in which not only molecular displacements are allowed, but also both the creation and destruction of molecules during a simulation. However, the methodology still remains in essence simple and can be represented by a flow diagram, figure 2.5.1.

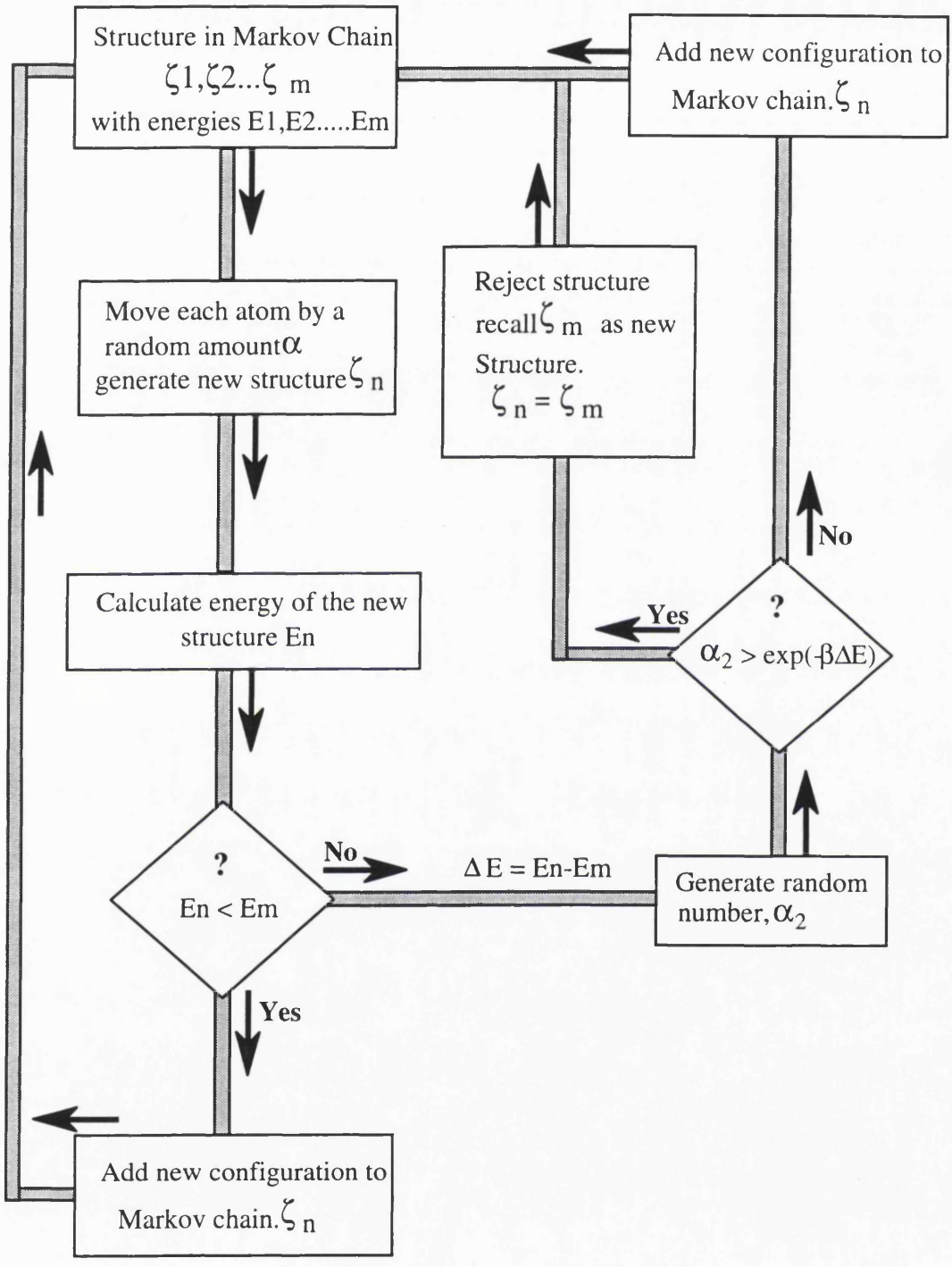

Figure 2.5.1 : Flow diagram of the methodology of the Monte Carlo technique.

From each accepted configuration, a new configuration is generated by making a random move, Δx, the magnitude of which is derived from a Gaussian distribution of random numbers distributed about zero. The energy is calculated by the use of interatomic potentials or increasingly possible via *ab-initio* techniques[67]. The energy or calculated property is then compared to the previous value and then depending on the sampling algorithm is accepted or rejected. The example given in the flow diagram, is for the Metropolis Importance Sampling Algorithm and is one of the simplest to implement in a computer program. The result of such a simulation is to produce a Markov chain of structures, which for a sufficient length of simulation provides an ensemble from which average properties may be calculated. An excellent review which contains many other uses of the MC methods e.g. finite integral evolution can be found in reference [68]. Such calculations, as previously stated, yield no direct information on properties which depend on time evolution, e.g. continuous molecular diffusion but MC, can yield amplitudes of thermal vibrations (Debye-Waller factors) and structural information, in particular time-averaged radial distribution functions which may be readily calculated. MC may not however, be used in a straightforward manner to model diffusion of molecules in zeolites for example. It may however, be useful in investigating jump diffusion processes, especially when the energy barriers are too large to be overcome by an MD simulation at a reasonable simulation temperature or in a reasonable simulation time. MC has the advantage over MD when the inclusion of ionic polarisation is required, as the methodology can easily accommodate the Shell model.

Since the MC method is straightforward, general purpose simulation programs are not normally used, it being more efficient to tailor the program the to a particular application.

2.6 Local Density Functional Theory, LDF.

The methodologies described previously, all employ interatomic potentials without any direct inclusion of electronic effects. For certain problems, it is necessary to include electronic effects explicitly and techniques which solve the Schroedinger equation explicitly must be used. One such method is that of the Local Density Functional theory, (LDF), which addresses the problem without explicit recourse to the many particle wave function, as in Hartree-Fock techniques. Instead, electronic densities and first order density matrices are used directly for the electronic ground state variational calculations. However, this feature of LDF makes the methodology unsuitable for the study of excited state systems. Formal justification for using the electron density directly in the variational calculation arises from the theory of Hohenberg and Kohn[69] "regarding the electrons as a collection of non interacting particles with the important additional concept of collective excitations ". Hohenberg and Kohn showed that the total energy and in fact all ground state properties are functionals of the charge density, ρ, enabling us to write :-

$$E_{Total} = T(\rho) + U(\rho) + E_{xc}(\rho) \qquad (2.6.1)$$

$T(\rho)$ = Kinetic energy of a system of non-interacting particles of density, ρ.

$U(\rho)$ = Classical electrostatic energy due to Coulombic interactions.

$E_{xc}(\rho)$ = All many body contributions to the total energy, in particular the exchange-correlation energies.

By representing the wave function as anti-symmetrised products (Slater determinants) of one particle functions, i.e. molecular orbitals which also are required to be orthonormal.

$$\Psi = A(n)\left|\Phi_1(1),\Phi_2(2).....\Phi_n(n)\right| \quad \text{and} \quad \left\langle \Phi_i \middle| \Phi_j \right\rangle = \delta_{ij} \tag{2.6.2}$$

The charge density is given by:-

$$\rho(\vec{\mathbf{r}}) = \sum_i \left|\Phi_i(\vec{\mathbf{r}})\right|^2 \; : \; \vec{\mathbf{r}} = \text{Integration points.} \tag{2.6.3}$$

Both spin restricted, (same Φ_i used for α and β) and spin unrestricted (different Φ_i for α and β electrons) functions are possible. The kinetic energy, T, and the potential energy, V, can be evaluated by close analogy with the Hartree-Fock calculations, but the final term in equation 2.6.3, the $E_{xc}(\rho)$ requires an approximation. It is this that is at the heart of the Local Density Approximation[70]. Analytical representations of this approximation, which is based on the known exchange-correlation energy of the uniform electron gas, have been determined by several groups[71,72], but in all, the charge density is assumed to vary slowly on the atomic scale i.e. each region of a molecule represents a region of uniform electron gas. The total exchange correlation energy may be obtained by integrating the uniform electron gas result :-

$$\varepsilon_{xc}(\rho) \cong \int \rho(\vec{\mathbf{r}}) \varepsilon_{xc}[\rho(\vec{\mathbf{r}})] \partial \vec{\mathbf{r}} \tag{2.6.4}$$

$\varepsilon_{xc}(\rho)$ is the exchange correlation energy per particle in a uniform electron gas which is the form derived by Von Barth and Hedin[73]. Using variational constraints, orthonormal constraints[74], Lagrangian multipliers and differentiable exchange-correlation functions, one can reformulate the energy expression to be very close to the form of Kohn and Sham.

$$E_{Total} = \sum_i \varepsilon_i + \left\langle \rho(\vec{\mathbf{r}}_1) \left[\varepsilon_{xc}[\rho] - \mu_{xc}[\rho] - \frac{V_e(\vec{\mathbf{r}}_1)}{2} \right] \right\rangle + V_{NN} \tag{2.6.5}$$

ε_i = Lagrangian multipliers.

ε_{xc} = The exchange correlation energy per particle in a uniform electron gas.

μ_{xc} = The exchange correlation potential, which results from differentiating ε_{xc}

$\frac{V_e(\vec{r}_1)}{2}$ = The electron-electron repulsion.

V_{NN} = The nuclear-nuclear repulsion.

As with all *ab-initio* techniques it is possible to expand the Molecular Orbitals, MO's, Φ_i as a linear combination of atomic orbitals :-

$$\Phi_i = \sum_{\mu} C_{i\mu}\chi_{\mu} \qquad (2.6.6)$$

χ_{μ} = Atomic basis functions.

$C_{i\mu}$ = MO. expansion coefficients.

Several choices are possible for the basis set, χ, including Gaussians, Slater, Plane waves or numerical orbitals and it is with this choice that many of the available codes differ.

In the work contained within this thesis, the basis functions, χ_{μ}, are given as numerical values on an atomic centred spherical-polar mesh, rather than as a analytical function, e.g. plane waves that have been widely used in studies of metals and semiconductors. This is particularly useful when dealing with less dense systems, such as zeolites, as in the case of plane waves for example, most would be employed to model zero electron density and thus, a very large number would be required to represent the system. Also with a basis set centred on the atomic centres, the molecule can be dissociated exactly into its constituent atoms and with the quality of the orbitals, basis set superposition effects[75] are minimised. The number of numerical integration points has to scale with atomic number and the spacing of such points is

logarithmic, so that most points are located near the nuclei where oscillations in the wave function are more rapid and this avoids integration of the nuclei themselves because of the nuclear cusps[76]. An excellent review containing much of the detailed formulation is given by Yang and Parr[77]. This also includes a description of the three dimensional numerical integration required to evaluate the MO and the iterative techniques for the Self Consistent Field procedure, to ensure convergence of the exchange density and therefore the ground state properties. The LDF work reported in this thesis applied existing codes including DMOL[78], kindly supplied by BIOSYM Technologies which embodies a numerical atom centred basis set.

2.7 References.

1 Alder B.J.; Wainwright T.E.; *J. Chem. Phys.*, **27**, 1208, (1957)

2 Metropolis N.; "*Symposium on Monte Carlo Methods*", ed Meyer H.A.; John Wiley & Sons, N. York, (1954).

3 Born M.; Oppenheimer J.R.; *Ann. Physik.*; **84**, 457, (1927).

4 Car R.; Parrinello M.; *Phys. Pev. Lett.*, **55**, 247, (1985).

5 Herzberg G.; "*Molecular Spectra and Molecular Structure. I Spectra of Diatomic Molecules.*", Van Nostrand & Co.; New York. (1950).

6 Lennard-Jones J.E.; Devonshire A.F.; *Proc. Roy. Soc. London.*, **A169**, 317, (1939a).

7 Lennard-Jones J.E.; Devonshire A.F.; *Proc. Roy. Soc. London.*, **A169**, 464, (1939b).

8 Buckingham R.A.; *Proc. Royal Soc. A*; **168**, 264, (1936).

9 Price S.L.; Stone A.J.; Alderton M.A.; *Molecular Physics.*, **52,** 4, 987, (1984).

10 Willock D.; Leslie M.; Price S.L. Catlow C.R.A.; *In Press.*

11 Ewald R.P.; *Ann Physik.*; **64**, 253, (1921).

12 Tosi M.P.; *Solid State Phys.*; **16**, 1, (1964).

13 Jackson R.A.; Catlow C.R.A.; *Molec. Simm.* **1**, 207, (1988).

14 Dick B.G.; Overhauser A.W.; *Phys. Rev.*; **112**, 90, (1958).

15 Iishi K., Miura M.; Shiro Y.; Murata H.; *Phys Chem Minerals* **9**, 61, (1983).

16 Sangster M.J.; *J. Phys. Chem. Solids.*; **35**, 195, (1974).

17 Lindan P.J.D.; Gillan M.J.; *J. Phys. Condens. Mat.*, **5**, 1019, (1993).

18 Allinger N.L.; *J. Am. Chem. Soc.*; **99**, 8127, (1977).

19 Weiner S.J.; Kollman P.A.; Nguyen D.T.; Case D.A.; *J. Comp. Chem.*; **7**, 230, (1986).

20 Marple J.; Dinur U.; Hagler A.T.; *Proc. Nat. Acad. Sci.* USA, **85**, 5350, (1988).

21 Marple J.; Thacher T.S.; Dinur U.; Hagler A.T.; *Chemical Design Automation News.*; **5(9)**, 5, (1990).

22 Schaefer H.F., III; "*The Electronic Structure of Atoms and Molecules*"; Addison-Wesley; Reading, (1972).

23 Press W.H.; Flannery B.P.; Teukolsky S.A.; Vetterling W.T.; "*Numerical Recipes, The Art of Scientific Computing*".; Cambridge University Press; Cambridge, (1986).

24 Press W.H.; Flannery B.P.; Teukolsky S.A.; Vetterling W.T.; "*Numerical Recipes, The Art of Scientific Computing*".; Cambridge University Press; Cambridge, (1986).

25 Fletcher R.; "*Practical Methods of Optimisation, Volume 1*".; J. Wiley & Sons, New York, (1980).

26 Fletcher R.; Powell M.J.D.; *Comp. J.*, **6**, 163, (1963).

27 Allen M.P.; Tildesley D.J.; "*Computer Simulation of Liquids*"; Clarendon Press; Oxford; (1987).

28 DISCOVER; Biosym Technologies Inc.; 9685 Scranton Road; San Diego, CA 92121, USA.

29 Catlow C.R.A.; Doherty M.; Price G.D.; Danders M.J.; Parker S.C.; *Mater. Sci. Forum.*, **7**, 163, (1986).

30 Leslie M. Daresbury Laboratory, Report, *In Press.*

31 Gale J.D.; General Ultility Lattice Program, GULP; The Royal Institution of Great Britain, London.(1993).

32 Leslie M.; Gillan M.J.; *J. Phys. C.*, **18**, 973, (1985).

33 Mott N.F.; Littleton M.J.; *J. Trans. Farad. Soc.*; **34**, 485, (1938).

34 Lidiard A.B.; Norgett M.J.; "Computational Solid State Physics", ed Herman F., Dalton N.W.; Koehler T.R.; Plenum, N. York, (1972).

35 Norgett M.J.; Catlow C.R.A.; U.K.A.E.A. Report A.E.R.E. M2936, United Kingdom Atomic Energy Authority, Harwell, (1976).

36 Norgett M.J.; Fletcher R.J.; *J. Phys. C.*; **3**, L190, (1970).

37 Leslie M.; Daresbury Laboratory Report No. DL/SCII/TN31T, (1982).

38 Born M.; Huang K.; "*Dynamical Theory of Crystal Lattices*"; Clarendon Press; Oxford, (1954).

39 Parker S.C.; Price G.D.; *Adv. Solid State Chem.*; **1**, 295, (1989).

40 Maradudin A.A.; Montroll E.W.; Weiss G.H.; Ipatova I.P.; "*Theory of lattice Dynamics in the Harmonic Hpproximation.*"; Academic Press; New York, (1971).

41 Bruesh P, "*Phonons, Theory and Experiments I*", Springer Verlag Berlin (1982).

42 Elcombe M.M.; *Proc Phys. Soc.* ; **91**, 946, (1967).

43 van Santen R.A.; Vogel D.L.; *Adv. Solid State Chem*, **1**, 151, (1989).

44 Adams D.M.; Newton D.C.; "*Tables for Factor Group and Point Group Analysis*", Beckmann-RIIC Ltd, Croydon, England, (1970).

45 Ferraro J.R.; Ziomek J.S.; "*Introductory Group Theory and it's Application to Molecular Structure*"; Plenum Press, New York, (1964).

46 Colthup E.B.; Daly L.E.; Wiberly S.E.; "*Introduction to Infrared and Raman Spectroscopy*"; Academic Press, New York, (1972).

47 Kleinman D.A.; Spitzer W.G.; *Phys. Rev.*; **125**, 16, (1962).

48 Dowety E.; *Phys. Chem. Minerals.;* **14**, 67, (1987).

49 Miecznikowski A; Hanuza J.; *Zeolites* ; **7**, 249, (1987).

50 Laughlin R.B.; Joannopoules J.D.; *Phys. Rev. B.*; **16**, 2942, (1977).

51 Demontis P.; Suffritti G.B.; "*Modelling of structure and reactants in zeolites.*" ed. Catlow C.R.A.; Academic Press, San Diego, 79, (1992).

52 Dolling G.; "*Calculations of Phonon Frequencies*"; in Gilat G. (ed); "*Methods in Computational Physics*"; 15, (1976).

53 Dowty E.; *Phys. Chem. Minerals*; **7**, 249, (1987).

54 Gillan M.J.; Dixon M.J.; *J. Phys. C.*; **13**, 1901, (1980).

55 Hagler A.T.; Osguthorpe D.J.; Dauber-Osguthorpe P.; Hemple J.C.; *Science*; **227**, 1309, (1985).

56 Norman G.E.; Filinov V.S.; *High Temp. USSR.*, **7**, 216, (1969).

57 Leggetter S.; Tildesley D.J.,; *Mol Phys.* **68**, 519-546,(1979).

58 Gear C.W.; Report ANL 7126, Argonne National Laboratory, (1966).

59 Gear C.W.; "*Numerical Initial Value Problem in Ordinary Differential Equations*", Prentice-Hall, Englewood Cliffs, New Jersey.

60 Verlet L.; *Phys. Rev*; **159**, 98-103; (1967).

61 Vessal B.; Leslie M.; Catlow C.R.A.; *Molecular Sim.*; **3**, 123-136, (1989).

62 Dornford-Smith A.; In Prep.

63 Metropolis N.; Ulam S.; *J. Am. Stat. Ass.*, **44**, 335, (1949).

64 Metropolis N.; Rosenbluth A.W.; Rosenbluth M.N.; Teller A.H.; Teller E.; *J. Chem. Phys.*, **21**, 1087, (1953).

65 G. Comte de Buffon; *Essai d'arithmetique morale Supplement a l'Histoire Naturelle*, Vol. **4** ,(1777).

66 Yao J.; Greenkorn R.A.; Chao K.C.; *Mol. Phys.*, **46**, 587, (1982).

67 George A.R.; Catlow C.R.A.; In Prep.

68 Kalos M. H.; Whitlock P.A.; "*Monte Carlo Methods*", Vol 1: BasicsWiley Interscience (1986).

69 Hohenberg P.; Kohn W.; *Phys. Rev. B*; **136**, 864, (1964).

70 Lundqvist S.; March N.; eds. " *Theory of Inhomogeneous Electron Gas*"; New York, (1983).

71 Hedin L.; Lundqvist B.I.; *J. Phys. C.*; **4**, 2064, (1971).

72 Ceperley D.M.; Alder B.J.; *J. Phys. Lett.*; **45**, 566, (1980).

73 von Barth U.; Hedin L.; *J. Chem. Phys.*; **88**, 3322, (1988).

74 Kohn W.; Sham L.J.; *Phys. Rev. A.*; **140**, 1133, (1965).

75 Delley B.; J. *Chem Phys.*; **92**, 508, (1990).

76 Hirschfeld F.L; *Theor. Chim. Acta B*; **44**, 129, (1977).

77 Parr R.G.; Yang W.; "*Density-Functional Theory of Atoms and Molecules*"; Oxford University Press; New York, (1989).

78 DMOL; Biosym Technologies Inc.; 9685 Scranton Road; San Diego, CA 92121, USA.

Chapter 3

Structural investigation of the Nickel-Sodium- Zeolite-Y Catalyst.

3.1 Determining the environment of transition metal ions in zeolitic catalysts: A combined computational and synchrotron based study of Nickel ions in zeolite-Y.

The results contained within this chapter and in the Appendix of this thesis, deal with several of the structural aspects of the dehydrated Ni-zeolite-Y catalyst. Whereas, the work presented in chapter 4 is primarily concerned with the activation and reaction mechanism of the catalyst.

3.1.1 Introduction.

How is one to locate the precise position of catalytically active metal ions in a zeolitic catalyst? The best experimental approach is to use synchrotron radiation techniques with a special in-situ cell which permits the recording of both X-ray powder diffractograms and X-ray absorption spectra under the actual reaction conditions. Successful studies of this type have been reported, allowing the unambiguous identification of extraframework cation positions and their changes during catalyst activation. However, in studies of such complex systems, it is still desirable to achieve greater structural detail and insight by invoking supplementary methods. In particular, the use of computational techniques of the kind we describe in this section are of great value. Such studies can reveal subtle changes in the local atomic environment at active sites in the large family of uniform heterogeneous catalysts.

As noted, an extensive experimental study of Ni-zeolite-Y was reported by Dooryhee *et al.*[1,2], who found, after dehydration, approximately 66% of the Ni^{2+} ions in the hexagonal prismatic S_I site, (see figure 3.1.1), while the remaining cations are located at a variety of sites within the sodalite cage. EXAFS experiments showed that

for the S_I site the Ni-O bond length was 2.02Å with a co-ordination number of approximately 4.0 ±1.0; whereas Rietveld analysis[3] of the high resolution diffraction data locates the Ni^{2+} at the S_I site, co-ordinated to 6 framework oxygen atoms at 2.28Å. The interpretation given to these observations was that there is a contraction of the framework structure surrounding the Ni^{2+} in the S_I site. As there is only fractional occupancy (by Ni^{2+} ions) of the S_I site (estimated at 0.66), the observed bond length determined by diffraction will be the weighted average of the relaxed and unrelaxed lengths. EXAFS, however being a "local" structural technique sees the true relaxed bond length.

The work contained within this section sets out specifically to determine, by computational methods, first the magnitude of the structural relaxation around the S_I site occupied by Ni^{2+} ions. In addition, we lay the foundation of the more sophisticated studies of structural rearrangement in the vicinity of active sites which are discussed later in this thesis.

In the later section of this chapter, we calculate the IR. spectra of the Ni-Y system for comparison with experiment. We also explain in detail the dynamics of this system by explicit MD simulations.

We note that Ni^{2+} ions situated at the S_I site, are not themselves, catalytically active for reactions such as the trimerisation of acetylene[4]. Experimental evidence indicates that migration from these sites takes place during activation, and the Ni^{2+} ions are closer to S_{II} sites in the catalytically active state. The work contained in chapter 4 of this thesis investigates this reaction and the associated mechanism.

3.1.2 Computational procedure.

In all the calculations reported in this section, we investigated the insertion of a Ni^{2+} into the centre of the D6R, double hexagonal site of the faujasite structure. We employed the energy minimisation techniques available in the CASCADE[5] code, to perform a full minimisation on a surrounding spherical region of the lattice. The polarisation of more distant regions has been calculated by approximate methods based on the procedure, developed by Mott and Littleton[6]. The methodology, potentials and application[7] of which have been discussed in detail in the previous chapter, (chapter 2). All calculations employed a region radius of 7.5Å, as this gave an acceptable balance between computational cost and accuracy. The potentials employed were those used by den Ouden et al[8], in a previous study of Ni containing zeolites. A shell model was used to represent the polarisation of the framework oxygen ions and the extra-framework nickel cations.

In the first set of calculations we examined a purely siliceous faujasite, before progressing to attempt a crude simulation of the incorporation of Al by modifying the effective charge of the tetrahedral atoms which were reduced from 4 to 3.69 corresponding to an Si:Al ratio of 2.25, which relate to the experimentally observed ratios for the samples experimentally studied in ref [9]. A modification of this approach retained a purely siliceous matrix but adjusts the average tetrahedral charge in the 12 Si atoms of the six-rings comprising the hexagonal prism.

The next stage of sophistication was to replace explicitly a number of Si by Al ions, which is a far more realistic model for the real structure. Thus, into the inner region of the simulation, one included an Al ion distribution around the double hexagonal prism. Na^+ ions were also added to achieve electroneutrality (after inclusion of Ni^{2+}). The Al ions were distributed according to Löwenstein's rule[10] in which Al-O-Al bridges are forbidden. Figure 3.1.1 describes the explicit aluminium arrangements and nomenclature used in these simulations, (only the T atom connectivity is shown as the oxygen ions have been omitted for clarity).

Figure 3.1.1 : The various explicit aluminium arrangements and nomenclature used in this investigation.

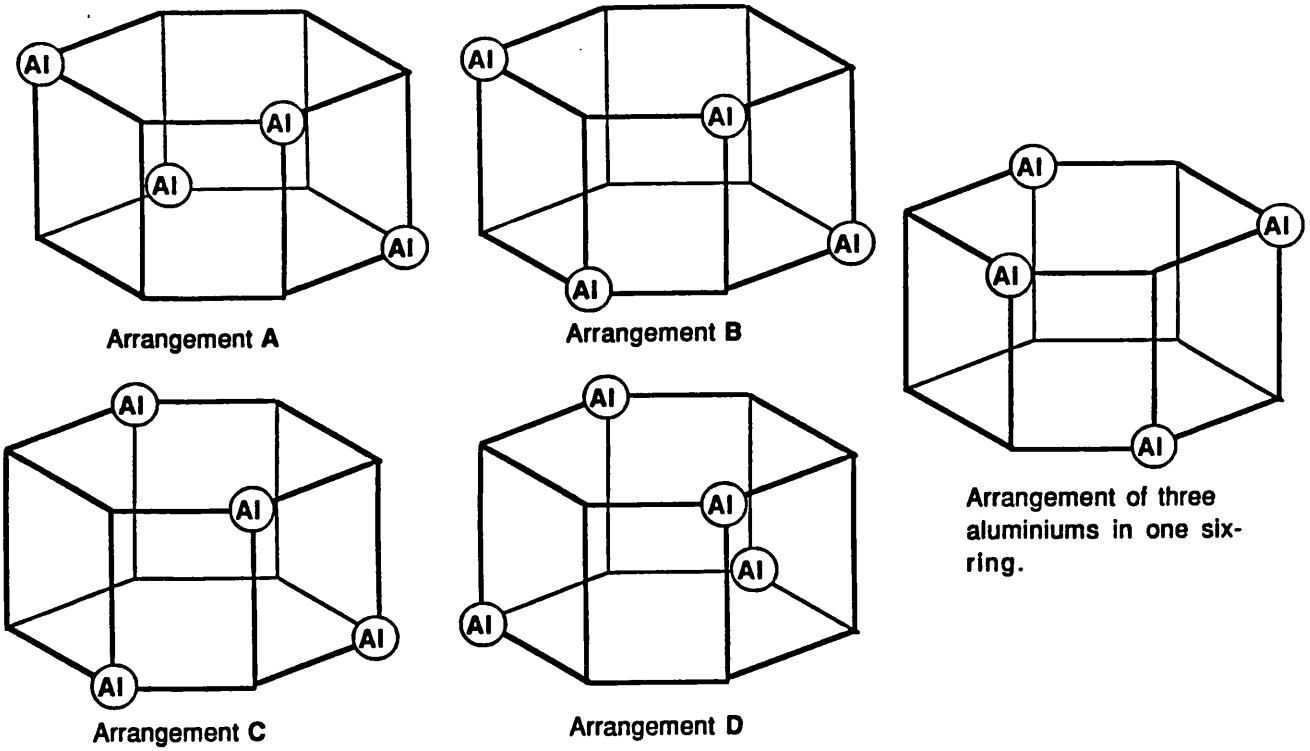

Into these host structures, an Ni^{2+} cation was placed and anchored at the centre of the S_I site and the surrounding zeolite cage was then allowed to relax.

3.1.3 Results and discussion.

Both relaxed and initial Ni^{2+} framework atomic distances are given in table 3.1.1 for each of the types of calculation discussed above

As can be seen from table 3.1.1B the purely siliceous zeolite distorts symmetrically, unlike all the other systems, which have some representation of aluminium character, which distort asymmetrically. For the pure SiO_2 system, the framework oxygen ions relax inwards by 0.5Å. In contrast, those calculations where an average tetrahedral atom with a reduced charge was used, (table 3.1.1C), the oxygen ions relax inwards by 0.3Å indicating such models are less satisfactory. When the reduced tetrahedral change is localised, a larger inward oxygen ion relaxation is once more simulated, table 3.1.1D, with an asymmetrical inner distortion.

When Al ions were added explicitly, the first configuration comprised an aluminium, in the six-ring and another in a sodalite cage; hence the Ni cation is only close to one Al. The results, (table 3.1.1E), indicate a sharp drop in the minimum Ni-O distance; but the other oxygen atoms are not significantly pulled towards the extraframework Ni^{2+}.

Next, two Al ions were included in the double six-ring, D6R, and these were positioned at opposite sites in the rings, in order to minimise the Al-Al interactions. Again, as seen in table 3.1.1F, the oxygen ions relax towards the Ni^{2+} ion; but the minimum Ni-O distance is seen to be greater than that when only one Al was present in the double six-ring, although more oxygen ions have been pulled closer. Thus, there is an overall increase in the inward relaxation of the six-ring.

Table 3.1.1 : Initial and relaxed cation-framework distances. Distances reported in Å.

Table 3.1.1A : Initial distances from the defect site to the surrounding framework.

Co-ordination number	*Ni-O distance*	*Co-ordination number*	*Ni-Si distance*
6	2.85	12	3.61
6	3.77		
12	5.18		

Table 3.1.1B : Relaxed geometries for the purely siliceous system.

Co-ordination number	*Ni-O distance*	*Co-ordination number*	*Ni-Si distance*
6	2.36	12	3.41

Table 3.1.1C : Relaxed geometries for an effective tetrahedral charge of 3.69|el.

Co-ordination number	*Ni-O distance*	*Co-ordination number*	*Ni-Si distance*
2	2.53	2	3.59
2	2.59	4	3.62
2	2.65	6	3.68

Table 3.1.1D : Relaxed geometries for effective tetrahedral charges 3.69 ion in the T sites in the double hexagonal prism.

Co-ordination number	*Ni-O distance*	*Co-ordination number*	*Ni-Si distance*
2	2.30	2	3.40
2	2.32	4	3.41
2	2.33	4	3.42
		4	2.43

Table 3.1.1E : Relaxed geometries for a calculation based on explicit inclusion of one aluminium in the double six-ring.

Co-ordination number	*Ni-O distance*	*Co-ordination number*	*Ni-Si distance*	*Ni-Al distance*
1	2.11	1	3.29	3.55
1	2.24	1	3.35	
4	2.40	1	3.37	
		2	3.38	
		2	3.41	
		2	3.43	
		2	3.47	

Table 3.1.1F : Relaxed geometries for a calculation based on explicit inclusion of two aluminium in the double six-ring.

Co-ordination number	***Ni-O distance***	***Co-ordination number***	***Ni-Si distance***	***Ni-Al distance***
2	2.14	2	3.32	3.49
1	2.38	1	3.38	3.50
2	2.42	3	3.40	
1	2.43	1	3.44	
		1	3.46	
		2	3.47	

In the preceeding systems, the Si/Al ratio is not close to that experimentally observed. An increase to four Al ions in the double six-ring yields a ratio of 2:1 which is near the ratio used in the experimental study of Dooryhee *et al* [1]. For electroneutrality, it was necessary to add to this system two additional cations, hence two Na^+ ions were placed at the S_{II} site, which is the experimentally observed occupancy site for Na^+. There are many possible combinations of four Al ions between twelve atoms, but due to the highly symmetric structure and the restrictions due to Loewenstein's rule, only a few of these are possible. These combinations were investigated and the results are given in table 3.1.2. The Al ion distributions used have been previously indicated in figure 3.1.1. As can be seen the resulting relaxed distances depend upon the Al configuration, but overall the first oxygen shell is drawn substantially closer to the Ni^{2+}.

The anti-symmetric splitting of the shells can also be seen in the Ni-Si distances, the shell is symmetric in the purely siliceous system but is distorted in the Al containing systems. The relaxation of the hexagonal prism, illustrated in figure 3.1.2 is typical of all the calculations.

The magnitude of the relaxations tie in well with the information from the EXAFS spectra, (an Ni-O distance of 2.02Å), which showed inward movement of the Ni-O bonds of 0.5Å and indicate a complex range of Ni-O spacings, a result which is well reproduced by our calculations based on four Al substituents.

Table 3.1.2 : Relaxed cation-framework distances when four aluminium ions are included explicitly in the simulation. Distances reported in Å.

Arrangement **Al4_A**.

Co-ordination number	*Ni-O distance*	*Co-ordination number*	*Ni-Si distance*	*Ni-Al distance*
1	2.18	2	3.29	3.45
2	2.20	1	3.34	3.46
1	2.24	1	3.38	3.49
1	2.46	3	3.45	3.52
1	2.49			

Arrangement **Al4_B**.

Co-ordination number	*Ni-O distance*	*Co-ordination number*	*Ni-Si distance*	*Ni-Al distance*
1	2.16	1	3.28	3.41
1	2.17	1	3.31	3.45
1	2.20	1	3.32	3.48
1	2.23	1	3.33	3.52
1	2.48	1	3.46	
1	2.53	1	3.48	
		1	3.56	
		1	3.61	

Arrangement **Al4_C**.

Co-ordination number	*Ni-O distance*	*Co-ordination number*	*Ni-Si distance*	*Ni-Al distance*
2	2.19	2	3.29	3.43
1	2.23	2	3.31	3.49
1	2.25	1	3.46	3.46
1	2.45	1	3.47	3.51
1	2.48	2	3.48	

Arrangement **Al4_D.**

Co-ordination number	*Ni-O distance*	*Co-ordination number*	*Ni-Si distance*	*Ni-Al distance*
1	2.19	1	3.29	3.46
1	2.23	1	3.32	3.47
2	2.24	2	6.32	3.47
2	2.55	1	3.44	3.50
		1	3.46	
		1	3.47	
		1	3.48	

Arrangement **AL3_1.**

Co-ordination number	*Ni-O distance*	*Co-ordination number*	*Ni-Si distance*	*Ni-Al distance*
1	2.19	1	3.30	3.47
2	2.20	1	3.31	3.48
1	2.24	2	3.33	3.49
2	2.46	1	3.41	3.51
		1	3.43	
		1	3.44	
		1	3.48	

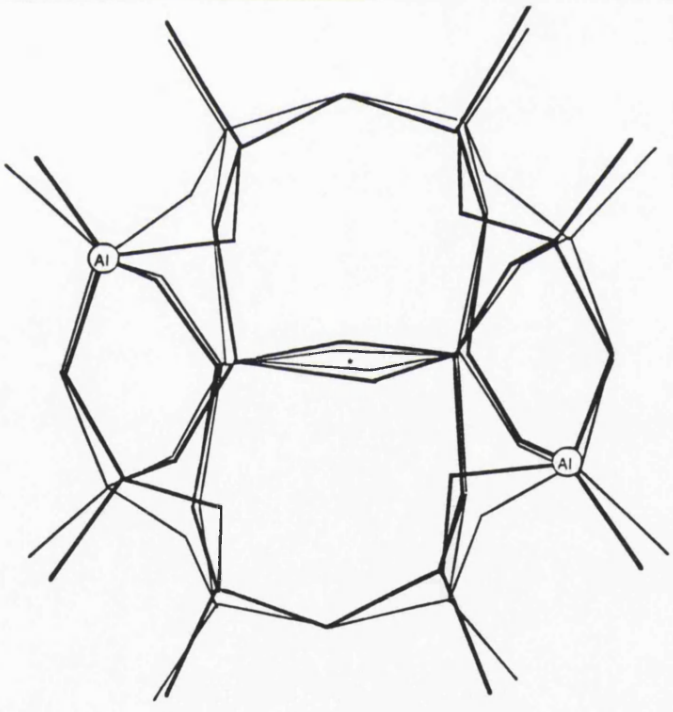

Unrelaxed.

Relaxed.

The Ni^{2+} ion has been excluded from the diagram for clarity, and should appear in the (*) position.

Figure 3.1.2 : The relaxed geometry overlaid with the initial geometry for the inclusion of Ni^{2+} into the S_I site with the arrangement of two aluminium ions in the D6R.

3.1.4 Conclusion.

Overall, the results demonstrate the flexibility of zeolite frameworks and the ability of extra framework cations to effect extensive perturbations of the framework structure. Moreover the possibility of simulating these subtle effects by computational methods has been clearly demonstrated in this section. Such methods are an invaluable tool in these complex structural studies and indeed, the results from this work can be extended to the calculation of other structural properties as described in the subsequent sections.

3.2 A Comparison of the Experimental and Predicted IR. Spectra of Nickel Zeolite-Y.

3.2.1 Introduction.

The experimental technique of Fourier Transform Infrared, (FTIR) and the ability to conduct such an experiment *in-situ*[11], has brought about significant advances in the understanding of catalytic systems. Yet the information gained from such techniques can be difficult to interpret, as is indeed found for the dehydrated Na-Ni-Zeolite-Y system, where the differences observed in the spectra of the hydrated and dehydrated material are significant. New peaks emerge that cannot be readily explained without detailed reference to the structure and the associated perturbations that occur upon dehydration.

However, using the models and the relaxed structures previously calculated in section 3.1, it is possible to calculate, via appropriate methods, IR. spectra which will be well defined for each specific model. Clearly, the experimental bulk system contains a variety of environments and combinations of these must be used if we wish to represent the bulk system.

3.2.2 Experimental Data.

The experimental data[12] reveals several contrasts between the hydrated and dehydrated IR. spectra of Nickel-Sodium Zeolite-Y. The conclusions from the experimental data are summarised below:-

In the hydrated system, the Nickel cations and associated solvation shells reside within the large supercages probably at or around the S_{II} sites. However, upon dehydration, the solvation shell is removed and most of the nickel cations migrate to the preferred S_I site. Thus is embedded deep within the hexagonal prism and the spectrum for the dehydrated system exhibits distinct peaks, which are not observed in the spectrum of the hydrated zeolite. Figure 3.2.1 is a direct reproduction of the experimental data from reference 12. The differences which arise from the dehydration and subsequent migration of the cations are typified by peak splitting, first of the high field peaks, 850-1250cm^{-1}, into three distinct peaks. In addition, however, and of special interest is the splitting into a doublet at 1050cm^{-1} and the emergence of a shoulder at 1155cm^{-1} on the broad 1184cm^{-1} peak. A new group of peaks has emerged between 650-850cm^{-1}, with 4 maxima at 798, 745, 703 and 647cm^{-1} respectively. More specifically, new vibrational peaks at 432, 323 and 305cm^{-1} have been observed. Several more general effects are clear from the experimental data including a reduction in the O-T-O bends and the associated large scale pore opening modes. This is perhaps indicative of a possible reduction in the local symmetry of the system due to increased interaction of the cations with the framework; in the hydrated system we would expect the coupling to be very loose.

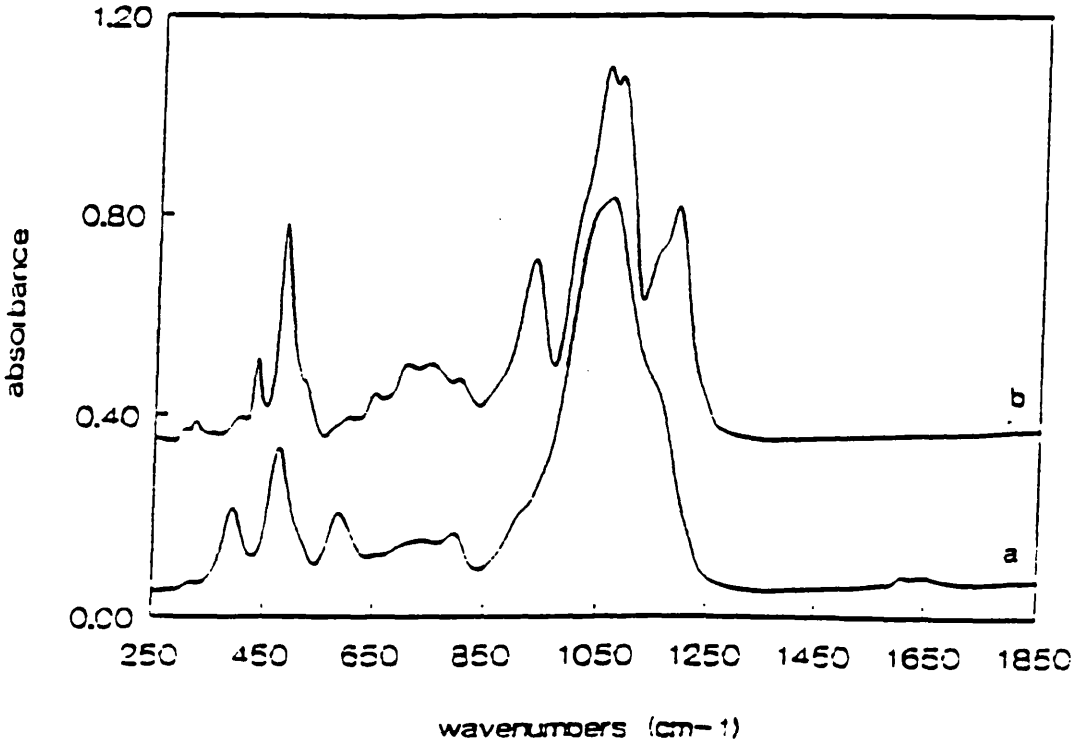

Experimental infrared spectra: hydrated (a) and dehydrated (b) NiY.

Figure 3.2.1 : The experimental spectra for both the hydrated and dehydrated systems, reproduced from reference 12.

3.2.3 Methodology.

Several models have been used to describe the distribution of aluminium over framework sites and of Nickel in extraframework positions, within the Ni-Zeolite-Y system. Figure 3.1.1 depicts the spatial arrangement of the models used in this study which are the same as those used in section 3.1 of this chapter. The structures were simulated using Born model potentials with a shell model treatment of oxygen polarisability and standard lattice energy minimisation techniques. The method and application of such techniques have been previously discussed in more detail in chapters 2.2 and 2.3 of this thesis. The nickel cation was anchored at the S_I site and all the ions within a radius of 10Å were allowed to adjust until equilibrium, i.e. zero force. This cut-off is larger than that used for section 3.1, as the properties under investigation require a larger relaxed region I than those structural properties previously investigated. The resulting structures are highly similar to those described in section 3.1.

The generation of the predicted IR. spectra is performed using the calculated relaxed structures derived from the previous section 3.1 and then embodied within Periodic Boundary Conditions. We employ standard lattice dynamical theory based on the harmonic approximation. Again a detailed account of this methodology has been reported previously in section 2.4 of chapter 2.

The inherent complexity of the system studied means that we require calculations on several configurations, the results of which must be convoluted together to give a possible representation of the experimental results. Our convolution procedure used both a simple numerical averaging technique and a weighted average, with the weighting factors being derived using Boltzmann factors.

3.2.4 Results and Discussion.

The implication of our calculations are most clearly understood by comparing the calculated spectra for the cation containing systems to that for the purely siliceous system. Such a comparison allows us to focus on the emergence and subsequent splitting of peaks in the dehydrated sample, and the extent to which the calculated spectra are in respect comparable to the experimental data. The purely siliceous spectrum was chosen as the base reference, as the aluminium distributions and compensating cations are closely coupled. Figure 3.2.2(a,b,c,d,e), reports the predicted spectra for the various aluminium and nickel arrangements with a calculated spectrum for the purely siliceous framework overlaid for a direct comparison, (the broken line in all cases). There is a downward shift of the asymmetric stretches, 900-1100cm^{-1}, (in the former), with a splitting of these high field peaks. The region of 650-850cm^{-1} in the calculated spectra, shows the emergence of a new group of peaks as compared to the purely siliceous structure, but the intensity, number and splitting are highly correlated to the arrangement of the aluminium ions. The pore modes, hexagonal prism vibrations and the O-T-O angle bends which occur at lower frequencies and are all reduced in intensity. A new peak has emerged around 430cm^{-1} which can occur either as a shoulder in the **AL3_1** arrangement or as a distinct peak in the **Al4_D** arrangement. Peaks at 305cm^{-1} and 323cm^{-1} have emerged and the peaks around this region appear to be more intense for all the aluminium/Ni arrangements than in the purely siliceous spectra and the peak at 305cm^{-1} is particularly pronounced in the **AL3_1** arrangement. These latter observations indicate that the cation-framework interaction perturbs not only the bond stretches but also the pore vibration modes which occur in this lower region of the spectrum. These observations are typical for all the aluminium distributions used in this investigation and are in agreement with the general trends concluded from the experimental data, as reported in the previous section, 3.2.2.

Figure 3.2.2(a-e) : The calculated IR. spectra for the various arrangements of aluminium around the D6R in zeolite-Y. (The intensity is measured in arbitrary units).

Figure 3.2.2(a) : **AL3_1** arrangement of aluminium ions around the D6R.

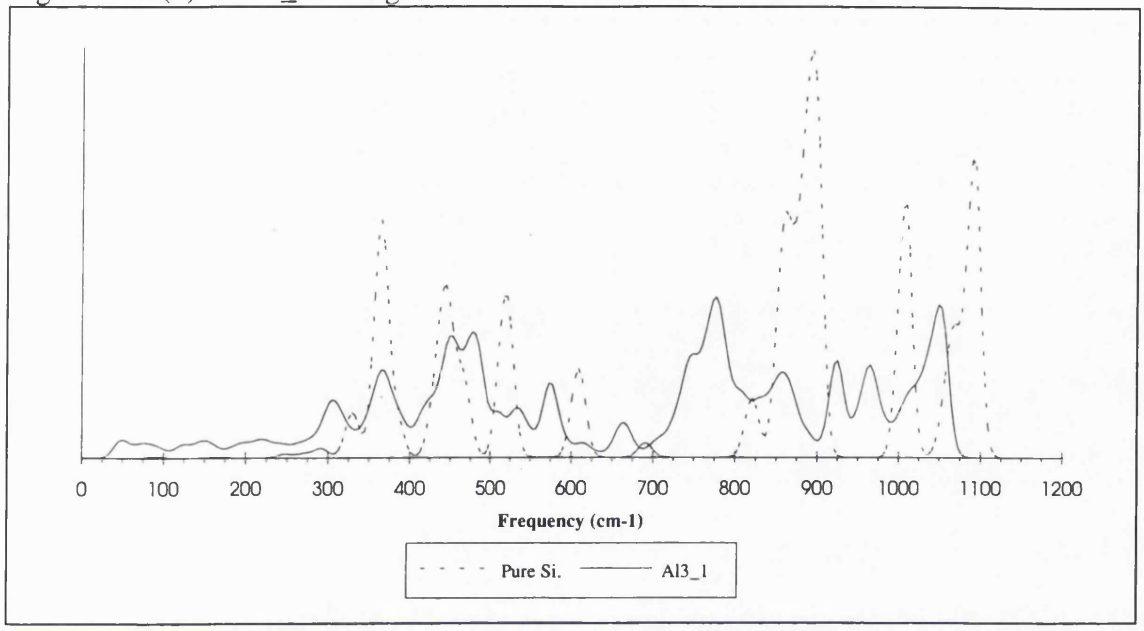

Figure 3.2.2(b) : **Al4_A** arrangement of aluminium ions around the D6R.

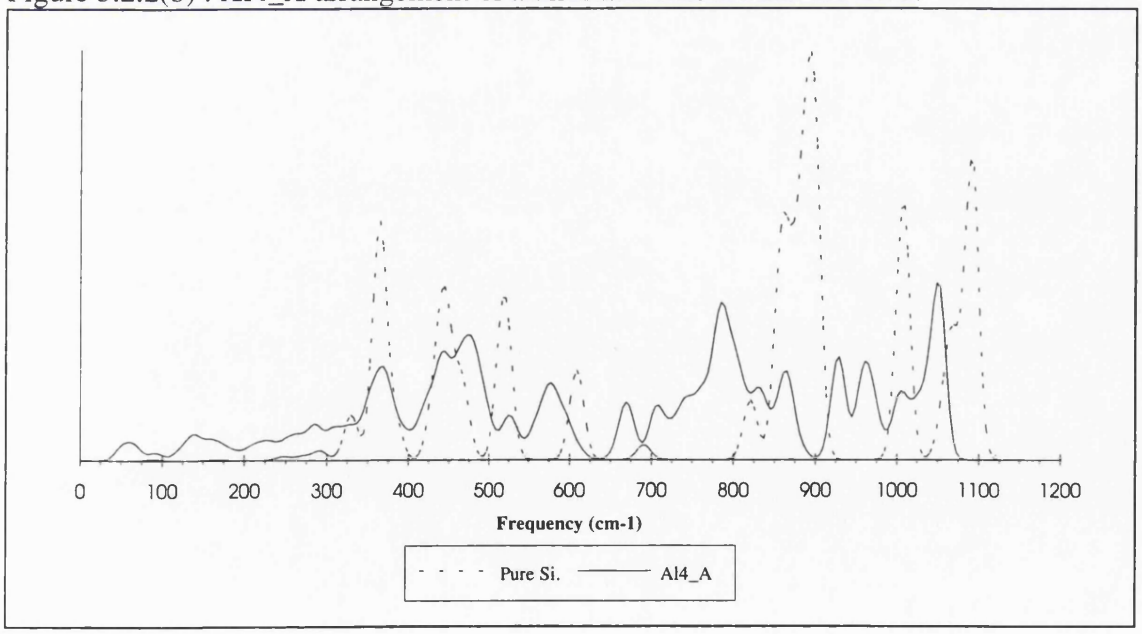

Figure 3.2.2(c) : **Al4_B** arrangement of aluminium ions around the D6R.

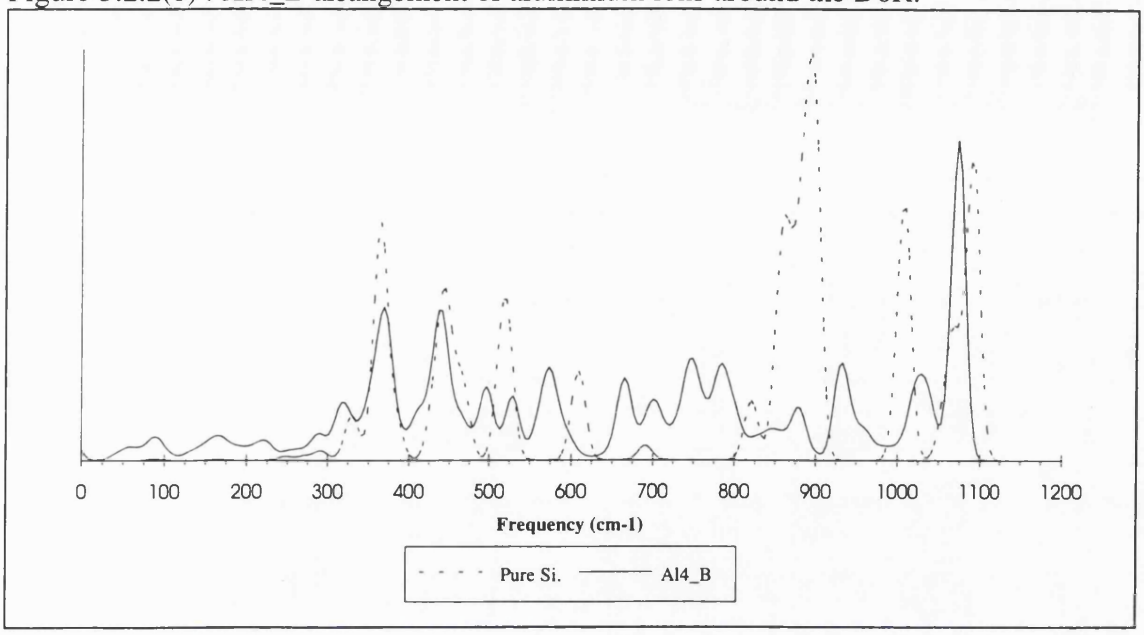

Figure 3.2.2(d) : **Al4_C** arrangement of aluminium ions around the D6R.

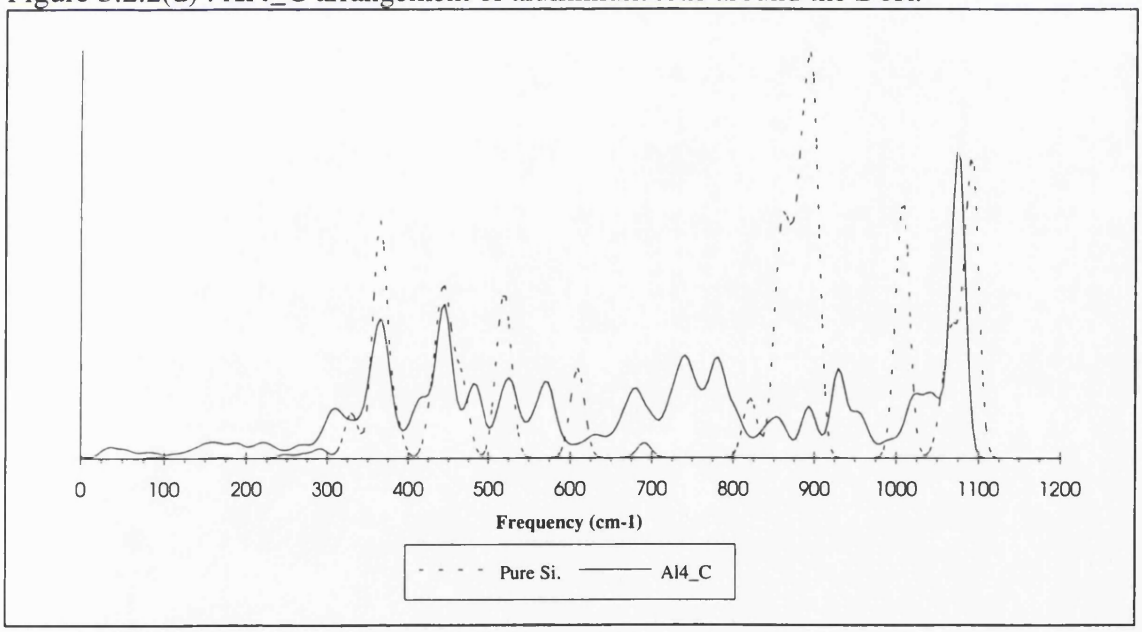

Figure 3.2.2(e) : **Al4_D** arrangement of aluminium ions around the D6R.

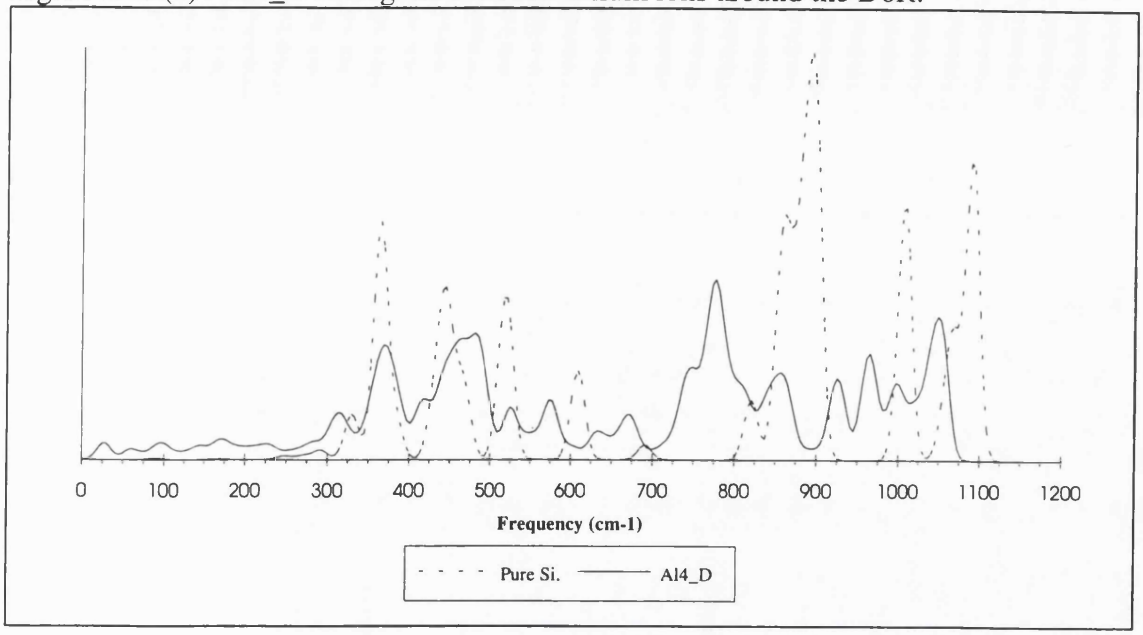

However, upon comparison with the experimental data directly, no one model completely satisfies all the experimental observations. Indeed, one Al arrangement seems to enhance a specific peak or region of the spectrum, whilst another arrangement shows little activity in the same region. This emphasises the need to convolute the results for specific models in a way which can accurately represent the real system in which these and many other distributions are expected to be present. This result also highlights the dependence of observable properties, such as IR., on the spatial distribution and arrangement of ions within the framework structure.

As already discussed, the convolution of the individual aluminium arrangements to represent the real system can use either a simple or a weighted average, with the weighting factors being derived using the Boltzmann factor obtained from the calculated energies, as discussed in section 3.1. However, a subtle problem arises concerning whether the energy difference can be taken solely as the energy to introduce the Nickel ion into the framework, or whether the energy difference concerned with the prior formation of the different Al arrangements before inclusion of the Ni ion should be used. In this investigation, we examined both types of Boltzmann weighted superposition. On comparing calculated with experimental

spectra, we note that due to the nature of the Born model potentials used and the restriction to the harmonic approximation, the asymmetric stretches are shifted downfield, typically by approximately $100cm^{-1}$, but for the symmetric stretches, bends and pore vibrations which generally occur below $800cm^{-1}$, the calculated wavenumbers are in good agreement with experiment.

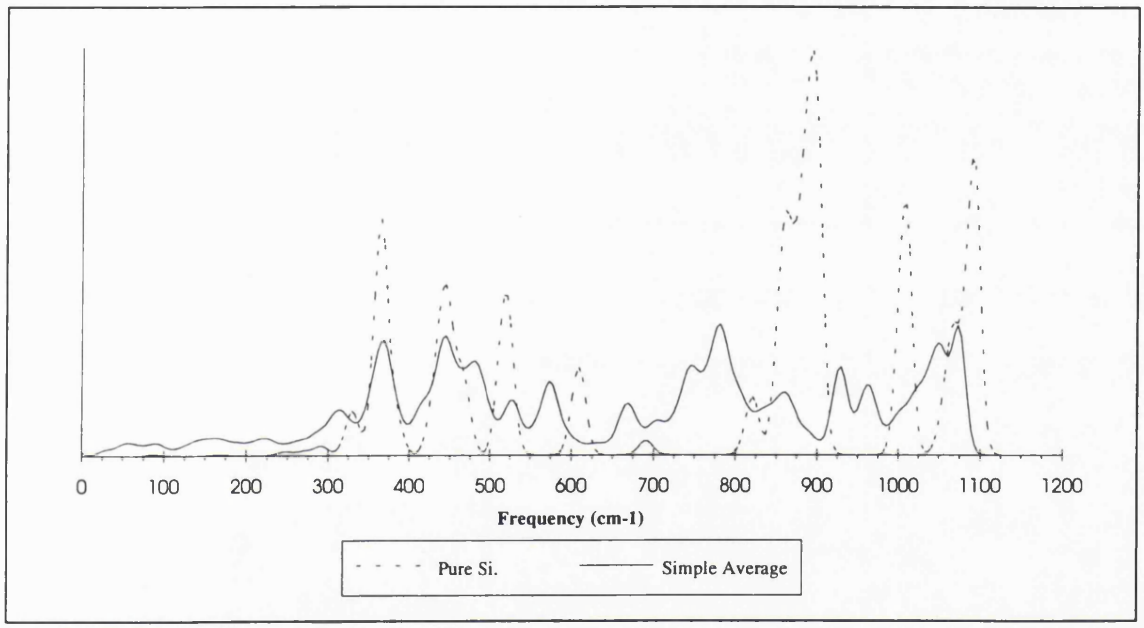

Figure 3.2.3 : The simple numerical averaged spectra.

Table 3.2.1 : Peak maxima for the different combinations and permutations of the aluminium arrangement models as a possible representation of the bulk environment.

	Combinational method.			
	Simple Average	**Boltzmann** Ni-framework energies.	**Boltzmann** Framework energies only	**Experiment**
	cm^{-1}	cm^{-1}	cm^{-1}	cm^{-1}
Peak 1	1073	1073	1049	1184
	1049	1029	997	1155
Peak 2	961	961	965	1076
	929	929	925	1053
Peak 3	861	877	857	930
	781	781	777	798
	745	745	745	745
	705	701	669	703
	669	665	633	647

The major asymmetric stretches are described and labelled in table 3.2.1. Peak **1** is a doublet in the predicted spectrum and is comparable to experiment, despite a downward shift of approximately 100cm^{-1}. Indeed, the experimentally measured difference between the two maxima is 29cm^{-1}, which is in excellent agreement with a difference of 24cm^{-1} for the calculated spectrum. This doublet only appears in the calculated spectrum upon combination of the different Al arrangements which serves to emphasise the fact that the experimental system is a mixture of a wide variety of arrangements, many of which will not have been included in this study. Indeed, our description based on periodic boundary conditions must necessarily over simplify the description of a disordered system. Peak **2** displays a doublet split, which is observed in the experimental data, the difference in frequency between the two components is 23cm^{-1} and in the simple combined spectrum is 32 cm^{-1}. As the calculated spectrum for the purely siliceous spectrum gives a singlet in this region, we again see that the inclusion of aluminium into the framework is required for a satisfactory model. Peak **3** is only a singlet, both in the calculated and experimental spectrum. The new group of peaks identified earlier are also evident in the calculated spectra; they occur at, 781, 745, 705 and 669cm^{-1}, which are very close to the maxima reported for the experimental measurement. This result provides support for the hypothesis that the harmonic approximation and the associated potentials used in this study give good results for the pore and symmetric vibrations but the calculated frequencies for the asymmetric stretches are shifted downfield. This is due partly to inaccuracies in the short range potential but is also to the use of the harmonic approximation[13]. Indeed using such insight, one could use the harmonic approximation methodology to simulate the IR. frequencies of the pore bends and the associated symmetric vibrations and use standard *ab-inito* techniques to calculate the asymmetric tetrahedral stretching frequencies. The additional advantage of the harmonic method is that for more complex zeolitic structures, it is possible to distinguish between the stretching modes of tetrahedral atoms in different topological environments, for example a member in a six ring or a channel intersection.

The Boltzmann weighted combined spectra described at 600K, are shown in figure 3.2.4(a,b). Figure 3.2.4a considers the weighting factor to be a function of the Boltzmann distribution of the energy differences, calculated for introducing the cation into a pre-existing Al distribution, (referred to subsequently as type A weighting). Figure 3.2.4b includes the effects of the energetics of the different Al distributions and only terms arising from the interaction with framework species; i.e. it includes only the energies of the different Al distributions without reference to the Ni^{2+} framework interactions; we refer to this as type B weighting. Indeed, using an analysis analogous to the one performed for the simple unweighted average, several crucial differences were observed between the two different types of Boltzmann weighting. Peak **1** has been moved downfield, (approximately 10-15cm^{-1}); type A weighting, than in the type B weighting methodology as is again highlighted by the increase in the difference between the wave numbers of the doublet. Peak **3** is observed to be shifted to lower wavenumbers as are some of the peaks in the 650-800cm^{-1} region of the spectrum. Clearly from such observations, type A Boltzmann weighting appears to be the more satisfactory. A Boltzmann weighting based on the total energies of both cation inclusion and Al substitution was also investigated but the calculated spectrum was not in as good agreement as for the type A weighting. Indeed, this is because the framework with the associated Al arrangement exists prior to ion exchange and the effect of including extraframework ions does not alter the Al/Si distribution in the framework.

Indeed from this investigation, it can be shown that two types of combination method could be used to represent the bulk - either a simple numerical averaging technique or a Boltzmann distribution of the energy using the type A procedure. The methodology and techniques described here works well, especially when one considers the complexity of the system modelled.

Figure 3.2.4(a,b) : The convolution of the individual IR. spectra with respect to the two types of Boltzmann weighted distributions.

Figure 3.2.4(a) : Cation introduction into a **pre-existing** aluminium arrangement. Type A.

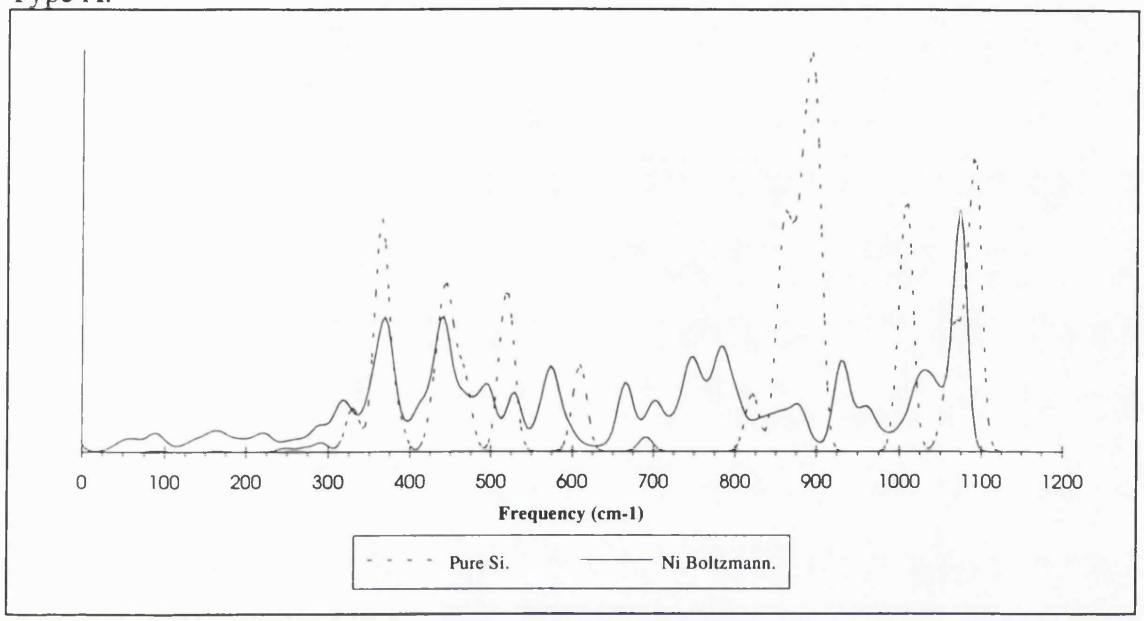

Figure 3.2.4(b) : Convolution with respect to the **prior** formation of the aluminium arrangement. Type B.

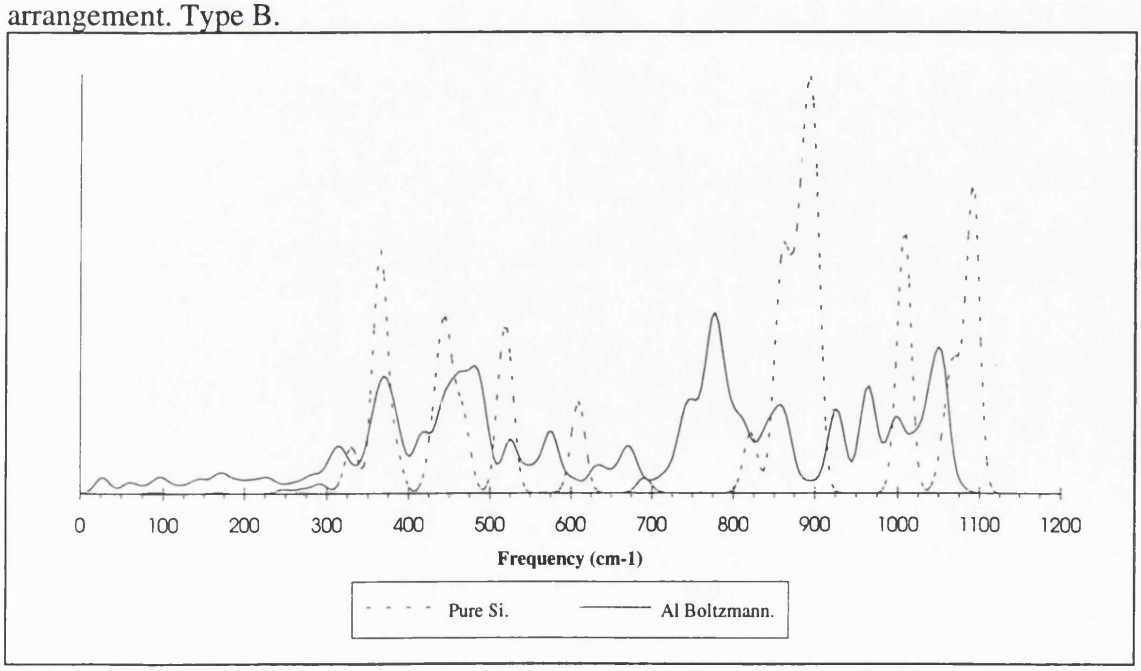

3.2.5 Conclusion.

Using the harmonic approximation and Born model potentials, it is possible to simulate the IR. of very complex catalytic systems, namely Ni-Na-Zeolite-Y, which would prove unfeasible with current *ab-initio* techniques. Indeed, it has been shown that the local symmetry of the zeolite distorts, resulting in the emergence and splitting of peaks in the IR. spectra. By modelling four different possible aluminium distributions and combining the resultant spectra, new features emerged that did not exist in the spectra of the individual models. Both an unweighted and a Boltzmann weighting yield results which reproduce some of the main experimental features. Indeed, this work is in good agreement with experimental results, for which no one simple model could be used to represent such a complex catalytic system.

3.3 The Dynamical Behaviour of the Dehydrated Ni-zeolite-Y Catalyst.

3.3.1 Overview and Conclusions.

The structural investigations so far conducted into the Ni-zeolite-Y catalyst have involved static energy minimisation calculations, as typified by the results presented in section 3.1 and the subsequent investigation of the vibrational spectra based on the energy minimised configuration as described in section 3.2. The results of these simulations as previously demonstrated, are in good agreement with the available experimental data. However in calculations of this type, although we can demonstrate relaxation effects we cannot investigate the dynamical nature of the cation behaviour. In this section, we investigate the dynamical properties for varying temperatures, extraframework ion loading and for different possible aluminium arrangements, utilising the Molecular Dynamics, MD, technique.

A detailed account of the results and discussions are reported in the appendix to this thesis and only the main conclusions that can be drawn from this work are reported below.

The results of this investigation into the dynamical motions of the complex Ni-Na-Zeolite-Y catalyst, show some remarkable behavioural patterns, which are exhibited by the oscillatory motion of the non-bonded cations either in the S_{II} site and to a lesser extent in the S_I site. The effect of increasing loading of the extra-framework cations is to perturb the local structure but at high loadings these local distortions begin to influence each other. The subtle effect of loading are obscured via peak broadening and coalescence as the temperature is increased up to 900K.

One effect of explicit aluminium inclusion around the D6R is that the instantaneous motions are less correlated, although the time-averaged properties are approximately independent of aluminium distribution.

The peak shapes for some of the systems deviate from Gaussian distributions being more asymmetric in shape. Such a peak shape has implications for the fundamental analysis of certain experimental techniques, most notably the Debye-Waller factor.

Overall, the results presented in this chapter serve to emphasise the complexity of the system and the dependence of the dynamics of the extraframework cations on the Al distribution in the framework.

3.4 References.

1 E. Dooryhee, G.N. Greaves, A.T. Steel, R.P.Townsend, S.W.Carr, J.M. Thomas C.R.A. Catlow, *Faraday Discussions Chem. Soc.*, **89**, (1990).

2 J.W. Couves, R.H. Jones, J.M. Thomas and B.J. Smith, Adv. Materials, 2 ,181, (1990).

3 Rietveld H. M.; *J. Appl. Crystallogr.*, **2**, 65, (1969).

4 P.J. Maddox, J.Stachurshi and J.M. Thomas, *Catal. Lett.*, **1**, 191, (1988).

5 Leslie M.; Daresbury Labratory Report No. DL/SCII/TN31T, (1982).

6 N.F. Mott and M.J. Littleton, *Trans Farad Soc.* **34,** 485, (1938).

7 C.R.A. Catlow, R. James, W.C. Mackrodt and R.F. Stewart, *Phys. Rev B*, **25**, 1006, (1982)

8 C.J.J. den Ouden, R.A. Jackson, C.R.A. Catlow and M.F.M. Post, *J. Phys Chem.* **94**, 5286, (1990).

9 E. Dooryhee, C.R.A. Catlow, J.M. Couves, P.J. Maddox, J.M. Thomas, G.N. Greaves, A.T. Steel and R.P.Townsend, *J. Phys. Chem.*, **11**, 4514 (1991).

10 Löwenstein W.; *Amer. Mineral.*, **39**, 92, (1954).

11 McQuire M.W.; Rochester C.H.; *J. Catal.*, **2**, 355, (1993).
McQuire M.W.; Rochester C.H., *J. Chem. Soc. Farad. Trans.*,**7**, 1117, (1993).

12 Jacobs W.P.J.H.; van Wolput J.H.M.C. van Santen R.A.; *Zeolites*, **13**, 170, (1993).

13 de Man A.; Ph.D thesis; Eindenhoven Holland, (1992).

Chapter 4.

Computer Simulation of the Reaction Mechanism of the Nickel Zeolite-Y catalyst.

4.1 The Determination by Computational Techniques of the Mechanism of Activation of the Ni-Zeolite-Y Catalyst.

4.1.1 Introduction.

In this chapter, we continue our account of the Ni-zeolite-Y catalyst by a detailed study of the mechanism of activation of the catalyst and the subsequent cyclotrimerisation reactions effected by the activated system.

Transition metal ions figure in a wide range of homogeneous reactions involving alkynes, alkenes, alkanes and alkanols. Such ions are embedded in both framework and extraframework sites in the cavities and channels of zeolitic aluminosilicalites, where their catalytic specificity and efficiency is often dramatically enhanced. For example, the oxidation of phenol to hydroquinone by Ti-ZSM5 is now being commercially exploited by the Enichem company in Italy. Many other such reactions can be found compiled in work of Maxwell[1] and Holderich *et al*[2].

Normally, however, the as-prepared transition metal ion exchanged zeolite is catalytically inactive; it has to be "activated", in a manner that varies both with the nature of the catalyst and the reaction that is catalysed. Thus, when either Na-H-Zeolite-Y or Li-H-Zeolite-Y are partially exchanged using aqueous solutions of $NiNO_3$, the resulting material, $Ni_{19}Na_{21}Al_{59}Si_{133}O_{384}$, is inert, so far as the cyclotrimerisation of ethyne (acetylene) to benzene is concerned, (a process discussed in much greater detail in the next section). However, after prolonged exposure to N_2 gas saturated with acetylene, the inert solid becomes an active catalyst and as such it has become activated. *In-situ* X-ray powder diffraction which, via the Rietveld profile refinement procedure, enables the precise location of extra-framework ions[3] to be determined. During the course of activation reveals, that the critical feature during the process of activation of the NaNiH-Y catalyst is the "migration" of Ni^{2+} cations, initially embedded at the S_I sites, located within the hexagonal prisms and their translation to S_{II} sites that lie in the supercages. Figure 4.1.1 is a schematic diagram of

the framework and shows only tetrahedrally co-ordinated atoms only, with the various extraframework cation sites. Whereas S_I sites constitute highly restrictive environments, the S_{II} sites are accessible to bulky reactants and products. These become centres at which catalytic conversions in the intercrystalline volume of zeolites can take place.

The activation process, of which the above is a good example and is one of the most significant, yet least well understood aspects of catalytic science. In the present study, we chart this process using a combination of computational techniques which enable us to calculate the energy of the nickel ion as it migrates through the zeolite structure and the way in which this is modified by the interaction with ligands. The calculations reported in this paper will allow us to determine; the minimum energy trajectory to identify the saddle point and its associated energy and to determine the interaction energies of ligands with the metal ions at the saddle point. The synthesis of these computational results leads to a detailed model of the activation process.

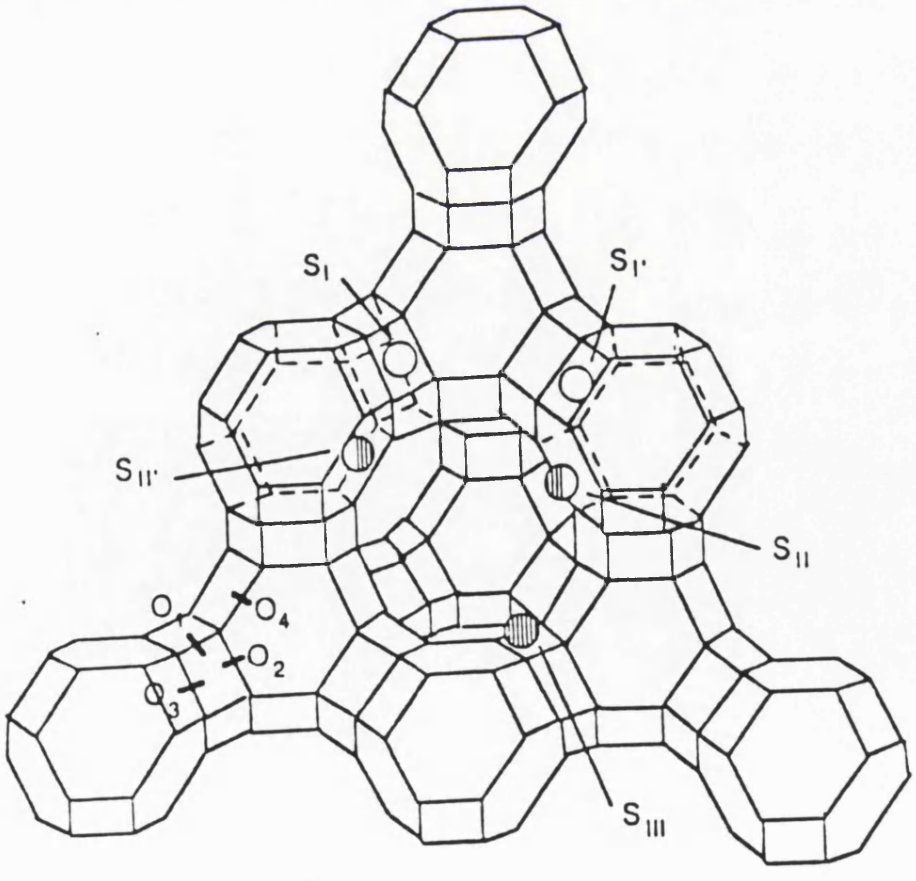

Figure 4.1.1 : Schematic diagram of the Zeolite-Y highlighting extraframework cation sites.

4.1.2 Methodology.

Our explorations of the energetics of the nickel ions within the zeolite pores use simulation techniques based on Born model potentials which have been extensively and successfully used in modelling the structures and energetics of zeolites[4,5,6]. The framework model includes long range Coulombic, as well as two and three body short range potentials, with a shell model treatment of oxygen polarisability[7], while the Nickel-framework interaction comprises both Coulombic and short-range pair potentials. The potential parameters employed for both the framework and extra-framework species were taken from references 8 and 9.

Having defined the potential model, we may then calculate the total potential energy of the Ni^{2+} cation at any point within the zeolite lattice. In performing such calculations three key features of our procedure should be noted :-

i) Coulombic sums are taken to infinity using the Ewald technique[10]. Short range potentials are set to zero for distances > 20Å.

ii) A Single Ni^{2+} ion was introduced into a purely siliceous zeolite lattice.

iii) The lattice is relaxed, i.e. all ions, including the framework, are adjusted until zero force, out to a radius of 10Å from the nickel cation.

Such calculations may be conveniently and efficiently carried out using the CASCADE code developed by Leslie[11], (as detailed earlier in chapter 2.3). To search the potential energy hypersurface experienced by the nickel cation, it proved necessary to divide the proposed area of investigation into 2 parallel planes, separated by 0.75Å. Plane 1 was taken along the [1,1,1] of the asymmetric unit cell, and plane 2 was taken so as to cut the proposed S_{II} exit window. Each plane was divided equally into a 121 point square grid and an isolated nickel cation anchored successively at each of these sites. The surrounding lattice was then allowed to relax as described above. A contoured energy surface was generated for each plane by performing a simple linear interpolation between the calculated points on the surface simulated to obtain energies between the calculated points.

Quantum mechanical calculations were also undertaken on the interactions between an isolated Ni^{2+} ion and respectively water, ammonia and acetylene. These employed the Local Density Functional, (LDF), approach[12], available in the DMOL code[13]. A numerical atomic centred basis set approach was employed. Details of the basis orbitals used are listed in table 4.1.1. and a comprehensive discussion of the *ab-initio* technique is described in chapter 2.6. The work of Delley[14] has shown that the use of numerical orbitals reduces basis set superposition effects and thus an excellent description of weak bonds is possible. These calculations included geometry optimisation of the hydrogen atoms of the molecule at a specific nickel-ligand distance. This enabled the bond angles in the water, for example, to change as the cation approached.

Table 4.1.1 : Numerical atomic orbitals used in the Local Density Function calculation.

Nickel	1S	2S	2P	3S	$3S^{**}$	3P	$3P^{**}$	4S	$4S^{**}$
Oxygen	1S	2S	$2S^{**}$	3P	$2P^{**}$				
Nitrogen	1S	2S	$2S^{**}$	2P	$2P^{**}$				
Carbon	1S	2S	$2S^{**}$	2P	$2P^{**}$				
Hydrogen	1S	$1S^{**}$							

Note : ** denotes a high exponent orbital.

4.1.3 Results and Discussion.

As noted above, a crucial aspect of this study is the inclusion of framework relaxation, with respect to the perturbation provided by the cation, which is of major significance when modelling highly flexible polar systems. Indeed, a contour plot of the Madelung (electrostatic) energy, before and after relaxation shows a distinct difference, (figure 4.1.2). The effect of framework relaxation is to smooth the electrostatic field with a less structured variation than obtained for the rigid framework model.

Figure 4.1.2 : The Madelung Energy **before** and **after** relaxation.

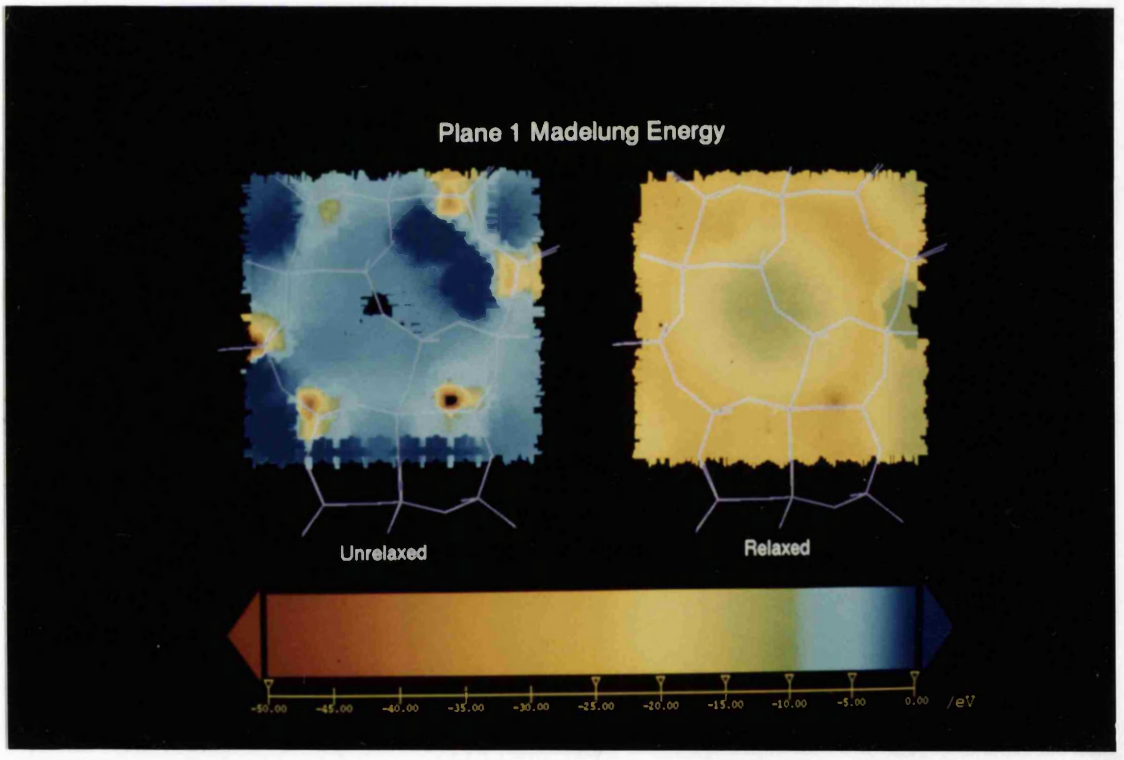

The results of our exploration of the potential energy surface of Ni^{2+} is shown diagrammatically in figures 4.1.3a and 4.1.3b, which represent the contour map for planes 1 and 2 respectively. There is an obvious trajectory for the migrating Ni^{2+} ion which can be elucidated from the figure, (the red lower energy pathway). The saddle point configuration can also be identified by closer investigation of the potential energy surface. The energy of the latter with respect to the Ni^{2+} at the stable S_1 site is 1.66 eV. This value may be taken as the activation energy for what we shall denote as "unassisted migration".

Although we used a purely siliceous framework model for the calculations of the energetic hypersurface experienced by the Ni^{2+}, it is possible to include the effects of aluminium in the framework. First we may include Al ions at specific framework sites, as in reference 15. However, the number of possible configurations in such a system is very large, so an alternative simpler approach involving an average tetrahedral ion was used. The charge on the average T atom was calculated, so as to represent the Si:Al ratio observed in the experimental system. The unassisted activation barrier, for this "average" representation of the aluminium character present within the system, is 1.04 eV, which is significantly less than that obtained for the purely siliceous model. Such a reduction in the activation energy is due to the greater relaxation of the lattice in the Al containing lattice. The main consequence of this increased flexibility is that the framework oxygen ions move closer to the cation, because of the reduction in the force constants for O-Al interactions compared with those for O-Si. The general effect of increased lattice flexibility can be observed experimentally in the Infrared spectra of zeolites with varying Si:Al ratios. The increased Al content within the framework reduces the frequency of the bond stretching modes and generally increases the intensity of the pore vibrational modes[16]. The effect has also been investigated via computer simulation[15], where relaxations of 0.5Å in the Ni^{2+}-O distance around a Ni cation and S_1 site are observed for the purely siliceous model, but relaxation of approximately 0.7Å are calculated when Al is included within the framework.

Figure 4.1.3a : The energetic contour map, as seen by the Ni^{2+} cation moving in plane 1.

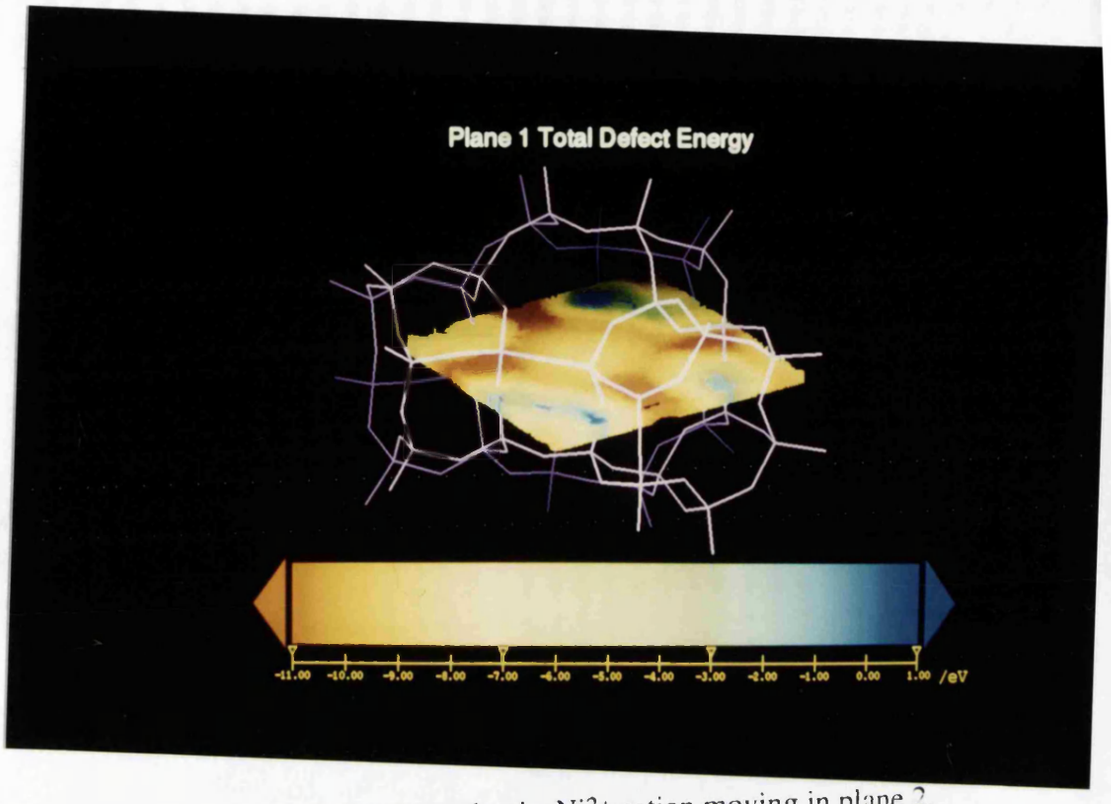

Figure 4.1.3b : The energetic contour map, as seen by the Ni^{2+} cation moving in plane 2.

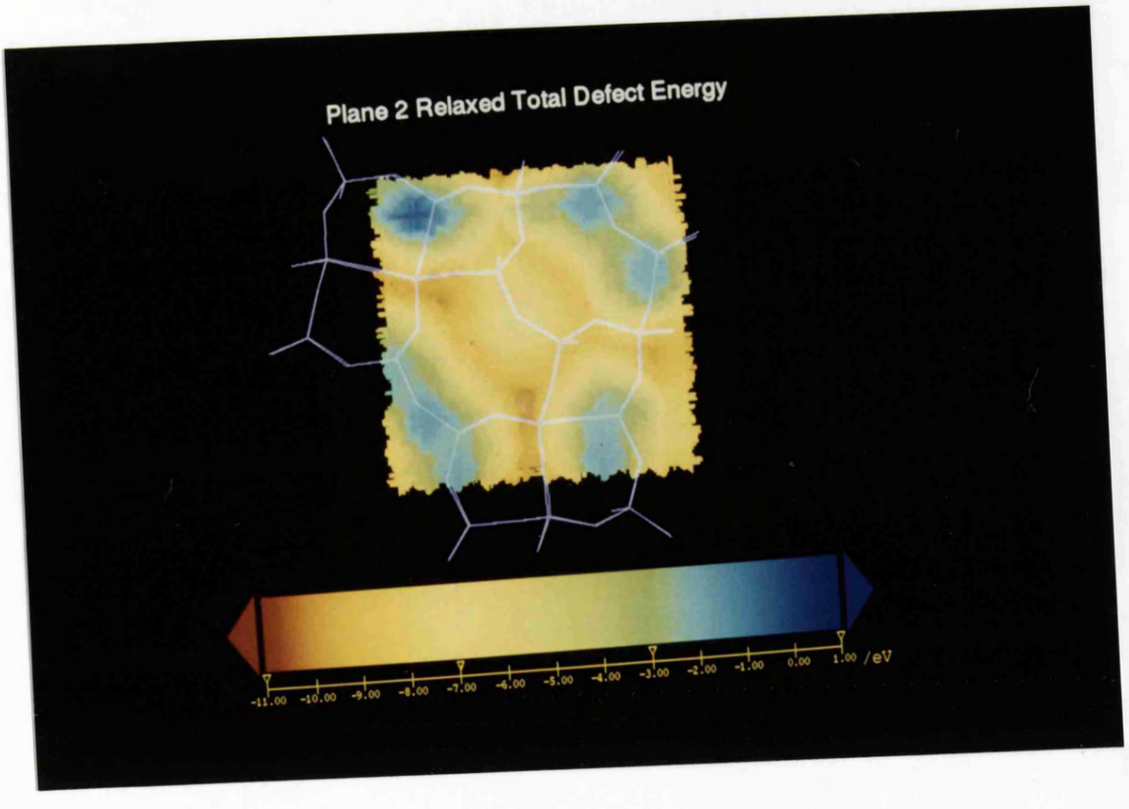

Indeed, the value of the activation barrier in the purely siliceous model must be considered as an upper bound and as such any other interaction which is strong enough to overcome this barrier will invariably overcome the lower energy barrier which should be present in the Al containing system.

Small molecules may readily diffuse into the supercage of the zeolite lattice[17] and up to the S_{II}, 6-ring site shown in figure 4.1.1. We propose, however, that molecules such as H_2O, NH_3 and C_2H_2 at the 6 ring site may interact strongly with the migrating nickel ion and thereby assist its transition from the S_1 site into the supercage. This proposal is strongly supported by the quantum mechanical calculations. We calculated the energies of interaction of the Ni^{2+} ion with the three ligands for a range of distances. The values corresponding to the saddle point configuration derived from the atomistic calculations for a purely siliceous model are reported in table 4.1.2 and are in general agreement with the value calculated from a Born-Haber thermodynamic type of approach.

Table 4.1.2. : *Ab-initio* calculated interaction energies for the Ni^{2+}--ligand interaction at the saddle point distance.

Ligand		Interaction energy (eV)
Water.		-5.4
Ammonia.		-7.1
Acetylene.		-5.9

At these separations we find that the interaction energy is substantially greater than the activation energy for the unassisted migration. The quantum mechanical calculations in essence simulate the in-vacuo reaction and as such neglect the interaction with the zeolite framework. At present, it would be computationally very difficult to include the framework explicitly and the effect of using a rigid point charge array would be unsuitable, as the Madelung field and its subsequent deformation during the cation migration would not be accurately represented. However, the magnitudes of the cation-ligand interactions are clearly sufficient to overcome the Ni^{2+} migration barrier, even if the former are substantially modified by the interacting framework atoms.

4.1.4 Conclusion.

The mechanism of activation of the catalyst is therefore revealed. The migrating nickel ion follows the proposed trajectory shown in figure 4.1.4. The energy barrier opposing the process is, however, overcome by the interaction between the migrating Ni^{2+} cation and the appropriate ligand at the 6-ring site. One can also conclude that to model zeolites and their associated interactions reliably one must include the framework relaxation of these highly flexible solids. Having charted the migration of the Ni^{2+} ion into the supercage where it can play its rôle in catalytic processes, we continue by elucidating the mechanism of the catalytic trimerisation of acetylene which, as discussed earlier is effected by the Ni-zeolite-Y catalyst.

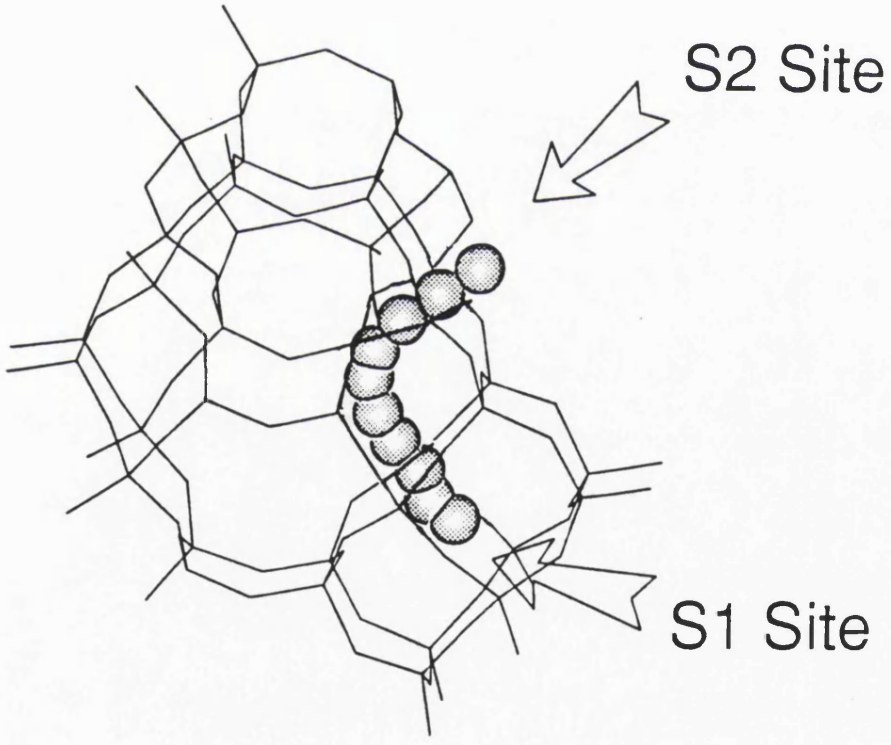

Figure 4.1.4 : The proposed trajectory of the Ni^{2+}cation migration from the S_I site to the S_{II} site.

4.2 The Elucidation by Theoretical Means of the Cyclotrimerisation of Acetylene to Benzene.

4.2.1 Introduction.

As discussed in chapter 1 and 4.1.1, transition metal cations play an important role in many heterogeneous and homogeneous catalysed reactions, involving numerous compounds containing many different functional groups. Yet, although their presence inside heterogeneous systems, (typically aluminosilicalites), is known to enhance dramatically the efficiency and specificity of the catalytic reaction, the actual mechanism of reaction is still unknown. However, with advances in *ab-initio* techniques and "raw" computer power, it has become possible to trace the precise geometry and energies associated with the various steps in a catalytic process[18].

In 1866, the French scientist Berthelot found that acetylene undergoes trimerisation to form benzene[19], a substance discovered at the Royal Institution by Michael Faraday in 1826. In more recent years this reaction has again attracted attention, as the need for chemical feedstocks, other than from petro-chemical sources increases and thus detailed experimental investigations have been reported on such processes. At elevated temperatures, (1100K to 1800K), acetylene is converted homogeneously to benzene[20,21] but, in the presence of a Nickel ion-exchanged zeolite, the conversion occurs catalytically at around 400K[22], with greater selectivity to benzene than for the purely thermal process. With the aid of theoretical calculations we can gain insight into the mechanism of the heterogeneous reactions. We achieve this by simulating several possible reaction pathways and proposing plausible intermediates, the energies and geometries of which may be computed quantum mechanically. In the work reported in this section, we investigate and indeed, propose a mechanism for the cyclotrimerisation of acetylene to benzene in the presence of a Ni^{2+} cation, represented schematically in figure 4.2.1. This work neglects the effect of

the framework and its subsequent influence on the mechanistic steps of the catalytic cycle because there is experimental evidence that the cations undergo reaction in the supercage and thus, the zeolite host can be considered to act as a support. The nature of this support could be to maintain an environment suitable for the existence of a "naked" Ni^{2+} cation, which remains unbound and is free to migrate, as reported in chapter 4.1. This approach to the description and rôle of the zeolite framework is consistent with experimental chemistry, in which other Ni^{2+} containing species do not effect this reaction. In these cases the Ni^{2+} is not "isolated", but moreover contains either, several shells of solvent or strongly bound ligands which must first be dissociated before reaction can proceed.

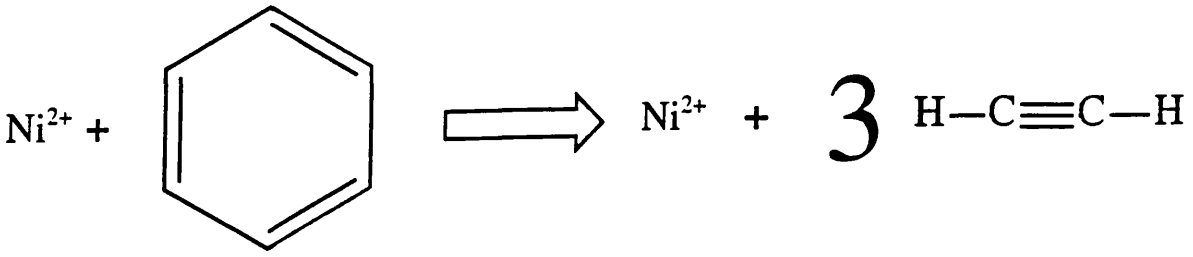

Figure 4.2.1 : A schematic of the trimerisation of acetylene to benzene.

Several models for the mechanism have been investigated and range from a Frontier orbital type of approach, whereby the Highest Occupied Molecular Orbital, HOMO, of one complex interacts with the Lowest Unoccupied Molecular Orbital, LUMO, of another or vica versa. Another plausible model proposes that it is the effective charge density gradient after the docking of a molecule to the Ni^{2+} ion that predetermines the orientational approach of the next acetylene molecule. A clue to the mechanism can be achieved by examining the reverse process, i.e. the dissociation of benzene to the constituent three acetylene molecules, again shown schematically in figure 4.2.2.

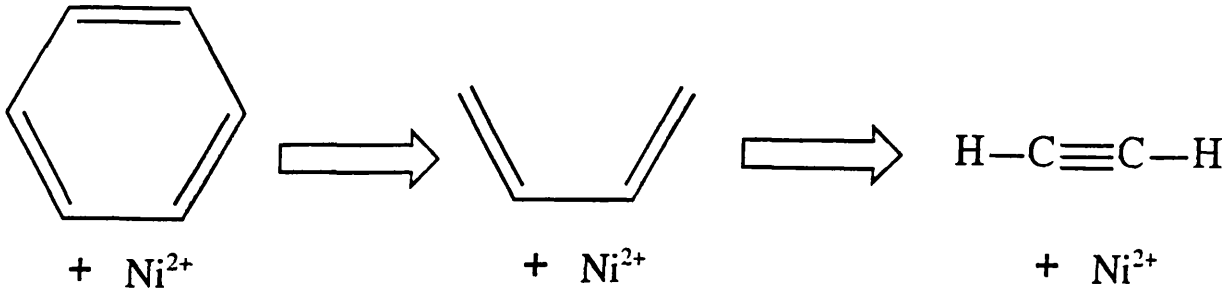

Figure 4.2.2 : The dissociation of benzene to three molecules of acetylene, used in investigating the major mechanistic precursors.

4.2.2 Methodology.

The Local Density Functional, LDF, methodology was chosen for these simulations, the theoretical details of which were described previously in chapter 2.6. As noted earlier (section 2.6), this technique is most effective for the complex electronic ground state which is important for simulations involving transition metal cations because of the numerous low lying electronic excited states. The basis set chosen in the present work was an atomic centred numerical one and the orbitals used to represent the atoms are described in table 4.2.1. The inclusion of **3d** orbitals on the carbon atoms, **2p** on the hydrogen atoms and **4p** orbitals on the nickel ion allows us to model the polarisation effects which will undoubtedly be significant. The DMOL[13] code was used to perform the calculations.

Table 4.2.1 : The "DNZ" numerical basis set used for these calculations.

C	:	1s, 2s, 2s**, 2p, 2p**, 3d
H	:	1s, 1s**, 2p
Ni	:	1s, 2s, 2p, 3s, 3p, 3d, 3d**, 4s, 4s**, 4p

Note : ** denotes a high exponent orbital.

We simulated the mechanism for the addition of acetylene molecules to the Ni^{2+} cation in a variety of ways. Firstly, an acetylene molecule was added to the complex using a HOMO/LUMO approach and then secondly, on the basis of the charge density gradient, which via the long range Coulombic interactions could determine the approach of the subsequent acetylene molecules. The results from the two approaches are discussed separately, we note that all the energies reported in this section are with respect to an isolated Ni^{2+} cation and the relevant number of acetylene molecules, with the interaction energies being described by a positive value indicating a favourable interaction.

i) The Frontier orbital approximation.

The theory and justification for such an approach resides in the application of Molecular Orbital theory. The approach employed was originally laid out in the work of Woodward and Hoffman[23], who showed that the interaction and subsequent bonding process was a function of the overlap of molecular orbitals. This can be justified in that during a reaction, the electrons in the Highest Occupied Molecular Orbital, HOMO, are partially transferred into the Lowest Unoccupied Molecular Orbital, LUMO, of another molecule and hence an implied covalent bond is formed via this overlap.

In using this method to investigate the mechanism we attempt to maximise the overlap of the HOMO/LUMO orbitals of the complex with the orbitals of the acetylene molecule. In defining the 3D spatial extents of the orbitals we took the extents corresponding to the electron density contour of ±0.01|e|. This value is arbitrary but was found to be the most suitable for representing the general features of all the complex's orbitals considered. Figure 4.2.3(a) represents the calculated 3-dimensional contour used to define the HOMO/LUMO respectively of the acetylene molecule below. Figure 4.2.3(b) shows the classic Hoffman representation of the HOMO and LUMO orbitals.

In the subsequent simulations, the interacting complexes were brought into contact and oriented in 3-dimensional space so as to maximise the overlap of the HOMO of one species with the LUMO of the other or vica-versa. Indeed, when all the possible combinations are considered, four resulting orientations of three acetylene molecules around a Ni^{2+} ion are possible. It has to be emphasised that the orientation and approach of the subsequent acetylene molecule depends on the HOMO or LUMO calculated for the entire previous complex, which can dramatically change in shape; the new orbital is not just a union of the two previous isolated orbitals. Figure 4.2.4 is a representation of the possible combination of HOMO and LUMO molecular orbitals and it also contains the nomenclature used for the related discussion, i.e. C2 represents

the LUMO(Ni+acetylene) interacting with the HOMO(Acetylene) and C3h_l relates to the HOMO(C3) and the LUMO(Acetylene).

Figure 4.2.3(a) : The calculated HOMO/LUMO orbitals of an isolated acetylene molecule.

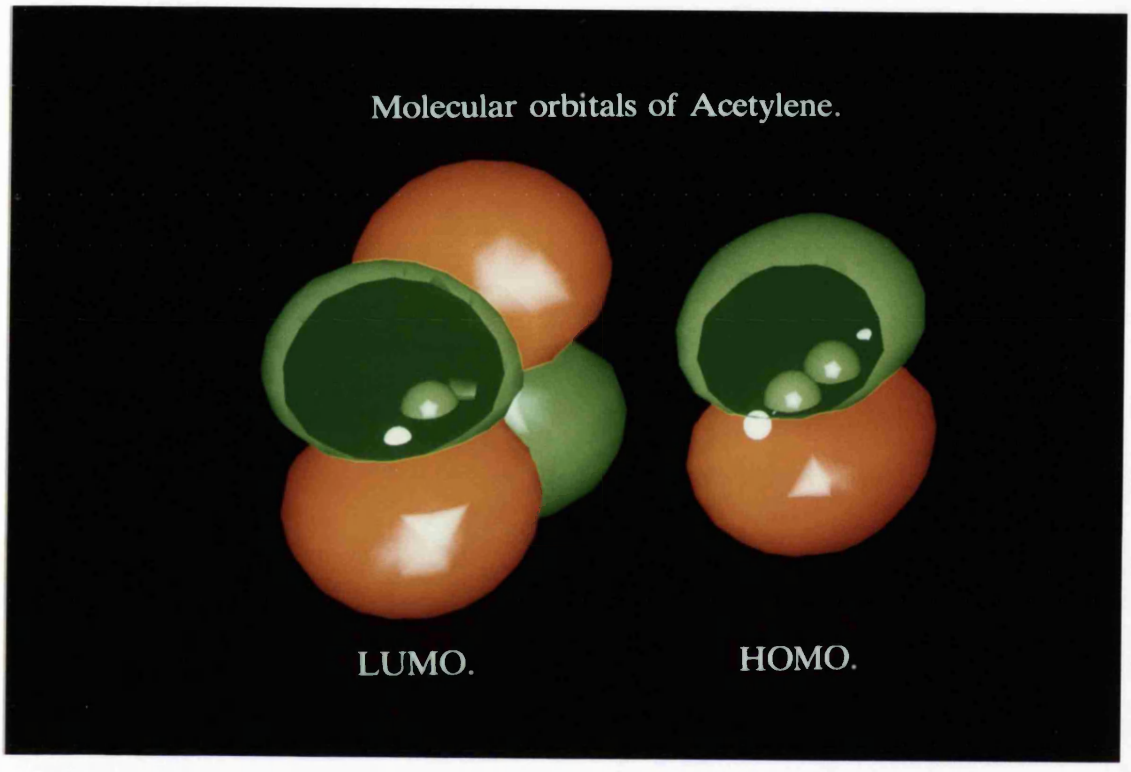

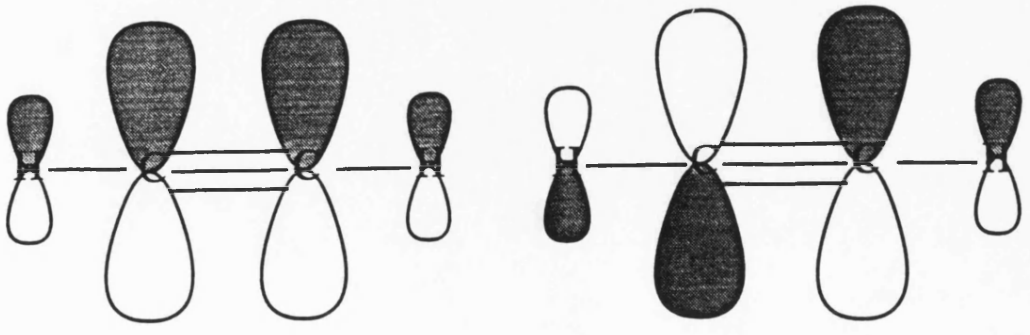

Acetylene Homo

Acetylene Lumo.

Figure 4.2.3(b) : The classic text-book representation of HOMO/LUMO orbitals of an acetylene molecule.

Figure 4.2.4 : Schematic representation of the HOMO/LUMO Frontier orbital approach to the elucidation of the mechanism.

ii) The Charge Density approximation.

This method of iteratively docking the acetylene molecules onto the Ni^{2+} cation, is based on electrostatic criteria and may be of considerable utility as the long range force extends further into space than does the short range orbital overlap. Indeed, the long range Coulombic effect can be thought of as predetermining the orientation of the approaching molecule, before the short range forces can be considered a major factor in the potential energy. This methodology uses the gradient of the charge density to determine the molecular approach, the larger the gradient the stronger the force exerted on the acetylene from that orientation in 3-dimensional space. This type of approach is commonly used in protein modelling, where the interacting molecule is often assumed to have acquired a docking conformation some way away from the active site. Figure 4.2.5 depicts a charge density contour through a nickel-acetylene complex. The closer the contours, the steeper the charge density gradient and thus the greater the electrostatic force extending from the system. The contours in figure 4.2.5 are in increments of 0.01|e| and once the density is above 0.6|e| the contours merge and for clarity have not been represented in this diagram.

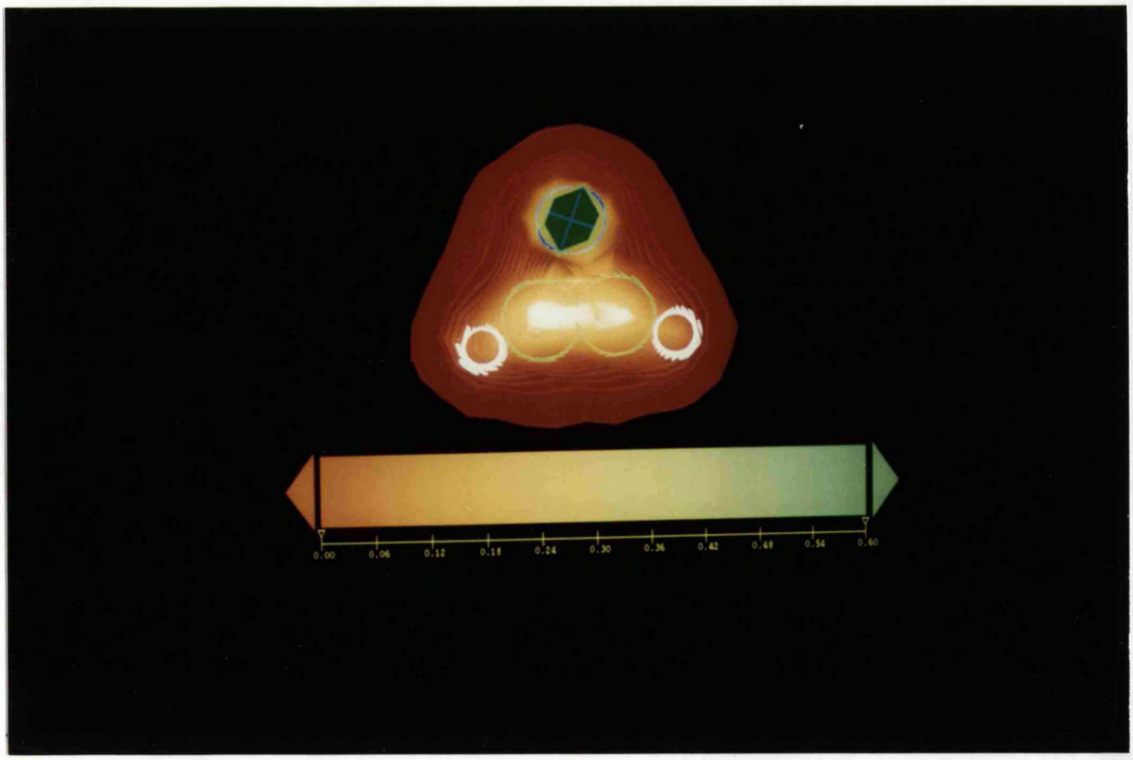

Figure 4.2.5 : A charge density contour map of a possible nickel-acetylene interaction.

iii) The reversal of the mechanism to identify intermediates.

Since the mechanism is necessarily "molecular" in nature, i.e. invoking successive docking of the intact acetylene molecules, (although a free radical type of species could possibly be observed as in the homogenous reaction[24]), it is easier to postulate the forward reaction if key intermediates are known. It is perhaps simpler to do this in reverse, i.e. to start with the finishing products and successively remove acetylene molecules to end with the starting products. Figure 4.2.6 shows this schematic reverse mechanism and from these key intermediate structures, important conformational information about the major structural precursors involved in the unknown forward reaction is acquired.

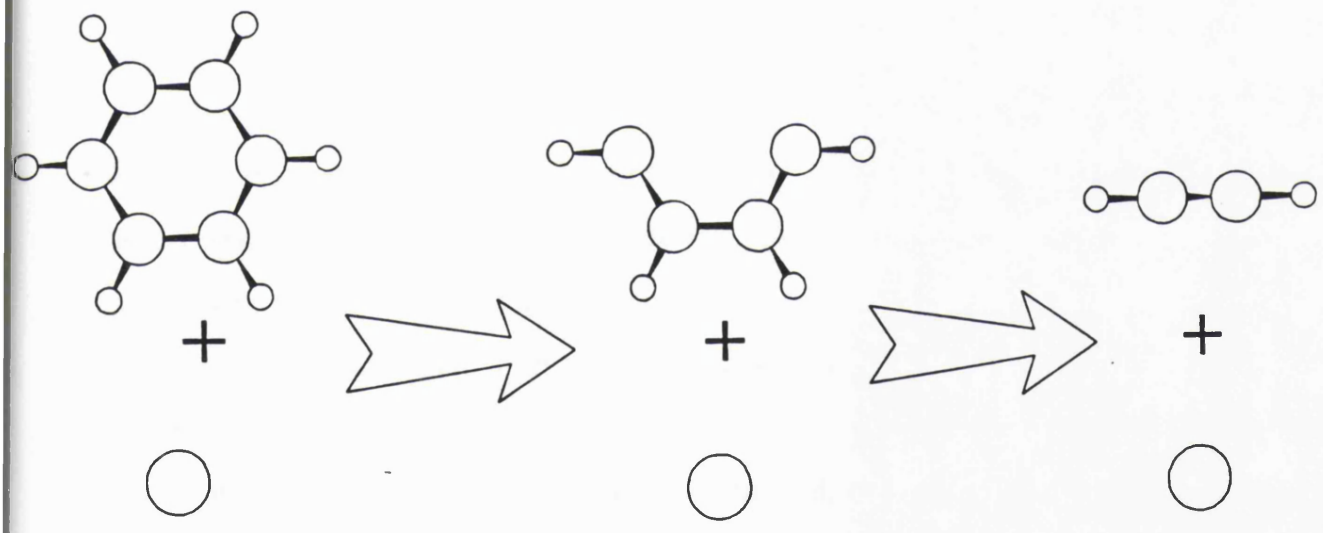

Figure 4.2.6 : A schematic representation of the reverse of the trimerisation process, showing the key intermediate structures.

Using this simple mechanistic approach, we now begin to investigate the precise mechanism of the cyclotrimerisation of acetylene to benzene around a Ni^{2+} cation.

4.2.3 Results and Discussion.

Basic reversal of the mechanism.

As described above, the mechanism was first considered in reverse as this helps us to identify the intermediates. These structures are usually reaction intermediates with a finite lifetime and are expected to be local minima within the potential energy hypersurface of the reaction. Such species only provide information on important stages of the mechanism and do not yield enough information to construct a detailed reaction mechanism, although many previously reported mechanisms have been based largely on such intermediates. Figure 4.2.6 describes the process schematically, whereas figure 4.2.7(a,b,c) reports the detailed structures located by *ab-initio* geometry optimised calculations. Clearly from figure 4.2.7a, the effect of the Ni^{2+} cation on the benzene molecule is marginal. However, upon closer inspection the C-C bond length has increased from 1.39Å to 1.42Å, and the cation resides at the centre of the ring, approximately 2.15Å away from each of the carbon atoms. The internal ring angles are within ±0.1° of the isolated values, yet the ring has a noticeable perturbation to a slightly out of plane conformation, that is the H-C-C-H torsion angle increases from 0° in the isolated state to +0.6° on interacting with the cation.

When a complete acetylene molecule is removed, to give the structure shown in figure 4.2.7b, the structure changes from the flat conformation to a twisted conformation with the terminal hydrogen atoms being forced down away from the cation. The complex is now beginning to resemble two acetylene molecules; two C-C bond lengths of 1.33Å and the third at 1.52Å. The cation has also moved so that the carbons are split into two groups with distances of 1.86Å and 2.03Å.

After the removal of another connected C_2H_2 unit, only the cation and one acetylene molecule are left. The resulting conformation of the acetylene molecule is far from linear, the molecule has a C-C-H bond angle of approximately 159°, which is

substantially different from the linear value of 180° for the isolated molecule.

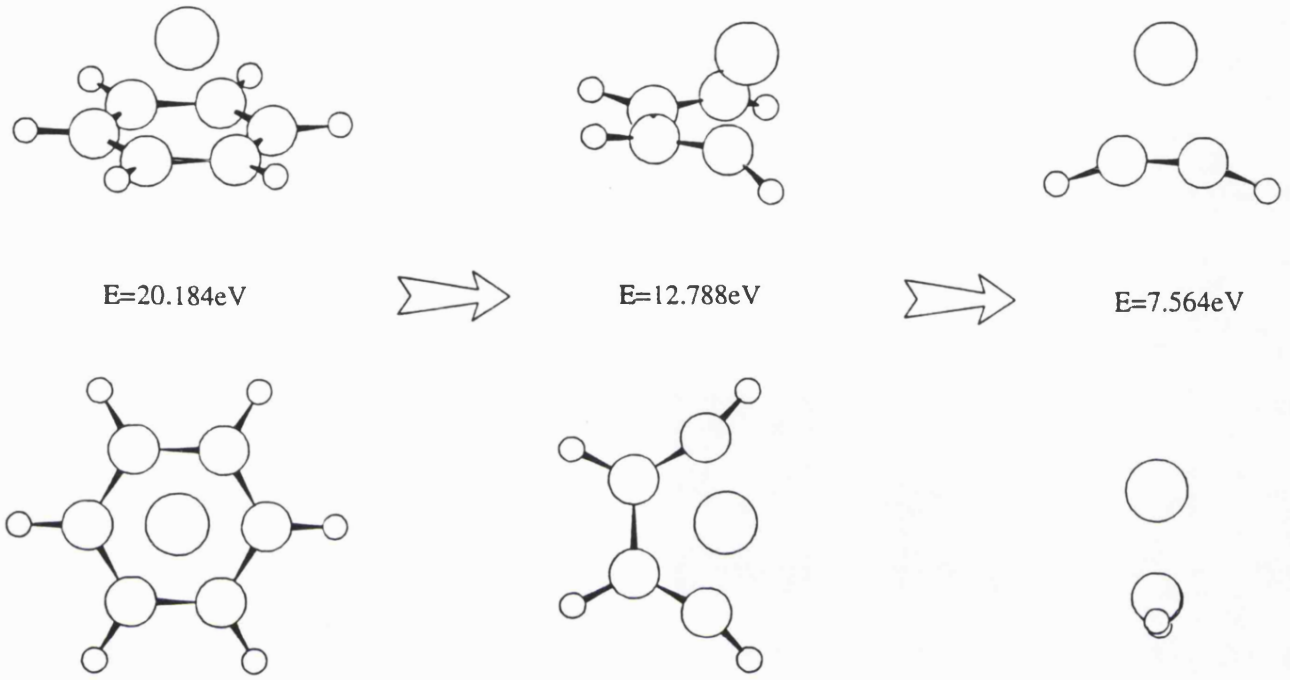

Figure 4.2.7(a,b,c) : The calculated structures for the key intermediates in the "reverse" of the trimerisation reaction. The conformations are shown for two different viewing orientations.

(Note **positive** energies indicate a favourable interaction).

From these results we may infer the potential energy profile which is described in figure 4.2.8.

Figure 4.2.8 : A calculated energy profile for the devolution of the trimerisation process. (Energy is with respect to the isolated species, i.e. Ni^{2+} and acetylene molecules.) Note, a **positive** interaction energy indicates a favourable interaction.

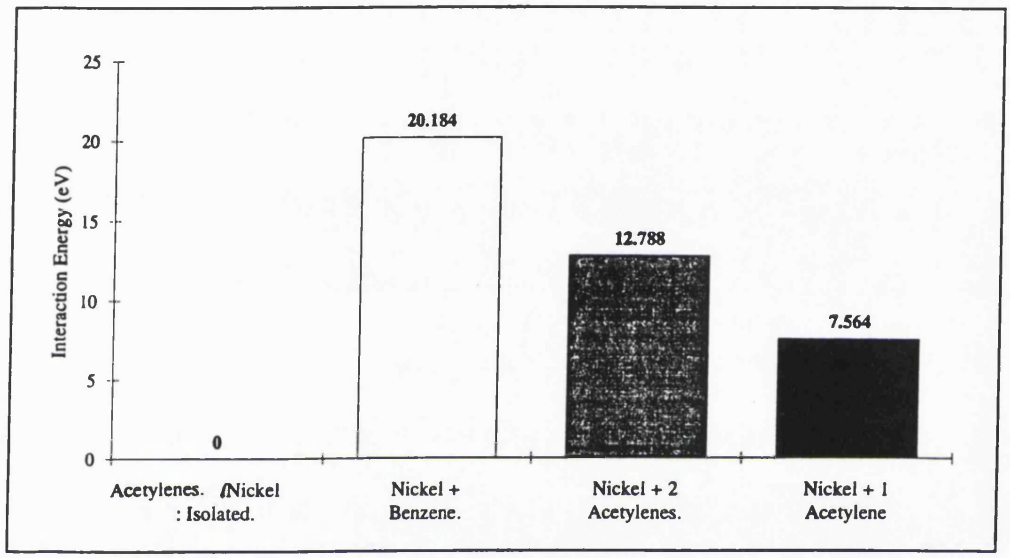

The profile described above only details the proposed local minima and contains no information on how they are interconverted via the transition states or activation barriers. The interaction energy of a "naked" Ni^{2+} cation and an acetylene molecule is large, 7.564eV. Thus is predominantly due to the back donation of electron density from the electron rich acetylene π bond into the empty **4s** and **3d** orbitals on the cation. Table 4.2.2 reports the orbital occupations of the Ni^{2+}-acetylene complex, (figure 4.2.7(c)) and compares the orbital occupations of the isolated species. The orbital overlap contributions for the major covalent bonding orbitals are also tabulated. In the isolated acetylene molecule, 30% of the electron density resides in the π orbitals and the C-C bond is extremely electron rich. However, once the acetylene interacts with the cation, the orbital overlap is very different. Indeed, once bonded the carbon $2p^0$ orbital occupation is reduced by 44% with this density being

redistributed onto the low lying cation orbitals. This type of bonding results in a non-linear conformation for the acetylene molecule, due to the lowering of the conjugation, because of back-bonding with the cation.

Table 4.2.2 : Orbital occupations for the Nickel-acetylene interaction located by the devolution of the mechanism.

Property			***Isolated***	***Interacting***
Orbital Occupations. |el|	Carbon	**1s**	2.00	2.000
		2s	1.36	1.522
		2p	2.93	2.468
		3d	0.00	0.084
	Hydrogen	**1s**	0.619	0.402
		2p	0.045	-0.034
	Nickel	**1s**	2.00	2.000
		2s	2.00	2.000
		2p	6.00	6.000
		3s	2.00	2.002
		3p	6.00	6.004
		3d	8.00	8.539
		4s		0.393
		4p		0.186
Orbital Overlap |el|				
C - H Bond.	H **1s**	C **2s**	0.146	0.100
	H **1s**	C $2p^{+1}$	0.179	0.137
C - C Bond.	C $2p^{+1}$	C **2s**	0.164	0.123
	C $2p^{-1}$	C $2p^{-1}$	0.288	0.128
	C $2p^{0}$	C $2p^{0}$	0.271	0.158
	C **2s**	C $2p^{+1}$	0.164	0.123
	C $3d^{+1}$	C $2p^{0}$	0.010	0.015
Ni - C Bond.	Ni **4s**	C **2s**	0.00	0.050
	Ni **4s**	C $2p^{0}$	0.00	0.077
	Ni $4p^{-1}$	C $2p^{-1}$	0.00	0.012
	Ni $4p^{0}$	C $2p^{0}$	0.00	0.022
	Ni $4p^{0}$	C **2s**	0.00	0.030
	Ni $3d^{-1}$	C $2p^{-1}$	0.00	0.042
	Ni $3d^{+1}$	C **3s**	0.00	0.011
	Ni $3d^{+1}$	C $2p^{0}$	0.00	0.031

Frontier Orbital Approximation to the elucidation of the mechanism.

As described in the methodology section, this approach into the investigation of the mechanism invokes maximising the overlap of the HOMO of one species with the LUMO of another or vica-versa. An initial starting configuration is required for the interaction of a Nickel cation and one acetylene molecule, for which two initial configurations are possible. The first is the one discussed above, whereby the cation interacts in a perpendicular fashion with the acetylene π bond and the second, involves the cation approaching the acetylene molecule end on. Indeed, any number of initial configurations are possible but these two cases represent the two extremes. Figure 4.2.9(a,b) shows the energy optimised structures for the two starting structures, the Ni^{2+} cation dramatically changes the molecular conformation of the acetylene molecule in both cases. In the perpendicularly oriented approach of the cation, 4.2.9(a), the hydrogen atoms distort symmetrically and the resulting structure is of course exactly the same as the last step shown in figure 4.2.7(c). The binding energy of the structure, with respect to the isolated starting species is, as noted, 7.564eV. Whereas, when the cation is introduced "endwise" to the acetylene molecule, an asymmetric distortion of the hydrogen atoms is calculated, figure 4.2.9(b). The π bonding overlap between the carbon atoms and the low lying Ni orbitals is not so pronounced as for the previous case and this is reflected in the lower interaction energy of 7.479eV. The starting structure for the subsequent frontier orbital approach calculations will be that shown in figure 4.2.9(a), as the interaction energy is lower and is consistent with our previous mechanistic discussion.

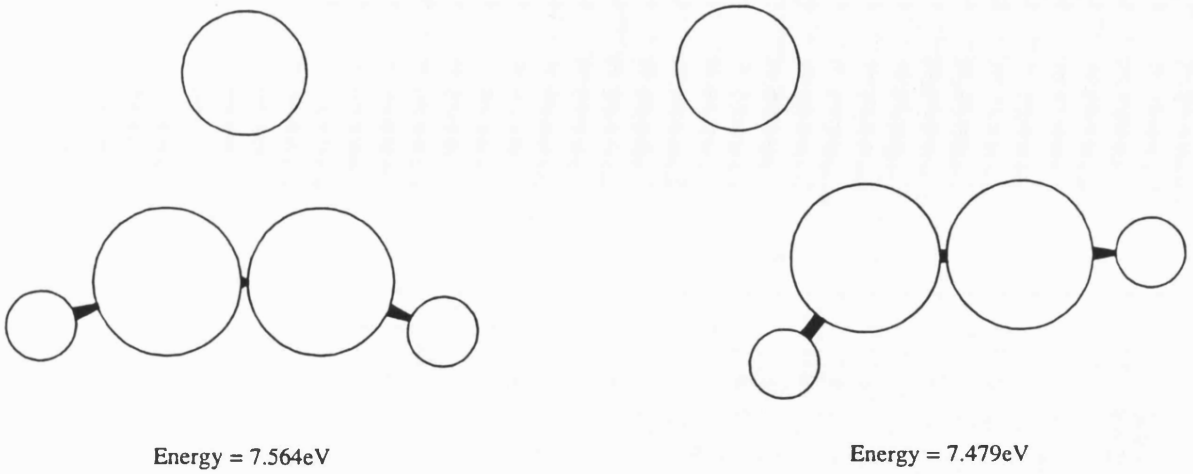

Energy = 7.564eV

Energy = 7.479eV

a)

b)

Figure 4.2.9(a,b) : The optimised structures for one acetylene molecule interacting with the Ni^{2+} cation.

Figure 4.2.4 shows the various possibilities investigated and the terminology employed in the naming of the complexes to be used in this section. This scheme was followed through and three acetylene molecules were iteratively docked and minimised in the appropriate HOMO/LUMO determined positions. Figure 4.2.10 reports the pathway, the energies of each complex and the resulting geometry optimised structures for each combination under investigation. Indeed, starting with the (Ni+acetylene) complex, figure 4.2.9(a), the resulting HOMO/LUMO docked structures, C3 and C2 respectively, have different interaction energies. C3 has an energy of 11.505eV with respect to the isolated species, whereas the structure represented by the C2 complex has an energy of 12.161eV and is thus more thermodynamically favourable. However, none of the conformational arrangements yet formed resemble the intermediate shown in figure 4.2.7(b), which is also thermodynamically more stable than C2 or C3, with an interaction energy of 12.788eV. At first glance, it would appear that the frontier orbital type of approach is unsuitable for the modelling of this mechanism, but the procedure used by DMOL optimisation, involves a Conjugate Gradient energy minimisation technique[25]. This as

with any minimisation procedure finds the nearest local minimum, if there is a potential energy barrier then it will not surmount it and produce the more stable conformation. There is almost certainly an energy barrier between the different configurations shown in figure 4.2.10 as the precursors illustrated in figure 4.2.7b.

When the third acetylene molecule is docked, four new possible combinations are achieved depending on the HOMO/LUMO combinations used. Two of these structures, C3h_l and C2l_h, reveal that the acetylene molecules are still isolated and are arranged uniformly around the cation. This ligand type of arrangement is reflected in the interaction energies, 13.403eV for C3h_l and 13.543eV for C2l_h. These structures are typical of those in classic transition metal chemistry, whereby a ligand donates electrons to the transition metal but does not undergo reaction.

Alternatively, for the structures named C3l_h and C2h_l, there has indeed been a reaction between the two previously docked acetylene molecules upon addition of the third. This is not the classic concerted ring closure favoured by many text books but rather, the third acetylene molecule forces the previous two ligands to adjust position, so that the carbon atoms can bond as the hydrogen atoms have been forced away by the cation. The C3l_h, energy 16.059eV, has formed a structure dissimilar to the intermediate proposed in figure 4.2.7b. However, C2h_l with an interaction energy of 16.539eV, has formed an intermediate structure very similar to that structure: interestingly for this species to be produced, a third acetylene molecule must first bind onto the cation to force the other two acetylene molecules to bond. On a thermodynamic energetic basis, this is the most likely product of all the systems simulated so far with three acetylene molecules.

Figure 4.2.10 : The conformation and interaction energies of the structures located via the frontier orbital approach to the mechanism.

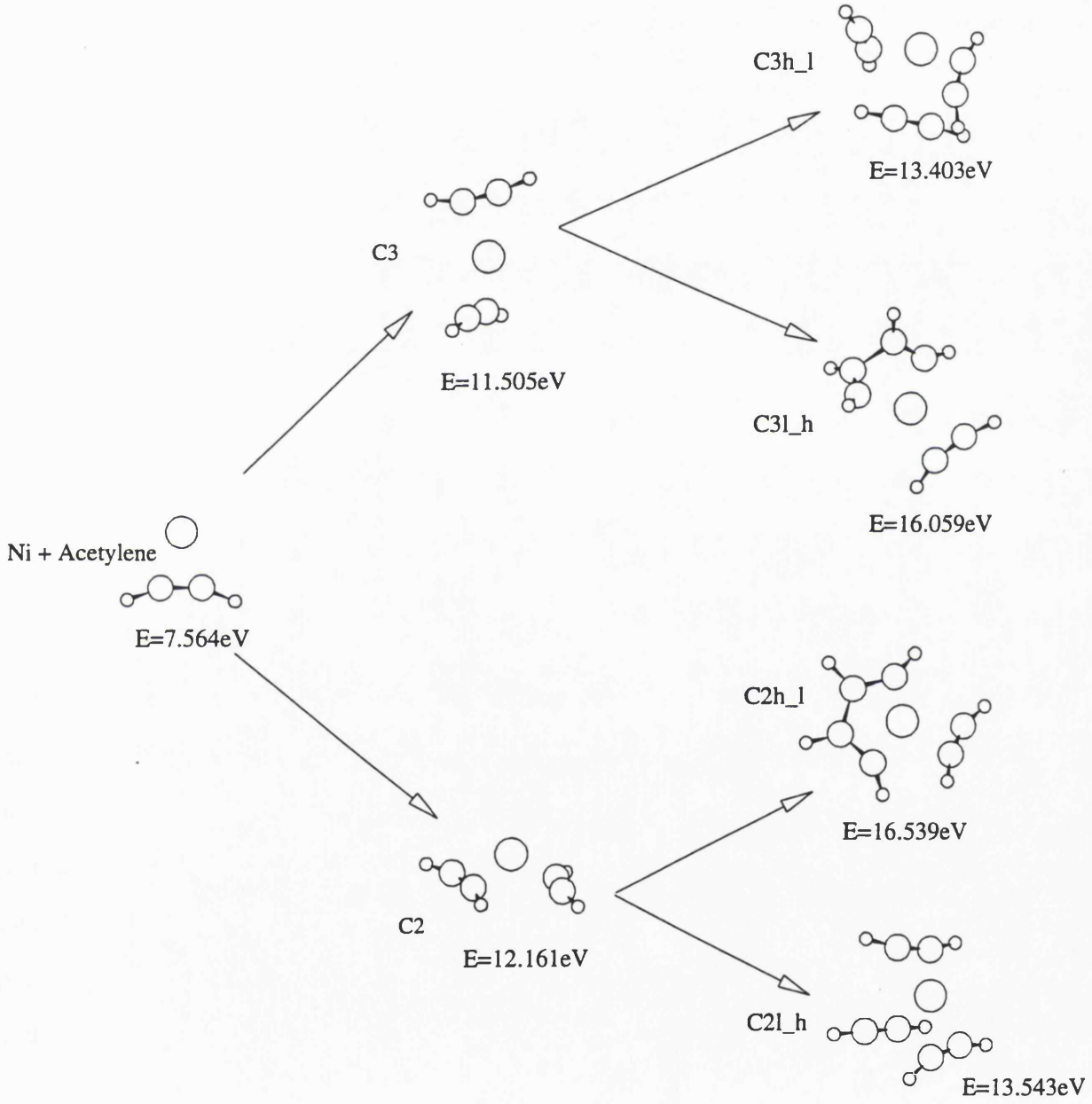

A key rôle in the mechanism is played by the back bonding of the acetylene π orbitals which forces the hydrogen atoms to distort out of plane and it is this disruption in the bonding that allows the carbon atoms to begin to change from an sp^1 type of arrangement into an sp^2 type of bonding. The cation interacts with the **2p** orbitals on the carbon atoms and thus breaks the symmetric sp^1 configuration. This effect is reinforced by the orbital overlap of the Ni^{2+} **4s, 4p** and **4d** orbitals with the carbon orbitals. Indeed, for the (Ni+acetylene) complex, (table 4.2.2), there is a total orbital overlap with the low lying cation orbitals of 0.225|e|, a value nearing that of a typical covalent bond.

The results so far indicate that the reaction mechanism for the trimerisation of a settling to benzene via a nickel catalyst is far from simple and indeed, it is definitely not a simple concerted ring formation. The addition of the third acetylene molecule seems to help the two previously non-bonded molecules to react, providing they are in the correct original orientation. Only half of the systems studied form conjugated species, the other conformations just orientate themselves as ligands around the cation.

Of course in the real system thermal effects will cause the acetylene molecules to both bind and disassociate from the cation. It is proposed that the third acetylene molecule just added could either dissociate from the complex, thus leaving only two acetylene molecules bound to the cation, or undergo a complex rotation involving an activation barrier until it is in the correct orientation for which to react. For the C3h_l and C2l_h, the unreacted complexes, this dissociation will result in the reversal of the previous addition step and the structures will remain as previously reported, i.e. C3 and C2 respectively. However, for the newly reacted structures, C3l_h and C3h_l, it is possible that upon removal of the third acetylene, the newly formed conjugated species will remain bonded and could form an intermediate transition state with a finite lifetime. Figure 4.2.11(a,b) reports the structures derived once the third molecule has been removed. The structures are indeed stable: C3l_h_less, (figure 4.2.11(a)), has a binding energy of 12.331eV and C2h_l_less, 4.2.11(b) has an

interaction energy of 12.779eV and the conjugated systems remain intact. Indeed, the structures are more stable than C2 or C3 which contain the same number of molecular constituents. C2h_l_less, 4.2.11(b) is almost identical to the reaction intermediate proposed in figure 4.2.7(b).

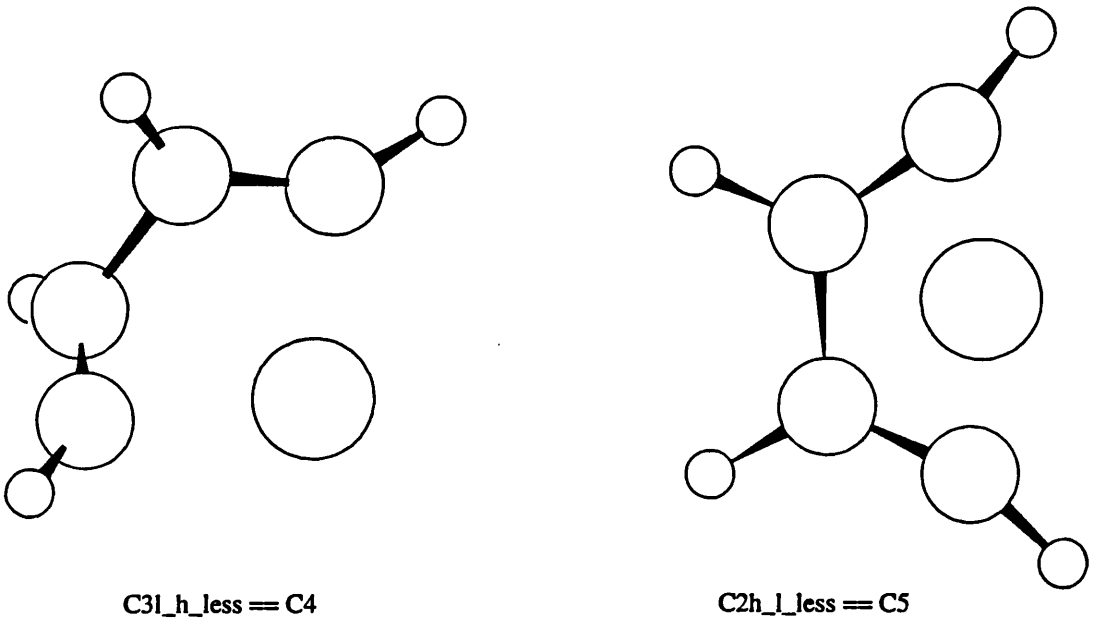

C3l_h_less ≡ C4 C2h_l_less ≡ C5

Figure 4.2.11 : Models representing possible intermediate structures.

(a) : C3l_h_less ≡ C4: (b) C2h_l_less ≡ C5

At this stage in the mechanism, it is possible for another third acetylene molecule to interact with these new complexes, again modelled by a frontier orbital type approach. Alternatively, it could be possible for these complexes to be detached from the cation. This is a model for the reaction of by-products and will be discussed later in this chapter. The frontier orbital type approach was applied to these new conjugate systems and figure 4.2.12 reports the schemes examined for the addition of a third acetylene molecule to these complexes, the naming conventions used, and the structures calculated after energy minimisation. Figure 4.2.13 reports the HOMO/LUMO contours of the HOMO(C5) + LUMO(Acetylene) interaction using a

visual aid to help clarification of the frontal orbital approach. The C5l_h system shows that the third acetylene is simply acting as a donor ligand to the cation, whereas the result for the C5h_l, (the interaction described in figure 4.2.13), results in an open benzene ring, i.e. there are five C-C bonds which are approximately planar, yet the ring is not fully closed as the hydrogen atoms are oriented out of plane and thus the electronic conjugation required for the ring to be flat is not yet achieved. Remarkably, a benzene like derivative has been formed and when the cation is removed from the system, the open ring topology closes to yield a flat conjugated benzene ring.

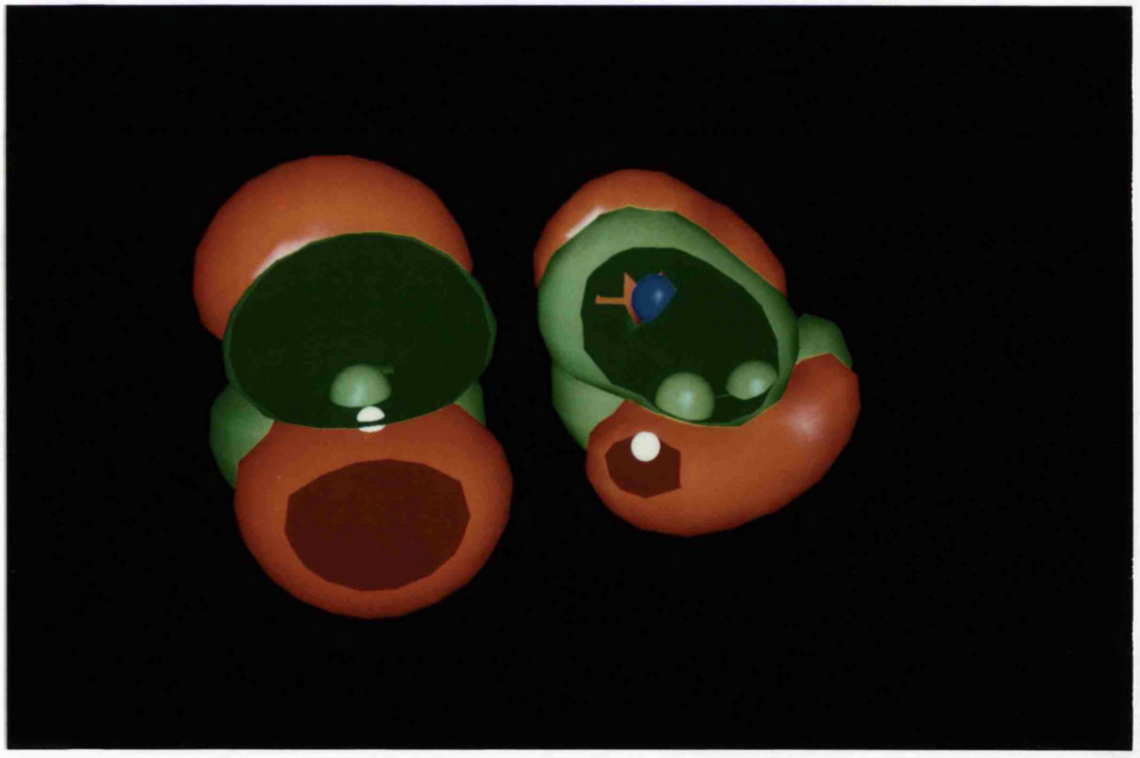

Figure 4.2.13 : A visual aid to the frontier orbital approach to the mechanism.

HOMO(C5) and the LUMO(Acetylene).

Figure 4.2.12 : The addition of a third acetylene molecule to the conjugated intermediates, C4 and C5.

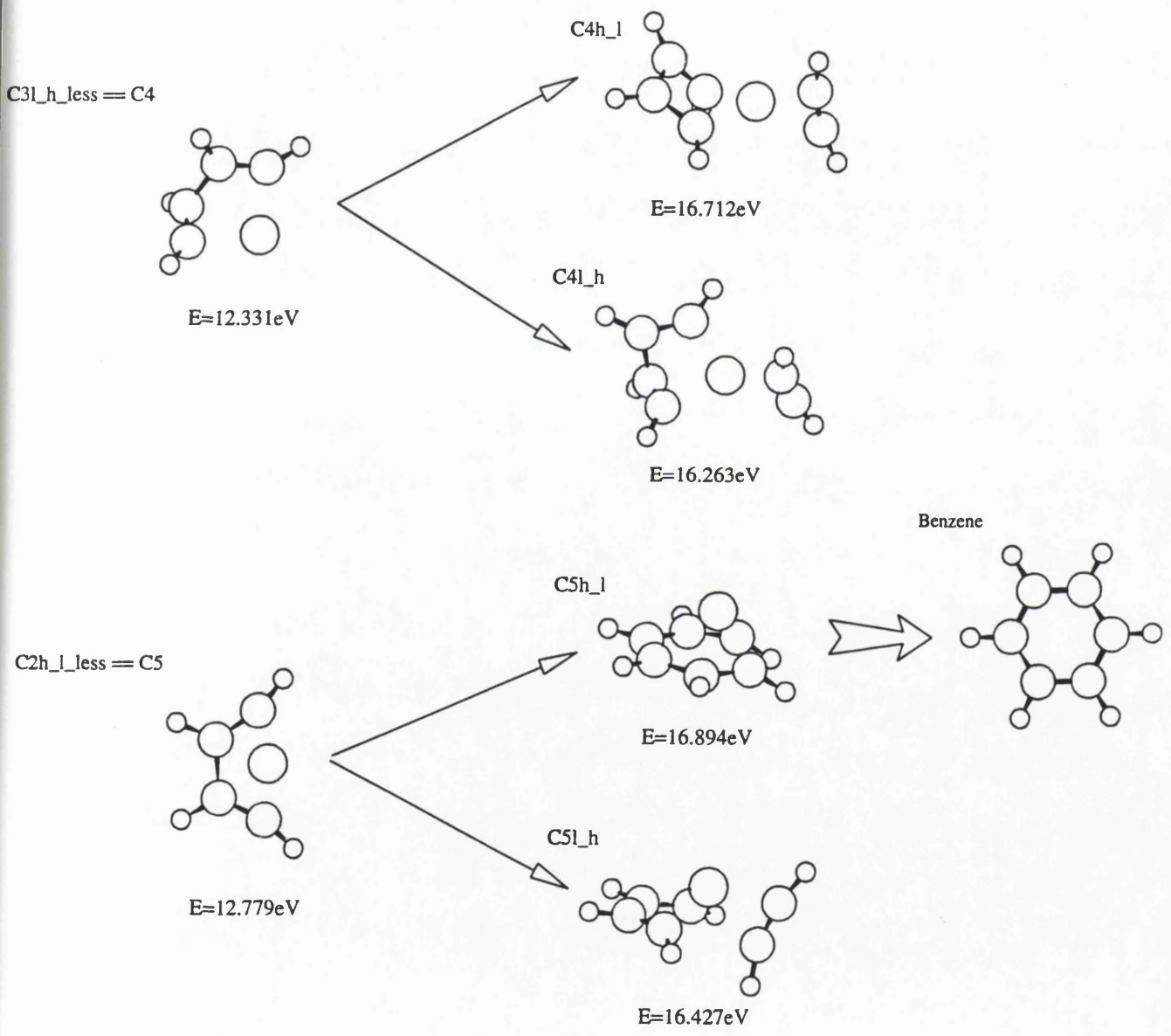

When the frontier orbital approach is applied to the C4 conjugated intermediate, two systems are produced. The C4l_h shows that the third acetylene acts as a ligand with the conjugated species retaining the same conformation, whereas for the C4h_l interaction, the conjugated species has changed conformation upon inclusion of the third acetylene molecule. This new conformation resembles that exhibited by the C2h_l system, which was found to be a key precursor in the reaction to benzene. Again, the docking of a third acetylene molecule onto the cation complex helps, either via stereochemical or electronic factors, the previous two acetylene molecules to adopt a suitable conformation. The mechanism proposed here involved the dissociation and recombination of the third acetylene, yet it could be possible for the third molecule to undergo a complex orientational rearrangement whilst attached to the cation. However, from mechanism elucidated either pathway yields an activation barrier, and it is this stage in the mechanism that is the probable rate determining step.

Using the frontier orbital approximation, it has been possible to elucidate one possible mechanism for the cyclotrimerisation of acetylene to benzene not only to provide information on the key transition states but moreover to provide information as to the reasons why the acetylene bonds in such a manner.

Charge Density approach to the mechanism.

As described in the methodology section, 4.2.2, this approach involves the iterative docking of acetylene molecules as determined by the interaction with the steepest charge gradient. Such an approach emphasises the rôle of the long range electrostatic or Coulombic effects.

From the lowest energy starting structure located for one acetylene binding to the cation, figure 4.2.9(a), a second acetylene molecule was oriented around the complex according to the steepest charged gradient represented by the contours in figure 4.2.5. The closer the contours obviously the steeper the electrostatic gradient. Figure 4.2.14(a,b,c) reports the optimised structures and interaction energies with respect to isolated species, for this method of docking acetylene molecules onto the cation. Clearly, the final structure, with three acetylene's around the cation, (figure 4.2.14(c)), resembles the classic transition metal chemistry with the acetylene molecules acting as simple ligands and the addition of the third acetylene does not force the previous two molecules to interact, as observed for some of the previous structures. The complex represented in figure 4.2.14b resembles the C2 complex located in the frontier orbital type of approach, although it is more planar in nature than the C2 complex, which shows the cation raised out of the plane. For three acetylene molecules oriented around the cation, an interaction energy of 14.834eV is calculated which is the lowest of all the arrangements of three molecules around the cation, where the acetylene molecules remain unassociated. Indeed, it would indicate not surprisingly that this approach is more suitable for orientating unreacting ligands, rather than in elucidating reaction mechanisms.

Figure 4.2.14 : The structure and interaction energies derived from methodology based on electrostatic gradients.

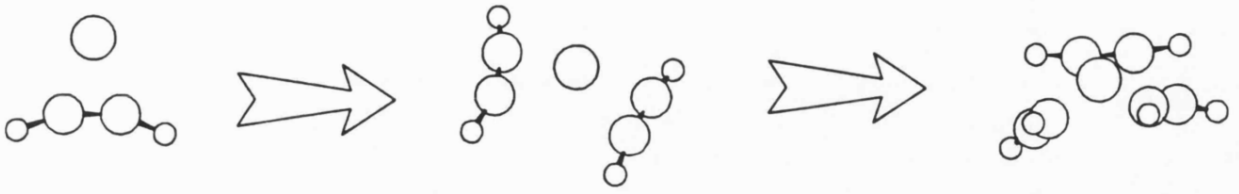

E=7.564eV E=12.108eV E=14.838eV

To summarise some of the key points of the mechanism, it seems likely that the pathway for the cyclotrimerisation of molecular acetylene to benzene is as follows :-

Step One:

The first acetylene molecule approaches with the C≡C π bond perpendicular to the cation, due to the electrostatic attraction of the cation and the π bond. The resulting structure, (figure 4.2.9(a)), shows π back bonding onto the empty low lying **4s**, **3d**, **4p** orbitals of the cation. The result of such bonding is to change the character of the previous sp^1 carbons to sp^2 carbons when associated with the cation. The hydrogen atoms are also displaced from their previously linear position, to a symmetrically distorted position.

Step Two:

The second acetylene molecule can interact in a variety of ways but it was discovered both by optimising overlap of the LUMO of the previous complex with the HOMO of an acetylene molecule, and by following the electrostatic gradient that we can generate a stable structure with interaction energies of 12.108eV and 12.161eV

respectively. These two structures are not significantly different, thus either approach would be equally valid. The resulting geometry is that reported for C2, (figure 4.2.10).

Step Three:

The third acetylene molecule reacts with the complex described above, in a frontier orbital type of approach, where by the HOMO(acetylene), interacts with the LUMO of the C2 or similar structure. This third molecule does not produce benzene as in the classic concerted ring formation but rather, forces the previous two molecules to react forming a key intermediate, C2h_1.

Step four:

The third acetylene molecule now either dissociates from the complex, leaving the other two molecules still forming a bonded conjugated system, or undergoes a rearrangement so as to obtain the correct orientation, as described in step 5. This key precursor is expected to have a finite lifetime and is considered to be the probable rate determining step for the overall reaction.

Step five:

A third acetylene molecule now approaches or re-orientates on complex, C5, in such a way as to optimise the overlap of the HOMO(C5) with the LUMO of the acetylene molecule. The result is a structure very similar to benzene, except that the ring is not fully closed.

Step six:

This structure becomes detached from the cation and closes the ring to yield benzene.

The other structures produced are intermediates, and the binding or dissociation of acetylene molecules, only facilitates the forward or reverse of the reaction. The only exception, is the complex designated C4 in which the two acetylene molecules bond, but not in the way required to yield benzene. Indeed such intermediates can be thought of as representing by-products. We also note that the forward reaction to benzene is driven by thermodynamic factors and the results reported here indicate that the mechanism does not necessarily have to be a free radical one as proposed by several groups. Interestingly, the Ni^{2+} cation is reduced in all the intermediate steps located by the technique and has been calculated to exist as an effective Ni^{+}, which agrees well with the experimental data[26]. Though once benzene has been formed and dissociates from the complex, the cation returns to a +2.0 ionic charge.

Reaction By-products.

The results described, so far, only relate to the reaction with production of benzene, but it is possible that due to the dynamical nature of the reaction, some bonded intermediates could dissociate from the cation to form by-products. The species suited to by-product formation are the complexes C4 and C5, which contain two bound conjugated acetylene molecules. Indeed, if the organic species is simulated alone, i.e. without the effect of the cation, then information on the by-products can be inferred. Figure 4.2.15(a,b) reports the starting structures, C4 and C5 without the cation and the final energy minimised structures, as possible representatives for the possible by-products in the molecular reaction. From the C4 starting structure, the two acetylene molecules dissociate to yield two interacting acetylene molecules, (figure 4.2.15(a)), which lowers the internal energy by 0.100eV. Whereas, once the cation is removed from the C5 complex, the open structure closes to form a four member ring, (figure 4.2.15(b)). This ring is stable with a binding energy of 1.433eV. The "squarene" structure is a highly conjugated molecule, though not quite completely symmetrically conjugated as in benzene, with the splitting of the C-C distance, 1.34Å and 1.56Å, and is a possible by-product for the molecular reaction, although the high reactivity of this molecule is likely to result in it subsequently leading to other species.

Figure 4.2.15(a,b) : The structures of some of the plausible by-products.

a)

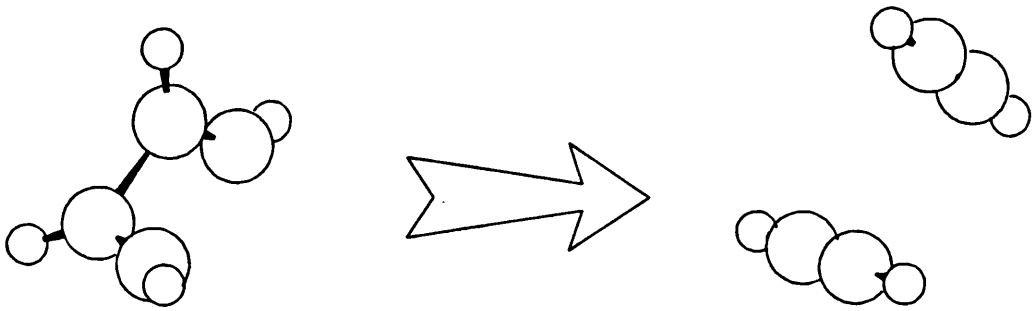

E=0.100eV

b)

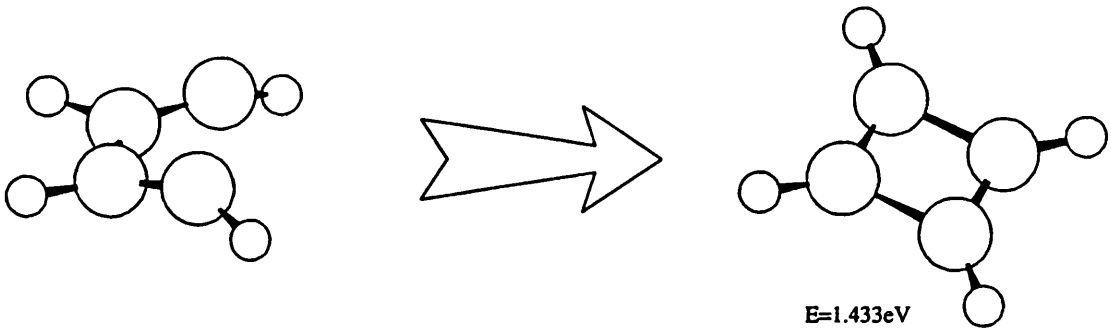

E=1.433eV

Vibrational frequencies and experimental IR. data.

The work of Couves *et al*[27,28], has shown that in *in-situ* FTIR[29,30] experiments, the spectra and in particular the frequency of the C-C stretch changes during reaction and table 4.2.3 reports the major frequencies obtained from such experiments. The peaks at differing run times and their tentative interpretations are also tabulated. From their results, there appears to be a very slight reaction after 3 hrs with the peak at 1475cm^{-1} increasing slightly in intensity, though this region of the spectrum has several features which have not as yet been fully identified. However, after being left overnight at 50°C, there is a vast change, with many new peaks emerging in the 3000cm^{-1} region and a triplet being formed between 1710cm^{-1} and 1686cm^{-1}.

Time						
Initial			*3 Hrs*		*Overnight*	
ν /cm^{-1}	*I*	***Interpretation***	ν /cm^{-1}	*I*	ν /cm^{-1}	*I*
3233	vs	ν(C-H)	"	vs	"	m
2920	w	Acetone impurity	"	w	"	w
1957	w	Normal mode	"	w	"	w
1936	w	ν(C≡C)	"	w	"	w
1976	w	ν(C≡C)	"	w	"	w
1686	m	Dimers of Acetylene.	"	m	"	s
1475	w	Benzene Complex.	"	m	"	s
1436	s	Acetone impurity	"	s	"	s
1360	m	Acetone impurity	"	m	"	m
		Supported Benzene.	3087	w	"	m
		Supported Benzene.	3065	w	"	m
		Supported Benzene.	3026	w	"	m
					1988	m
					1851	m
					1710	s
					1619	s

Table 4.2.3 : The major peaks, intensities and tentative interpretations form the experimental *in-situ* FTIR work of Couves *et al.*

(vs = very strong; s = strong; m= medium; w = weak.)

It is possible to calculate the vibrational frequencies for the structures so far derived in this study, but due to constraints of computer time, this type of calculation was only performed for several key intermediates. Table 4.2.4 reports the calculated vibrational frequencies for several of the structures. Clearly, for the isolated acetylene molecule, the average ν(C-H) is 3373cm^{-1} and is a little larger than the experimental value of 3233cm^{-1}, the error in this case is approximately 4.3%. The ν(C≡C) is around 1992cm^{-1} which is close to the experimental value of 1936cm^{-1}-1976cm^{-1}. However, upon addition of acetylene to the cation, the spectra change dramatically with the ν(C-H) moving down field to between 3068cm^{-1} and 2912cm^{-1}, depending on the type of Ni^{2+}-acetylene interaction, whilst the ν(C≡C) has also shifted downfield to either 1653cm^{-1} or 1546cm^{-1}. The effect of acetylene binding onto a cation weakens the acetylene C≡C bonds and hence the vibrational frequencies are shifted downfield.

Structure	*Calculated vibrational frequencies. (cm^{-1})*						
Pure Acetylene	3434	3312	1992				
Ni+(Acet)1	3068	2956	1546				
Ni+(Acet)2	3045	2912	1653				
C4	3105	3040	3021	2997	1566	1459	1278
C5	3320	3198	2946	2828	2058	1890	1399
Ni+Benzene	3130	3093	3076	3067	3062	3052	
	1501	1486	1460	1399	1381	1330	1300
Benzene	3139	3117	3106	3085	3072	3028	
	1633	1618	1488	1473	1423	1306	1271

Table 4.2.4 : The calculated vibrational frequencies for some of the proposed reaction intermediates.

The initial experimental spectra and the spectra after 3hrs show little of these vibrational frequencies calculated for the complexes because initially, once acetylene is introduced into the system, it immediately reacts with the cations embedded on the surface of the crystal, hence the peaks at 1686cm^{-1} and 1475cm^{-1}. Yet most of the acetylene remains unco-ordinated possibly because it has not had sufficient time to diffuse through the cavities and undergo reaction with the cations located inside the crystal. However, after 3hrs at 298K, a little of the acetylene will have migrated through the channels and interacted with the cations, hence the increase in intensity of the 1475cm^{-1} and 1686cm^{-1} peaks. Meanwhile at the surface of the crystal, the reaction has been proceeding as proposed in section 4.2.3 on the surface and benzene is beginning to be produced. This is experimentally observable in that a cluster of weak peaks is beginning to emerge around 3100-3000cm^{-1}. These peaks will not be intense since the number of molecules undergoing reaction will be small when compared to those still waiting to react or those migrating through the structure. After 24hrs at 50°C, acetylene will have diffused to the inner most part of the crystal and thus the majority will be bound to a cation and the trimerisation process will be well under way. The spectrum at this time is completely different from the initial one, with the initial very strong peak of the ν(C-H), 3233cm^{-1} being significantly reduced in intensity and the complete emergence of the group of peaks around 3100-3000cm^{-1}. Similar values can be derived from the reported calculations and are typical of acetylene bound to the cation; an average ν(C-H) of 3080cm^{-1} is calculated for benzene bound to a Ni^{2+} cation, with similar values obtained for the other complexes. For the benzene molecule bound to the cation, there are no calculated frequencies between 1500-3000cm^{-1}; thus any peaks within this region can be interpreted as probably due to intermediates in the mechanism, e.g. the C4 complex with a vibration frequency at 1890cm^{-1}.

Clearly, the experimental *in-situ* FTIR is a very powerful technique for studying the reaction mechanism but the interpretation of such data is extremely difficult. However with the aid of theoretical studies such as those used here, the elucidation of this type of spectra is beginning to be more straightforward.

4.2.4 Conclusions.

The work contained within this section, shows how modelling techniques maybe used to determine the mechanism of very complex reactions. However, unlike most mechanistic studies which only chart the progress from transition state without revealing how the molecules are orientated during the early stages of the reaction. The approach used here, shows how the molecules achieve the appropriate relative orientations for reaction. As the results demonstrate, electrostatic interactions play an early rôle early on in the mechanism but when the molecules become close, the more subtle orbital effects take over.

Moreover, our methodology not only describes the mechanism but, can even indicate plausible by-products. A likely factor in the high selectivity of the reaction is that the molecules are tightly bound to the cation, i.e. with binding energies in excess of 7eV; therefore once associated with a cation, few side chain reactions are possible. This high selectivity of the reaction is also emphasised by the calculated formation of one other plausible molecule, "squarene", which is experimentally unstable and therefore derivatives of such a molecular arrangement are expected. The elucidated mechanism has not identified any molecular barrier to the catalytic process, although one potential barrier does exist and this is the dissociation of the third acetylene molecule as identified in step 4 of the described process.

The methodology described here is general and has very considerable possibilities in subsequent applications to other catalytic cycles.

4.3 References.

1 Maxwell I.E.; "*New perspectives in catalysis*"; Eds. J.M. Thomas and K.I. Zameraev; Oxford IUPAC-Blackwell 1990.

2 Holderich W.; Hesse M.; Naumann F.; *Angew Chem Intl Ed. Eng.*, **27**, 226, (1988) .

3 Couves J.W.; Jones R.H. Thomas J.M.; Smith B.J.; *Adv Mater.*; **2**, 181, (1990).

4 Catlow C.R.A.; James R. Mackrodt W.C.; Stewart R.F; *Phys Rev.*; **25**, 1006, (1982).

5 Parker S.C.; Price G.D., "*Advances in Solid State Chemistry*"; Vol **1**; 295, (1989).

6 Gale J.D.; Cheetham A.K.; *Zeolites*; **12**, 674, (1992).

7 Dick B.G.; Overhauser A.W.; *Phys. Rev.* **112**, 90, (1958).

8 Jackson R.A.; Catlow C.R.A.; *Molec. Sim.*; **1**, 207, (1988).

9 Den Ouden C.J.J.; Jackson R.A.; Catlow C.R.A.; Post M.F.M. *J. Phys. Chem.*; **94**, 5286, (1990).

10 Tosi M.P.; *Solid State Phys.*; **16**, 1, (1964).

11 Leslie M.; Daresbury Laboratory Report No. DL/SCI/TN31T, 1982.

12 Levy M.; *Proc Natl Acad. Sci.*; **76**, 6062 (1979).

13 BIOSYM Technologies, 9685 Scranton Rd. San Diego, CA. USA.

14 Delley B.; *J. Chem. Phys.*; **92**, 508, (1990).

15 George A.R.; Catlow C.R.A.; Thomas J.M.; *Catal Lett.*, **8**, 193, (1991).

16 De Man A.J.M.; Ph. D Thesis, Eindenhoven University, Holland (1992).

17 Goyal R; Fitch A.N.; Jobic H; *J. Chem Soc. Chem. Comm.*, **17**, 1152, (1990).

18 Koga N.; Morakuma K.; "*The Challenge of d and f electrons: Theory and Computation*", Ed Salahub D.R.; Zerner M.C.; *A.C.S. Symp. Series.* **394**, 79, (1989).

19 Berthelot M.; *Ann. Chim.* **9**, 445, (1866).

20 Kiefer J.H.; Von Drasek W.A.; *Int. J. Chem. Kin.* **22**, 747, (1990).

21 Colket M.B., III, 21st Symp. (Intl.) on Combust., The Combustion Institute, Pittsburgh, **851**, (1986).

22 Maddox P.J.; Stachviski J.; Thomas J.M.; *Catal. Lett.*, **1**, 191, (1988).

23 Woodward R.B.; Hoffmann R.; "*The Conservation of Orbital Symmetry*", (1970).

24 Back M.H.; *Can. J. Chem.*, **49**, 2019, (1971).

25 Press W.H.; Flannery B.P.; Teukolsky S.A.; Vetterling W.T.; "*Numerical Recipes, The Art of Scientific Computing*".; Cambridge University Press; Cambridge, (1986).

26 Maddox P.J.; Stachviski J.; Thomas J.M.; *Catal. Lett.*, **1**, 191, (1988).

27 Couves J.W.; Che M.; Private comm.

28 Lepetit C.; Kermarec M.; Che M.; Thomas J.M.; *Collids & Surfaces*, **72**, 265, (1993).

29 McQuire M.W.; Rochester C.H.; *J. Catal.*, **2**, 355, (1993).
McQuire M.W.; Rochester C.H.; *J. Chem. Soc.; Farad. Trans.*, **7**, 1117, (1993).

30 Mestl G.; Knozinger H.; Lunsford J.H.; *Intl. J. Phys. Chem.*; **3**, 319, (1993).

Chapter 5.

An Investigation into the Substitution of Ge into Microporous Solids.

5.1 Computational Study of the Energetics and Lattice Dynamics of Germanium Containing Zeolitic Solids.

5.1.1 Introduction.

The quest for new types of microporous, microcrystalline solids continues unabated. To the substantial number of naturally occurring (aluminosilicate) zeolites, a variety of new zeolitic aluminosilicates, having structures not yet found in nature, have been added during the past forty years[1]. Chapter 1 gives a detailed description of zeolites and their important rôle in modern day chemistry; below is a brief outline of why the proposal of new structural frameworks is important in solid state chemistry. Great strides have also been made in producing families of microporous aluminophosphates (ALPOs), some of which have unique structures while some are exactly akin as regards their framework structures, to those of natural and synthetic zeolites[2,3] In addition, many ALPO structures have been synthesised[4,5] in which a transition-metal or main-group metal has been inserted into the framework structure. Indeed very recently, microporous structures containing germanium as the tetrahedrally co-ordinated atom with varying stabilities have been synthesised.[6]

Although it has not yet proved possible to prepare a range of germanium-based microporous structures comparable to those of the siliceous extremes of the well-known pentasils (typified by Silicalite-I - the SiO_2 extreme of ZSM5[7] and by Silicalite-II, the corresponding extreme of ZSM11[8]), or indeed of Mordenite[9] and other important zeolites, considerable insight may be gained into the theoretical possibility of the existence of such materials by computational analysis of the kind we describe within this thesis. As well as arriving at the energetics of the germanate analogues of the (alumino)silicate zeolites, we can also predict the vibrational frequency of the local and extended modes of these computationally predicted structures.

In this section, we investigate several structures ranging from α-quartz,

Mordenite, to Zeolite-Y[10] and finally to the large unit cell structure of Silicalite-I[11]. Zeolite-Y has a larger unit cell than Silicalite-I but due to resource constraints, we model the structure using F symmetry which reduces considerably the number of independent ions. Mordenite is especially interesting since it has four distinct tetrahedrally co-ordinated crystallographic sites and it presents an ideal example for studying the effect of substitution at each site. Various mole-fractions (ranging from zero - purely siliceous, to unity - pure germanic) of Ge have been used in the modelling procedure. The spatial arrangement of the substituted ions (Ge^{4+} for Si^{4+}) is also varied between a variety of ordered models and arrangements that are as nearly as possible random (within the constraints of the periodic boundary conditions technique used in this study). It is hoped that our predictions will stimulate experimental studies into these systems.

5.1.2 Computational Method.

Lattice energy minimisation calculations were performed on each system, using shell model potentials[12] which describe polarisation effects simply and reliably as described in chapter 2.1. Potentials for alumino-silicates are readily available[13] as discussed in section 2.0. Details are given in the Appendix A, section 5.1.5 and parameters have recently been developed for the Ge-O interaction using an empirical fitting procedure by Bell[14]. The lattice energy calculations employ the now standard summation procedures for the short range and Coulombic interactions, with the latter evaluated using the Ewald[15] technique. Full energy minimisation is undertaken with respect to both cell dimensions and atomic co-ordinates and the THBREL[16] code was used for all the lattice simulations; it embodies the summation procedures summarised above, coupled with a Newton-Raphson minimisation[17] procedure.

The generation of the predicted spectra is performed using the relaxed structure and the corresponding interatomic potentials. We employ standard lattice dynamical theory based on the harmonic approximation, (which has been extensively applied to silicates by Parker and Price[18]). The calculations use the THBPHON[19] code, which generates both the frequencies and the atomic displacement vectors of the vibrational modes by diagonalizing the dynamical matrix of the system, without any use of the symmetry properties. The infrared (IR.) and Raman spectra can be derived from the vibrational frequencies, by dividing the modes into infrared active, Raman active and inactive modes using group theoretical projection methods[20]. The position of the spectroscopic lines can then be calculated, whilst the IR. line intensities are evaluated using the method of Kleinman and Spitzer[21]. As argued in reference [22], the spectrum obtained can be made more directly comparable with experiment, by fitting a Gaussian curve[23], with a half width of 10 cm^{-1}, to each peak.

A more detailed account of the theory is given in chapter 2 of this thesis; the brief description above outlines only the methodology and associated constraints used in this investigation.

5.1.3 Results and Discussion.

Part 1: Properties related to the energetics of the structure.

For each system, we present results for both the structure and energetics as a function of composition; in the former case the lattice cell parameters are given, while in the latter we report heats of mixing, $U_{mixEnergy}$, calculated from the following expression :-

$$U_{mixEnergy} = U_{Calc.}(x) - xU_{PureGeO_2} - [1-x]U_{PureSiO_2}$$

Where $U_{Calc.}(x)$ is the calculated lattice energy of the mixed system with mole fraction x of Ge, and $U_{PureGeO_2}$ and $U_{PureSiO_2}$ are the lattice energies of GeO_2 and SiO_2 respectively. The results for each structure are given below.

Quartz structure.

This structure has three tetrahedral atoms in the asymmetric unit cell, thus restricting the range of possible substitutions by Ge ions when only one unit cell is considered. When a supercell is used there is, however, a considerable increase in the possible substitutional arrangements; though as reported in section 5.2 of this chapter, this type of approach allows more degrees of freedom in the model. As can be seen in figure 5.1.1, there is a linear relationship between the energy and the mole fraction of Ge, suggesting the system is close to being an ideal solution. This conclusion is reinforced by figure 5.1.2, which shows the variation in the mixing energy (in eV per tetrahedral atom per unit cell) against mole fraction. The lowest energy ratio of Ge:Si is at the point, where the ratio is close to unity. The heats of mixing of only approximately 4 KJ/mole indicate only small deviations from ideality. Figure 5.1.3(a,b,c) describes the variation of the cell parameter with the mole fraction of

substituted Ge. These graphs show a distinct, if modest, deviation from the linear relationship observed in the energy plot. The deviation is of the order of +5% in the *a* and *b* directions and ± 5.5% in the *c* direction from the cell parameters of the purely siliceous form. Nevertheless, such deviations are largely attributable to the small unit cell employed in the simulation and our overall conclusion is that the SiO_2/GeO_2 system is close to ideality, with complete solid solubility.

The only data with which direct comparison can be made concerns the pure GeO_2 system[24] for which we overestimate the *a/b* ratio lattice parameter by 1.7%, (see Table 5.1.1), whereas Ge-O bond lengths are underestimated by approximately 3%.

Figure 5.1.1 : Energy of the unit cell of the α-quartz structure vs the mole fraction of Ge.

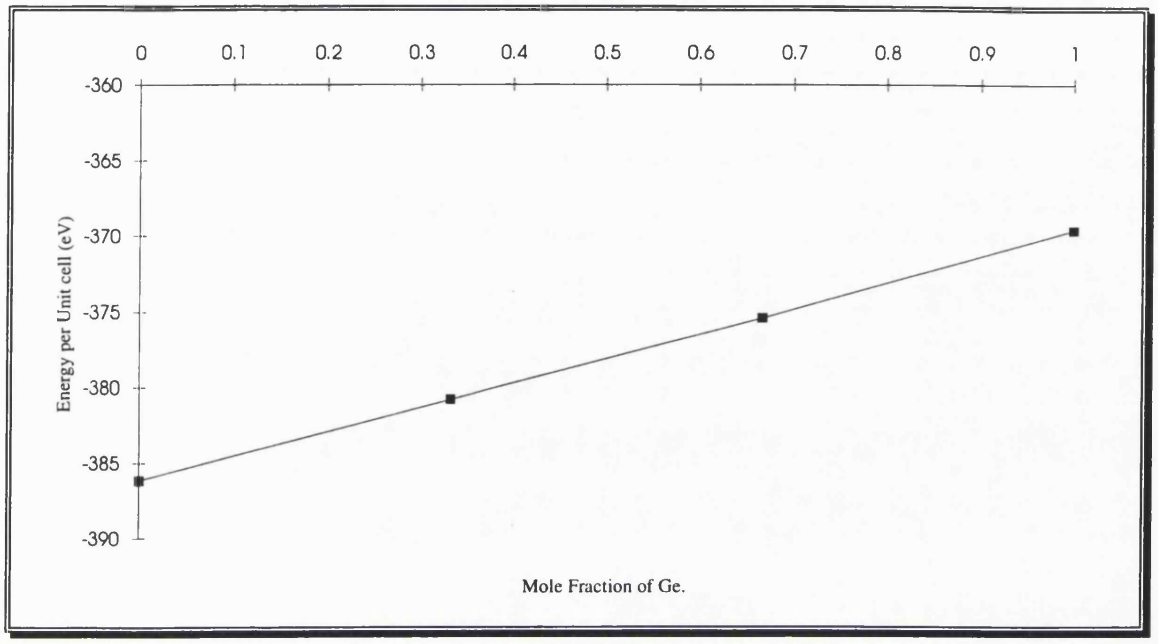

Figure 5.1.2 : The calculated mixing energy of the α-quartz structure vs the mole fraction of Ge.

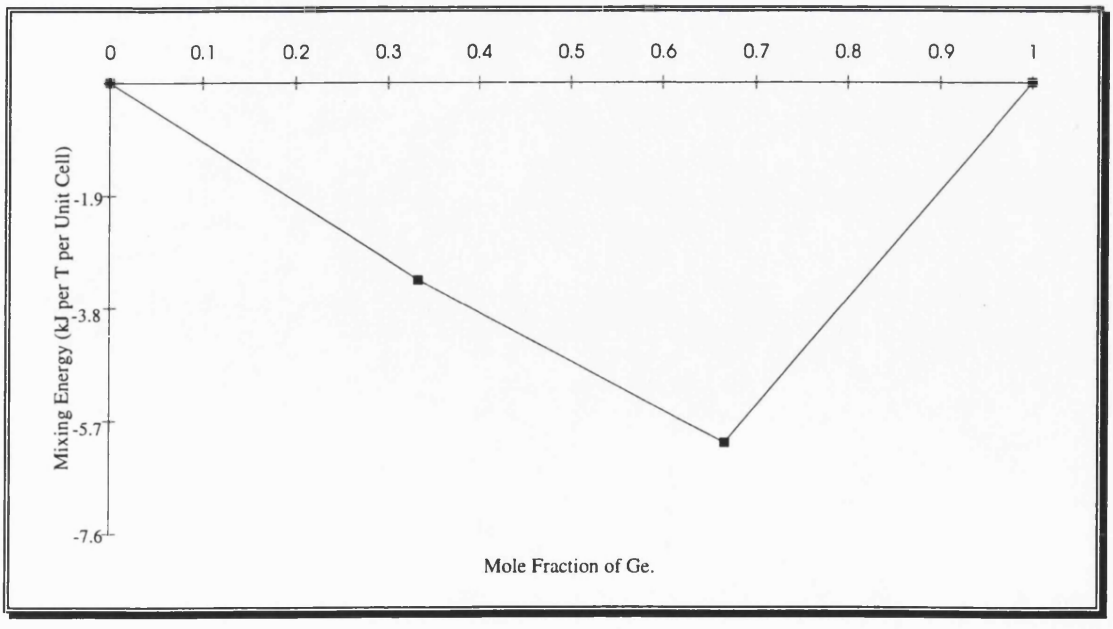

Figure 5.1.3 : (a) Lattice parameter *a*, (b) Lattice parameter *b*, (c) Lattice parameter *c* vs mole fraction of Ge substituted in the α-quartz structure. (All lattice parameters in Å)

(a)

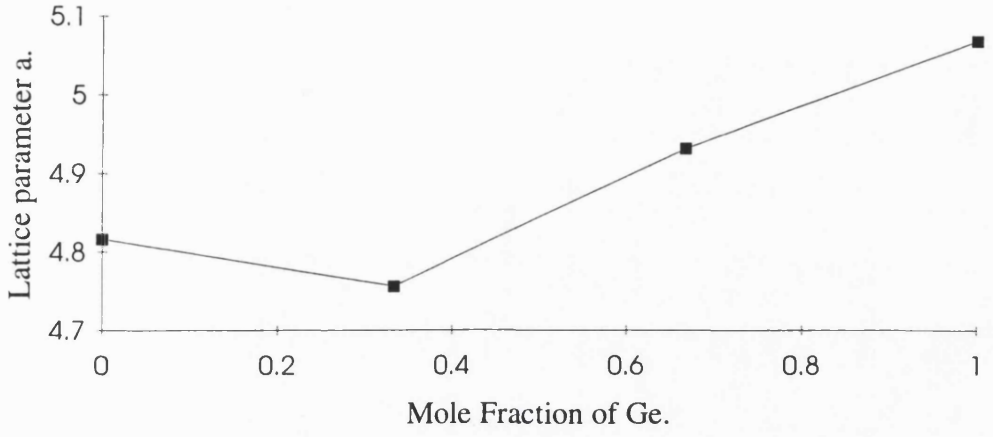

(b)

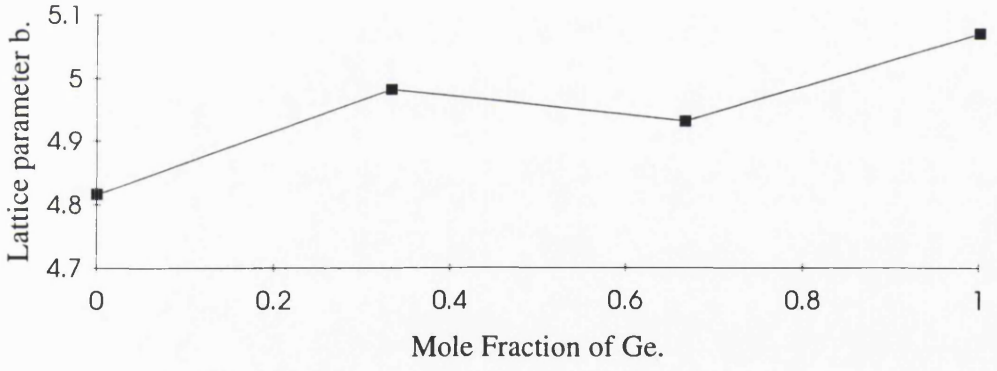

(c)

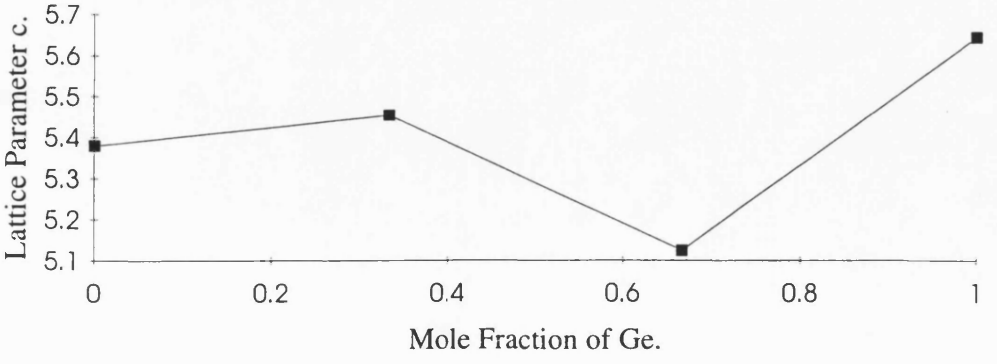

Silicalite-I.

Two models for the possible Ge arrangement have been used to study this structure. The first, is as nearly as possible, a random one, in which Ge and Si are permuted over the T sites in an unbiased way via a computer generated algorithm. It is of course, not possible to generate an entirely random arrangement, as our method is based on the use of periodic boundary conditions. However, the large unit cell of Silicalite-I permits an extensive range of distributions. The other model involves location of the Ge ions along the straight channel, forming layers of Si and Ge. Figure 5.1.4 presents a plot of the mixing energy for such systems.

Figure 5.1.4 : The calculated mixing energy for the Silicalite-I type structure vs mole fraction of Ge.

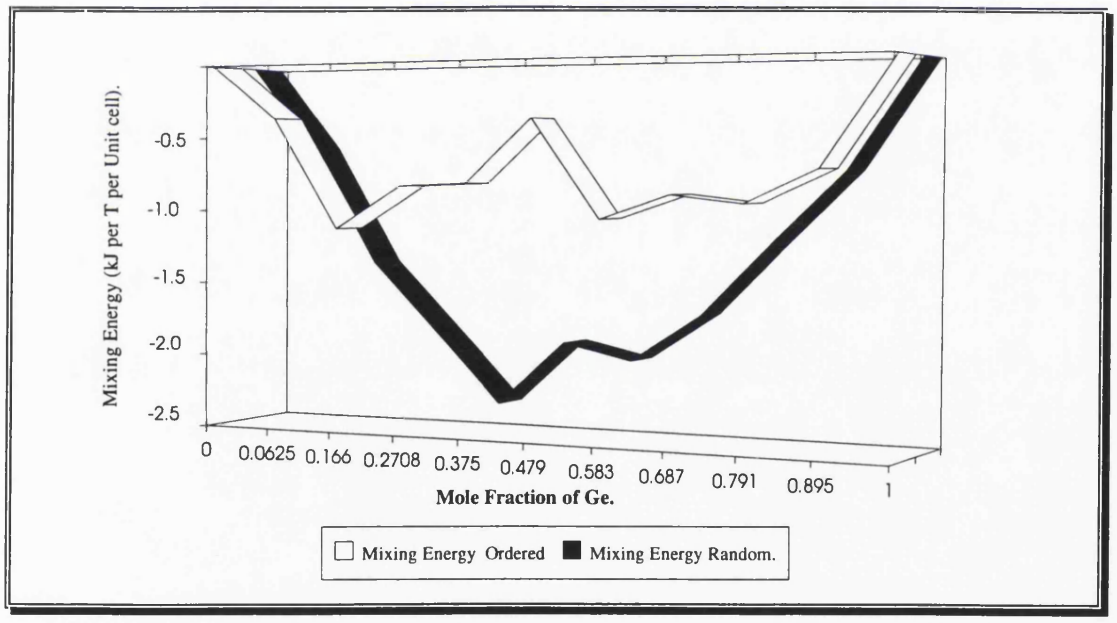

Interestingly, the random structure has the lower energy and a fitted second order polynomial yielded a minimum energy composition close to the 1:1 ratio. Figures 5.1.5(a,b,c) show plots of the lattice cell parameter versus mole fraction, which reveal the same non-linear trend as seen in the α-quartz type structure. For the

random structures, the relationship between the lattice cell parameter and the mole fraction is almost linear and is in good agreement with Vegard's law. However, the "ordered" arrangement gives lattice parameters which deviate from the linear relationship, which is in line with their lower stabilities. In the *a* and *b* direction there are "negative" deviations from linearity, while the *c* direction reveals a positive deviation. For the *b* parameter, the deviation is at most 1% from the value for the random system. These results indicate that the lattice cell parameter is sensitive to the arrangement of the two types of atom over the T sites. It is conceivable that kinetic factors could freeze in non-random Si/Ge distributions and the calculations show how such effects could be revealed by accurate lattice parameter measurements.

Table 5.1.2 : A comparison of random and ordered substitutions of Germanium in Silicalite-I with experimental data .

	Lattice Parameter. (Å).			
Composition	*Calculated*	*Experimental*		*Error.*
16.6% Ordered		17.1% Ge.		
a	13.415	*a*	13.428	0.06%
b	20.256	*b*	20.137	0.59%
c	19.907	*c*	19.939	0.16%
16.6% Random				
a	13.434			0.04%
b	20.197			0.30%
c	19.958			0.10%

Recent experimental work has been reported on the formation of Ge rich MFI type zeolites[25] and samples with as high as a 1:1 ratio have been synthesised, although the lattice parameters have not as yet been reported. Table 5.1.2 makes a comparison with the calculated lattice parameters and the experimental results for the mole fractions experimentally available. The agreement between data for a 17.1% synthesised germanium polymorph and a 16.6% Ge calculated polymorph is good with an overall error of less than 0.5%, although some of the accuracy of the simulations is due to error compensation. However, this result supports the reliability of the other calculations of the yet to be synthesised structures. We note that EXAFS studies of these compounds have confirmed that the Ge has four-fold co-ordination supporting the presence of Ge in the framework[26]. Indeed, our results for the random distribution model are in good agreement with the conclusions, that the lattice cell parameter increases regularly with Ge content. A calculated bond length of 1.67Å ± 0.02Å is found for 16.6% Ge and 1.67Å ±0.01Å for 6.2% Ge, as compared to experimental values of 1.71Å ±0.02Å for 8.33% Ge and 1.72Å ±0.02Å for 17.1% Ge. These experimental results were recorded after calcination, since the structural disorder is found to be lowered after such treatment. For the simulated pure GeO_2 phase of Silicalite-I a bond distance of 1.66Å ±0.01Å is calculated, with O-Si-O angles of 109.47° and Si-O-Si angles in the range of 105°-112°; the pure GeO_2 form of Silicalite-I has yet to be made.

Figure 5.1.5 : (a) Lattice parameter *a*, (b) Lattice parameter *b*, (c) Lattice parameter *c* vs mole fraction of Ge substituted in the Silicalite-I structure. (All lattice parameters in Å)

(a)

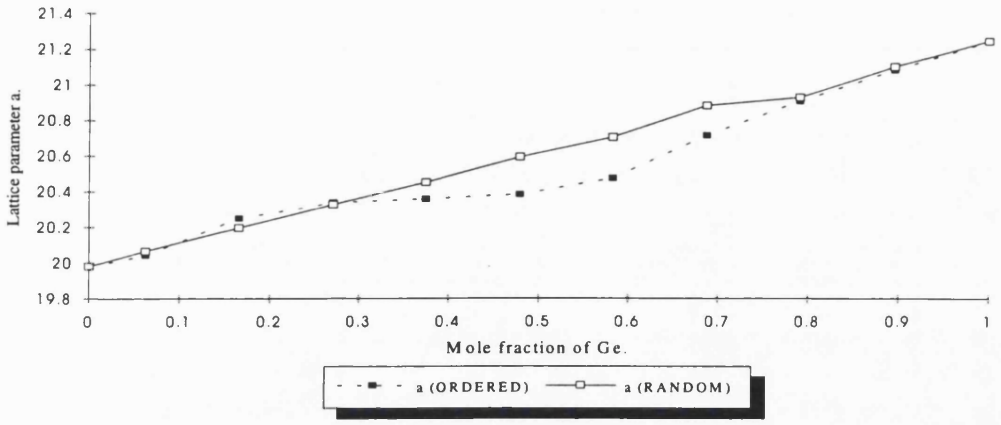

(b)

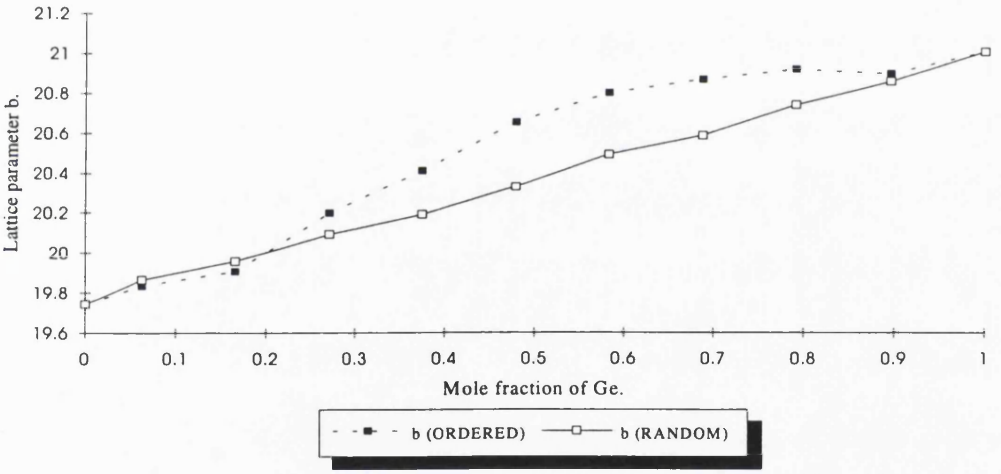

(c)

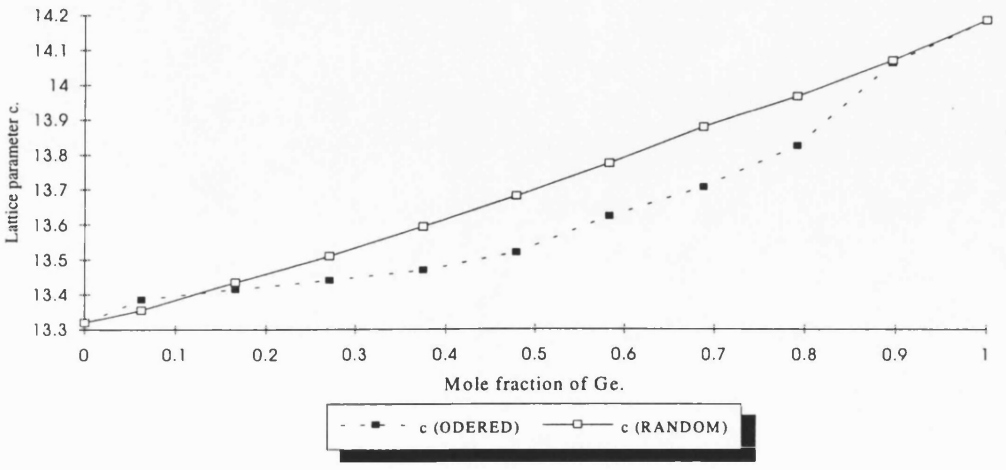

Zeolite-Y.

This is one of the less dense zeolite structures and includes large open cavities. We modelled the structure with F symmetry and not P_1 as in the previous simulations, due to the large number of independent atomic positions in the lower P_1 cell. Despite these necessary approximations the same trends are evident. Figure 5.1.6 shows the variation in the mixing energy with the mole fraction of Ge. One feature evident here is that the "ordered" arrangement is of lower energy than the random structure and is in contrast to the results obtained for the Silicalite-I structure. Again, we find that the properties are highly dependent on the arrangement of Si or Ge on the T sites, (see figure 5.1.7(a,b,c)); yet the calculated compositions of minimum energy are similar for both types of distribution.

Figure 5.1.6 : Mixing energy of a Zeolite-Y type structure vs mole fraction of Ge.

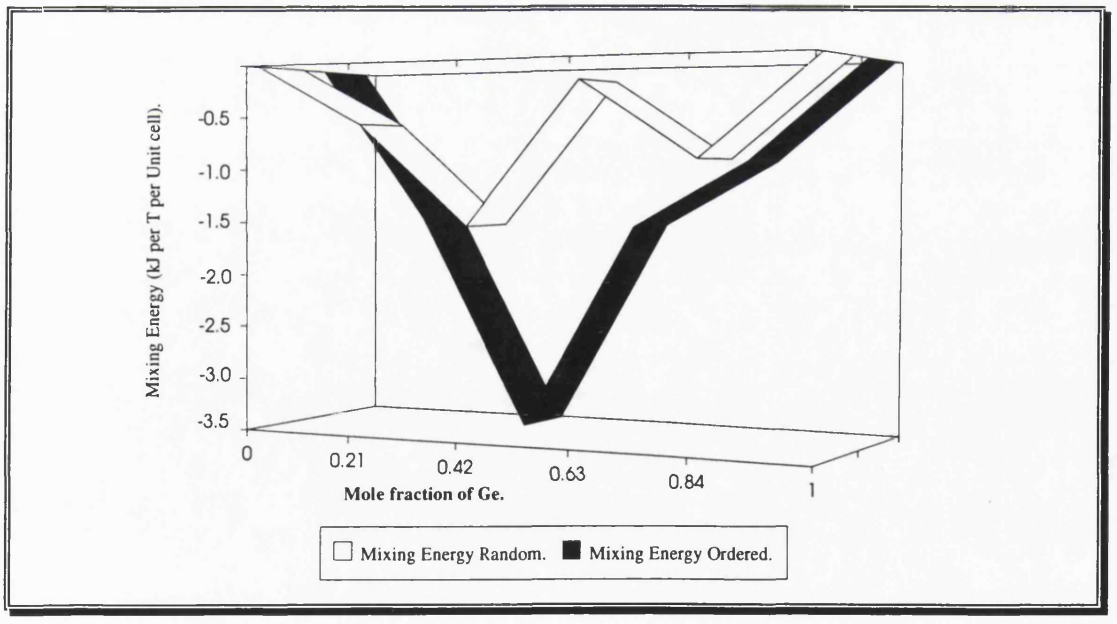

Figure 5.1.7 : (a) Lattice parameter *a*, (b) Lattice parameter *b*, (c) Lattice parameter *c* vs mole fraction of Ge substituted in the Zeolite-Y structure. (All lattice parameters in Å)

(a)

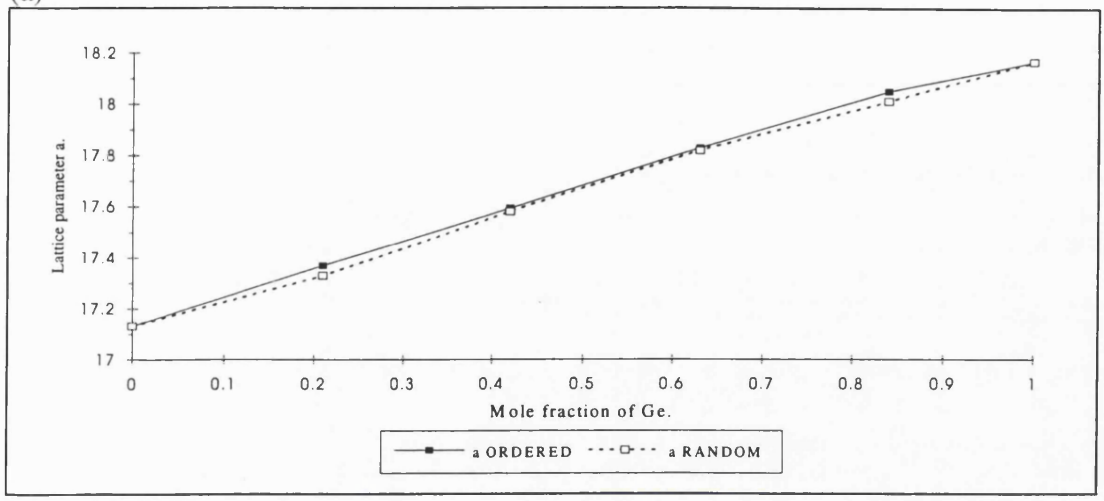

(b)

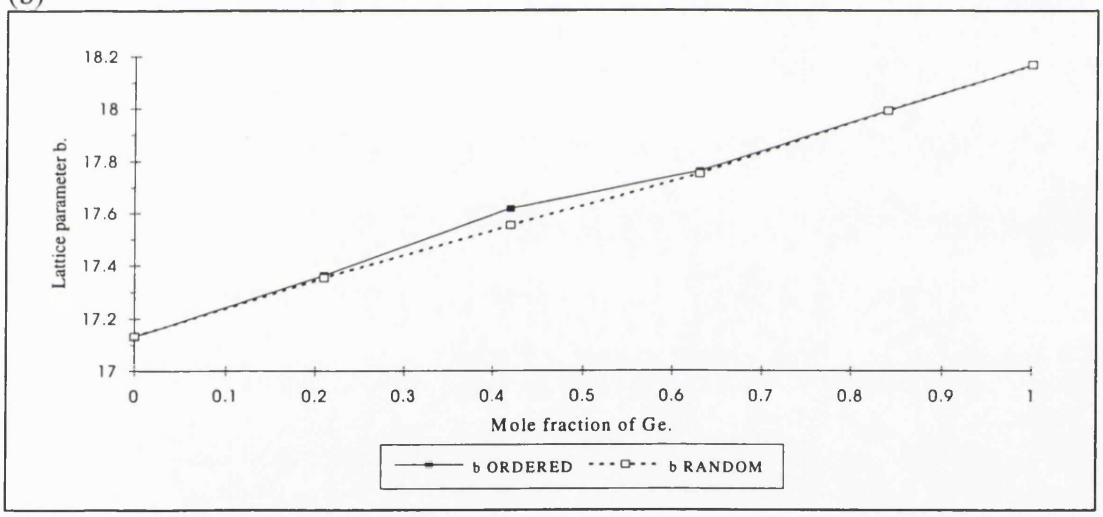

(c)

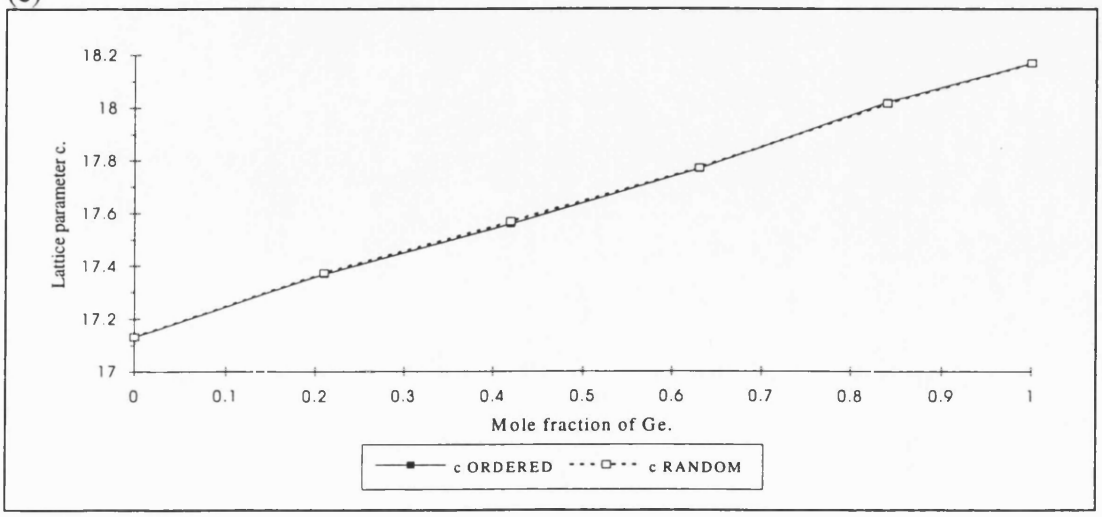

Mordenite.

Mordenite, differs significantly from the previous structures due to the presence of four distinct crystallographic sites: T1 and T2, (each occupying 16 sites in the unit cell), with T3 and T4, occupying 8 other positions. Therefore, we have the opportunity of studying the effect of substitution at distinct crystallographic sites. Again two models have been investigated; the first is a random model, (within the constraints of the PBC technique) and the second arrangement was based upon the specific doping of combinations of the different crystallographic T sites. Figure 5.1.8 depicts the structure of Mordenite with the solid spheres representing the independent crystallographic sites that were used for the substitution of Ge. Figure 5.1.9 shows the now familiar plot for the variation of the heat of mixing with composition. The composition of the minimum energy structure, obtained by fitting a suitable second order polynomial to the random arrangements, is close to a 1:1 Ge/Si ratio.

Figure 5.1.9 : The calculated mixing energy of a Mordenite type structure vs mole fraction of Germanium.

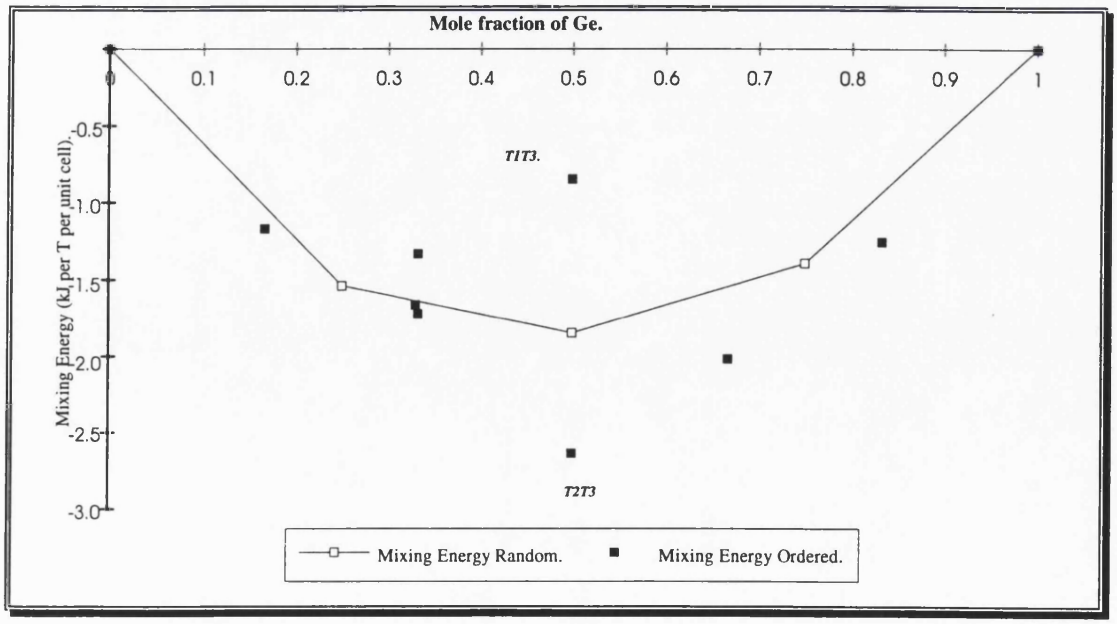

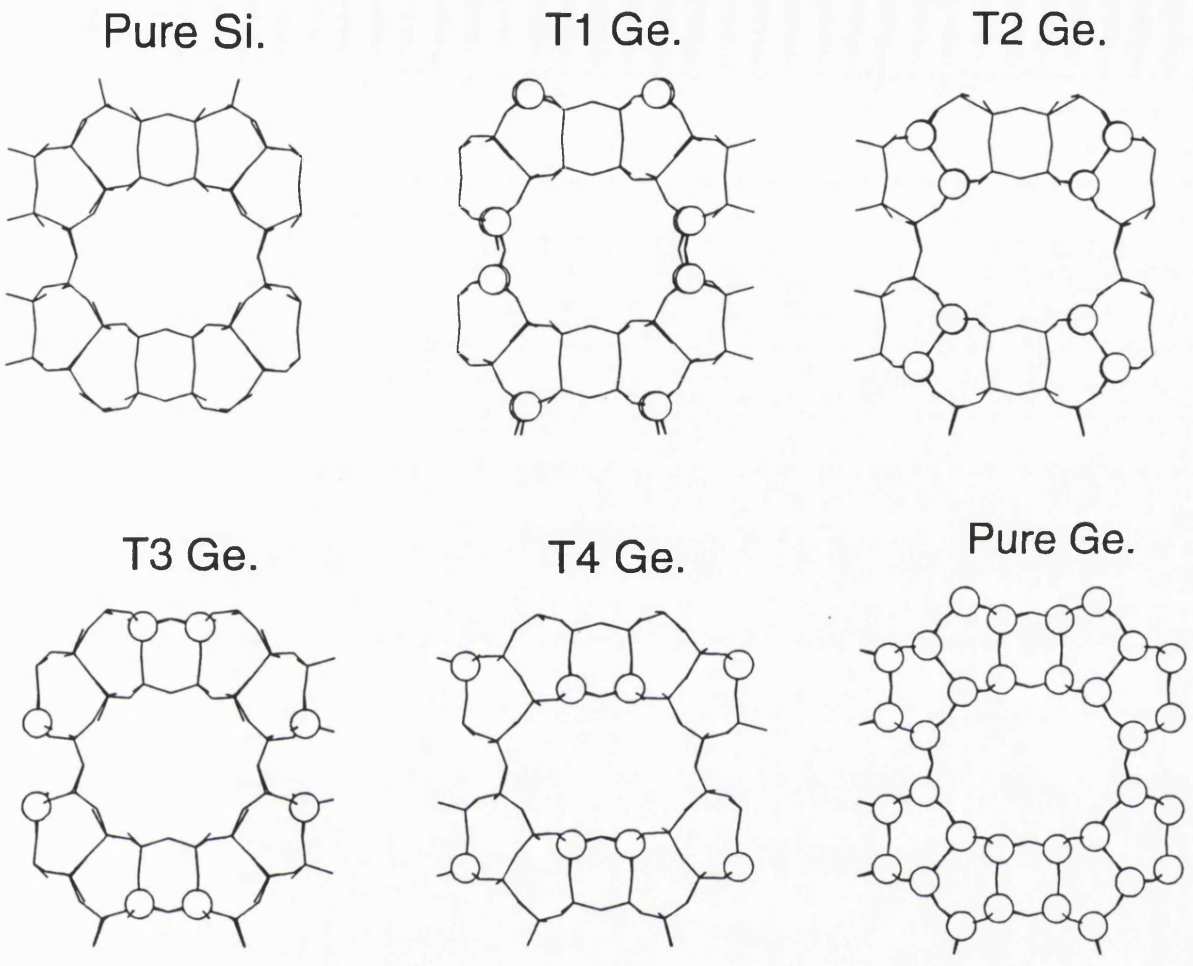

Figure 5.1.8 : A schematic representation of some of the Ge substituted polymorphs; Ge atoms are represented as a spheres.

It is clear that the energetics of substitution of the Ge are strongly dependent on the T site substituted even for the equimolar composition. The largest calculated difference occurs for the 1:1 ratio, with the value for the random arrangement lying in-between that for the two ordered arrangements which correspond to the loading of the T1T3 and T2T3 sites; a difference in energy of approximately 3.0kJ/mol is calculated. Substitution at one particular site can alter the overall energetics quite significantly.

Figure 5.1.10(a,b,c) describes the variation of lattice cell parameter with mole fraction. Both positive and negative deviations from Vegard's Law are observed. A point to note is that there appears to exist a cross over from negative to positive

deviations at around 30% Ge in each case. The effect of substitution at one T site can be markedly different from substitution at another, although the chemical compositions are the same and if Vegard's law applied then the effect should be similar. It would be of particular interest if these predictions could be tested experimentally.

Finally in table 5.1.1 we summarise the calculated and experimental lattice parameters for the pure GeO_2 polymorphs. As regards the calculated energies, it is best to relate the results to the α-quartz type structure allowing a sensible comparison to be made between the purely siliceous and purely germanic forms. Figure 5.1.11 presents such a comparison. For GeO_2, the Mordenite structure is closer in energy to that of the α-quartz, than is the case for SiO_2. This might have implications for the stability of the pure Ge Mordenite phase as compared to the Silicalite-I structure. Overall however, the relative energies of zeolitic GeO_2 polymorphs with respect to that of the α-quartz structure are broadly similar to those for the SiO_2 zeolitic and quartz polymorphs. Experimentally a loading of up to 50% Ge has been achieved for the Silicalite-I structure, and the experimental structures are in good agreement with the simulations (see Table 5.1.2), at the relevant mole fractions. Thus from the calculations and available experimental data it is likely that, a fully germanic analogue of Silicalite-I could be synthesised.

Figure 5.1.10 : (a) Lattice parameter *a*, (b) Lattice parameter *b*, (c) Lattice parameter *c* vs mole fraction of Ge substituted in the Mordenite structure. (All lattice parameters in Å)

(a)

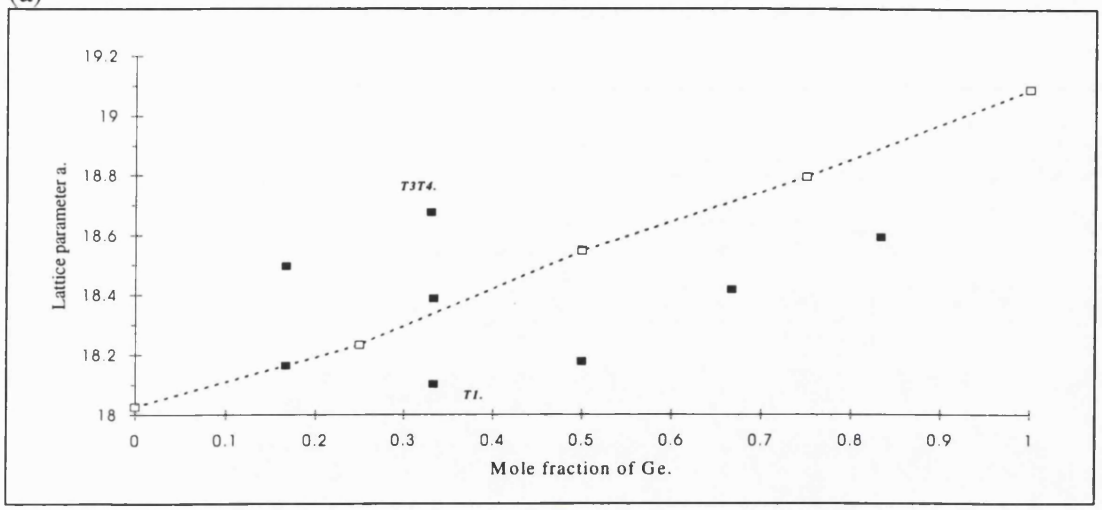

(b)

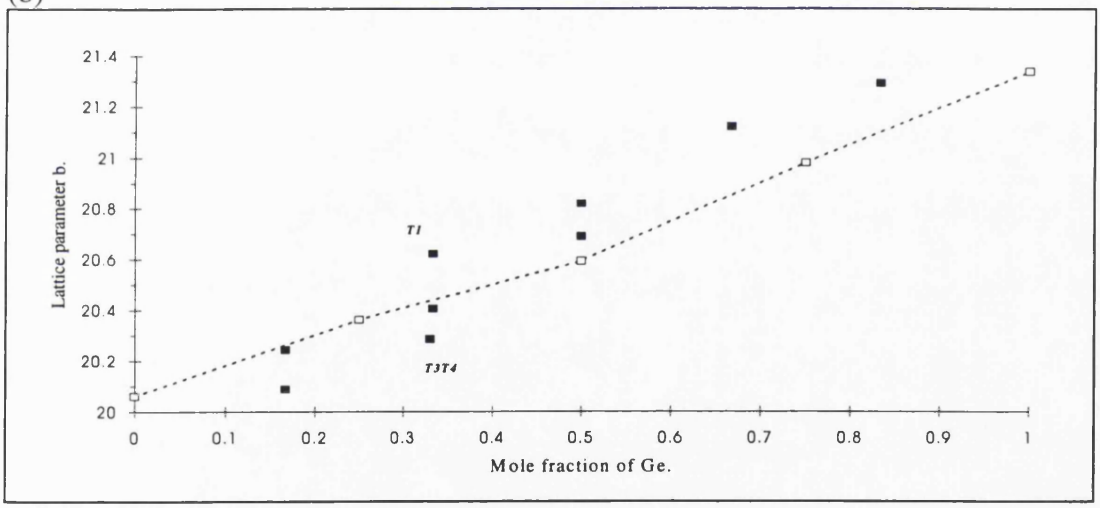

(c)

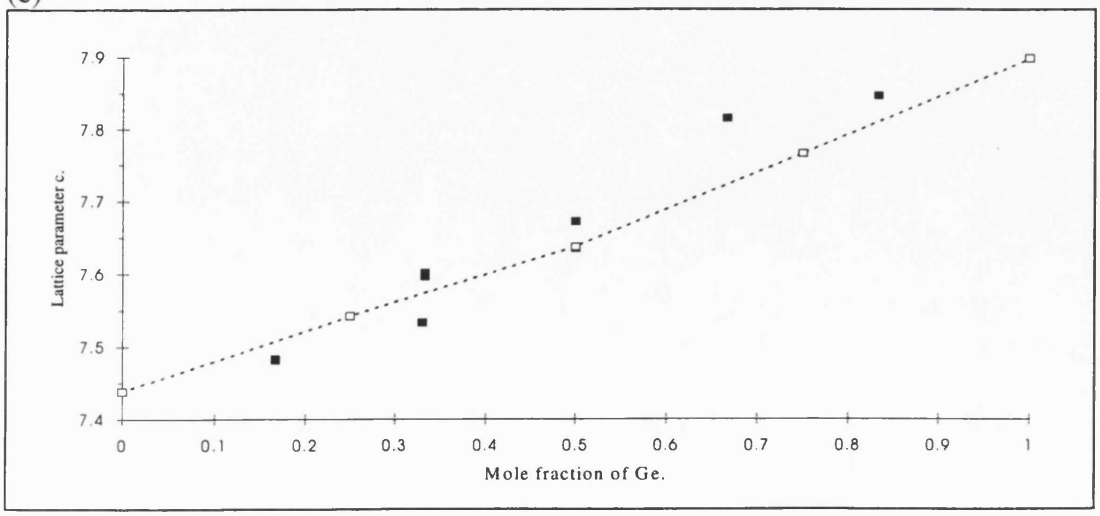

Table 5.1.1 : A summary of the lattice cell parameters for the pure germanic polymorphs.

	Calculated.		*Experimental*[27]	*Error*
	Lattice dimensions, Å	Lattice angles. °	lattice dimensions Å	
α-Quartz				
a	5.070		4.987	1.67%
b	5.070		4.987	1.67%
c	5.646		5.652	0.11%
Silicalite-I				
a	21.254	α 89.44		
b	21.004	β 90.0		
c	14.184	γ 90.0		
Zeolite-Y				
a	18.168	α 90.0		
b	18.168	β 90.0		
c	18.168	γ 90.0		
Mordenite				
a	19.088	α 90.0		
b	21.337	β 90.0		
c	7.898	γ 90.0		

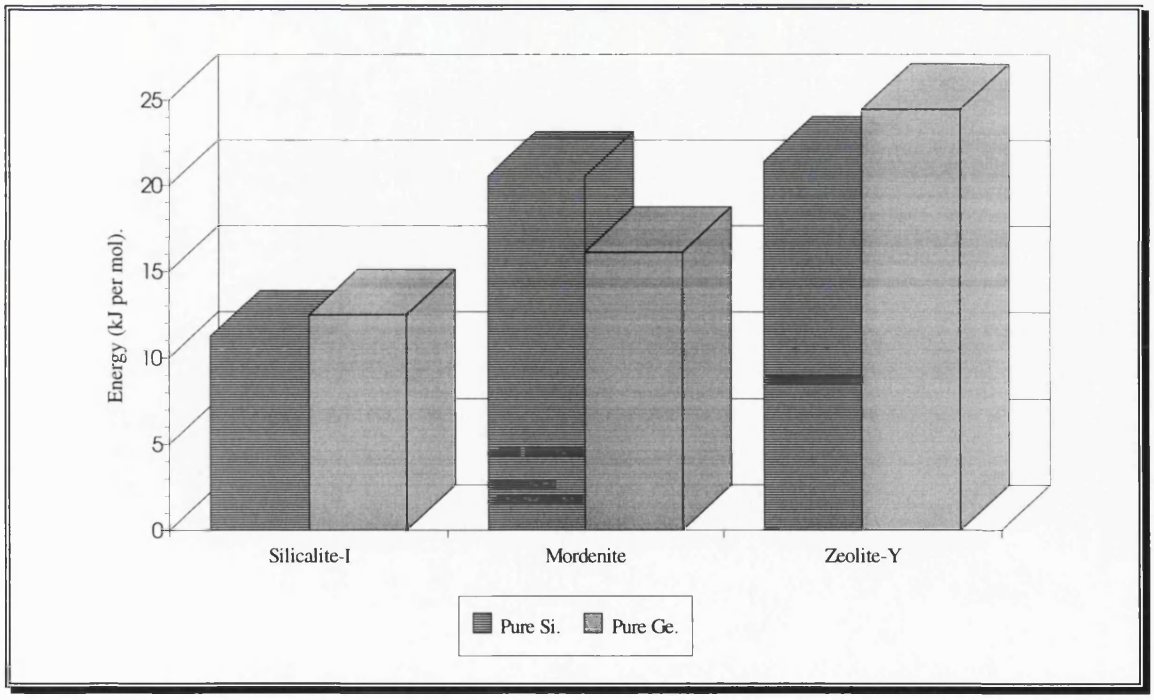

Figure 5.1.11 : The relative energies (per mole with respect to the α-quartz structure) of pure SiO_2 and pure GeO_2 polymorphs.

Part 2: Lattice Dynamical Calculations.

Calculated spectrum for α-Quartz.

Figure 5.1.12 shows the calculated IR. spectra for different mole fractions of Ge. A comparison of the calculated purely siliceous spectrum with the experimental spectrum has been given previously[28]. We are mainly interested here in the variation of the spectrum with the mole fraction of Ge and the question of, how we might extract quantitative relationships from such calculations? We immediately note that here is a definite downward shift of the peaks, owing to a weakening of the average T-O bond. But of greater interest is the increase in the intensity in the 570-750cm^{-1} range. In the pure SiO_2 structure, there is little intensity in this area; we predict that it increases as the Ge content rises.

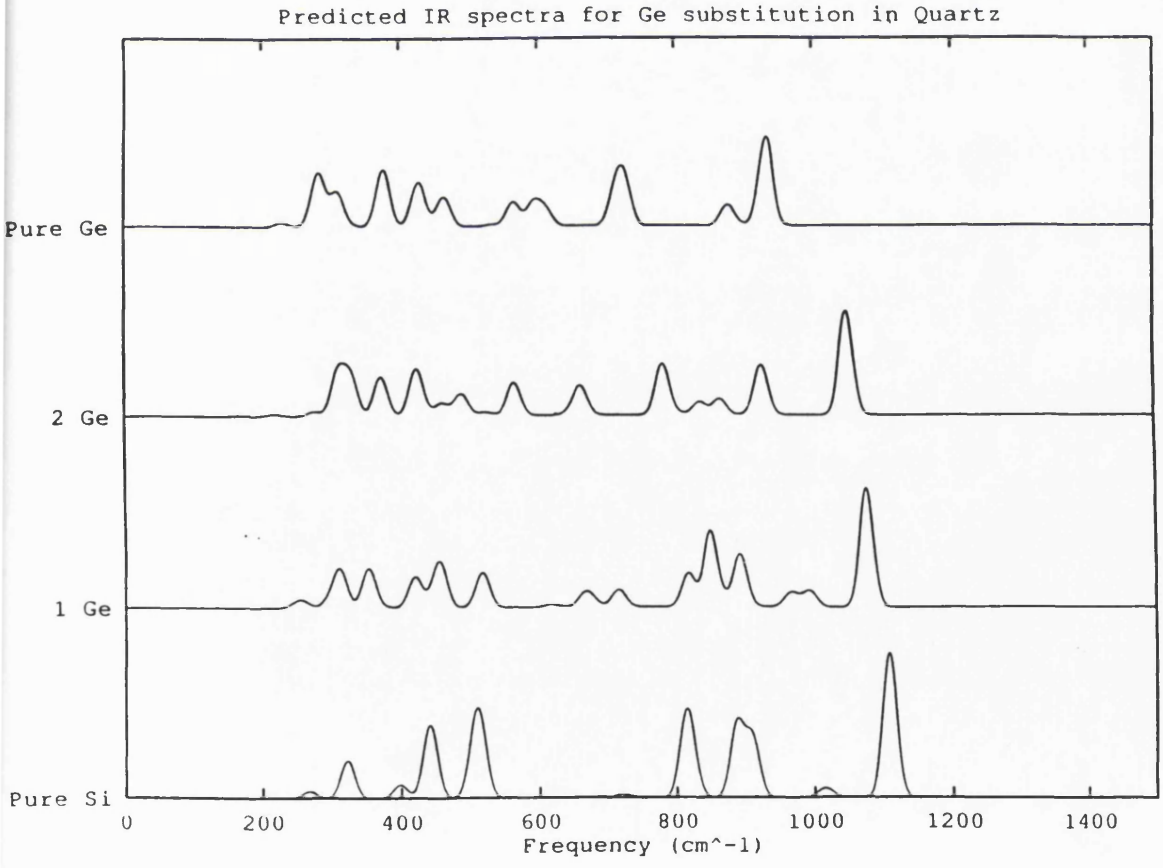

Figure 5.1.12 : Predicted IR. spectra for Ge substitution in α-quartz. (All intensities in this and subsequent figures in arbitrary units).

Calculated spectra for Silicalite-I.

Using the code and techniques previously described, the IR. spectra can be calculated for all the arrangements of Ge in Silicalite-I. Figure 5.1.13 shows these spectra for the random distribution at differing mole fractions of Ge. As can be seen, there is a gradual change from one spectrum through to the other, but the SiO_2 lattice vibrations; (e.g. the T-O asymmetric stretch at 900cm^{-1}) remain visible up to approximately 68% content of Ge. The GeO_2 lattice vibrations on the other hand only really take shape after about 60% Ge substitution. Again, there is an overall downward shift due to the weakening of the T-O bonds. On comparing the pure GeO_2 form and the purely siliceous form a splitting is clearly visible around 400cm^{-1}. It would be interesting to compare the experimental spectra of the pure polymorphs in order to test these predictions. The spectra of the compounds with an ordered Si/Ge distribution, exhibit all the trends that are observed for the structures with random arrangements. There are slight differences but again these can be attributed to the high dependence of the vibrational spectra on ion arrangements. Indeed the most notable differences occur around 50% substitution, where there is the greatest number of possible Si:Ge permutations.

Figure 5.1.13 : Predicted IR. spectra for RANDOM Ge substitution into Silicalite-I.

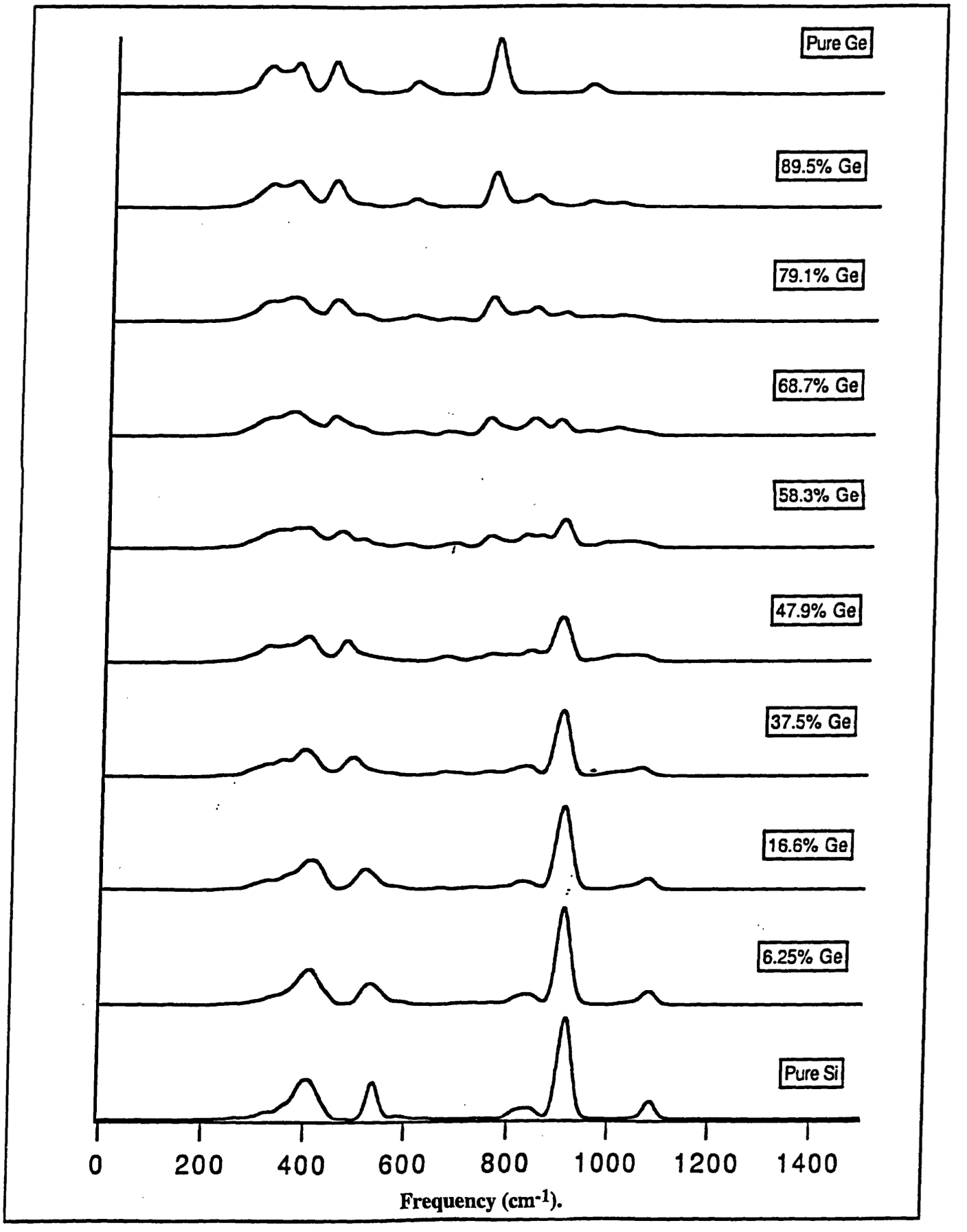

Calculated spectra for Zeolite-Y.

The calculated IR. spectra are shown in figure 5.1.14(a,b). The simulation of the purely siliceous spectrum has previously been compared to an experimental spectrum of a dealuminated compound in de Man *et al*[28]. Here we concentrate on the dramatic effect of differing Ge substitutions in the lattice framework. As can be seen the transition from a purely siliceous to a purely germanic form are substantial. When one considers the results for a purely random substitution model, the spectra change from an ordered set of peaks, through a highly diffuse set, to an ordered Ge spectrum. The effect of the Ge substitution is to shift the peaks to a lower frequency owing to the general weakening of the T-O bond.

In the spectra of the ordered structures, the transition is much clearer: the predominant T-O symmetric and asymmetric peaks are reformed as the concentration of Ge increases. The effect of introducing Ge into the purely siliceous lattice is somewhat dissimilar to that of including Si into the pure GeO_2 lattice; in the latter case the modification of the spectrum is substantially greater suggesting the SiO_2 is less perturbed by the introduction of disorder in the T sites than is the GeO_2 structure.

It would clearly be of considerable interest to compare these predicted spectra with experimental measurements, if and when the experimental synthesis of Ge substituted Zeolite-Y becomes possible.

Figure 5.1.14 : Predicted IR. spectra for (a) ORDERED and (b) RANDOM Ge substitution into Zeolite-Y.

(a)

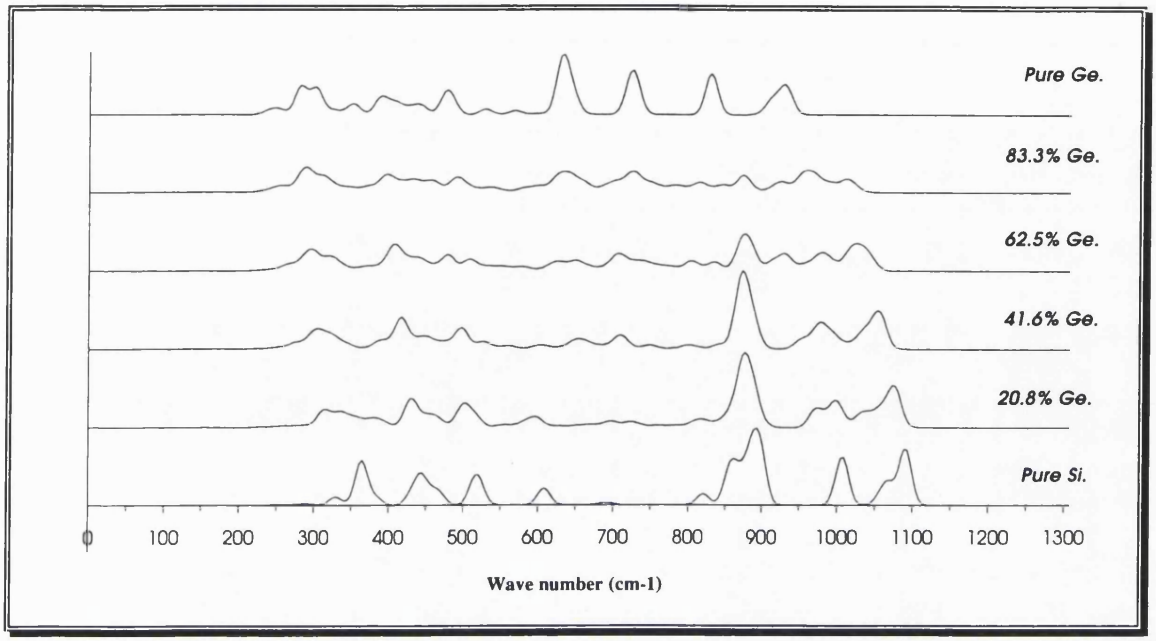

(b)

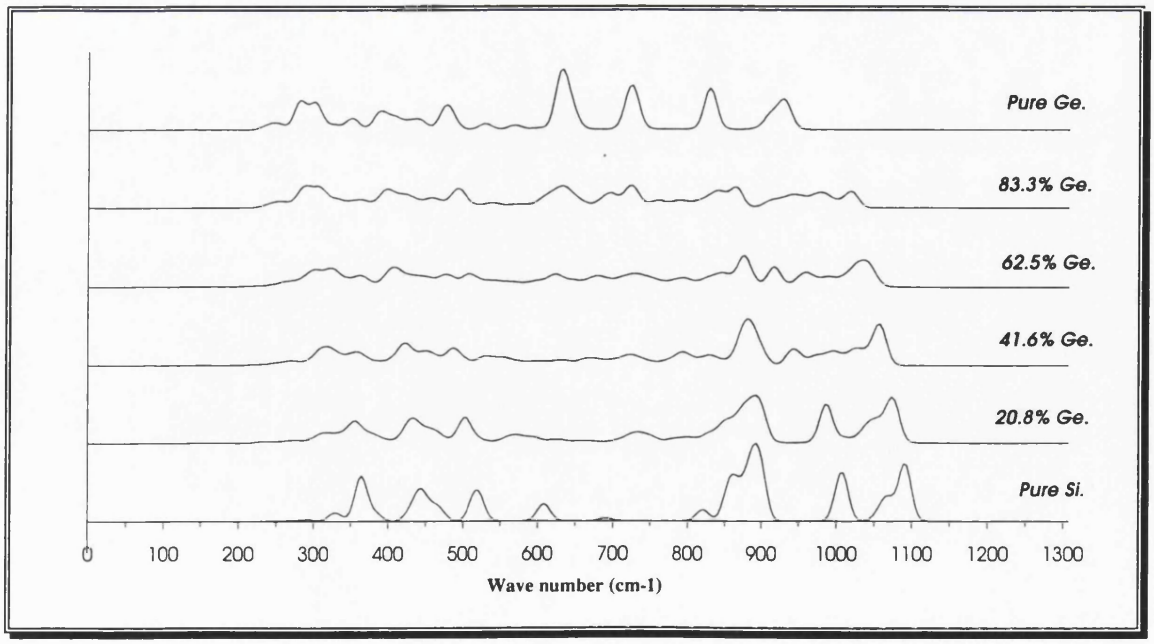

Calculated spectra for Mordenite.

Figure 5.1.15a shows the calculated IR. spectra for the random arrangement of Ge in Mordenite and it clearly demonstrates the transformation of the pure SiO_2 spectrum, to that for pure GeO_2 spectra. The peak at 375cm^{-1} is observed to decrease in intensity and reform at a lower wave number, which can be attributed to the weakening of the pore modes. The behaviour shown in the figure is typical of that observed for all the structures with random distributions of Ge substituted into zeolitic structures.

Figure 5.1.15b shows the spectra for the substitution of Germanium at differing crystallographic T sites. They are evidently considerable differences even though the mole fraction is constant. For substitution at each site we observe a distinct spectrum which differs markedly from the spectrum obtained from a random model of a similar mole fraction, where the spectra are less structured. Indeed from "doping" of certain crystallographic sites, one can analyse the importance of a specific site substitutions on the spectra. The peak at 1150cm^{-1} can be attributed to the intra-tetrahedral asymmetric stretch of the T1 and T2 sites; upon Ge doping of these sites the peak is observed to shift downward, due to T-O bond weakening. However, on substitution of only the T3T4 sites, it is still apparent at the frequency previously calculated; indeed, there is a great deal of potential information in these data. The T4 site gives rise to the T-O asymmetric stretch around 1050cm^{-1}, because upon substitution of all but this site, the peak is still observed in the spectra and can be compared with the pure Si spectrum since it is not shifted downward. Such independent T-O vibrations and their relative contributions are easily analysed but for the pore modes, (less than 600cm^{-1}), a more detailed study is required. However one conclusion that can be made, is that the 350cm^{-1} peak is due to the enhancement by the T1T2 sites. This peak is not observed when the T1 or T2 sites are substituted independently, but when both sites are substituted, a pore mode vibration of significant intensity is calculated. Once it becomes experimentally possible to create such Ge containing analogues of Mordenite, it would be of great interest to compare calculated and experimental spectra as the IR. spectrum is highly dependent upon the arrangement of framework ions.

Figure 5.1.15 : Predicted IR. spectra for (a) RANDOM and (b) ORDERED Ge substitution in Mordenite.

(a)

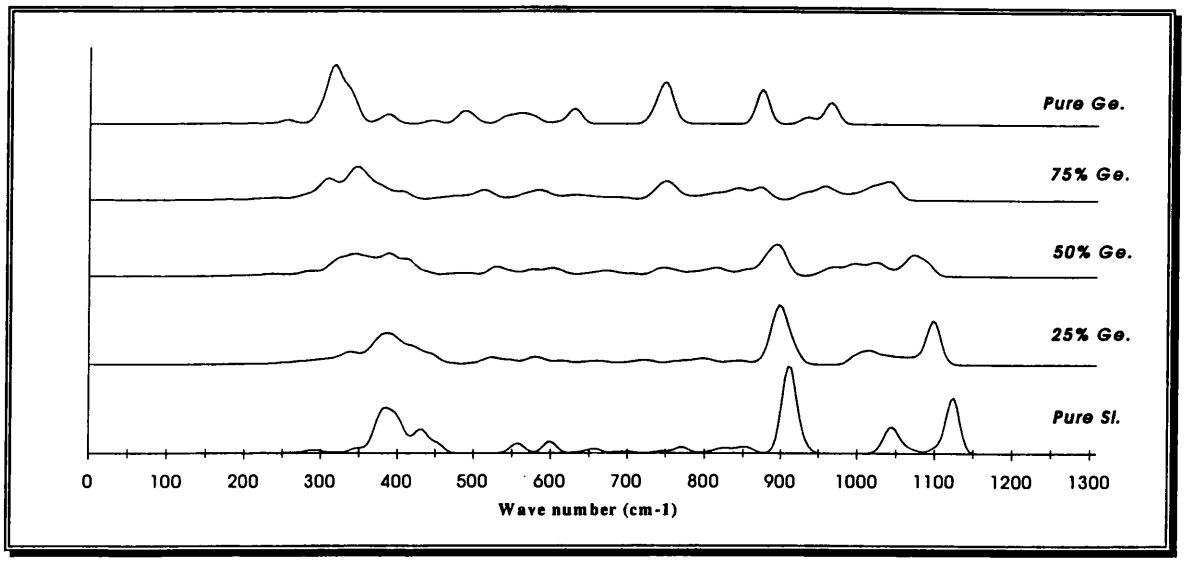

(b)

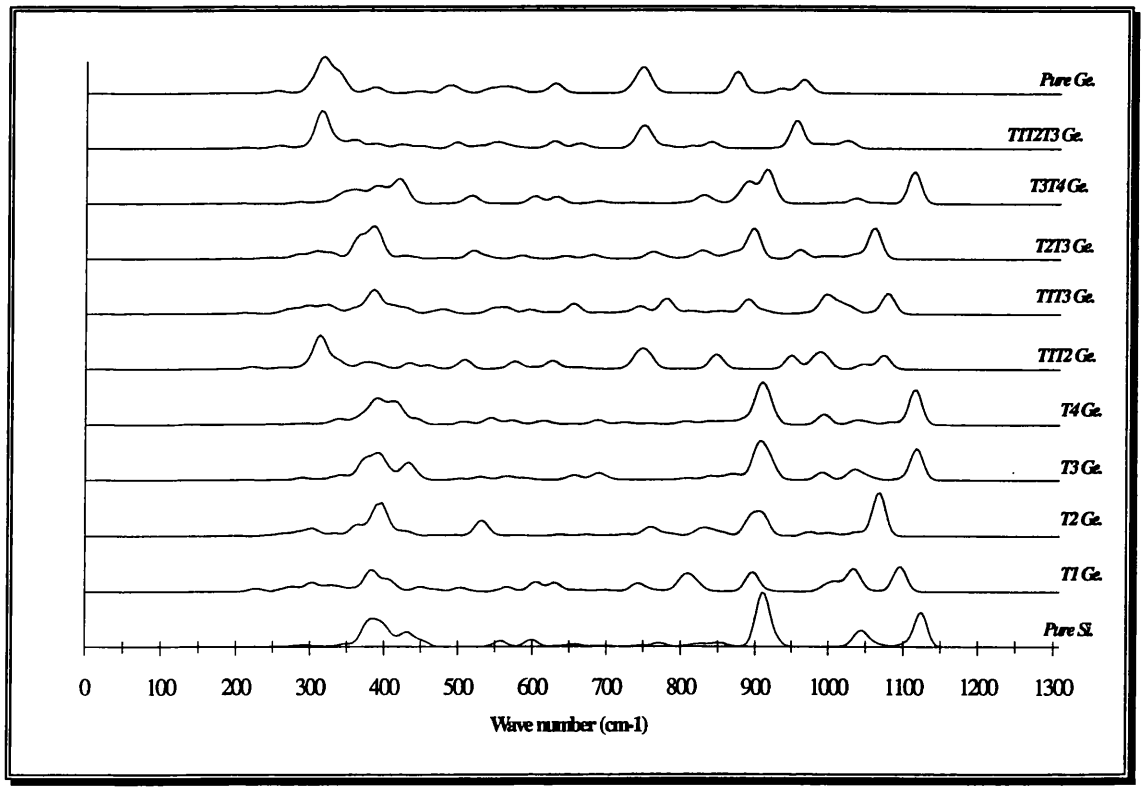

5.1.4 Conclusion.

GeO_2 polymorphs with zeolitic structures are predicted to have roughly the same thermodynamic stabilities with respect to the α-quartz polymorphs as do the corresponding SiO_2 polymorphs. Moreover, complete solid solutions of SiO_2/GeO_2 are predicted within the structures considered in this work.

Vegard's law is observed (as is expected), when there are random arrangements over the T sites, but not for ordered structures. The large deviations in the calculated lattice cell parameters might provide a method for deducing whether there is order in such zeolite structures.

The variation of the calculated IR. spectra with germanium substitution, show marked differences between the random and the ordered form. Indeed these indicate how the detailed spatial arrangement of framework ions can significantly change the vibrational properties of the solid.

Experimental studies of the structural and lattice dynamical properties of microporous GeO_2 polymorphs and of Ge/SiO_2 solid solutions would be of great interest.

5.1.5 Appendix A: Potentials used in this study.

Atomic parameters	Core Charge (|el|)	Shell Charge. (|el|)	Spring Constant. (eV/Å^2)
Silicon	4.0	----------	----------
Germanium	4.0	----------	----------
Oxygen	0.86902	-2.86902	74.92

Interatomic Buckingham potential terms. $Energy = A_{ij}\,\mathbf{exp}\left\{\frac{-r_{ij}}{\rho_{ij}}\right\} - \frac{C_{ij}}{r_{ij}^6}$

	A_{ij} (eV)	ρ_{ij} (Å)	C_{ij} (eVÅ^6)
Silicon - Oxygen (shell)	1283.907	0.32052	10.66158
Germanium - Oxygen (shell)	1980.02	0.3172	53.66
Oxygen (shell) - Oxygen (shell)	22764.0	0.149	27.88

Three-body terms : $Energy = k_{ijl}\left[\varphi_{ijl} - \varphi^o_{ijl}\right]^2$

O-Si-O	k_{ijl}= 2.09724 eV rad^{-2}	φ^o_{ijl}= 109.47°
O-Ge-O	k_{ijl}= 0.5861 eV rad^{-2}	φ^o_{ijl}= 109.47°

5.2 : Computational investigation of the phase transition from the pure GeO_2 α-quartz to the rutile structure.

5.2.1 Introduction.

As discussed in the previous section, we can create structures "computationally" and investigate their energetic and properties. Yet all the structures for all compositions studied, showed a large degree of similarity to the purely siliceous polymorphs. However, natural GeO_2 is known to be more stable in the rutile structure[29] than in the α-quartz[30] structure which is usually observed for pure SiO_2, that is the rutile form of GeO_2 has a lower energy, (under ambient conditions), than the α-quartz form previously investigated although both forms exist in nature. The aim of the following work is to investigate this structural difference and to model the rutile/quartz transition, and its dependence on the Ge:Si mole fraction. In the previous work, (section 5.1), the Ge/Si ratio was varied within a single unit cell of the α-quartz type structure and the resulting pure GeO_2 structure was minimised to that of α-quartz. However, in a single unit cell, there are only 3 tetrahedral sites which are available for substitution and indeed, the constraints imposed by such a small unit cell and the use of periodic boundary conditions could predetermine the α-quartz form, since no "instabilities" could ever occur in the structure. In this work, the number of unit cells of the α-quartz type structure is increased from 1 to a 2x2x2, supercell and finally to a 4x4x4 supercell, in order to provide more internal degrees of freedom. This will allow the phase change to be modelled via standard computational procedures provided the activation barrier is low enough to be overcome.

In this investigation we have investigated arrangements based on a the random T site substitution as the deviations from Vegard's Law, observed for the non-random arrangement, might mask or hinder the phase change process.

5.2.2 Methodology.

The methodology and computational techniques, as well as the potential model used in this investigation, are directly akin to those reported in section 5.1.2 of this thesis. In addition to the static modelling of the structure, a preliminary study of the dynamics of the system was investigated via Molecular Dynamics, MD[31]. The MD theory has already been discussed in detail, (section 2.5.1), so only the details on the ensemble and simulation box will be reported here. An NPT ensemble, (constant pressure, constant temperature and constant number of molecules) was employed, with the initial ion positions being derived from the results of the "static" constant pressure lattice energy minimisation on the supercell of GeO_2. To increase the internal degrees of freedom, this supercell was replicated to an independent 2x2x2 repeating cell; thus 64 unit cells of the α-quartz type structure have been investigated. In the new supercell, there are 588 independent atoms, comprising 192 germanium ions and 384 oxygen ions in the repeating unit cell. A Boltzmann distribution of velocities was assigned to the atoms in accordance with a thermal energy of 300K. The system was allowed to evolve over 50ps; numerical integration was performed over an integral time step of 1fs; structural data was collected over a period of 5ps. This length of simulation is not on the same order as other workers[32], because the purpose of this MD run is access the dynamical stability of the structure and not to calculate the relative diffusion coefficients, for which longer simulation runs are required.

The nature of the framework vibrations are reported both as radial distribution functions, RDFs, and as a mean square displacement, MSD, representation. The code FUNGUS[33] was used to perform the simulations as it embodies all the desired features required for this study and utilises the Verlet Leap Frog algorithm[34] in order to perform the numerical integration over time; an Ewald summation[35] is also used for the summation of the long-range Coulombic interactions. Once the MD simulation had been completed, lattice energy minimisation was once again performed on the resulting structure to show that the newly formed structure is stable.

In the subsequent investigation of this interesting phase transition, the newly formed MD structure was further subjected to lattice energy minimisation but not straight forward constant volume or constant pressure but a more sophisticated simulation in which the unit cell angles are varied in a systematic manner. In these calculations the hexagonal unit cell, $\alpha=\beta=90°$, $\gamma=120°$ is gradually changed by decreasing γ by increments 5° and performing a minimisation holding α, β and γ constant and allowing all other variables to vary, including the cell dimensions, *a,b,c*. Such a process was continued until $\gamma=90°$, after which constant pressure minimisation calculation was performed. This approach avoids constraints due to symmetry and reduces to a minimum the effect of box size. The results allow us to obtain a reasonable activation barrier for the transition from an hexagonal structure to one with orthogonal cell axes.

5.2.3 Results and Discussion.

Part 1 : "Static" calculations for pure GeO_2.

The work presented here is along very similar lines to that of section 5.1 but in the present calculation only structures based on the random arrangement of Ge ions over the T sites have been investigated. Figure 5.2.1(a,b,c) show plots of the lattice cell parameter against mole fraction of Ge substituted into the supercell of α-quartz. The *a* cell parameter, figure 5.2.1a, is observed to expand to a greater extent with Ge content compared with the single unit cell study but, a marked decrease in cell parameter is calculated on going from 50% to 66% Ge. The *b* lattice parameter, figure 5.2.1b, shows a steady increase in lattice cell parameter with mole fraction, as expected by Vegard's Law. However, the predicted change in the *c* lattice parameter with mole fraction is vastly different to that observed in any of the previously studied structures; for structures with mole fractions up to 50% Ge, the lattice parameter is observed to increase, as one might predict from the previous work but at 50%-66% Ge, there is a reduction of 17% in *c*.

Figure 5.2.1 : (a) Lattice parameter *a*, (b) Lattice parameter *b*, (c) Lattice parameter *c* vs. mole fraction of Ge substituted in the α-quartz supercell structure. (All lattice parameters in Å).

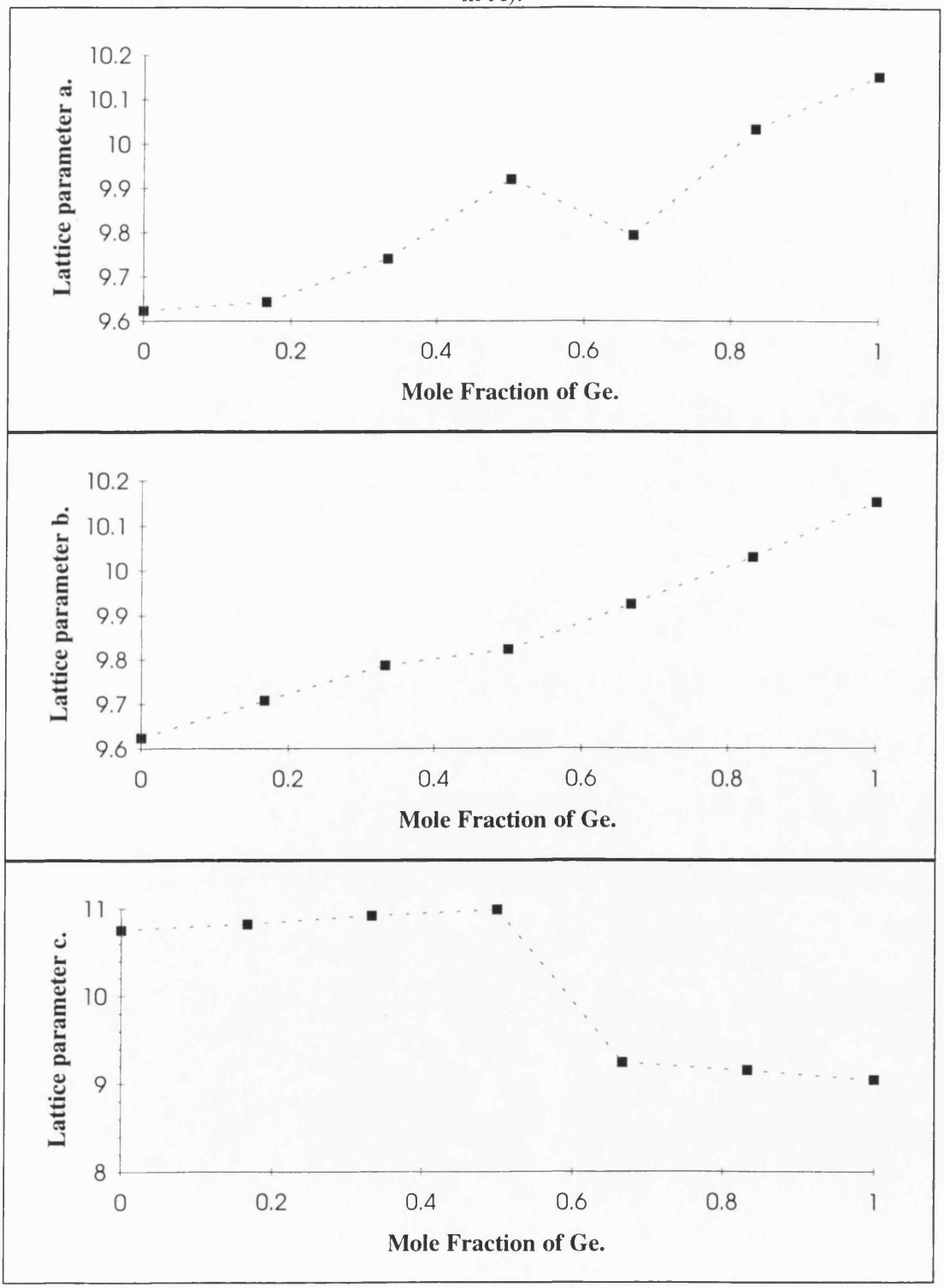

The explanation of this unusual behaviour is best performed by reference to the minimised structures shown in figure 5.2.2 (a,b). ((a) is a view down the *c* axis, [001] and (b) is an orientation viewed along the *b* axis, [010]). Clearly there is a structural change in going from 50% to 66% mole fraction of Ge and it is this structural change that is responsible for the marked change in the *c* lattice parameter versus mole fraction, (figure 5.2.1(c)). We note that the apparent increase in the intensity of the lines in the diagram is due to the near superposition of bonds in neighbouring layers; the lighter the line the better the symmetry along the axis being viewed. The process of lattice minimisation has modelled a structural phase transition. The new computationally derived structure has an open pore type topology with channel dimensions of 4.85 to 5.10 Å and has a screw like topology, though at this time no asymmetric unit cell and the appropriate space group has been derived.

Figure 5.2.2(a) : The resulting structures obtained on substituting Ge into a pure α-quartz structure in 16.1% increments up to pure GeO_2 : a) viewed along the [001].

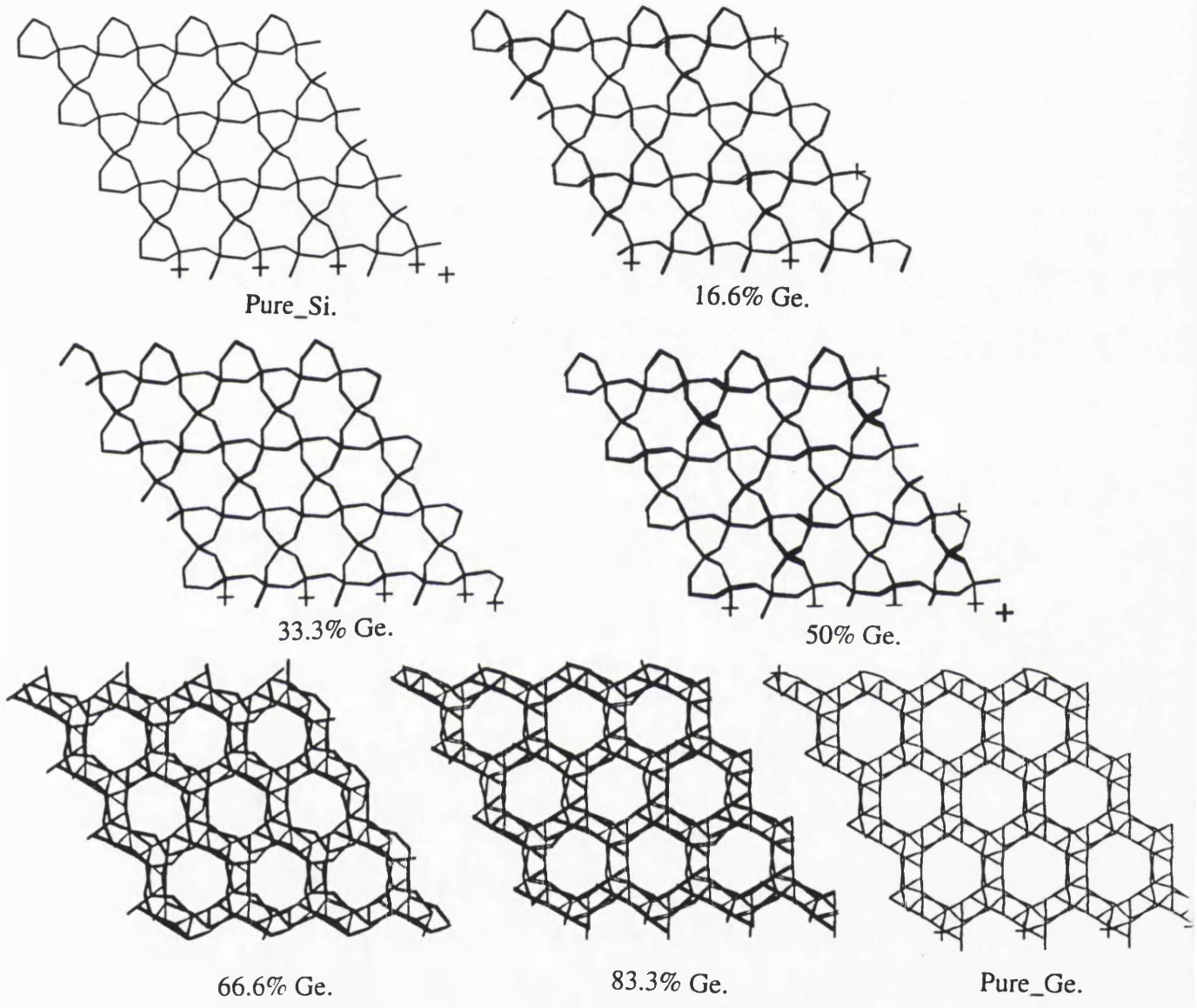

Figure 5.2.2(b) : The intermediate structures viewed along the [010].

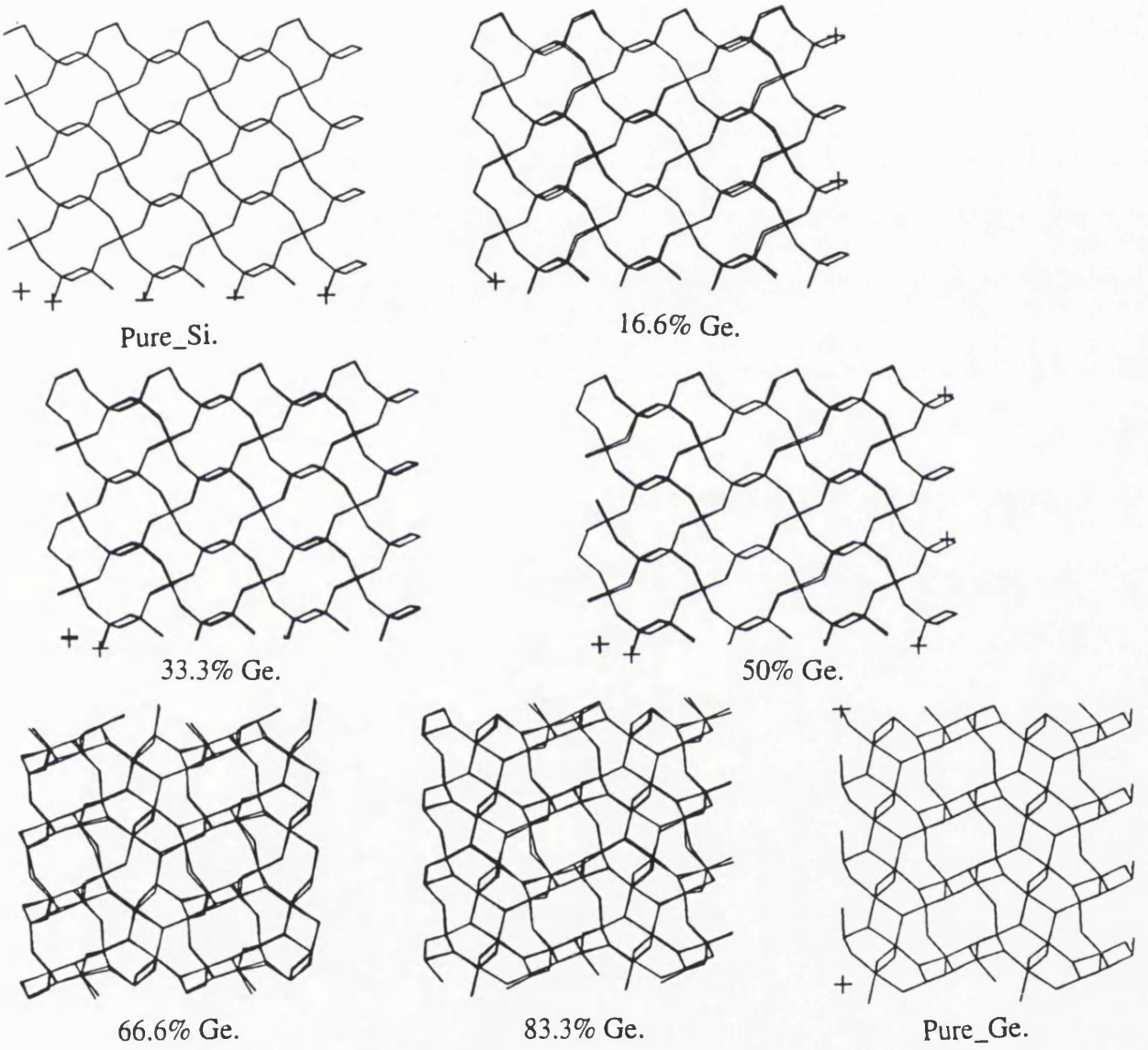

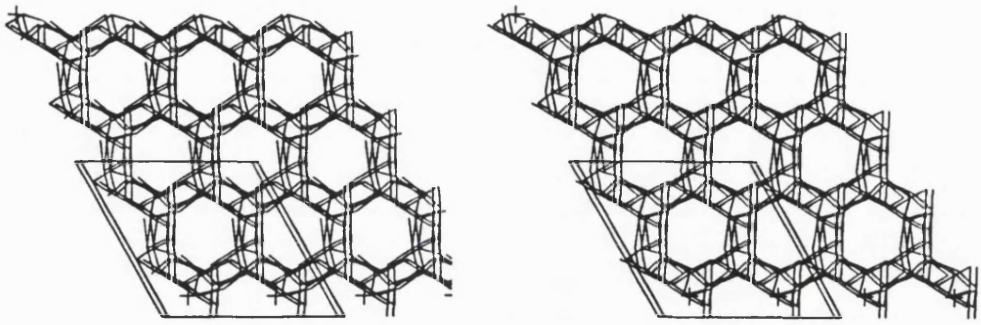

Figure 5.2.3 : Stereoscopic view of the new pure GeO_2 structure.

Clearly, from figure 5.2.3, some Ge atoms have increased their co-ordination shell from 4 to 6, implying there has been a substantial change in the structure. In the α-quartz type structure, all the T atoms are 4 co-ordinate, yet the rutile structure is based entirely on octahedral co-ordination. It is evident from the structure of the newly formed GeO_2 polymorph that there is a mixture of the Ge-O bond lengths and indeed, a proportion of the T atoms are octahedrally co-ordinated, although some retain tetrahedral character. This observation is in agreement with the proposal that this structure and the other structures calculated could be plausible intermediates in the phase change from α-quartz to rutile as the mole fraction of Ge increases.

The energy of the new GeO_2 structure, (-123.56eV per T site) is greater than that for the α-quartz structure (-123.23eV per T site), yet not quite as stable as the pure GeO_2 rutile form, -124.419eV. Indeed on a thermodynamic basis, the new structure is a possible intermediate in the structural phase change from α-quartz to rutile. This partial change to the rutile structure is also evident in the ratio of the lattice parameters, *a/c*; in the GeO_2 α-quartz structure the *a/c* ratio is 0.89 and in rutile is

1.39 and the calculated *a/c* ratio of the new structure found by lattice energy minimisation is 1.12.

As reported in Section 5.1.3, it is possible to calculate the IR. spectra of the solids simulated. We can also straightforwardly calculate the XRD spectrum since the atomic fractional co-ordinates and cell parameters are known, and indeed, figure 5.2.4 shows the predicted IR. spectra for the phase transition from the α-quartz to the new structure while figure 5.2.5 reports the changes in the XRD pattern during the gradual substitution of Ge into the supercell of the α-quartz structure. The phase change is plainly evident in these results.

Figure 5.2.4 : The computed IR. pattern for the iterative random substitution of Ge into α-quartz to yield the new structure. (Intensity in arbitrary units.)

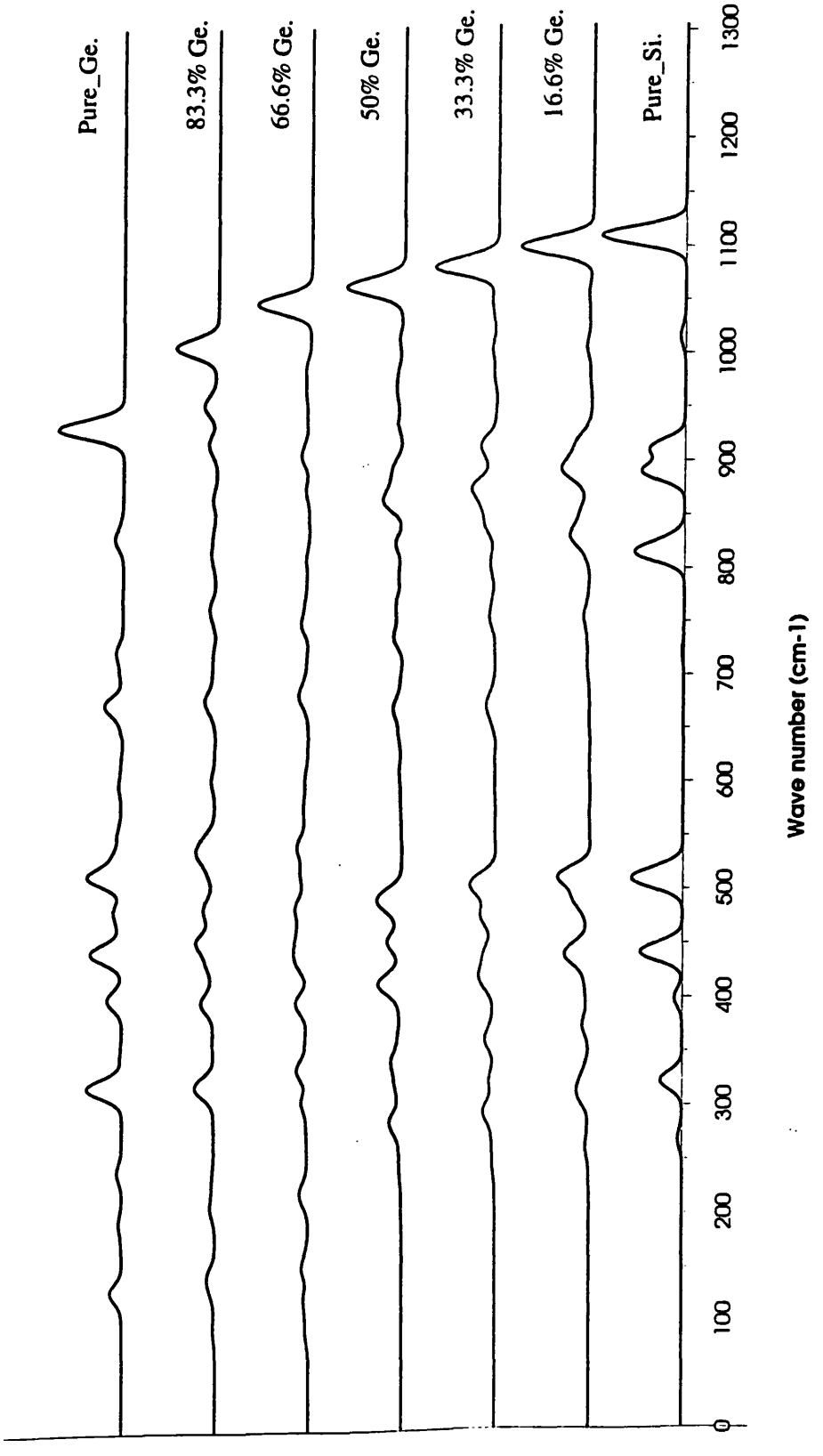

Figure 5.2.5 : The computed XRD pattern for the random substitution of Ge into the α -quartz structure. (Intensity in arbitrary units.)

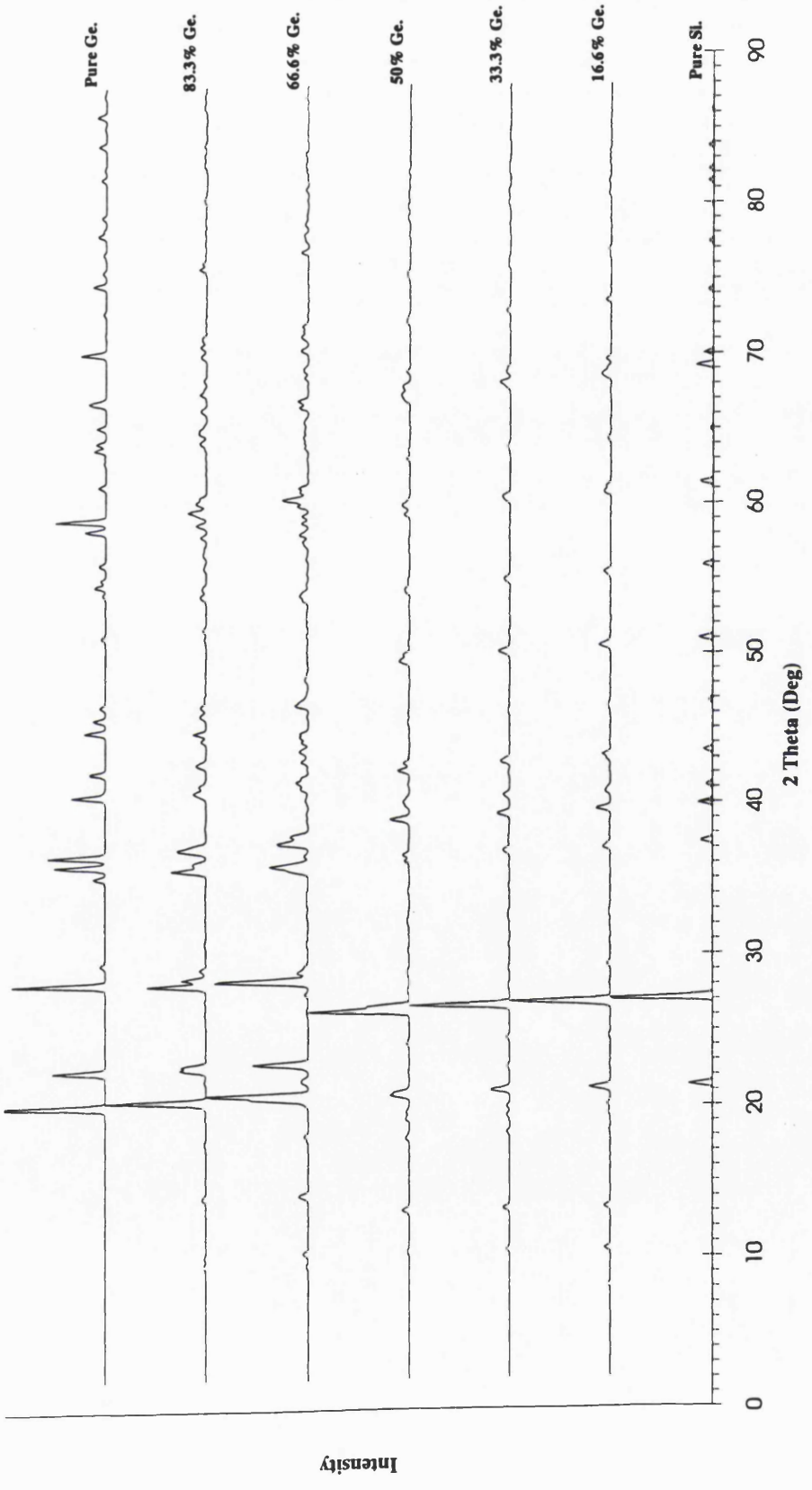

Part 2 : Dynamical calculations relating to the novel GeO_2 structure.

As reported in the methodology section, 5.2.2, a constant pressure/constant temperature molecular dynamics simulation was performed on the structure located via lattice energy minimisation, figure 5.2.3. The number of unit cells of this new structure was increased in size to a 2x2x2 supercell, hence 64 unit cells of the original α-quartz structure was simulated in section 5.1.3; this is also a factor of 8 larger than the cell used in the energy minimisation calculations. After an initial equilibration period of 50ps, data acquisition was carried out over a 5ps time period. As noted, this period is long enough to investigate the framework properties but would not be of sufficient time to elucidate information regarding diffusion parameters. Figure 5.2.5(a,b) is a snapshot of one of the conformations sampled by the MD run after the 50ps equilibration; (a) is a view aligned along the [001] and (b) is a view along the [010]. The structure is different from that produced by the energy minimisation procedure, (figure 5.2.3). The hexagonal nature of the cell is clearly retained even though the MD simulation was performed under constant pressure. The pores of the new structure are more clearly defined, (especially when viewed along the [001], figure 5.2.5a), than for the initial energy minimised structure and indeed they have increased in size to 5.17Å; (this value is the internuclear distance and does not include the effective van der Waals radii which will make the actual non-contact pore dimensions smaller.) However, when viewed along the [010] there is an increased connectivity; (two ions are said to be connected when the distance is within the sum of the ionic radii of the two species). The average co-ordination number of the T sites has increased compared to that of the initial structure. This can clearly be seen by a comparison of the connectivity when viewed along the 010, both before and after MD, (figure 5.2.2b and figure 5.2.5b respectively). When a molecular graphics movie of the atomic trajectory is made of the simulation, the framework is observed to "wobble" freely. However, there is no evidence of any further phase change following that previously observed. The structure derived after lattice energy minimisation and a

subsequent MD simulation bears no resemblance to the initial α-quartz structure. Indeed, the MD located structure has an energy of -123.83eV per T site which is lower than the starting structure, (-123.56eV per T site), though not as low in energy as the rutile structure.

Figure 5.2.5(a,b) : A snapshot of one conformation sampled in the MD simulation; a) [001], b) [010].

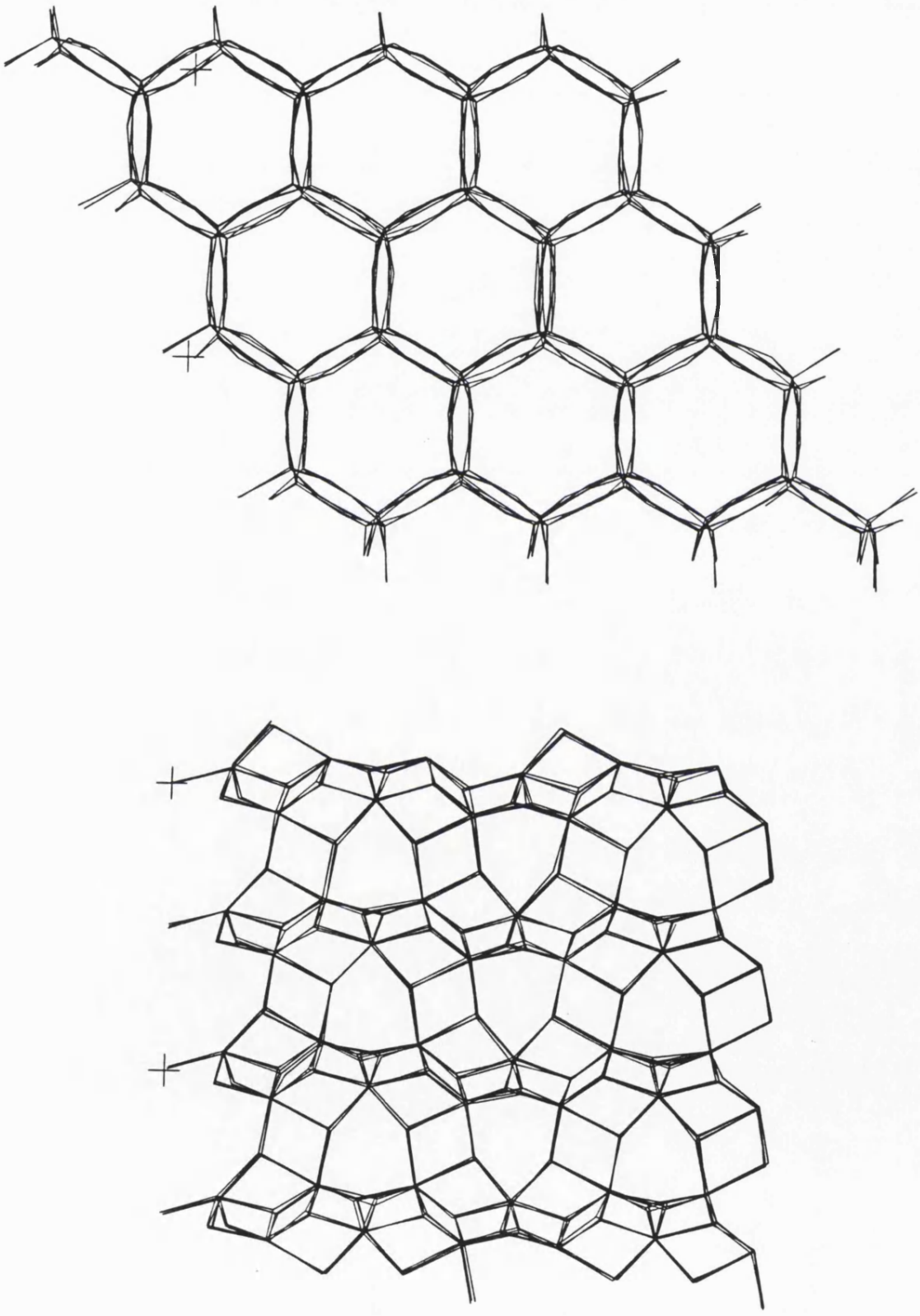

An MD simulation also provides information regarding the behaviour of the structure over a time averaged period at the defined temperature and one of the most effective ways of representing such structural vibrations is via normalised radial distribution functions, RDFs. Figure 5.2.6(a,b,c) shows the RDFs obtained from the MD simulation of the pure GeO_2 structure, based on that generated by lattice energy minimisation; these include O-Ge, O-O and Ge-Ge interactions. Figure 5.2.6(a) reports the O-Ge RDF, where evidently two different types of O-Ge bonds exist; such bonds are typified by two peaks in the RDF, centred on 1.77Å and 2.03Å respectively. Clearly, the first peak at 1.77Å is more intense than the second by a factor of approximately 3 (as can be verified by integrating under the peaks in the RDF). Thus approximately 75% of Ge-O bonds are at a distance of 1.77Å, with the remainder about 2.03Å in length. This observation discriminates between the oxygen atoms involved in tetrahedral bonding, (i.e. 4 co-ordinate) and those bonds involved in octahedral bonding i.e. 6 co-ordinate. In an α-quartz type structure only tetrahedral bonding occurs, thus only one O-Ge bond distance would be expected, whereas in a rutile structure 2 discreet O-Ge bond lengths are observed although the structure is entirely octahedrally co-ordinated. Indeed, the structure predicted via lattice energy minimisation followed by MD, is more akin to rutile with the 2 bond lengths than to the α-quartz type structure; this again emphasises that the new structure is a plausible intermediate in the phase transition from α-quartz to rutile. The other peaks in the Ge-O RDF show maxima at discreet values emphasising the crystalline nature of the structure.

The O-O RDF, figure 5.2.6(b), shows the first interaction distance at 2.21Å which is closer to the distance in rutile of 1.91Å, compared to that in α-quartz, where the first O-O peak would be at 2.61Å.; again a relationship between the new structure and the rutile form is implied. The distribution of peaks in the Ge-Ge RDF, figure 5.2.6(c), shows two maxima of 3.04Å and 3.41Å with a population ratio of 1:1. This is slightly different from the population distribution of Ge-Ge in rutile where peaks at 3.06Å and 3.59Å, with a ratio of 3:1 respectively is expected. However, this is very

different to the Ge-Ge RDF of an α-quartz structure, which has only one peak centred at 3.03Å and the second sited at greater than 4.0Å. The new structure following the dynamical simulations is observed to be more akin to that of rutile than the α-quartz structure, from which the simulations were initially started.

From MD simulations it is possible to extract Mean Squared Displacements, MSD, as defined by Tildesley *et al*[36]. These provide a measure of the time dependence of atomic displacements.

Figure 5.2.7 : Calculated total MSD values derived from the MD simulation. (Measured in $Å^2$).

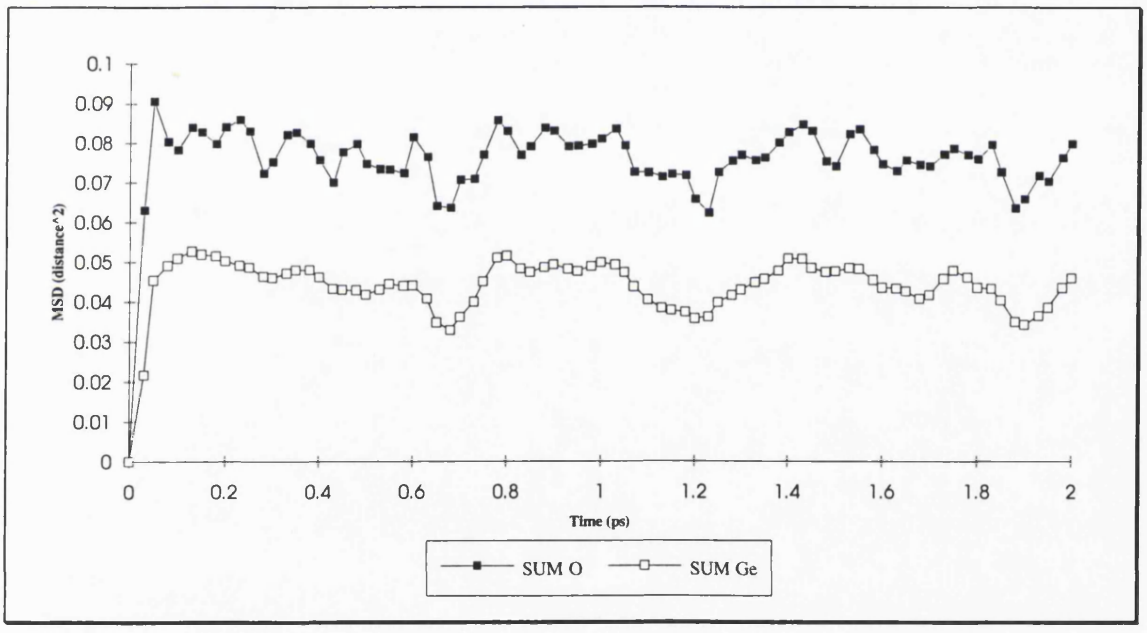

The total MSD of the oxygen atoms, figure 5.2.7 shows a roughly constant value after the initial rapid increase. If diffusion was occurring in the system then the MSD would increase steadily with time, but as can be clearly seen, the oxygen MSD remains approximately constant with an overall average of $0.0767Å^2$; hence the average amplitude of oxygen vibration around the oxygen ions is 0.277Å

Figure 5.2.6 : Radial distribution functions for the new GeO_2 structure; (a) O-Ge, (b) O-O, (c) Ge-Ge.

a) Ge-O RDF.

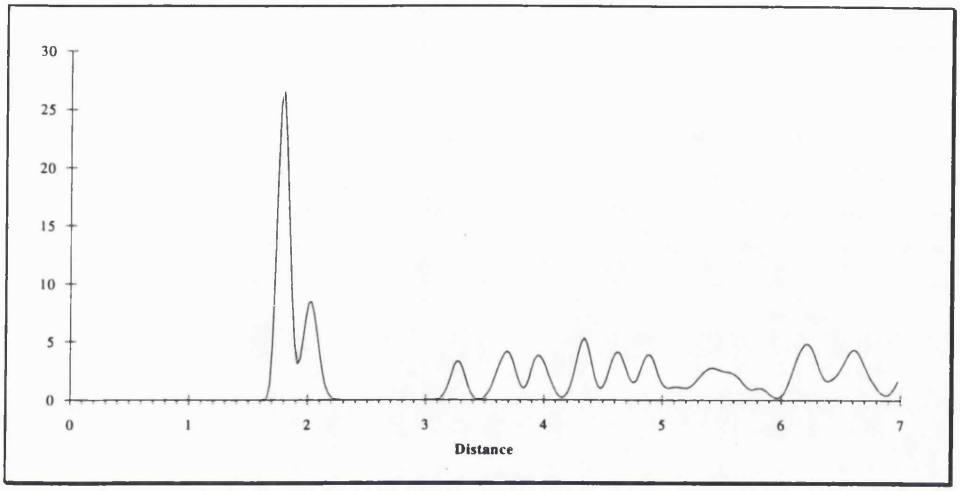

b) O-O RDF.

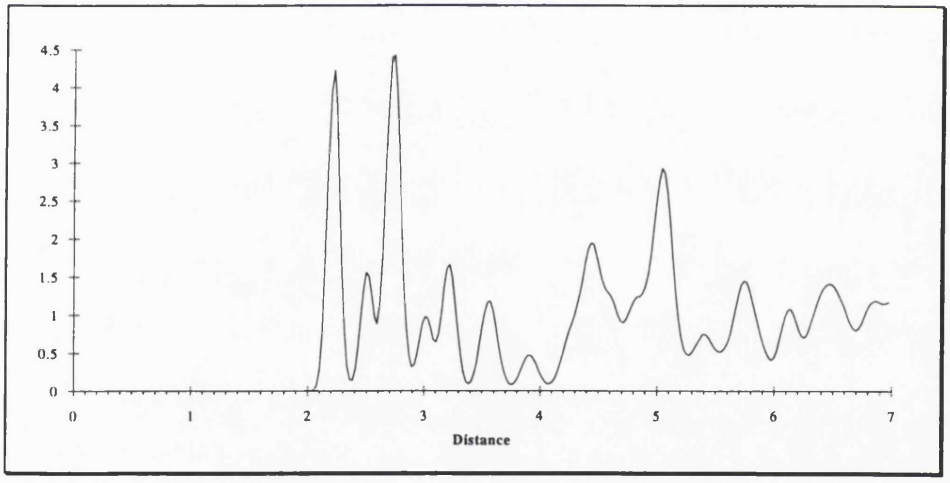

c)Ge-Ge RDF.

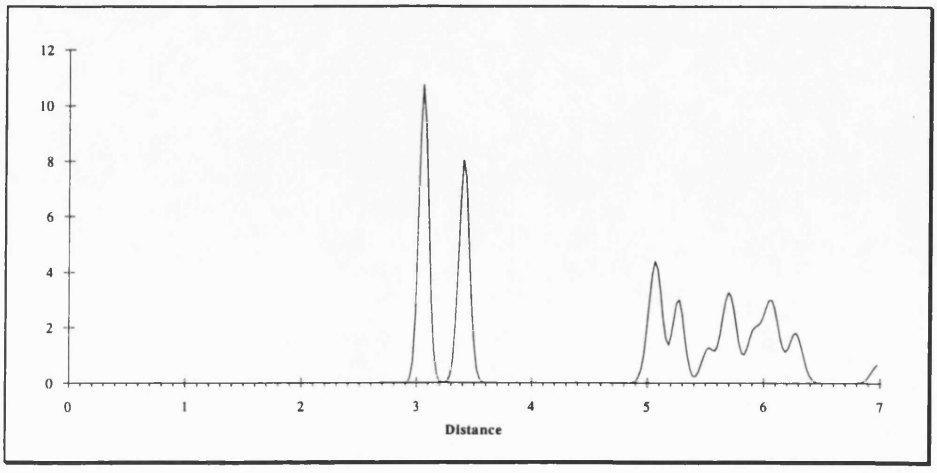

The Ge atom MSD, figure 5.2.7, is again roughly constant but has fewer features than the oxygen displacements; an average MSD of 0.04457Å^2 is calculated, corresponding to an average vibrational amplitude of 0.211Å, the lower amplitude compared with oxygen being due to the greater mass of Ge. The total MSD plots of the ions considered only the magnitude of the displacements and not their directions; but it is possible to gain MSDs corresponding to individual axes. Thus from figure 5.2.8, giving the fractional co-ordinate MSD displacements for the Ge atoms, we can see that the Ge atoms vibrate more along the *y* direction than either along the *x* or *z* directions.

Figure 5.2.8 : Cartesian MSD values for the Germanium ions in the new GeO_2 structure. MSD is reported in (fractional co-ordinates)^2

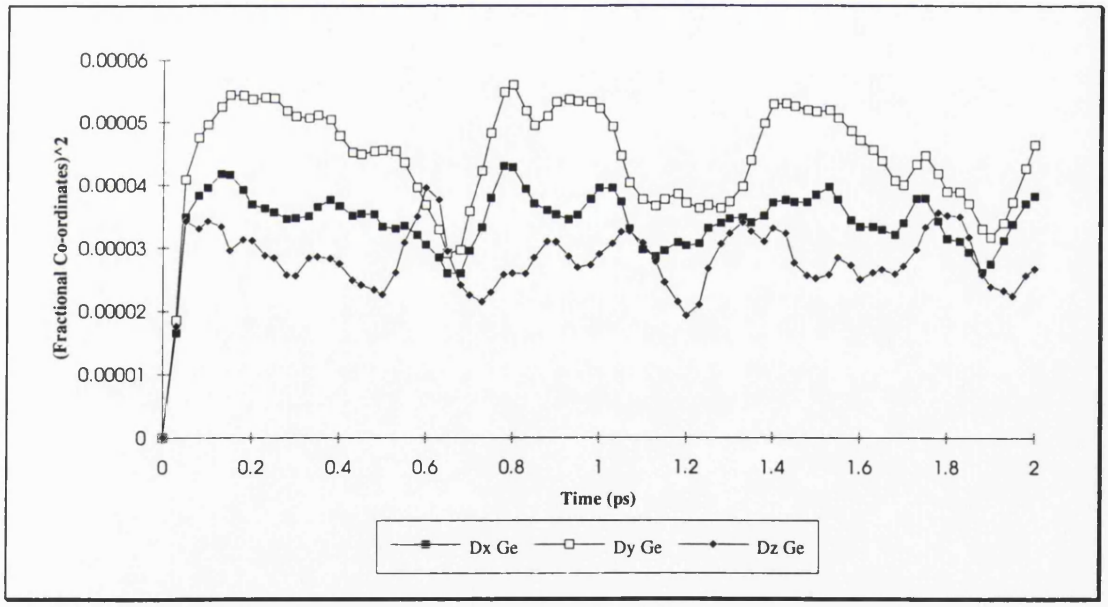

MD has thus provided a suitable methodology for the simulation of the initial stages of the phase change from α-quartz to rutile; yet although the T atoms have increased in co-ordination number, the rutile structure is not clearly evident.

Part 3 : Perturbation of the cell angles.

All the calculations considered so far have involved constant pressure simulations, in which the unit cell parameters, both dimensions and cell angles, have been allowed to change. Yet as we have already shown, the energy per T atom is -124.419eV in GeO_2 rutile which is significantly lower than -123.23eV in GeO_2 α-quartz. Clearly, the local minimum around the GeO_2 α-quartz structure is very well defined with large activation barriers that cannot easily be overcome. The work described in this section serves to take the structure derived from MD, with an energy of -123.83eV per T atom and forcefully change the unit cell angles, (as discussed in the methodology section 5.2.2), by decreasing the γ cell angle by 5° and performing lattice energy minimisation but keeping the cell angles fixed. Once γ has reached 90°, a full constant pressure minimisation was undertaken allowing both cell angles, dimensions and internal co-ordinates to change; this final minimisation has been termed "Free" for future reference.

Figure 5.2.9 : Variation in the energy per T atom as a function of the γ cell angle reduction.

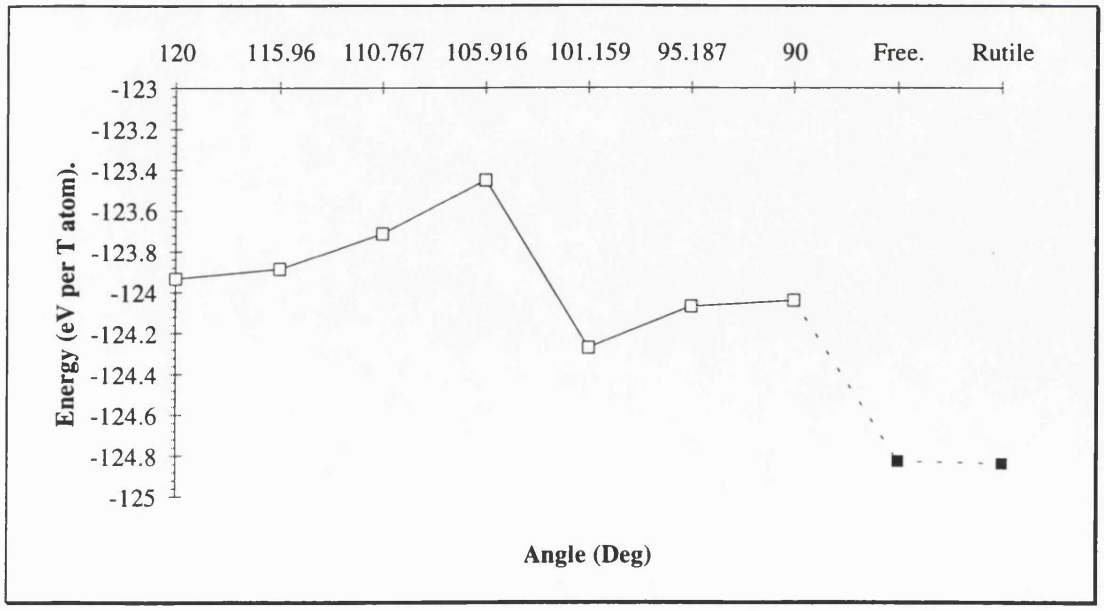

Figure 5.2.9 reports the variation in energy of the subsequent structures and also the final energy of the free minimisation and that calculated for the rutile structure. Clearly, there is an increase in the energy per T atom as the cell angle, γ is reduced; yet on going from γ=105° to γ=100°, a dramatic decrease in energy is calculated; this decrease continues until the free minimisation is performed and the energy is comparable to that of the rutile structure. For this study an activation barrier of +0.481eV per T atom was obtained for the quartz/rutile transition. Thus the local minima around the α-quartz structure are indeed well defined with an appreciable activation barrier and this is the reason why both the MD and previous constant pressure energy minimisation failed to locate the lower energy rutile structure. The intermediate structures obtained on varying the γ cell angle although unlikely to occur other than in a transient form are nevertheless of importance and are depicted in figure 5.2.10.

Indeed, the "Free" simulation and that of the rutile structure show distinct similarities even though the unit cell dimensions and angles are different; again as in the previous section it is possible to calculate the XRD patterns for the phase transition, figure 5.2.11.

The "Free" and rutile structures are very similar and only slight differences occur; these differences are due to the "free" system not containing the correct number or alignment of T atoms to fill a triclinic box of the rutile type structure. However, the phase transition of pure GeO_2 from the α-quartz type structure to the rutile structure has been successfully modelled within the limitations of the presently available computational techniques.

Figure 5.2.10 : The intermediate structures obtained during the variation of the γ cell angle.

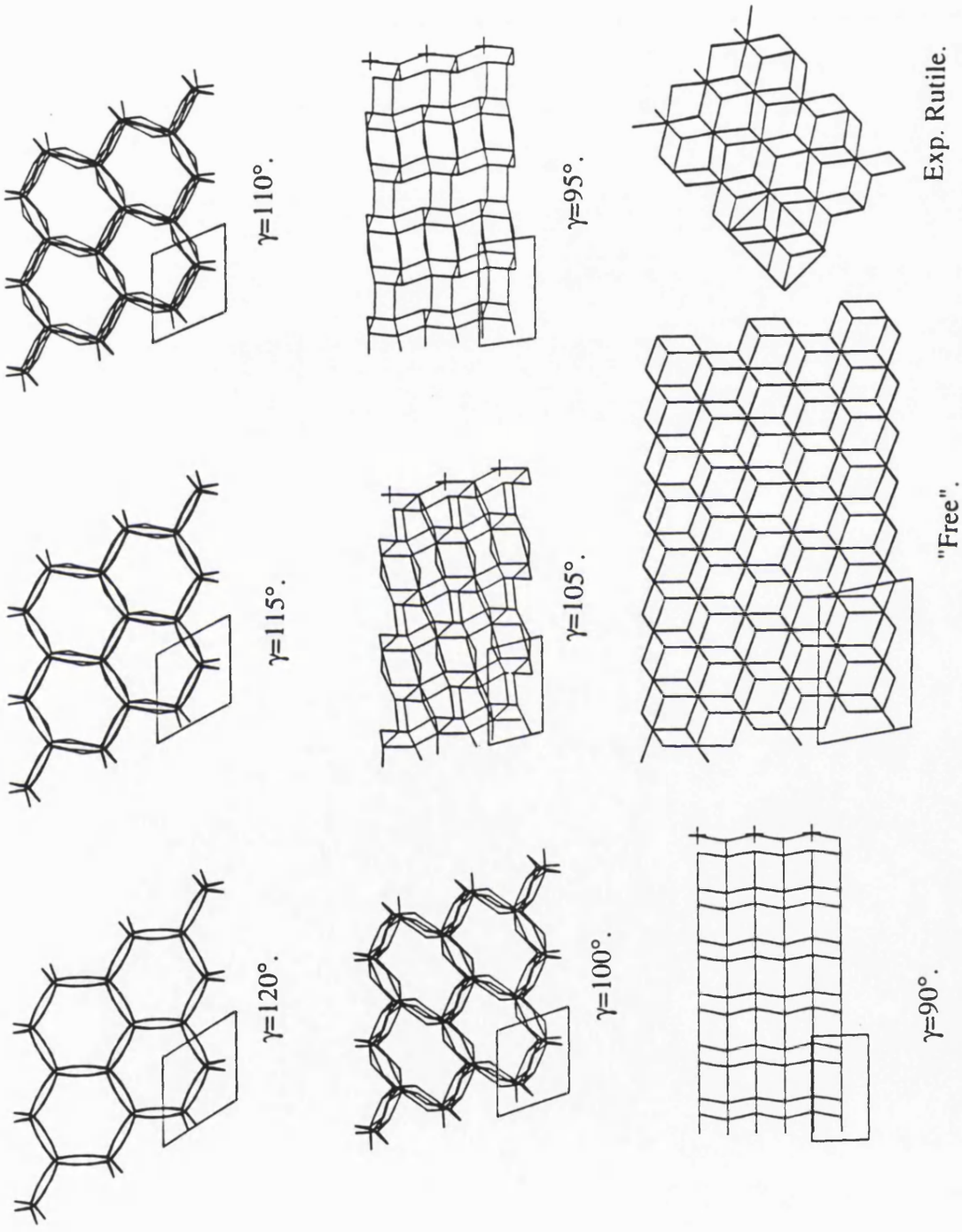

Figure 5.2.11 : The predicted XRD patterns for the decrease of γ in increments of 5°, also shown are the patterns of the "free" structure and that of rutile.

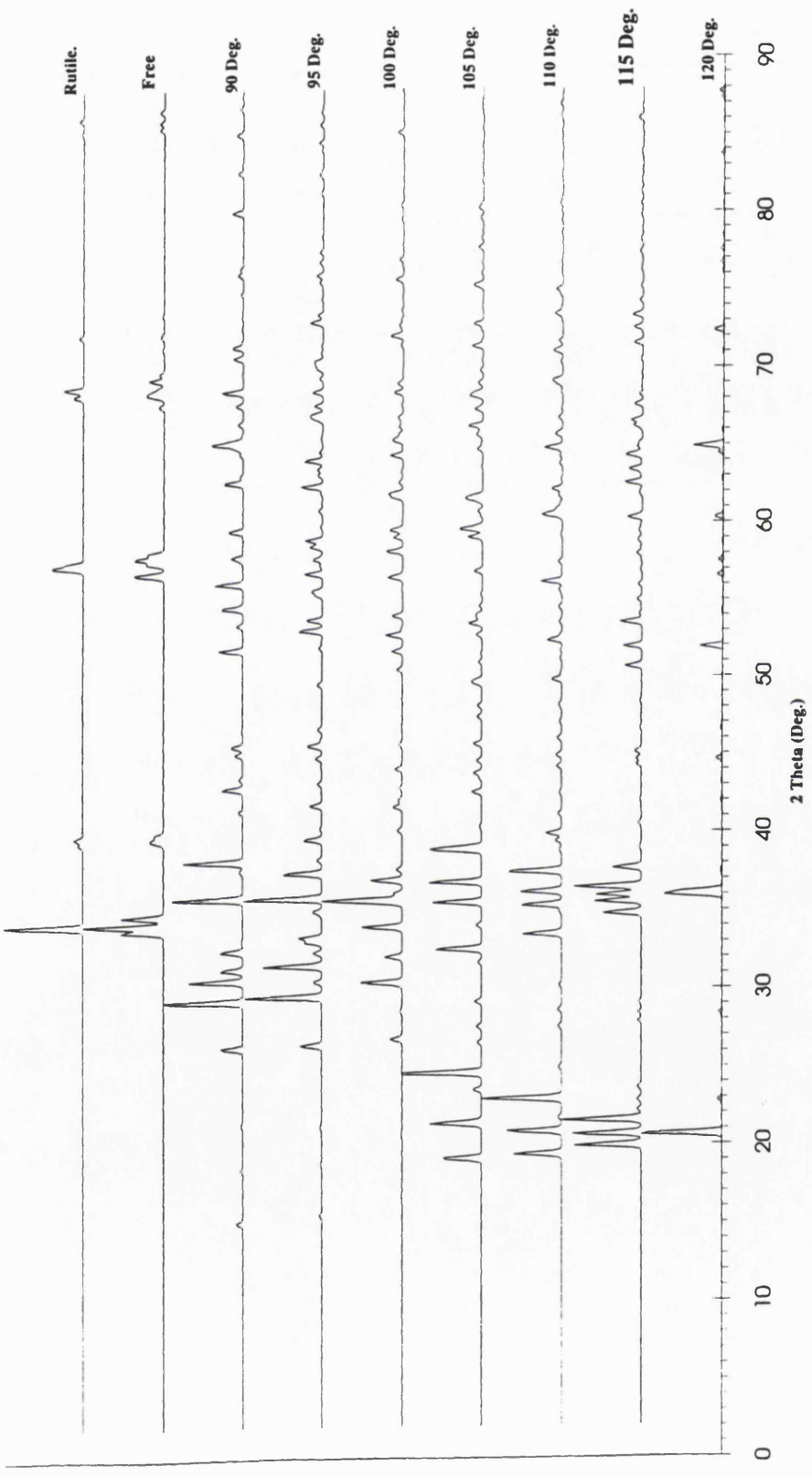

5.2.4 Conclusion.

It is possible to model the phase transition of the GeO_2 α-quartz structure to the GeO_2 rutile structure via computational means and indeed, a few key intermediates have been proposed for such a change. Yet, the local minimum around the α-quartz type structure is very well defined with an activation barrier of +0.481eV per T atom. However, by forcing the cell dimensions to change it has proved possible to model the interesting and important phase transition.

5.3 References.

1 Barrer R.M.; "*Zeolites and Clay Minerals*", Academic Press, New York, (1972).

2 Wilson S.; Lok B.M.; Menina C.A.; Cannon T.R.; Flanigen E.M.; *J.Am.Chem.Soc.*, **104**, 1146, (1982).

3 Flanigen E.M.;Lok B.M.;Patton R.L.; Wilson S.T.; in *"New developements in zeolite science and technology"*, P.A. Jacobs (ed); Elsevier, Amsterdam, (1986).

4 Vaughan D.E.W.; *Stud. Surf. Sci. Catal.*, **49A,** 95, (1989).

5 Wright P.A.; Natarajan S.; Thomas J.M.; Bell R.G.; Gai-Boyes P.L.; Jones R.H.; Chen J.; *Angew. Chem. Int.*; **31**, 11, (1992).

6 Jones R.H.; Chen J.; Thomas J.M.; George A.R.; Hursthouse M.; Xu R.; Li S.; Lu Y.; Yang G.; *Materials*; **4**, 808, (1992).

7 Kokotailo G.T.; Lawton S.L.; Olson D.H.; Meier W.M.; *Nature*, **272**, 437, (1978).

8 Bibby D.M.; Milestone N.B.; Aldridge L.P.; *Nature*, **280**, 664, (1979).

9 Meier W.M.; *Z. Kristallogr*, **115**, 439, (1961).

10 Costenoble M.L.; Mortier J.W.; Uytterhoeven J.W.; *J. Chem. Soc. Farad. Trans.*, **72**, 1877, (1976).

11 Flanigen E.M.; Bennet J.M.; Grose R.W.; COhen J.P.; Patton R.L.; Kirchner R.M.; Smith J.V.; *Nature*, **271**, 512, (1978).

12 "Computer simulation of solids", eds. C.R.A. Catlow & W.C.Mackrodt, *Lecture notes in physics*, **166,** Springer-Verlag, Berlin, New York.(1989).

13 Jackson R.A.; Catlow C.R.A.; *Molec. Sim.*, **1,** 207, (1988).

14 Bell R.G.; private communication.

15 Ewald P.P.; *Ann Phys.;* Leipzig, **64,** 253, (1921).

16 Leslie M.; *Daresbury Laboratory technical memorandum,* in prep.

17 Fletcher R.; "*Pratical Methods of Optimisation, Volume 1*".; J. Wiley & Sons, New York, (1980).

18 Parker S.; Price D.; "*Advances in Solid State Chemistry*", Ed. C.R.A. Catlow., **1**, 295, (1989).

19 Dolling S.; "Calculation of phonon frequencies " in Gilet G. (ed) *"Methods in computational physics*", **15**, (1976).

20 Maradudin A.A.; Montroll E.W.; Weiss G.H.; Ipatova I.P.; "*Theory of lattice dynamics in the harmonic approximation approach*", Academic Press New York, (1971).

21 Kleinman D.A.; Spitzer W.G.; *Phys. Rev.,* **125,** 16, (1962).

22 de Man A.J.M.; Ph.D. Thesis, Eindenhoven Univesity, Holland. (1992).

23 Mieiznikowski A.; Hanuja J.; *Zeolites,* **7,** 249, (1987).

24 Houser B.; Alberding N.; Ingalls R.; Crozier E.D.; *Phys. Rev. B.*; **37**, 6513, (1988).

25 Gabelica Z.; Guth J.L.; "*Zeolites: Facts, Figures, Future*", eds P.A. Jacobs; R.A. van Santen, Elsevier (1989).

26 Tuilier M.H.; Lopez A.; Guth J.L; Kessler H.; *Zeolites*, **11,** 662, (1991).

27 Smith G.S.; Isaacs P.B.; *Acta Cryst* , **17**, 842, (1964).

28 de Man A.J.D.; Van Beest B.W.H.; Leslie M.; van Santen R.A.; *J.Phys. Chem.,* **94,** 2524, (1990).

29 Hill V.G.; Chang L.L.Y.; *Am. Mineral.* , **53**, 1744, (1968).

30 Houser B.; Alderding N.; Ingalls R.; Crozier E.D., *Phys. Rev. B.*, **11**, 6513, (1988).

31 Demontis P.; Suffritti G.B.; "Molecular dynamics studies on zeolites.", in "*Modelling of Structure and Reactivity in Zeolites*" ed. Catlow C.R.A., Academic Press, San Diego, (1992).

32 Hernandez E.H.; Ph.D. Thesis, University College, London, (1993).

33 Vessal B.; Leslie M.; Catlow C.R.A.; *Molecular Sim.*; **3,** 123, (1989).

34 Verlet L. *Phys. Rev.*, **159**, 98, (1967).

35 Ewald R.P.; *Ann. Physik.*; **64**, 253, (1921).

36 Allen M.P.; Tildesley D.J.; "*Computer simulation of Liquids*"; Clarendon Press; Oxford; (1987).

Chapter 6.

Docking of Hydrocarbons in Zeolites.

6.1 Multiple Minimum Problem.

Before many of the complex computational techniques such as Molecular Dynamics, MD or *ab-initio* calculations can be applied to investigate the more complex properties of a system, it is necessary to locate a suitable starting configuration, usually the global energy minimum of the system. It is possible to use these computational techniques to locate the position of minimum energy and perform geometry optimisation but usually, the minimum is located by energy minimisation algorithms such as those described in chapter 2.2. At the energy minimum the potential energy has its lowest value on the potential energy surface and is, of course, characterised by a zero gradient of the energy. However, the energy gradient is zero at any extreme, (e.g. a maximum or transition state) although, many of the algorithms can now distinguish between many of the states. In more complicated cases, however, the potential energy surface contains many multiple or local minima as illustrated schematically in figure 6.1.1.

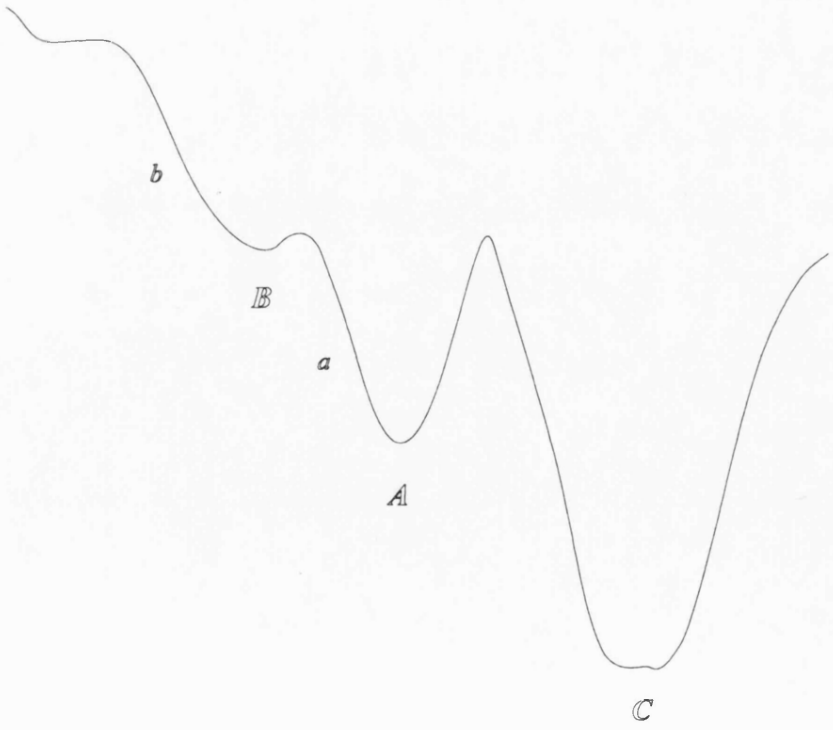

Figure 6.1.1 : A representation of the multiple minimum problem.

Starting at *a* is likely to lead to *A*, while starting at *b* could lead to *B* or *A* depending on the depth of *B* and the convergence criteria and type of algorithm chosen. Yet neither is likely to lead to the global minima *C*. The generation of local rather than global minima is inherent in most procedures. Some possible solutions to the problem of the multiple minima within a molecule have been suggested by the use of Monte Carlo, MC sampling[1] and by novel work of Scheraga *et al*[2,3], who has shown that a peptide can be initially started in a β-helix and minimised to the lower energy α-helix. However, the problem still remains for more complex problems, particularly those involving the "docking" or interaction of two molecules and is most prominent if these two structures are both large and highly flexible. Such complex systems usually include a small, although highly flexible substrate molecule and a large complex macro-structure. Examples include, a target drug molecule and its associated protein receptor or long chain hydrocarbons within microcrystalline solids.

In the following work, I will address this problem with reference to a large range of hydrocarbons absorbed into two different zeolite structures and to the location and description of the different multiple minima within the zeolite as a function of sorbate loading. Both examples use a subtle combination of MD, MC and energy minimisation techniques to tackle docking of small highly flexible substrates into large complex macro-structures. Moreover, the methodology could be applied to many problems of this nature. The work yields the calculated global minima of these systems and could serve as an initial starting configuration for subsequent detailed studies, for example, MD simulations to calculate diffusion constants, for which a low energy starting configuration is preferable.

6.2 Location and Description of C_2-C_8 Hydrocarbons within Zeolites.

6.2.1 Introduction.

Zeolites, alumino-silicate framework structures have been used in industry for separation purposes for a number of years[4] as discussed in chapter 1. Typical examples are found in the selective isomerisation of paraxylene from metaxylene by ZSM-5[5] and in the ASATI and Parex[6] process, which exploits Zeolite X or Y as sorbates in the separation of aromatic C_8 isomers. Yet little is known concerning the detailed behaviour of sorbants in these materials. The present study focuses on the location and sorption energies of a series of n-alkanes (C_1-C_8) and a similar series of n-1-alkenes, within two different zeolite structures, namely Silicalite-I[7] and Chabazite[8]. The zeolite topologies were chosen as representatives of the two possible extremes in topology within the zeolite family; Silicalite-I has two interconnecting straight and sinusoidal channels, whereas Chabazite is a cavity type structure, although in principle any zeolite structure could have been chosen. The framework lattices are assumed to be purely siliceous and rigid; this is a reasonable approximation for these systems because the alkanes are not highly charged and thus, do not incur significant electronic polarisation and therefore extensive structural relaxation of the zeolite framework. This is however in stark contrast to the results presented in chapter 3.1 and 7.1, where extensive structural perturbations are observed around charged defects. By docking the various hydrocarbons into these zeolites, we gain insight into the primary absorption sites and their relative energies for each zeolite of each hydrocarbon within each zeolite, and from such static theoretical calculations a suitable absorbing zeolite may be suggested for specific industrial applications.

6.2.2 Methodology.

This work utilises an approach whereby sorbate species are "docked" into other larger macro-structures, by means of a combination of the Monte-Carlo, MC[9] and Molecular Dynamics, MD[10] techniques. This approach was developed originally for the investigation of the sorption of butene isomers into a purely siliceous Silicalite-I type structure[11]. The procedure is as follows, first, an MD trajectory simulation is performed at a high temperature, (1500K in this simulation), thus generating a library of possible conformations accessible to the absorbing molecule. Such a library of conformations becomes increasingly important for larger more flexible molecules. A Monte Carlo algorithm is subsequently used to insert a randomly chosen conformation into a random position within the zeolite framework. Only those configurations whose energies fall below a user specified energy threshold are accepted for subsequent minimisation. The resulting docked structures are minimised with a Molecular Mechanics forcefield[12], holding the framework rigid. The work presented in this section used the potentials embodied within the CVFF forcefield, as incorporated in the DISCOVER[12] MD code. The procedure can be extended to include framework relaxation[13], but at increased computational cost. The global total energy minimum can be extracted from the sampled conformations and the average energy yields a measure of the host/guest affinity. Figure 6.2.1 illustrates six of the possible configurations sampled by the MC algorithm prior to energy minimisation, for the octane molecule within the Silicalite-I structure. The effect of energy minimisation is to relax the absorbed molecule into the nearest local minima sampled by the MC algorithm; figure 6.2.2 depicts the same six configurations as in figure 6.2.1 but after energy minimisation.

It is possible to describe this methodology by means of a flow diagram as shown in figure 6.2.3; also included on the diagram is one possible extension to the methodology which has been used in section 6.3 of this thesis to investigate sorbate loading.

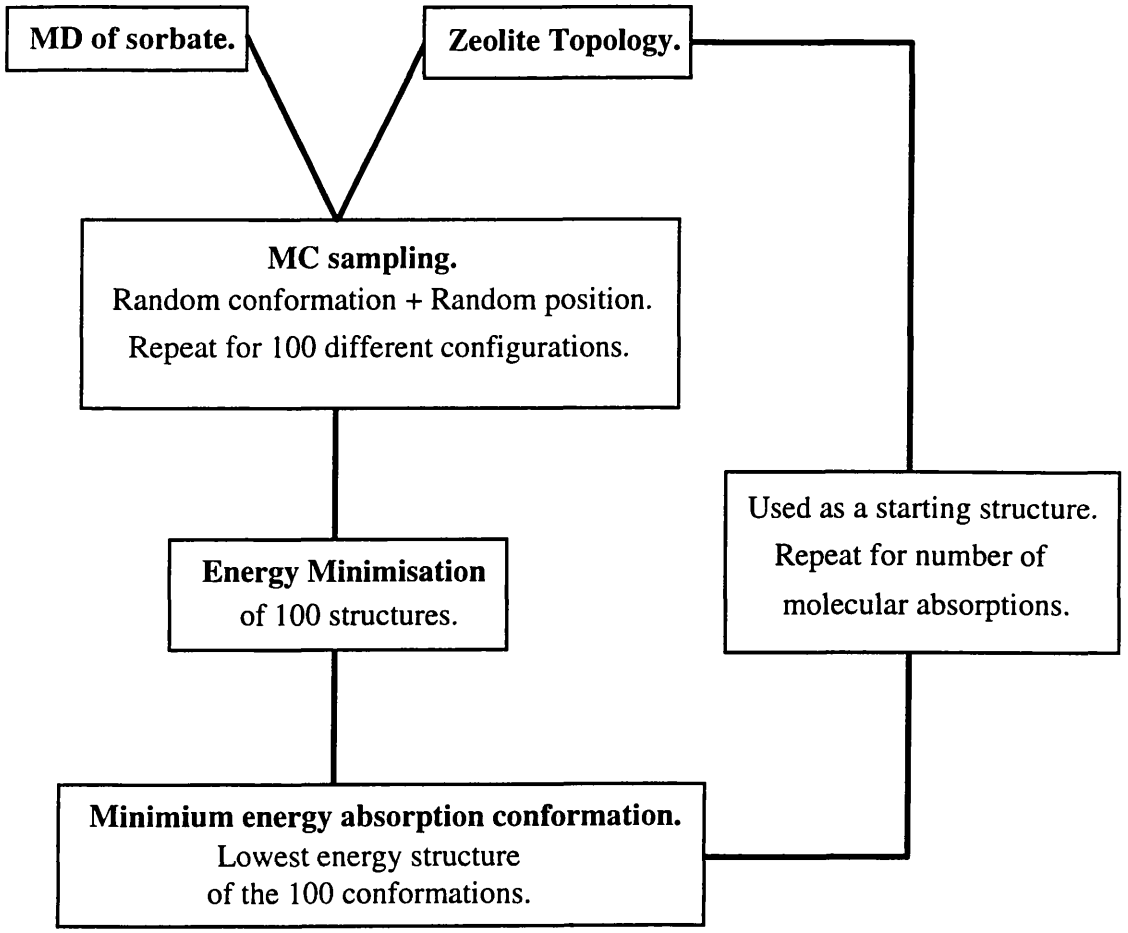

Figure 6.2.3 : A flow diagram representation of the "Docker" methodology.

Figure 6.2.1 : Six of the possible configurations for the octane molecule within the Silicalite-I structure. These were sampled by the MC algorithm, **prior** to energy minimisation.

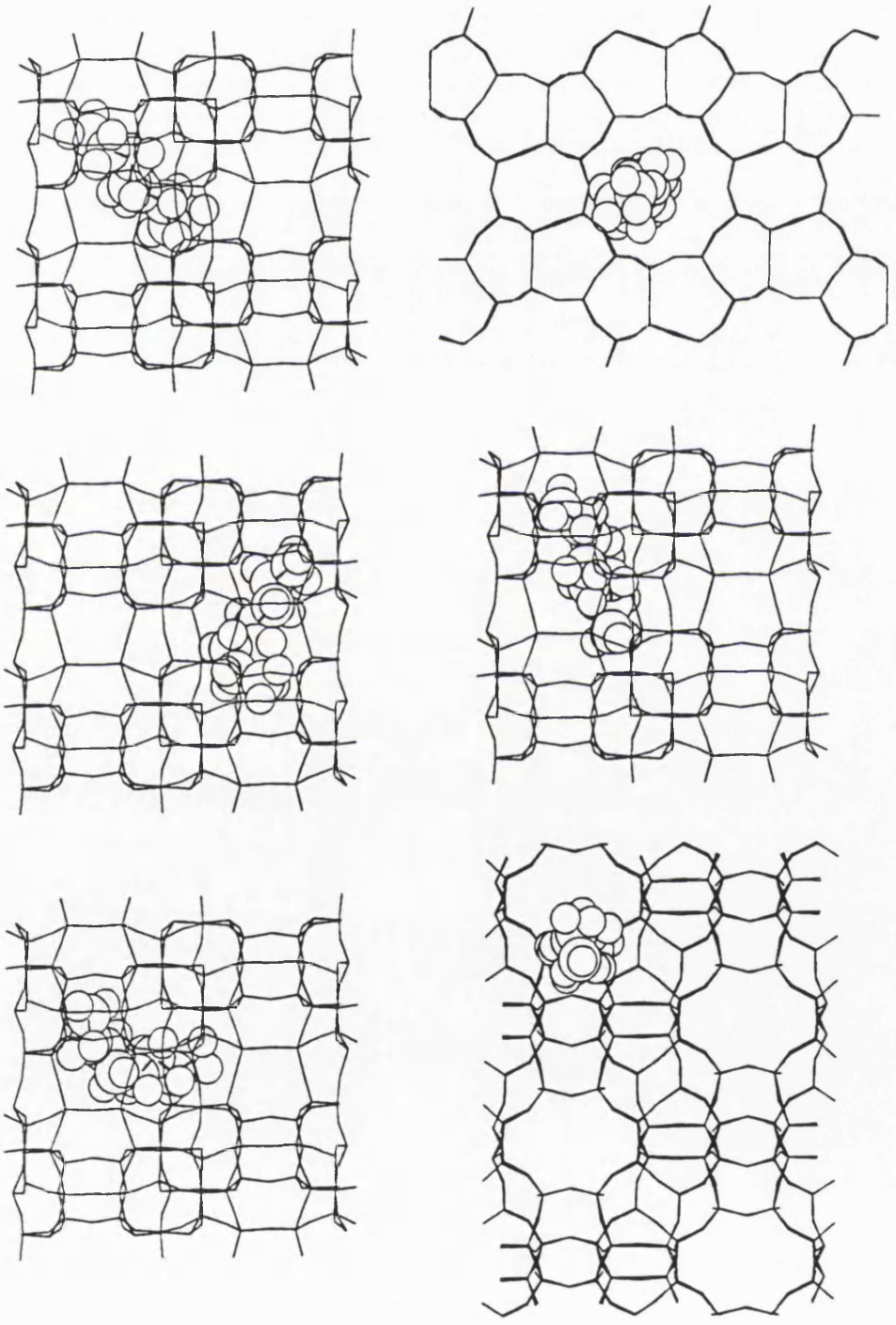

Figure 6.2.2 : Shows the same configurations as figure 6.2.1, but after energy minimisation.

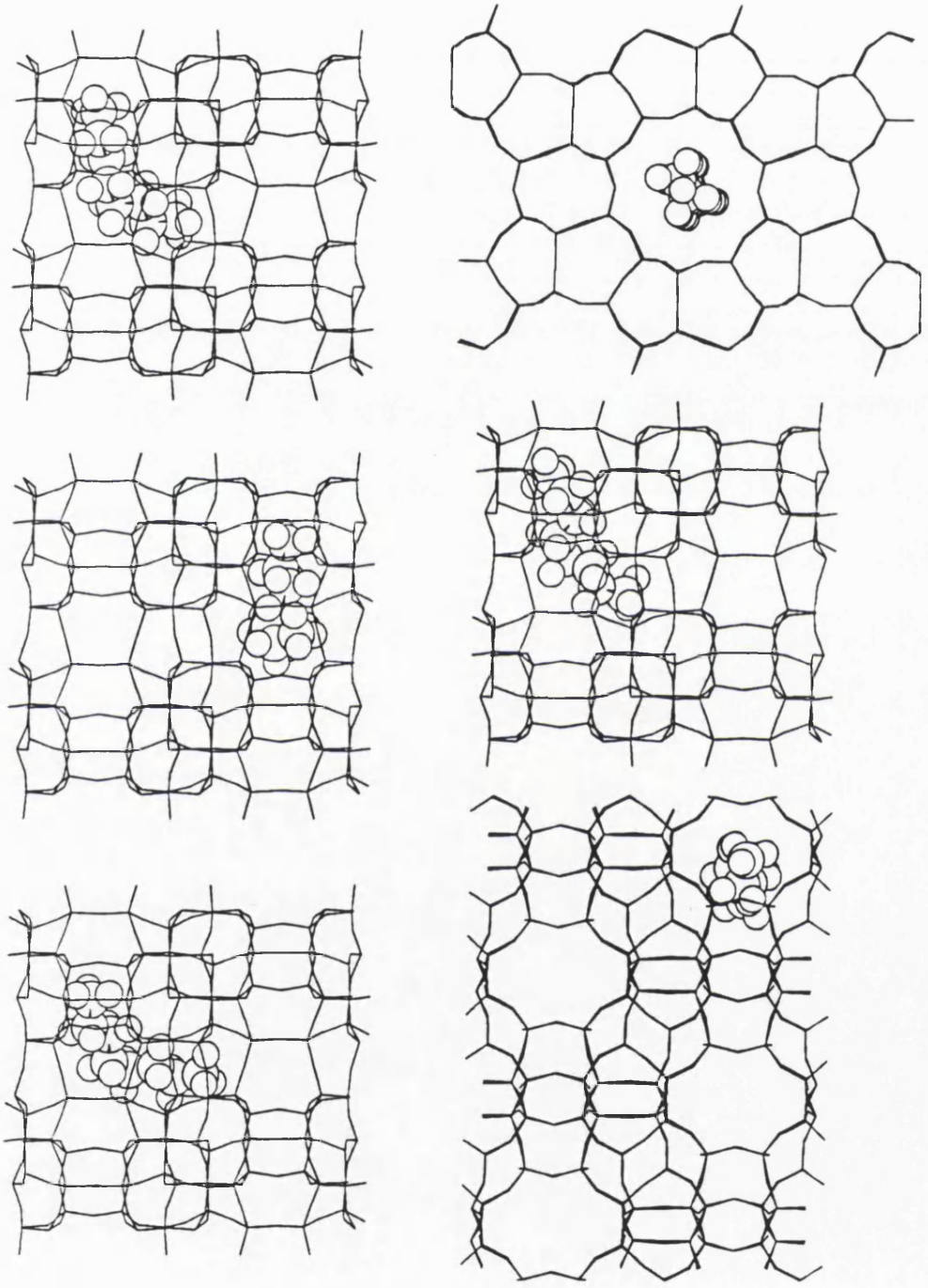

6.2.3 Results and Discussion.

The docking procedure was performed for both the alkanes and alkenes in each of the purely siliceous zeolite structures. Table 6.2.1 reports the global energy minimum for each possible combination of hydrocarbon and zeolite. The average energy of the lowest 20 configurations sampled is also reported. This average value coupled with information relating to the standard deviation of the lowest 20 minima, can give insight into the nature of the potential energy hypersurface for absorption. Indeed, the standard deviation may give an indication of the ease of diffusion in the system, as large deviations indicate a large spread of minima which may aid diffusion. Although, it must be stressed that to obtain a better understanding of the diffusion process, we require more detailed simulations such as the MD work of Hernandez[14] combined where possible with experimental studies such as that undertaken by Rees *et al*[15].

Figure 6.2.4(a,b) shows that there exists an approximately linear relationship between the absorption energy and the number of carbons in the sorbed hydrocarbon. Thus by fitting a straight line and calculating the gradient, an estimate can be made of the relative absorption energy per additional methylene group, table 6.2.2.

Table 6.2.2 : The relative absorption energy per methylene group with topology.

Energies in Kcal per methylene group.

		Silicalite-I		Chabazite.
n-Alkane		-2.65		-1.66
n-1-Alkene		-2.67		-1.79

Table 6.2.1 : Sorption energies (Kcal/mol.) of C_2-C_8 alkanes and alkenes in Silicalite-I and Chabazite.

Carbon Chain Length.	Alkane Minimum Energy in Silicalite-I	Alkane Minimum Energy in Chabazite.
2	-10.644	-8.864
3	-15.068	-12.268
4	-18.529	-15.489
5	-21.966	-16.966
6	-25.460	-20.310
7	-30.007	-22.807
8	-32.211	-24.611
Carbon Chain Length.	Alkane Average Energy in Silicalite-I	Alkane Average Energy in Chabazite.
2	-10.535	-8.595
3	-15.998	-13.268
4	-19.121	-16.381
5	-22.633	-17.553
6	-26.106	-17.596
7	-28.409	-23.189
8	-32.288	-22.948
Carbon Chain Length.	Alkene Minimum Energy in Silicalite-I.	Alkene Minimum Energy in Chabazite.
2	-12.554	-10.254
3	-15.438	-12.488
4	-19.449	-16.049
5	-22.546	-17.286
6	-26.720	-21.620
7	-29.737	-23.307
8	-34.641	-26.991
Carbon Chain Length.	Alkene Average Energy in Silicalite-I.	Alkene Average Energy in Chabazite.
2	-12.525	-10.165
3	-16.218	-13.468
4	-20.391	-16.741
5	-23.073	-18.493
6	-26.766	-21.956
7	-29.309	-22.809
8	-34.648	-24.338

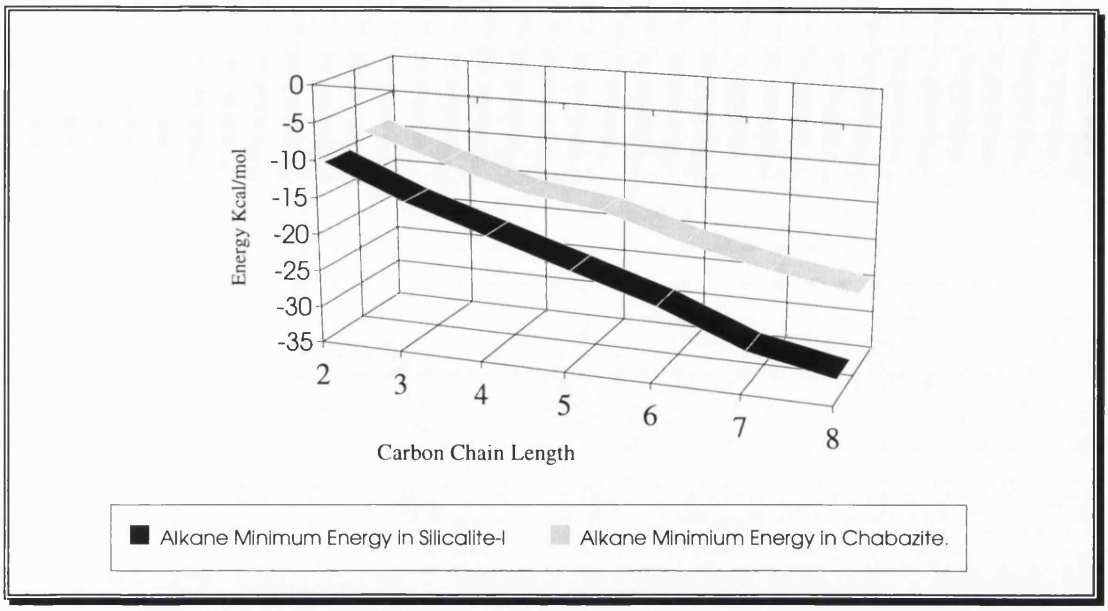

Figure 6.2.4a : Plot of the lowest absorption energy for the alkane series in both Chabazite and Silicalite-I.

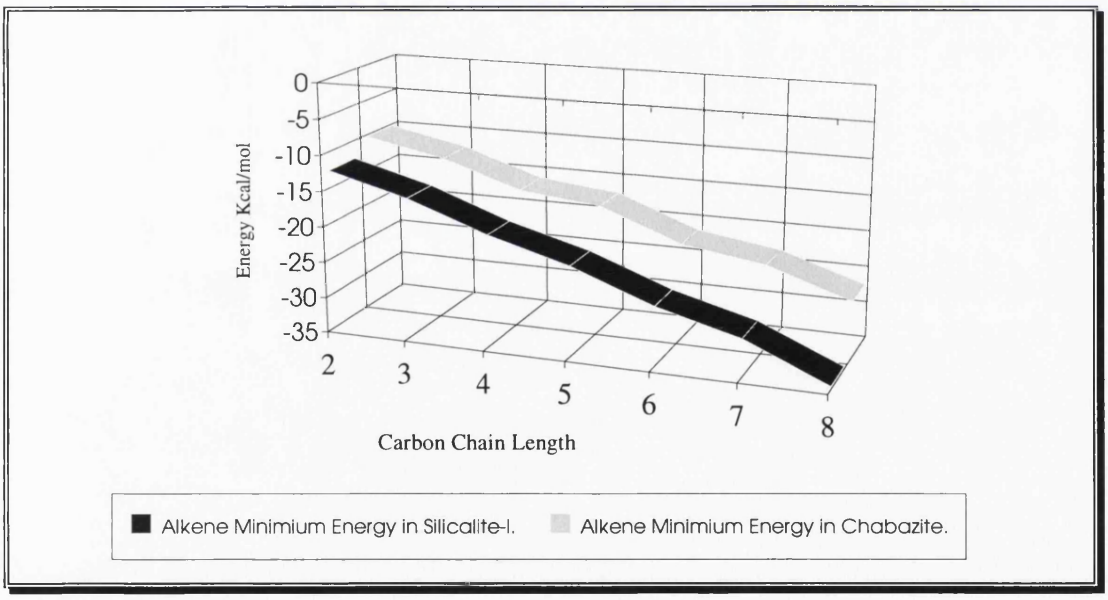

Figure 6.2.4b : As for 6.2.4a but relating to the n-1-alkene absorption.

In the plot of the absorption energy, the hydrocarbon, either an alkane or alkene, is more favoured in the Silicalite-I than in the Chabazite structure. Therefore on the basis of these results, the interconnecting channel topology of Silicalite-I would seem to be more suitable to the absorption of hydrocarbons than the cavity topology of Chabazite.

The conformation of these global minima can be immediately obtained from the data and if one considers the conformation corresponding to the global minimum, for example, the octane molecule in Silicalite-I, compared with that for octane in Chabazite, the difference is evident, as in figure 6.2.5. The n-octane molecule in Silicalite-I resides in the centre of the straight channel, preferring to avoid the open cavities corresponding to the channel intersection, although these positions are sampled. Figure 6.2.2 depicts an octane molecule in the sinusoidal channel, the channel intersection and then the straight channel. However, the n-octane molecule within Chabazite, which is a cavity type topology and has no such channels, is forced to hug the walls and can be described as being "curled up", due to the restricted dimensions of the cavity. If this study was extended to include longer alkanes, this curling up would be increased to such a point that the molecule would have to cross cavities, thus incurring an associated energy penalty because of excessive non bonding interactions. Figure 6.2.6(a,b) shows plots of the lowest absorption energy versus chain length but grouped by framework structure. As can be seen, neither of the structures can be envisaged as effective sieves for the separation of n-alkanes from 1-n-alkenes.

Figure 6.2.5a : The minimum energy configuration of octane in Silicalite-I.

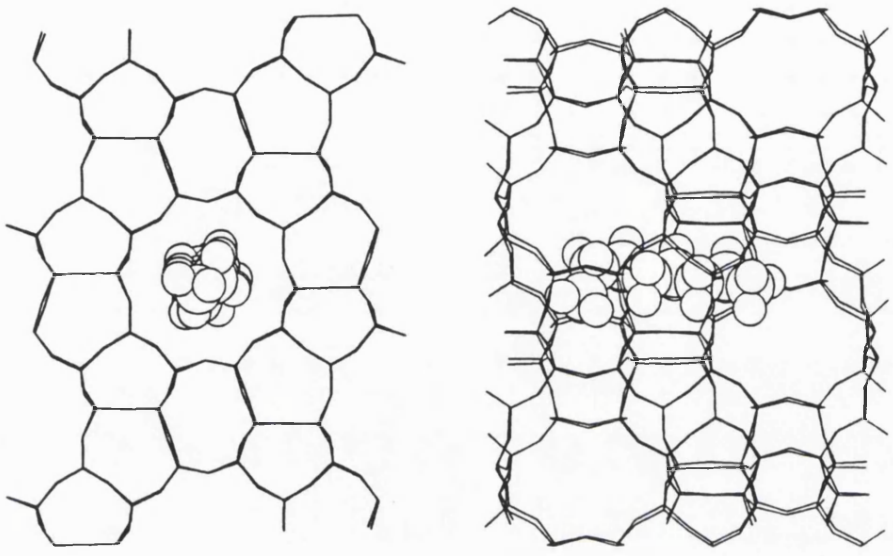

Figure 6.2.5b : The minimum energy configuration of octane in Chabazite.

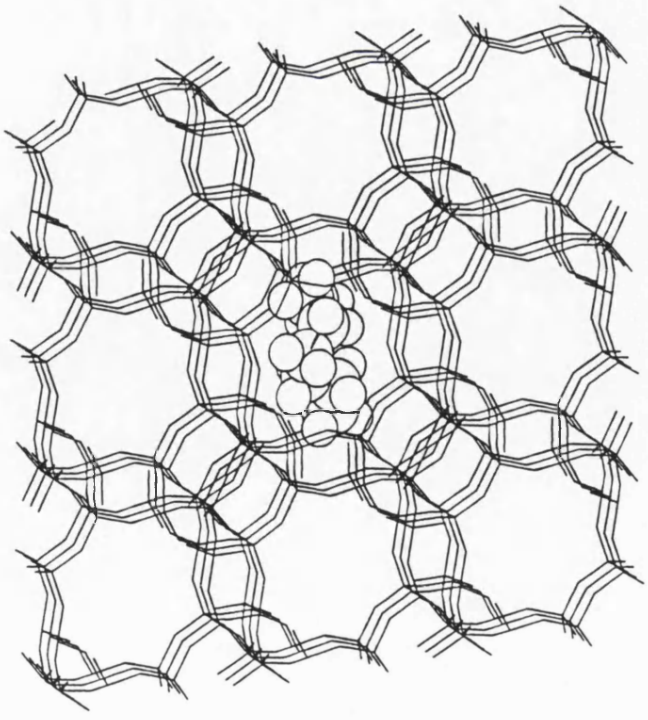

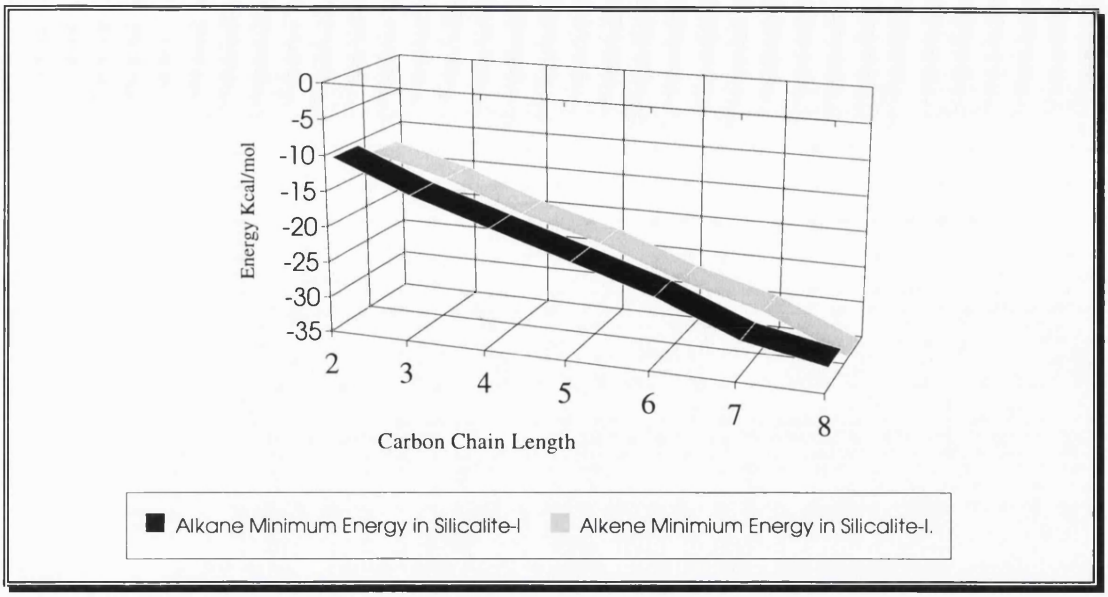

Figure 6.2.6a : Lowest absorption energy for hydrocarbon absorption in Silicalite-I.

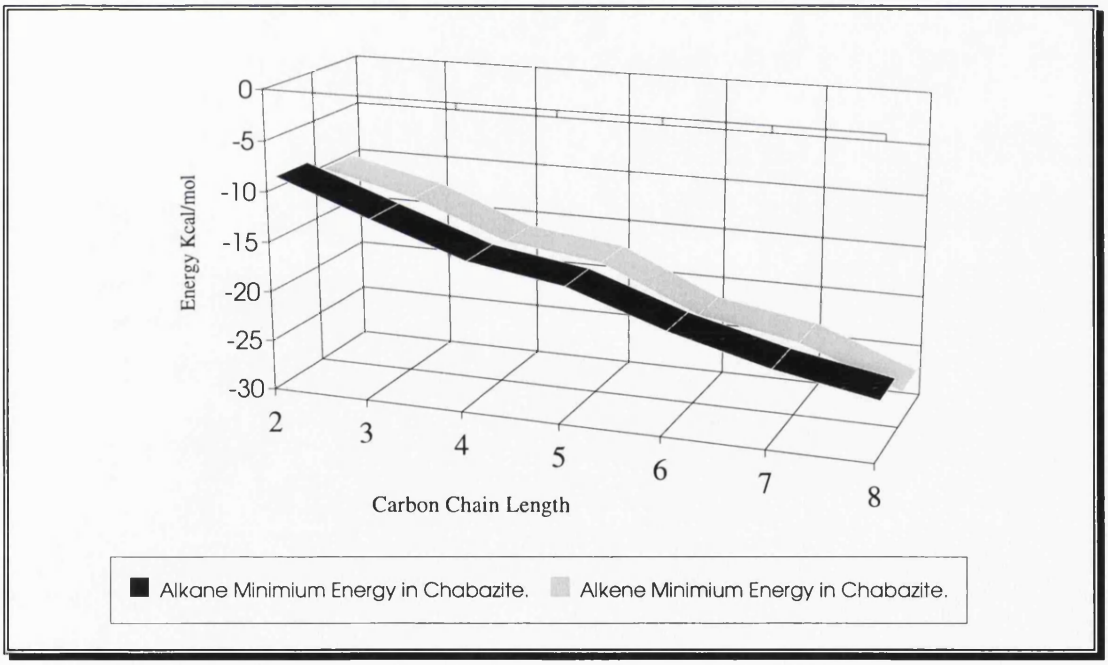

Figure 6.2.6b : Lowest absorption energy for hydrocarbon absorption in Chabazite.

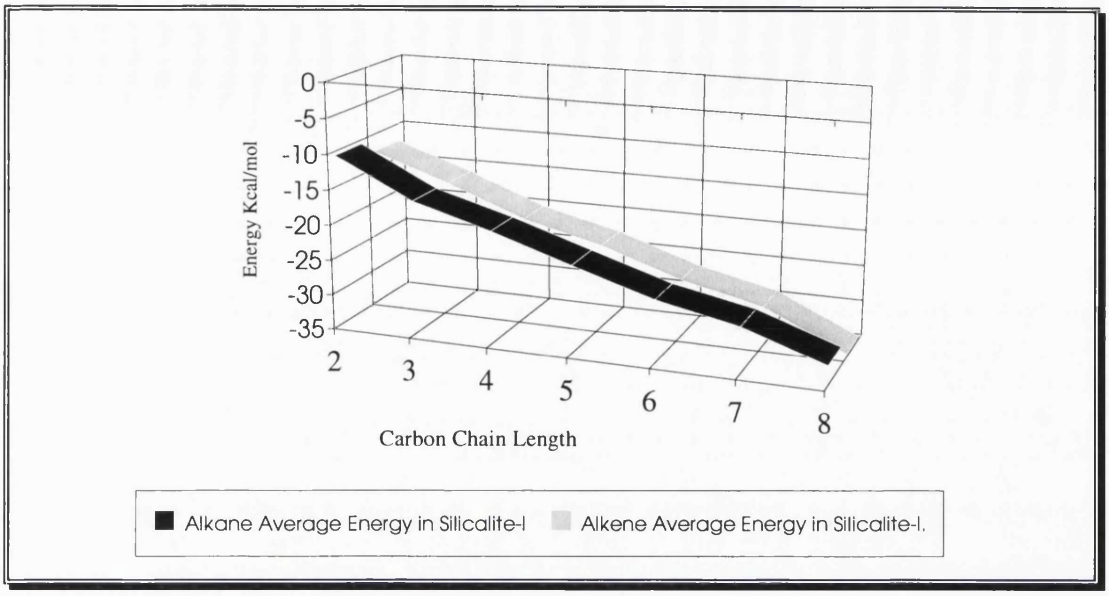

Figure 6.2.7a : The average energy of the lowest 20 minima versus chain length for hydrocarbons in Silicalite-I.

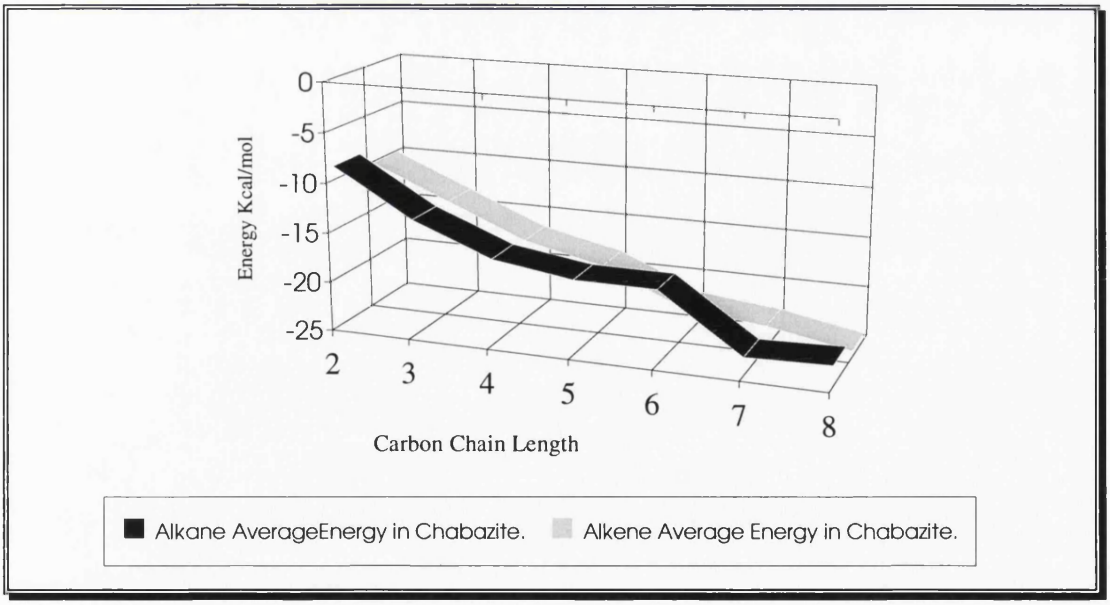

Figure 6.2.7b : The average energy of the lowest 20 minima versus chain length for hydrocarbons in Chabazite.

In addition to minimum energies, we can calculate the average energies of the accepted minimised configurations which are illustrated in figure 6.2.7 for the Silicalite-I structure. We note that there is little difference between alkanes and alkenes which could probably not be effectively separated. Whereas, for the Chabazite structure (figure 6.2.7b), we find similar relative absorption values up to pentane, but differences are observed between odd or even chain lengths in the alkene series. The hexane and octane systems show a higher average absorption energy than those corresponding to alkenes or even heptene. We suggest therefore that the Chabazite structure could be used to separate longer chain even alkenes from alkanes. This proposal is reinforced by the standard deviation in the average absorption energies, table 6.2.3, as the higher the value the larger the spread of minima which could aid in the diffusion process.

Hydrocarbon.	Standard Deviation.
Hexane	6.568
1-Hexene	0.424
Heptane	0.667
1-Heptene	0.751
Octane	1.687
1-Octene	1.678

Table 6.2.3 : The standard deviation of the energies for the longer chain hydrocarbons within Chabazite.

From our calculations, it is clear that the process of absorption, docking or targeting of a substrate with a host can also vary the conformational properties of the sorbant. Indeed, the energy obtained from guest-host binding can overcome the energy barriers found in the isolated molecule for the interconversion between the local multiple minima. From figure 6.2.3, the range of conformations of the hydrocarbon within a zeolite are numerous. Figure 6.2.8 is a representation of the conformation of the octane molecule in both an isolated state and an absorbed state within each

structure. As is clearly evident the absorbed molecular conformations are radically different from the isolated configuration. The octane molecule in Silicalite-I is in an almost *trans*-conformation, yet the isolated molecule has a proportion of *gauche* bonds, whereas in Chabazite the absorbed molecule is more distorted than in the above two cases. One can analyse the absorbed molecular conformation on such a basis but an alternative approach is to calculate the intramolecular energy, which may be compared with that of the isolated molecule. The molecular energy can be broken down into constituent parts as defined by the molecular mechanics forcefield. Thus energies relating to bond lengths, angles and torsional angle deviations are obtained. Table 6.2.4 reports the internal energies of the molecule in the lowest absorption energy conformation in both structures and in the isolated minimum conformation.

Molecule	*Isolated Conformation.*			*Chabazite Conformation.*			*Silicalite-I Conformation.*		
	Bond	*Angle*	*Torsion.*	*Bond*	*Angle*	*Torsion.*	*Bond*	*Angle*	*Torsion.*
Ethane	0.0006	0.238	0	0.0008	0.239	0.006	0.001	0.239	0.0001
Propane	0.0306	0.360	0.0127	0.037	0.372	0.014	0.029	0.384	0.014
Butane	0.0990	0.475	0.025	0.094	0.487	0.069	0.092	0.483	0.026
Pentane	0.1766	0.574	0.038	0.174	0.563	0.048	0.127	0.519	0.074
Hexane	0.3111	1.201	0.212	0.327	1.251	0.245	0.258	0.757	0.053
Heptane	0.3992	1.320	0.231	0.398	1.878	0.336	0.287	0.803	0.093
Octane	0.539	1.972	0.421	0.618	4.294	1.171	0.414	1.42	0.33
Ethene	0.0003	0.0421	0	0.0006	0.051	0.001	0.001	0.053	0.00016
Propene	0.0196	0.281	1.266	0.0244	0.305	1.193	0.023	0.361	1.159
Butene	0.096	0.464	1.274	0.0987	0.484	1.167	0.087	0.555	1.209
Pentene	0.178	0.562	1.284	0.1205	0.508	1.218	0.176	0.674	1.196
Hexene	0.315	1.189	1.692	0.258	0.698	1.23	0.202	0.641	1.251
Heptene	0.404	1.304	1.715	0.274	0.781	1.287	0.259	0.839	1.286
Octene	0.543	1.959	1.838	0.665	2.739	1.724	0.402	0.967	1.336

Table 6.2.4 : The intramolecular energies, (Kcal/mol), of the molecular conformation in the isolated and absorbed hydrocarbon conformations.

Figure 6.2.8 : The conformations of octane absorbed in Chabazite, Silicalite-I and for the isolated molecule.

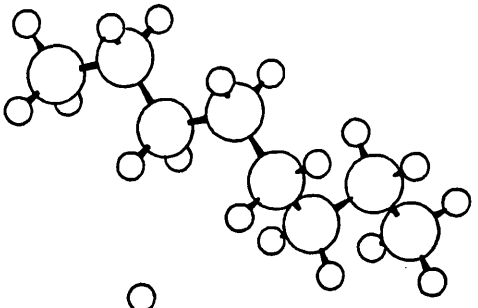

Isolated Octane molecule.

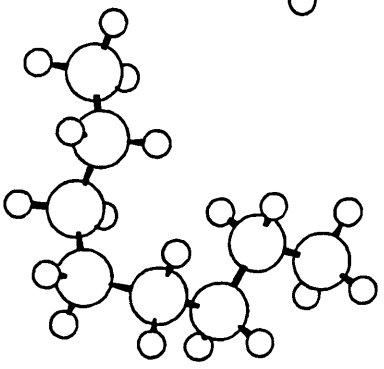

Octane molecule absorbed into Chabazite.

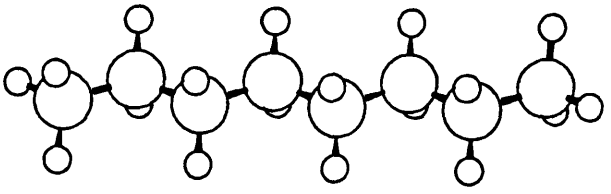

Octane molecule absorbed into Silicalite-I.

For the n-alkane series absorbed into the various structures, there is little change in the contribution to the intramolecular energy from the deviation of the bond lengths, although the contribution is slightly lower when the molecule is absorbed into Silicalite-I. For example heptane has an energy in Silicalite-I of 0.2866 Kcal/mol, as compared to the value for the isolated conformation of 0.3996 Kcal/mol and for the molecule when absorbed in Chabazite of 0.394 Kcal/mol. The effects are far larger when the bond angle and torsional contributions are considered. For alkane absorption, the lower length chains show little deviation in the energy contribution from that of the isolated molecule, which can be understood in terms of the fewer internal degrees of freedom, especially in the torsional variations. Yet this rapidly changes with chain length. Thus for Chabazite, which has a cavity of fixed dimensions in all three directions, the longer alkanes are much harder to accommodate and the internal strain increases dramatically: 1.972 Kcal/mol for the angle contributions for an isolated molecule of octane, as compared to 4.294 Kcal/mol when absorbed in the Chabazite structure, a change of approximately 200%, while an increase in the order of 300% is calculated for the torsional contribution. The octane molecule when absorbed into the Chabazite structure adopts a structural conformation very different from that found for the isolated molecule. However, for the case of alkanes absorbed into the Silicalite-I structure, little deviation is observed for the shorter chain lengths, as expected. For the longer chains all the internal energy contributions are reduced, (1.42 Kcal/mol for the angle contribution as compared to 1.972Kcal/mol in an isolated octane molecule). This does not mean that the intramolecular energy of the sorbed octane molecule is lower than that for the isolated state, since the energy contributions reported here do not consider cross-terms and non-bonded terms within the molecule. The lowering of these energy contributions is due to the torsional angles adopting values which are closer to equilibrium values used in the forcefield. Chapter 2.1.3 gives a more detailed explanation of forcefield parameterisation.

For 1-n-alkene absorption into Chabazite, a different trend is observed, which could be the an explanation for the variations in the absorption energies. In the lower chain length hydrocarbons more energy is stored in the angles than in the torsion angle, as compared to the isolated molecule, with the effect of the double bond making the molecule less flexible. After 1-n-pentene, the trend is reversed and torsion angles contain more energy than in the angle contribution. This is a consequence of the "curling up" of the molecule. This cross-over may not be responsible for the variations observed in the absorption energies but shows the effects of including a highly flexible molecule within a large macro-structure whose overall dimensions are too small. The deviations observed for 1-n-octene in Chabazite are significantly less than those observed for n-octane absorbed in Chabazite, they are more like n-heptane. This shows that the double bond can be considered as effectively altering the chain length to about a (n-1)-alkane. For 1-n-alkene in Silicalite-I the observations can be rationalised as previously described for the alkanes in Silicalite-I, as the channel topology can extend outward in one direction and thus does not constrain the molecule unnecessarily.

The work presented here, could be extended to include longer alkanes, up to C_{15} and to include framework relaxation, aluminium substitution and acid sites. However, overall this technique is a powerful tool for the problem of docking a highly flexible molecule with a large microporous structures, in a semi-automated way.

6.2.4 Conclusion.

From this investigation of the absorption of alkanes and alkenes into two different zeolite structures, we conclude that the channel and associated pore typology is overall more suited to the absorption of hydrocarbons than the cavity type topology of Chabazite. Calculations pertaining to the possible separation of alkanes from alkenes have proved indecisive for C_1 to C_5 but interesting results have been observed for longer chain lengths. These observations justify more computationally expensive calculations, such as long MD simulations to obtain theoretical diffusion coefficients. The methodology embodied within the "Docker" procedure, described here is an automated way of absorbing highly flexible molecules into large macro-structures and is the ideal springboard for future, more elaborate calculations. Such calculations could allow relaxation around the hydrocarbon and would utilise more sophisticated potentials than the ones used in this study.

This study also serves to emphasise the importance of conformational flexibility and the effect that the topology of the host structure plays in the distortion of the molecular conformation from that predicted for the isolated molecule. Moreover, the energy obtained from guest-host binding can overcome many of the energy barriers needed to interconvert between the multiple minima of the isolated molecule.

6.3 Loading and Location of Methane Molecules within Zeolites.

6.3.1 Introduction.

The location of sorbates within a zeolite is not only dependant on the size and the shape of the sorbate molecule relative to the dimensions of the zeolite pore, but also upon the energies of interaction with other molecules already absorbed. In this study, we examine the spatial and orientational distribution of molecules during the progressive loading of methane into several zeolite type structures, namely Mordenite[16], Silicalite-I and Chabazite. The range of zeolite structures being investigated, reflects not only the variation in structure and pore dimension but also their use and availability within industry. Mordenite has a uni-dimensional type structure; Silicalite-I has the two interconnecting straight and sinusoidal channels, whilst Chabazite has a cavity type structure. This study is different in nature to the MD and MC type simulations performed on the sorbate motions[17] within zeolites to predict the diffusion coefficients, as these simulations have to be performed for relatively long time scales, usually in excess of a 100ps. Whereas, simulations of this nature are much less computationally demanding and hopefully as we shall demonstrate, give a comparatively quick, yet detailed insight into the potential of a zeolitic framework for absorption, which can yield good starting structures, for the subsequent use by these more computationally exact but more demanding techniques.

6.3.2 Methodology.

This work is based on the "docking" methodology reported previously in chapter 6.2.2 of this thesis. Yet it is useful to outline how the methodology has been extended for use as a tool for the investigation on the effect of sorbate loading in zeolites. Indeed, an application such as this, only serves to emphasise the versatility of such a flexible methodology. One fundamental problem is how much of the zeolite structure is required before representation of the basic features of the zeolite is realised i.e. channel intersections, pores and cavities outside the constraints of periodic boundary conditions. For this investigation, it was considered that 1x1x2 unit cells of Silicalite-I was sufficient to represent most other fundamental structural features. For the calculations involving Chabazite, 3x3x3 unit cells were used to form a supercell and 1.5x1.5x3 unit cells for the Mordenite absorption. The use of such supercells has implications when one normalises energies to molecules per unit cell, as some of the topological features are not present in one unit cell or the molecule may sample one minimum in one unit cell and then the same minimum in another. This point will be discussed in detail later. Due to computer time constraints, the work was performed for 17 methane molecules per supercell which was found to be sufficient for the investigation and revealed very subtle effects in the "cluster directing" properties of certain zeolite structures.

6.3.3 Results and Discussion.

Using the methodology outlined in the previous section (6.2.2), 17 methane molecules were successively docked into the various, purely siliceous structures. The results are best represented as plots of the energy of absorption per methane molecule in the appropriate structure. This property could be either for global minimum, found using this technique or from the average energy obtained from the next 20 lowest minima. The corresponding standard deviation can be thought of as giving a qualitative measure of how difficult it was to locate the minimum and the spread of other local minima on the potential energy surface. Figure 6.3.1(a,b,c) reports both the lowest absorption energy and also the average of the next lowest 20 minima for the loading of methane into Mordenite, Chabazite and Silicalite-I respectively. This type of representation uses an incremental adsorption curve and not an average adsorption energy; the previously absorbed molecule plays a rôle in the absorption site of the next molecule, the total absorption energy for a particular methane loading can be considered to be a function of the integral under the curve.

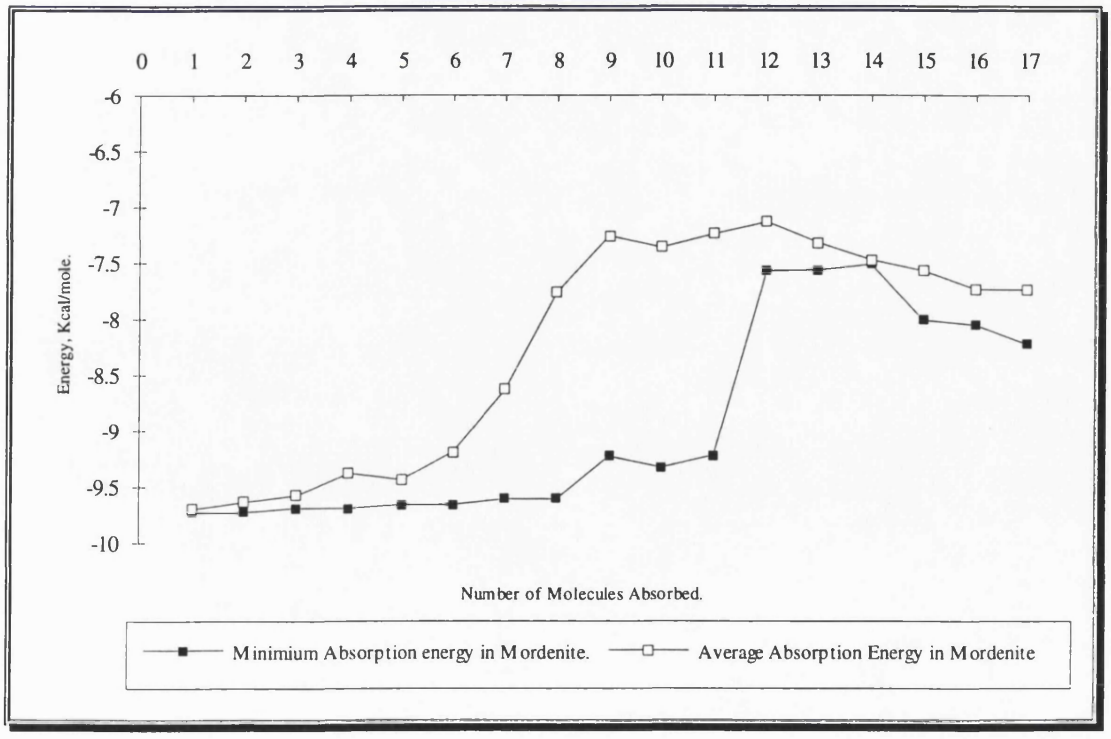

Figure 6.3.1a : Absorption isotherm for methane absorption into Mordenite.

The absorption of methane into the Mordenite type structure, (figure 6.3.1a), shows that the first 8 molecules all absorb with essentially the same relative energy, which implies that they are non-interacting and the addition of the next methane molecule has little or no dependence upon the previous molecule. The molecules reside in distinct minima within the structure. This proposal is supported by the average energy curve as this slowly increases up to a maximum, as it becomes more difficult for the MC algorithm to locate the appropriate global minimum. Yet once the global minimum configuration has been located, it is of a similar energy to the previous one. After the first 8 molecules there is a slight increase in the energy, although the average energy remains constant. This can be explained as the minima now being sampled are the same as the previous ones, except that they are located towards the edge of the finite crystal representation of the zeolite and do not have a lower energy sum because of boundary effects. Upon inspection of the minimum energy configurations of the first 11 members of the series, the mode of methane absorption becomes clear.

Figure 6.3.2 presents a plot of the conformations of subsequent minima found by the methodology for the absorption of 4 methane molecules into Mordenite. The methane molecules are observed to avoid the open channels, preferring to reside within the off-channel pores. The methane molecule is of sufficient molecular dimension to fill these pockets and, as can be seen for one methane molecule, the hydrogen atoms of the methane molecule locate with the framework oxygen ions almost exactly, hence the interaction is highly favourable. After 11 methane molecules have docked, all these off-channel pores are filled; the 12^{th} molecule then has to locate to the next minimum, which can be seen from the energy plot as 1.67 Kcal/mol less favourable, whereas the next two molecules fill approximately the same type of site. Yet once these have been located, the next molecules appear to find sites of lower energy than the previous one. This poses the question as to whether the MC algorithm been sampling correctly. It appears however, that molecules number 12, 13 and 14, act as "cluster directing" agents, resulting in subsequent methane molecules

grouping together in an attempt to lower the total potential energy. This clustering increases the intermolecular interaction with each pair of molecules and not with a predominantly favourable framework interaction. Figure 6.2.3 is a representation of the absorption of molecules 12 to 17 and, as can be clearly seen, the effect of certain molecules is to direct the absorption of subsequent ones to form a cluster and essentially fill the channel.

Figure 6.3.2 : The molecular configuration of 4 methane molecules absorbed into Mordenite.

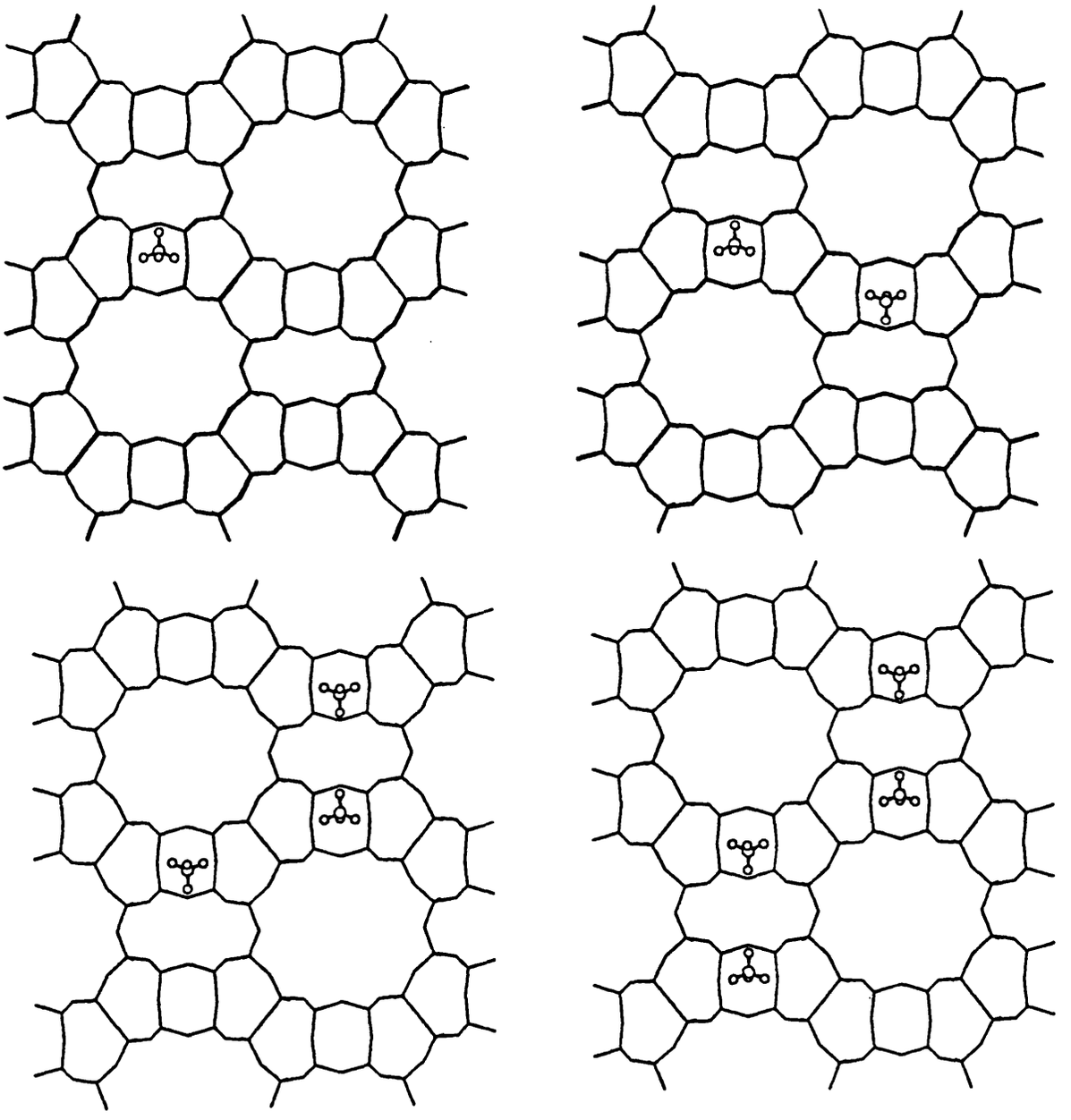

Figure 6.3.3 : Conformation of 12 - 17 methane molecules absorbed into Mordenite.

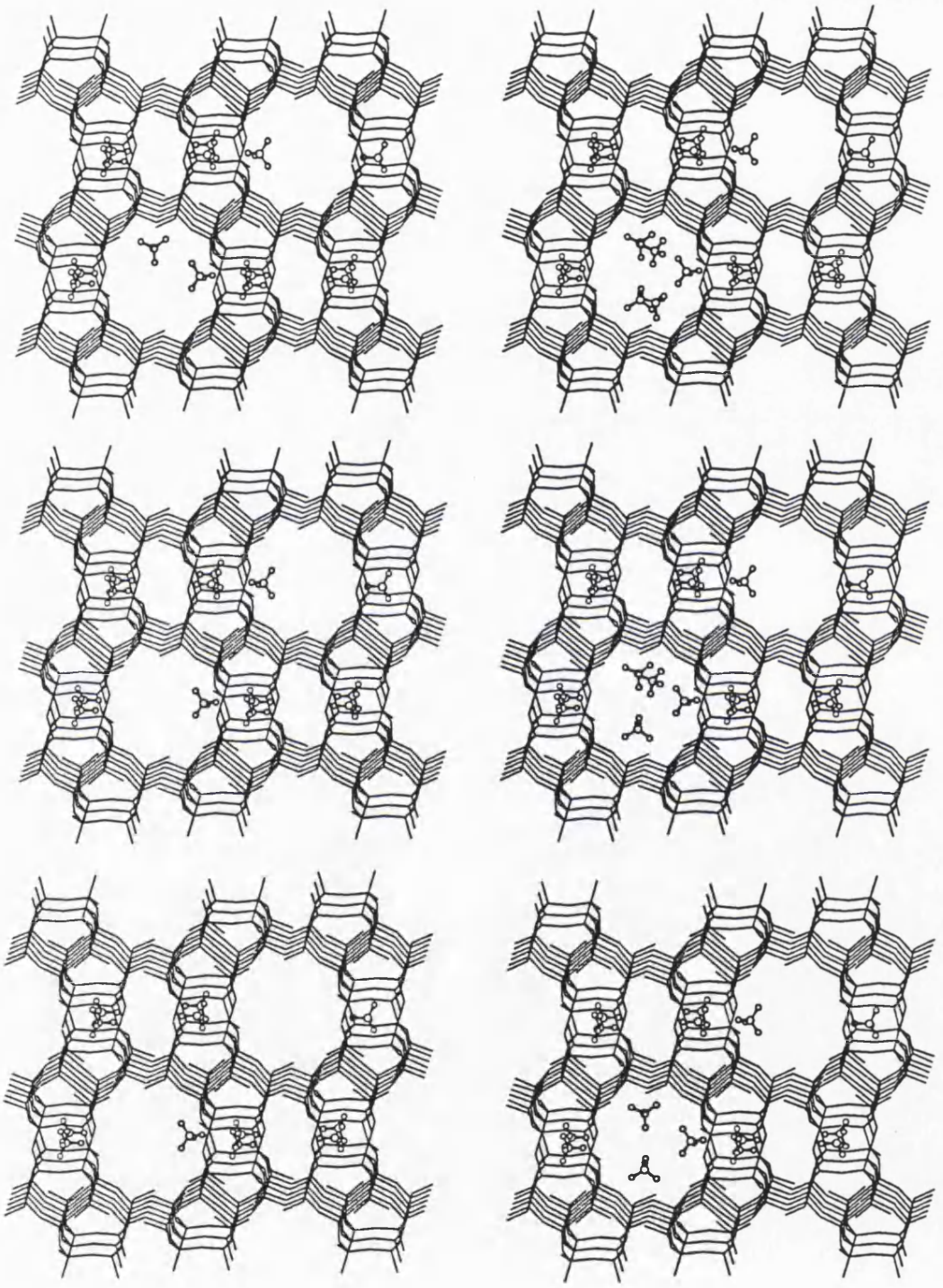

Next, the absorption of methane into a cavity type structure, such as Chabazite, was investigated. We recall that unlike the case of Mordenite, there are no pores in Chabazite which are of methane molecular dimensions. Instead it is composed of relatively large cavities, (although smaller than those in Faujasite[18,19] or VPI5[20]) and therefore, represents a significant alteration from the topology of Mordenite. Figure 6.3.1b, shows both the minimum and average energy of absorption of methane as a function of molecule number. The trends observed are very different from those seen for absorption within the Mordenite structure.

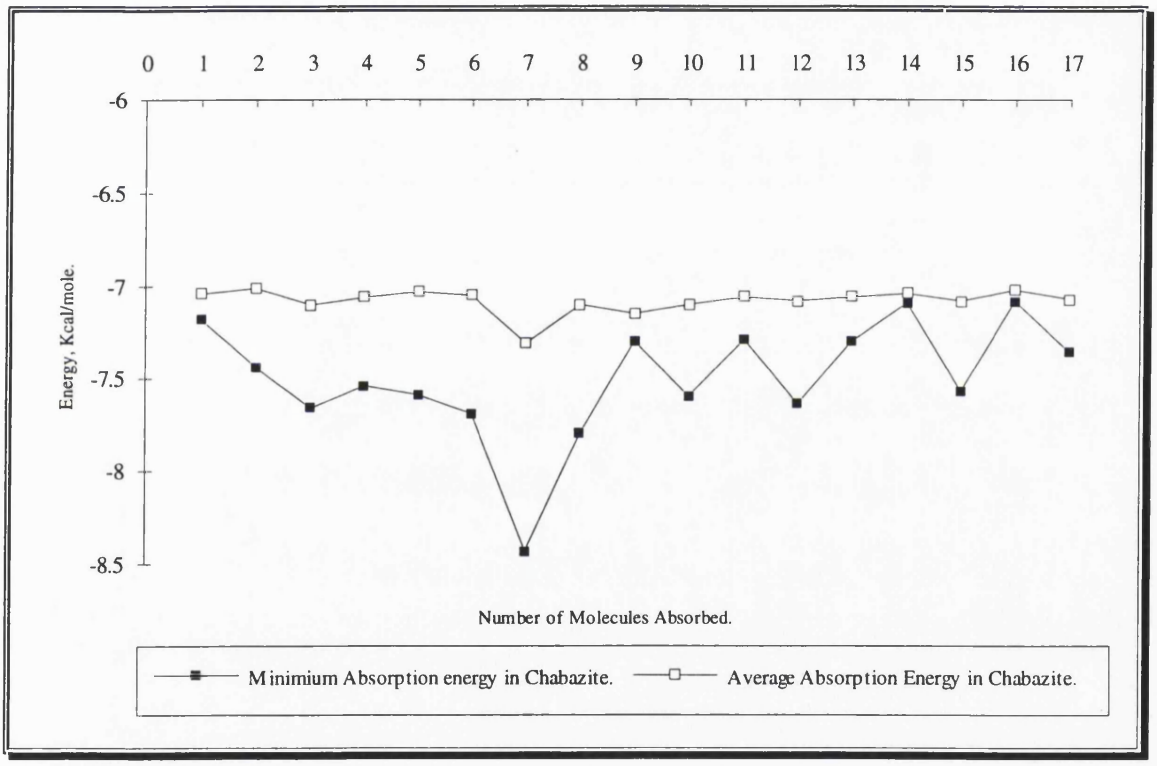

Figure 6.3.1b : Absorption isotherm for methane absorption into Chabazite.

After the initial insertion of one molecule into the structure, the relative absorption energy of the next 2 molecules is more negative. This as we observed for Mordenite, is caused by clustering and is a consequence of the lack of a particularly favourable interaction between the methane molecule and the framework. The first

molecule can be thought of as a cluster directing agent and indeed, it resides on the face of the 8-ring contained within the channel walls of the central cavity. The subsequent two methane molecules orientate themselves within close proximity, approximately 3.8Å, to the first and not as one would intuitively expect residing at the same position but within other cavities. Figure 6.3.4 shows the first three molecules to be absorbed within Chabazite and the clustering effect is clearly observed. Once this cluster has been formed within the central cavity, it directs the next methane to start forming a new cluster, still within the same cavity. The next two molecules reside in places similar to the previous ones. This arrangement of molecules continues until upon the addition of 7 molecules, the cavity is completely full and has started to spill over into the next cavity. Figure 6.3.5 shows seven molecules within the Chabazite structure; all the methane molecules cluster inside the central cavity. The next molecules dock in such a way as to extend these clusters out from the initially formed cluster in a way as to make groups of three. These effects are seen in the calculated energies, (figure 6.3.1b), in the form of alternation of higher energy absorption followed by a lower energy configuration. Each time an additional methane is added, clusters of three are formed; again this process is evident from graphical displays of the structures. Figure 6.3.6 shows conformations of 10 and 12 methane molecules respectively; each addition of 2 molecules forms in such a way as to yield a cluster of 3. This process continues, up to the addition of 17 molecules. Figure 6.3.7 is the final configuration of the Chabazite structure containing 17 methane molecules. This mode of absorption is unique and represents clustering of molecules within certain topologies and it can be clearly observed that once a cavity has been filled, the adjacent cavities are filled by first placing a molecule in the 8-ring window and the next in close proximity to form a cluster and it is the formation of these clusters that allows the sorption to spread throughout the structure. It would be of interest to investigate these systems experimentally using neutron scattering or NMR techniques.

Figure 6.3.4 : The first three methane molecules successively docked into Chabazite.

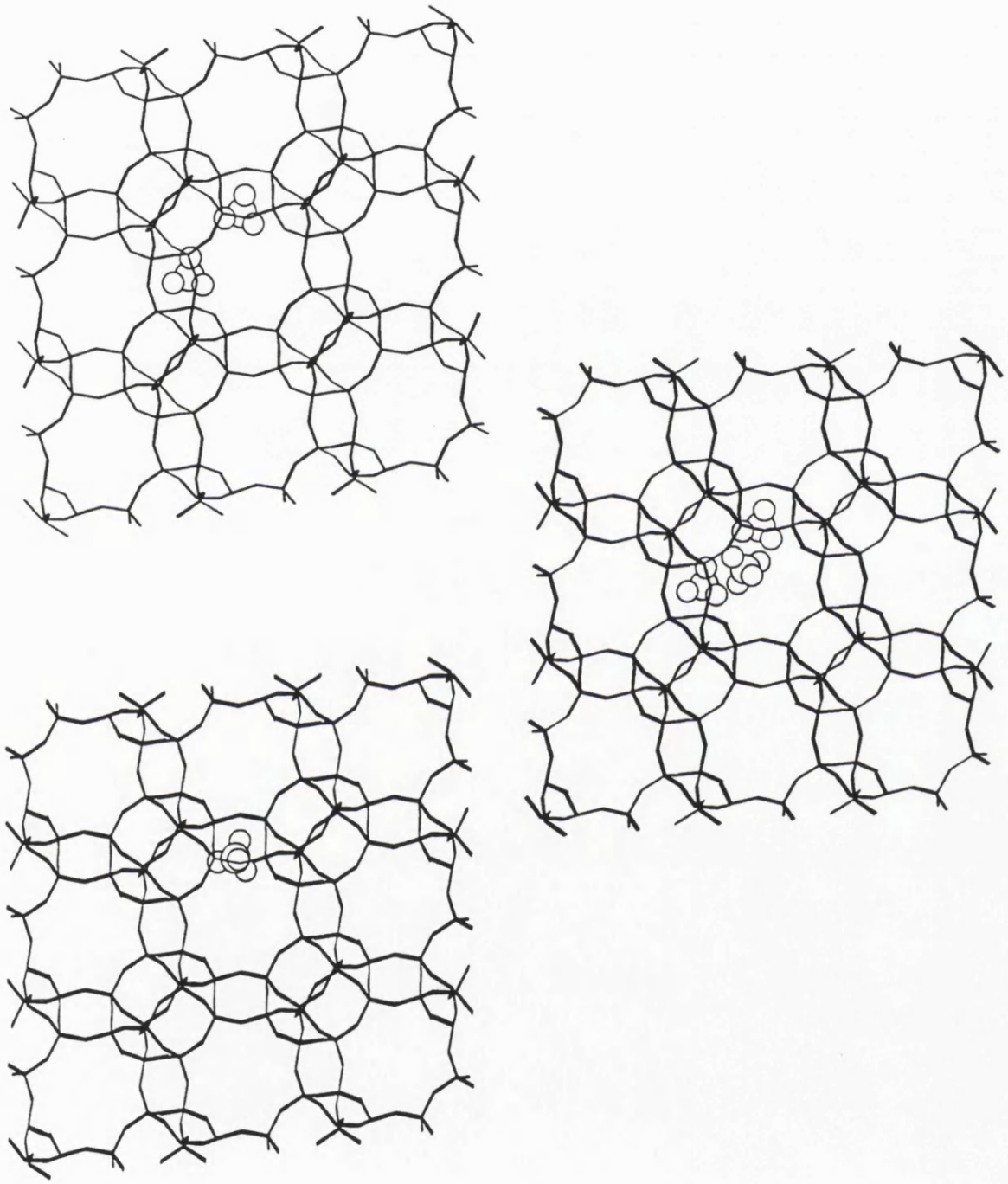

Figure 6.3.5 : The molecular conformation of 7 methane molecules in Chabazite.

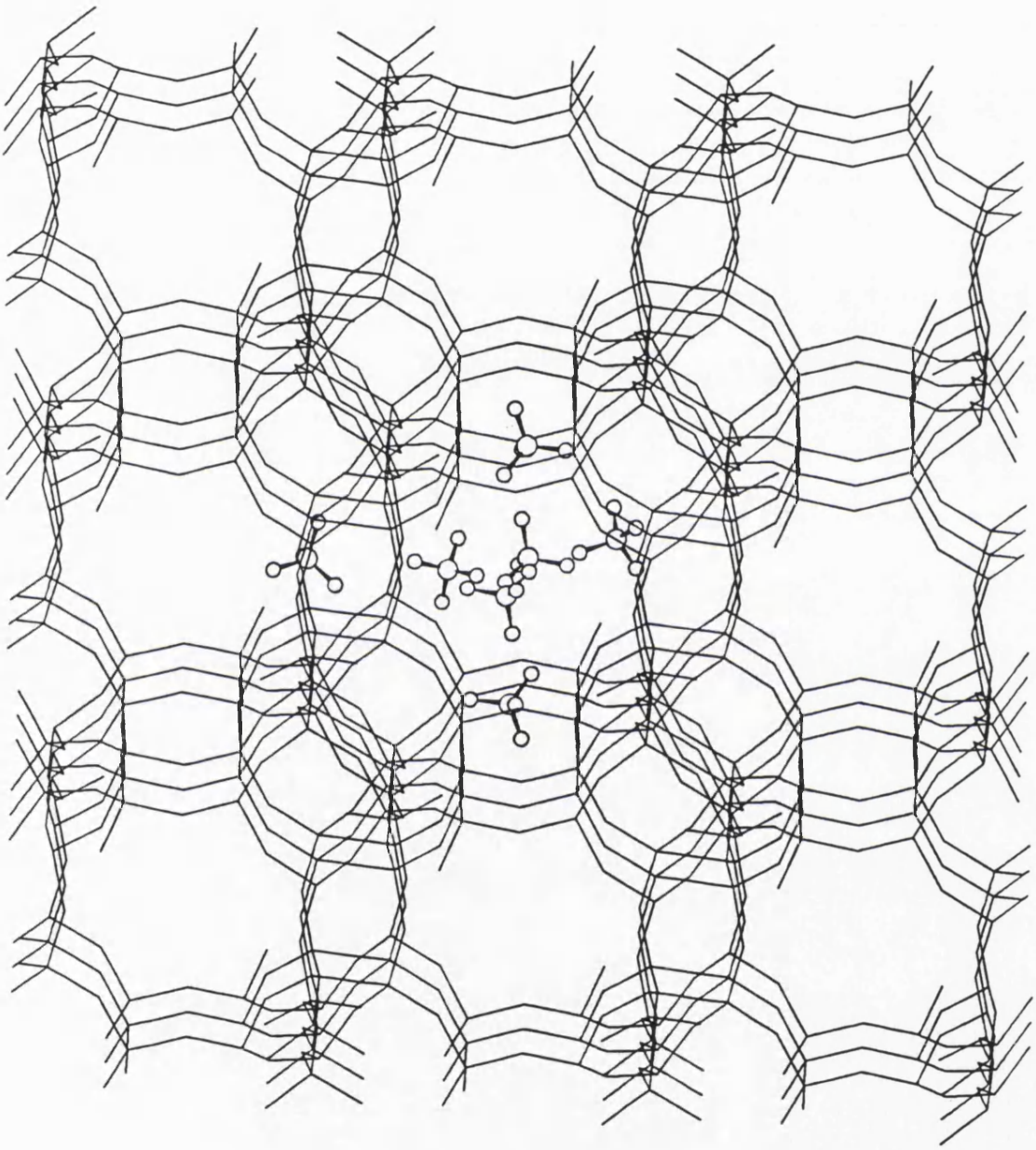

Figure 6.3.6 : The conformation of 10 and 12 molecules in Chabazite.

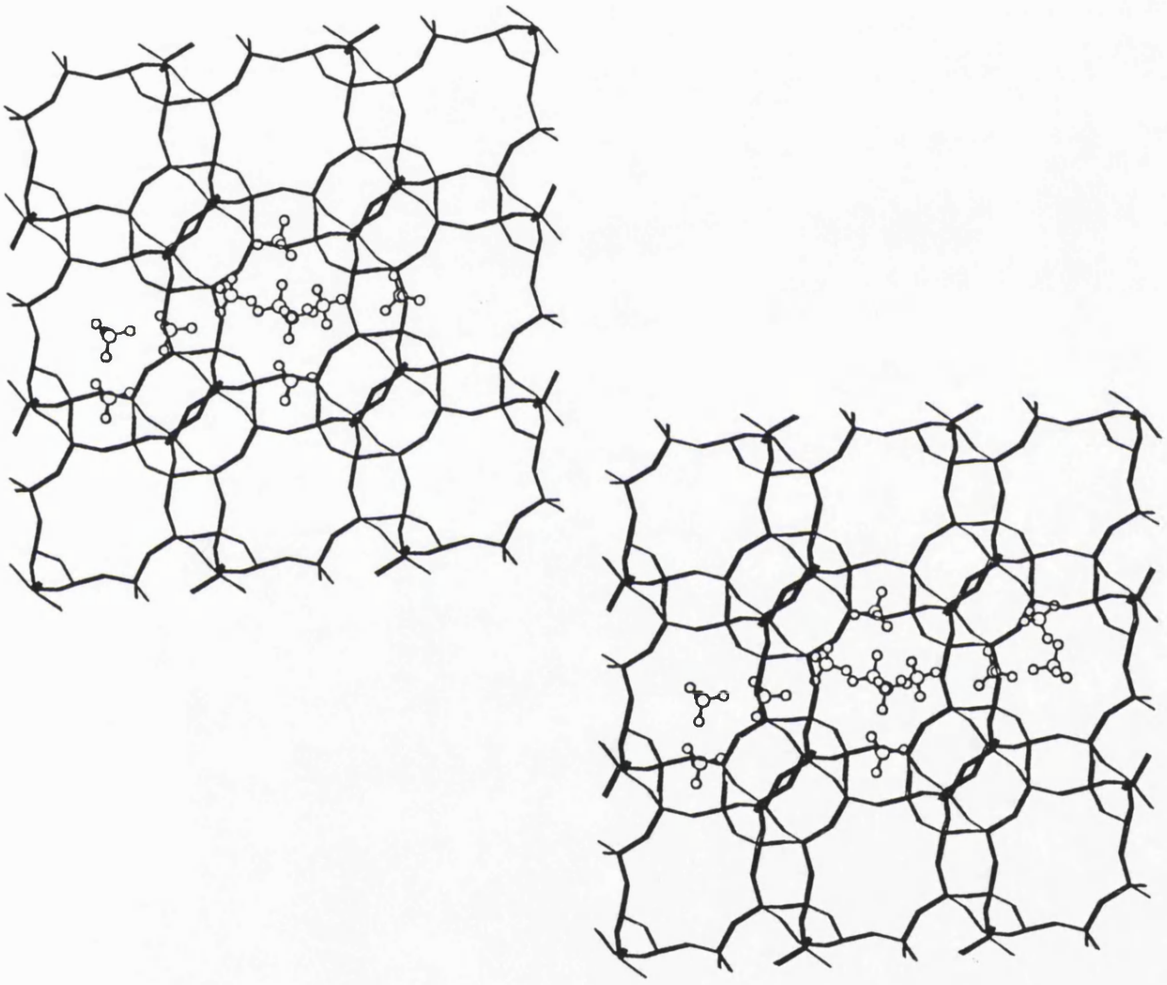

Figure 6.3.7 : The result of 17 methane molecules in the supercell of Chabazite.

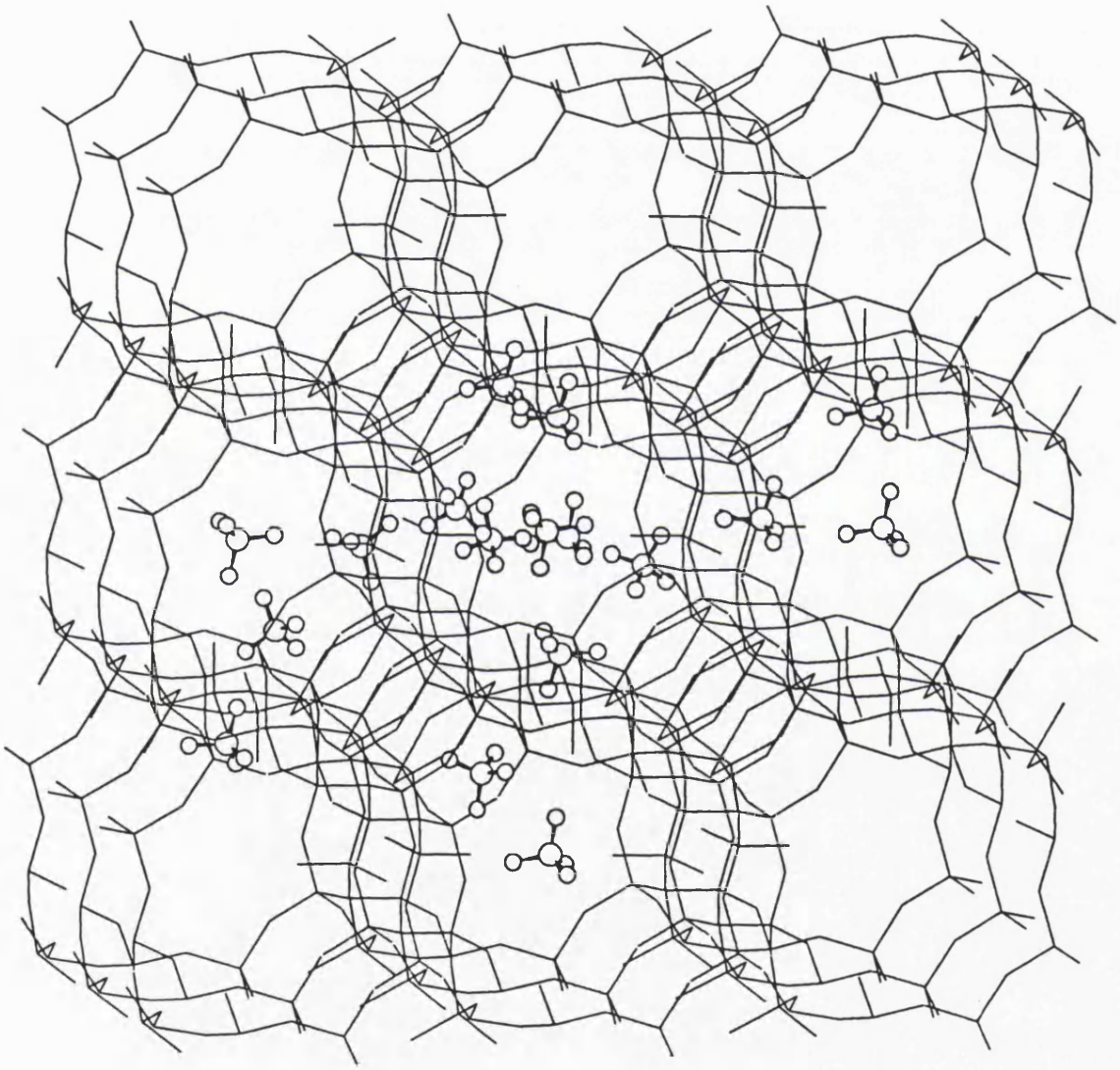

So far the two structures investigated represent extremes of the possible zeolite topologies; an intermediate type structure was thus investigated. The Silicalite-I type structure, provides such an intermediate, containing not only 12-ring straight channels but also 10-ring sinusoidal channels and the associated intersections which can be thought of as representing a cavity like topology. Indeed, many of the simulations in the literature to date, are concerned with the absorption of methane and its associated diffusion inside Silicalite-I. The reasons for this systems popularity are the industrial importance of ZSM-5[21], the alumino-silicate analogue of the purely siliceous Silicalite-I, the intrinsically anisotropic lattice structure, as described above and the lack of extraframework cations within the purely siliceous structure. This system has also been extensively investigated experimentally using Pulsed Field Gradient NMR, PFG NMR[22], which is an important experimental technique as it is a direct probe of intracrystalline self diffusion coefficients. Indeed, good data are available for comparison to MD or MC simulations. However, since this preliminary study involves only energy minimisation, it gives structural rather than dynamic information.

Figure 6.3.1c gives the now familiar plot of the minimum and average absorption energies against the number of absorbed molecules. The average energy is very similar to the minimum energy due to the size of the supercell under consideration, i.e. only two unit cells. The number of possible sites is therefore greatly reduced in comparison to the simulation of Chabazite discussed previously, which used 9 unit cells to represent the cavity structure. Analysis of the figure 6.3.1c, uses many of the ideas previously formulated. The first molecule resides at the minimum, which upon closer inspection is the segment part of the straight channel; the next four methane molecules reside in the channel segments of the sinusoidal channel, which is in good agreement with the MD work of June et al[23], who calculate a 4 - 6 kJ/mol energy penalty for methane located at channel intersections. So far no cluster directing effects have been observed. The next four molecules reside independently in the

straight channel. These are sited very near to the channel intersection but not quite in the intersection. It is only when these sites are filled that cluster directing occurs.

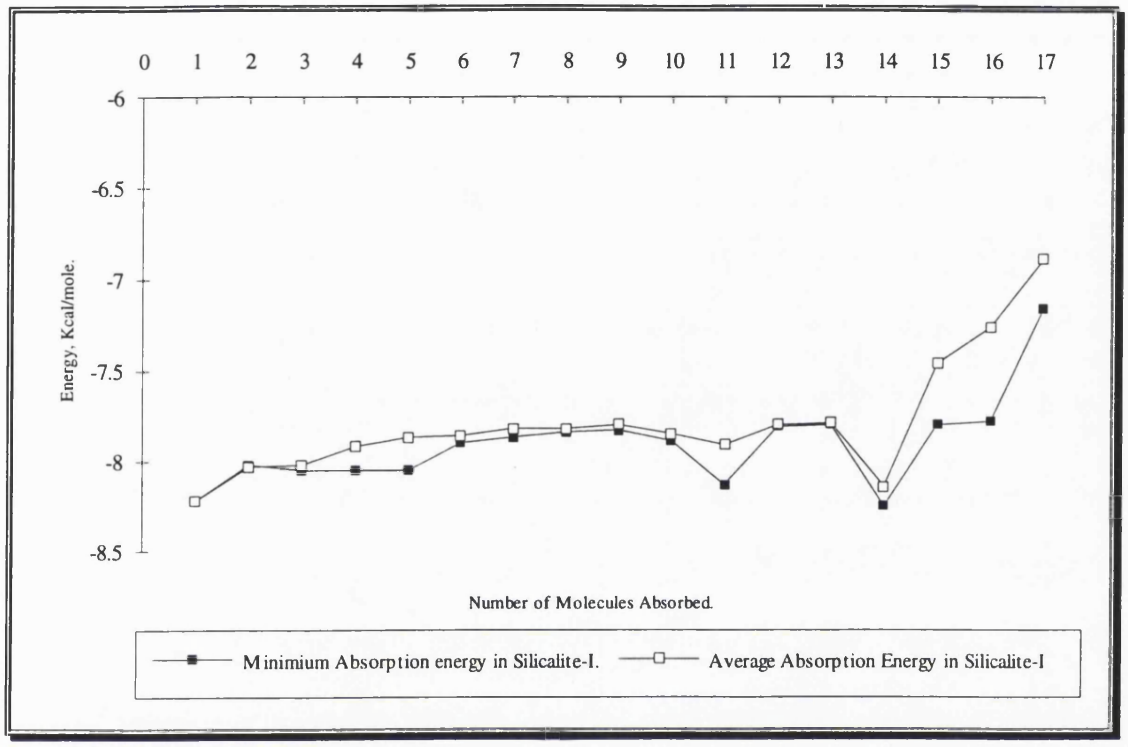

Figure 6.3.1c : Absorption isotherm for methane absorption into Silicalite-I.

When 10 and 11 methane molecules are absorbed the clustering begins, enabling occupation of a channel intersection to occur without the energy penalty referred to above. The latter is greatly reduced by clustering and the increased intramolecular attractions between the methane molecules. This effect continues with the filling of the other channel intersections in a similar manner. Subsequent methane molecules continue to fill these channels, until by 17 absorbed molecules the majority of free sites have been significantly reduced and increasingly molecules are forced to 'look for' different sites.

From the absorption data it is possible to calculate the isosteric heat of absorption at the zero coverage limit. In our simulations this is comparable to the value of absorbing one molecule since there is no interaction with other molecules for this system. 4.11 Kcal mol^{-1} unit $cell^{-1}$ are observed which is in excellent agreement with the values obtained from the much more sophisticated simulations of Goodbody *et al*[24] and is in agreement with 4.83 Kcal/mol determined experimentally[25]. This small difference between calculation and experiment could arise because of the approximation of a rigid and purely siliceous, non-defective lattice used in the simulations. From the work of Goodbody *et al*[24] the diffusion coefficients were calculated along each axis and D_x was seen to decrease more with loading than D_y, whilst the D_z remained approximately constant. These results can be related to the static calculations presented here, as upon successively absorbing methane molecules, the straight channel fills quicker than the sinusoidal or channel cavities. This implies that the rate of diffusion along the x-axis, i.e. straight channel, will decrease with loading in comparison to the sinusoidal channels aligned along the y-axis. A similar approach can be applied to the simulations of the other structures, allowing us to predict at least qualitatively the variation of diffusion coefficients with loading.

For the case of methane in Chabazite, cavity filling and clustering is observed. Thus, one intuitively expects that the diffusion coefficients will be lower, since the methane molecule has a higher activation energy for migration. The likely transport mechanism will involve methane moving between clusters which may not be effective for rapid diffusion. For methane in Mordenite, the diffusion constants are expected to change with concentration, because of the highly favourable interaction with the framework. As the concentration of methane absorbed in Mordenite increases, all the highly favourable absorption sites would be taken and hence the molecule would be forced to occupy the straight channel. Such occupancy of the straight channel at low concentrations and the complete occupancy of the highly favourable minima could lead to rapid diffusion along the channel. Indeed, in a recent study by Stockmeyer[26] hydrogen diffusion in Mordenite was probed by quasi-elastic neutron scattering and a

value of $2x10^{-7}$ m^2s^{-1} was reported which is much larger than expected from macroscopic data[27]. Such a discrepancy has been accounted for by obstacles located approximately every 60Å thus, hindering self-diffusion. This distance being estimated using the angular dependence of the measured elastic scattering intensities. Such speculation requires a detailed computational investigation before a more definitive diffusion mechanism can be proposed.

6.3.4 Conclusion.

The simulations presented in this chapter, have advanced considerably our knowledge of hydrocarbon sorption in the zeolites studied.

The results of the study of methane docking into Silicalite-I show good agreement with both the available experimental and computational data and show the strength of our straightforward methodology. This success also lends credibility to the simulations of methane adsorbed into the Mordenite and Chabazite structures and the conclusions drawn from this work. A novel phenomenon of "cluster directing" has been observed in the latter. This method overcomes absorption at an unfavourable lattice position and is shown clearly by the absorption of methane into Chabazite. Further studies (both theoretical and experimental) of this and relating systems, would clearly be worthwhile.

6.4 References.

1 Metropolis N.; Rosenbluth A.W.; Rosenbluth M.N.; Teller A.H.; Teller E.; *J. Chem. Phys.*, **21**, 1087, (1953).

2 Piela L.; Kostrowicki J.; Scheraga H.A.; *J. Phys. Chem.*; **93**, 3339, (1989).

3 Kostrowicki J.; Piela L.; Scheraga H.A.; *J. Phys. Chem.*; **95**, 4113, (1991).

4 Newsam J.M.; "*Solid State Chemistry Vol 2: Compounds*"; Eds Cheetham A.K.; Day. P.; Oxford University Press; (1990).

5 Chen N.Y.; Gorring R.L.; Ireland H.R.R.; *Oil Gas J.*; **75**, 165, (1977).

6 Ruthven D.M.; "*Principles of Absorption and Adsorption Process*"; Wiley-Interscience, New York, (1984).

7 Flanigen E.M.; Bennett J.; Grose R.W.; Cohen J.P.; Patton R.L.; Kirchner R.M.; Smith J.V.; *Nature*, **271**, 512, (1978).

8 Smith J.V.; Rinaldi R.; Dent-Glasser L.S.; *Acta. Cryst.*, **16**, 45, (1963).

9 Metropolis N.; Ulam S.; *J. Am. Stat. Ass.*; **44**, 335, (1949).

10 Alder B.J.; Wainwright T.E.; *J. Chem. Phys.*; **27**, 1208, (1957).

11 Freeman C.M.; Catlow C.R.A.; Thomas J.M.; Brode S.; *Chem. Phys. Letts.*; **186**, (2,3), (1991).

12 DISCOVER & CVFF90; Biosym Technologies Inc.; 9685 Scranton Rd, San Diego, CA, USA.

13 Shubin A.l Zamaraev K.; Thomas J.M.; Catlow C.R.A.; *Proc. Roy. Soc. A*; Submitted.

14 Hernandez E.; Ph.D. Thesis; University of London, (UCL), England, (1993).

15 Rees L.V.C.; Shen D.; *Zeolites*, **11**, 684, (1991).

16 Meier W.M.; *Z. Kristallogr.*; **115**, 439, (1961).

17 Catlow C.R.A.; Freeman C.M.; Vessal B.; Tomlinson S.M.; Leslie M.; *J. Chem. Soc. Farad. Trans.*; **87**(13), 1947, (1991).

18 Bergerhoff G.; Baur W.H.; Nowaiki W.; *Miner. Mh.*, **1958**, 193, (1958).

19 Baur W.H.; *Am. Mineral.*, **49**, 697, (1964).

20 Davis M.E.; Saldarriaga C.; Montes C.; Garces J.; Crowder C.; *Nature*, **331**, 698, (1988).

21 Kokotailo G.T.; Lawton S.L.; Olson D.H.; Meier W.M.; *J. Phys. Chem.* , **85**, 437, (1978).

22 Van-den-Begin N.; Rees L.V.C.; Caro J.; Bülow M.; *Zeolites*; **9**, 287, (1985).

23 June R.L.; Bell A.T.; Theodorou D.N.; *J. Phys. Chem.* **94**, 8232, (1990).

24 Goodbody S.J.; Watanabe K.; MacGowan D.; Walton J.P.R.B.; Quirke N.; *J. Chem. Soc. Farad. Trans.*; **87**, (13), 1951, (1991).

25 Chiang A.S.; Dixon A.G.; Ma Y.H.; *Chem. Eng. Sci.*; **39**, 1461, (1984).

26 Stockmeyer R.; *Zeolites,* **12**, 251, (1992).

27 Barrer R.M.; "*Molecular Sieve Zeolites II*"; in "Advances in Chemistry Series 102 (Eds. Flanigen E.M. & Sand L.B.) Amer. Chem. Soc.; Washington, (1971).

Chapter 7

Octadecasil and the Double-4-ring.

7.1 An investigation of the Octadecasil structure, by atomistic simulation.

7.1.1 Introduction.

With F^- as a mobilising agent a new range of Clathrasils, (usually defined as a silica-only porous tetrasilicates), ALPO's and zeolites have been synthesised[1]. Particular interest has centred on one member of the clathrasil family. Octadecasil, which is related to Zunyite and ALPO-16[2] and corresponds to net 215 in the Smith's list of 4-connected nets[3]. Recent work by Caullet *et al*[4] has characterised the pure phase of Octadecasil by Magic Angle Spinning NMR and XRD coupled with Rietveld refinement. A surprising feature of this structure is the location of the fluorine anion within the small $[4^6]$-cage, more commonly termed, the Double-4-Ring, (D4R) and following structure refinement, it has been proposed that approximately 85% of these D4R's were indeed occupied. Octadecasil can only be formed from an F^- containing gel and not via the standard preparation involving an OH^-/aqueous synthesis. Thus in this chapter we probe the structural consequences of such an unusual environment by computational methods.

This problem is well suited to investigation by computational techniques. In this chapter we therefore study the effect of including several different families of extraframework ions but also investigate the possibility of migration of the ion out of the D4R site. Indeed, such work relates to the elimination of the template, usually achieved experimentally by calcination. The anions investigated were F^-, which is found in the structure and OH^- which would usually be present following synthesis in an aqueous environment. The presence of extraframework cations can play a decisive rôle in both the structural and catalytic behaviour of the solid[5]. The cations included in the present investigation were firstly, those of the alkali metal group, Li^+, Na^+, K^+, Rb^+; in addition the Ni^{2+} cation was included, as this is a common extra framework cation in catalytic zeolite chemistry.

In the experimental characterisation of the Octadecasil phase, the Si/Al ratio was found to be very high, 300:1, i.e. the phase is close to being purely siliceous, an interesting observation since many microcrystalline solids exhibit some acidic nature and are usually found with relatively low Si/Al ratios[6]. This effect is also investigated computationally by the inclusion of an aluminium ion and the associated hydroxide group into the two crystallographically different framework T-sites.

7.1.2 Methodology.

The structure derived via Rietveld refinement[7] was used to define the initial positions for the framework atoms, figure 7.1.1. The framework model includes long range Coulombic, as well as two and three body short range potentials, with a Shell model treatment of oxygen polarizability[8] as discussed in the relevant sections of chapter 2. The inclusion of the shell model is important for these calculations, since charged defects cause significant electronic polarisation of the ions in the surrounding region. The ion-framework interaction comprises both Coulombic and short-range pair potentials. The potential parameters employed for both the framework and extra-framework species are reported in appendix A, (section 7.1.6), and are from references 9, 10, 11, 12.

Constant pressure lattice minimisation was performed on a P_1 unit cell, i.e. no symmetry constraints were applied and the structure was free to deviate from the original space group of I4/m. The code THBREL[13], see chapter 2.2, was used to perform the lattice energy minimisation calculations.

Having defined the potential model and relaxed the framework structure we may then calculate the total potential energy of the extraframework ions at any point within the clathrasil structure. In performing such calculations three key features of our procedure should be noted :

i) Coulombic sums are taken to infinity using the Ewald technique[14]. Short range potentials are set to zero for distances > 20Å.

ii) A single ion was introduced into a purely siliceous relaxed clathrasil lattice.

iii) The lattice is relaxed, i.e. all ions, including the framework, are adjusted until zero force, out to a radius of 10Å from the ion.

Such calculations may be conveniently and efficiently carried out using the CASCADE code[15] as discussed in chapter 2.3.

The methodology which has been briefly described here, is described in more detail in chapters 2.2 and 2.3, which review energy minimisation and the defect calculations respectively.

From calculations performed using the above methods one can gain an insight into the stability of the extra framework cations at the centre of the D4R cage. However, this approach only relates to the stability of the ion once incorporated into the ring and does not the probe possible migration process of these extraframework ions. The energy of the saddle point for this process is calculated by fixing the relevant extraframework ion in the plane, described by the four tetrahedral atoms in the D4R window and allowing the subsequent relaxation of the framework. This latter configuration is a likely model for the saddle point for the migration process, as the migrating ion must pass through the D4R on migrating into the main cavity.

7.1.3 Results.

The Octadecasil framework was simulated as described above, firstly without any extra framework atoms and later with the ions placed at possible positions within the structure, which is represented in figure 7.1.1a with all the atoms shown, while figure 7.1.1b illustrates only the connections of the tetrahedral atoms. The results for the constant pressure lattice energy minimisation of the purely siliceous material are given in table 7.1.1.

Table 7.1.1 : A comparison of the calculated and experimental structural parameters of the Octadecasil phase.

Property.	*Calculated.*	*Experimental*	*Error.*
a (Å)	9.1937	9.194	0.003%
b (Å)	9.1937	9.194	0.003%
c (Å)	13.482	13.396	0.64%
α (°)	90.0	90.0	
β (°)	90.0	90.0	
γ (°)	90.0	90.0	

As can be seen the agreement with the structural experimental data is excellent, with an maximum error of less than 1%. The structure is predicted to be stable without the presence of the extra framework ions. Indeed, from such calculations one can surmise that the removal of the F^- ions from the structure would leave the framework intact; if one relates the energy to that of α-quartz[16] and Silicalite-I[17], two forms that are known to exist in a purely siliceous phase, the energy is -128.5 eV per SiO_2 unit for Octadecasil, as compared to values of -128.64eV for α-quartz and -128.59eV for Silicalite-I. The phase is therefore marginally less stable thermodynamically than the others cited but it has approximately the same energy as ZSM-18[18], another observed metastable phase of SiO_2.

Figure 7.1.1a : The framework of Octadecasil illustrating the positions of all ions.

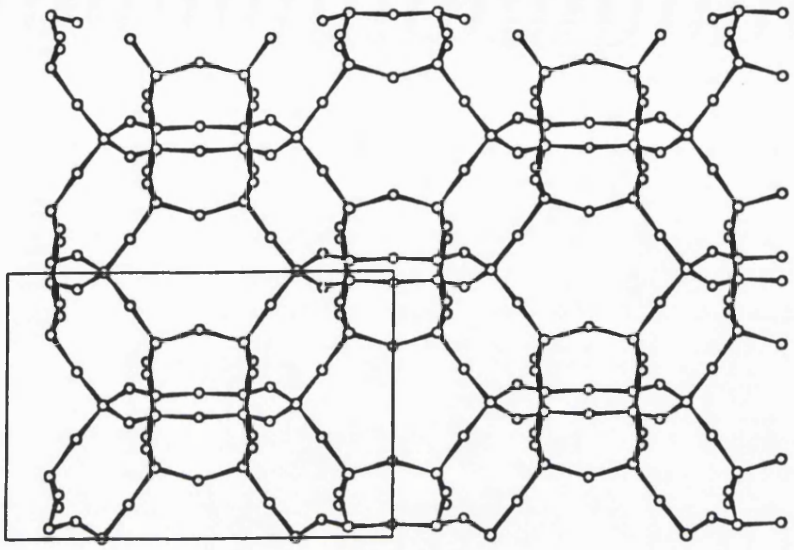

Figure 7.1.1b : A skeletal model of the structure of Octadecasil with the oxygen ions omitted for clarity.

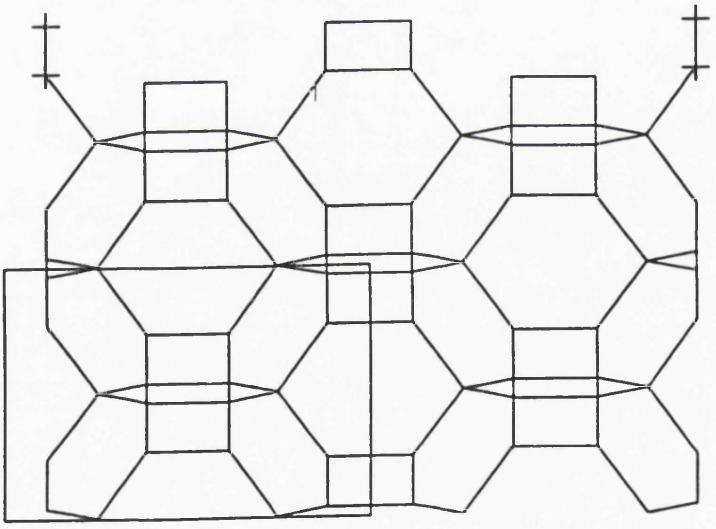

The next stage of our study concerns the calculation of the energy of replacing a silicon with an aluminium ion. There are two distinct asymmetric T-sites in the Octadecasil structure: one is a member of the D4R and the other is present in the cavity; figure 7.1.2 illustrates the two different framework positions with the aluminium ions represented as solid spheres. Table 7.1.2 gives the relative substitutional energies of aluminium ions within the framework at the two possible sites; this table also reports the relative protonation energies of these sites. These relative proton energies were calculated using the effective O-H potential derived by Saul *et al.*[19] which was based on empirical relationships fitted to calculations derived by *ab-initio*, methods.

Figure 7.1.2 : The two different T-sites used for aluminium substitution into the framework.

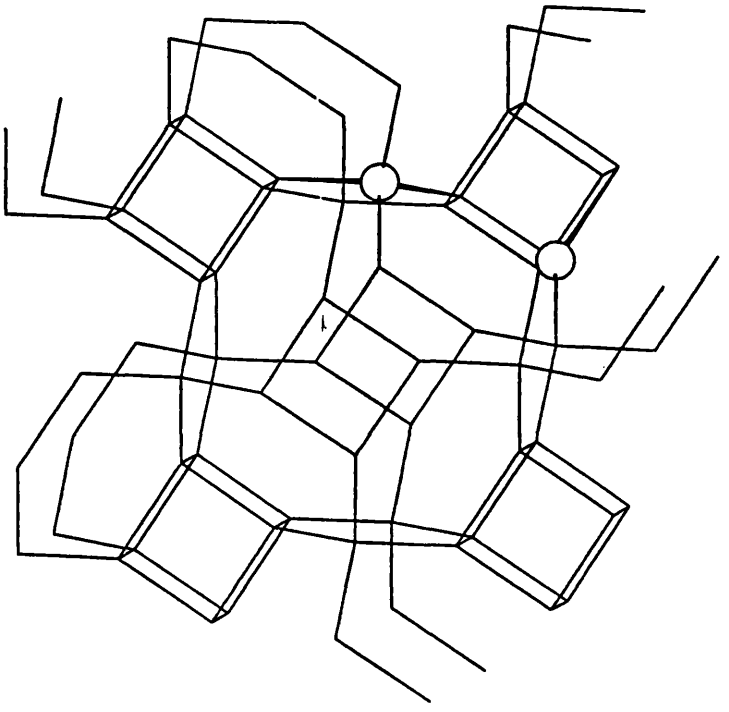

Table 7.1.2 : The substitutional energy of aluminium substitution into the Octadecasil phase and the relative protonation energy of the two sites.

	Substitution Energy (eV)	*Protonation Energy (eV)*
Al in the D4R	38.18	0.0
Al in the Cavity.	38.08	1.52

The substitutional energy for an aluminium ion into the framework structure is similar to that obtained for other zeolites[18]. Of course in any real system the negative charge of the Al substitution requires a counter cation to retain electrostatic neutrality. The simplest of such species is the proton which is normally assumed to reside on the oxygen adjacent to the aluminium ion. The proton could of course bind to any one of the oxygen ions within the system but its' binding energy is expected to be greater for the nearest neighbour position. As noted, we also therefore report in table 7.1.2 the defect energies for protonation adjacent to the aluminium, relative to the most stable protonation site. We find that the site next to the aluminium ion in the D4R is the more stable position upon protonation, even though in the charged Al defective system, the Al in the cavity is slightly favoured. Clearly the protonation energy is the dominant factor in determining site preferences as opposed to the Al substitution energies alone.

As outlined in the summary of the methodology earlier in the chapter, it is possible to investigate the extraframework ions using existing defect modelling codes. Thus we investigate the inclusion of several of the more commonly occurring ions, within the structure at different sites with special reference to the perturbations of the framework by their presence. It is useful to consider the anion and cations substitutions separately. The former are relevant to synthesis and the latter to ion exchange. Table 7.1.3 reports the energy to introduce various framework ions into the

D4R. It is important to note that the ions and the framework are not held rigid and all internal degrees of freedom are allowed to vary within the constraints of the experimental lattice parameter.

Table 7.1.3 : The substitutional defect energies of various ions placed at the centre of the D4R.

Ion Included.	*Energy of Inclusion. (eV)*
F^-	-3.53
OH^-	-7.41
Li^+	-3.19
Na^+	-1.36
K^+	-7.76
Rb^+	9.33
Ni^{2+}	-12.03

As can be seen there is a wide range of insertion energies. There is a large difference between the relative energies of F^- and OH^- implying that the OH^- ion would be more thermodynamically stable within a D4R than the F^- ion. Indeed, this implies that the D4R is more stabilised by OH^- than F^- and it is interesting to note that D4R precursors have been observed in tetraalkylammonium hydroxide/silicate solutions[20]. The F^-/D4R system is however, stable according to our simulations and with respect to the gaseous F^- anion.

With regard to cation location within the D4R, the first three members of the alkali metals are observed to be stable which is consistent with their ionic radii being small enough for the ions to fit inside the D4R, whose diameter is about 2.5Å; but when the radius becomes too large to allow a comfortable fit, the substitutional defect energies increase dramatically, as observed for the substitution of Rb^+, with an effective ionic radius of 1.47Å inside the D4R.

Overall, our calculated energies show that the D4R has the ability to accommodate a wide range of extra framework ions. The framework structure can facilitate their incorporation by means of extensive structural relaxation with the mode of relaxation varies from ion to ion. The first two members of the alkali metals, Li^+ and Na^+, best display the variation in relaxation; figure 7.1.3(a,b) depicts the final relaxed geometry of either a Li^+ or Na^+ ion inside the D4R with the initial framework geometry overlaid in each case.

Figure 7.1.3a : The relaxed geometry, overlaid with the initial geometry for the inclusion of Li^+ into the D4R. The initial geometry is described in a lighter grey.

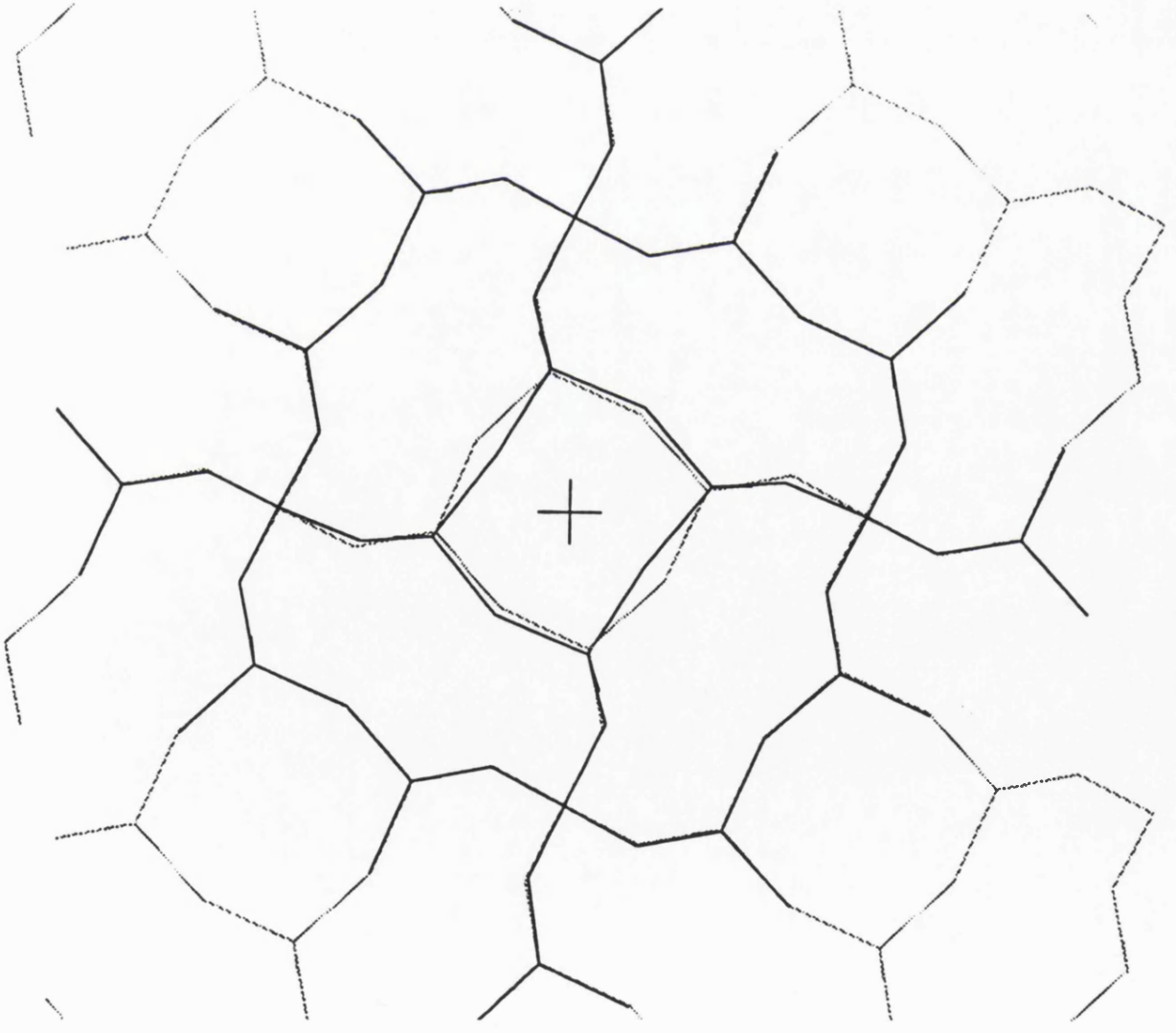

Figure 7.1.3b : The relaxed geometry, overlaid with the initial geometry for the inclusion of Na^+ into the D4R. The initial geometry is described in a lighter grey.

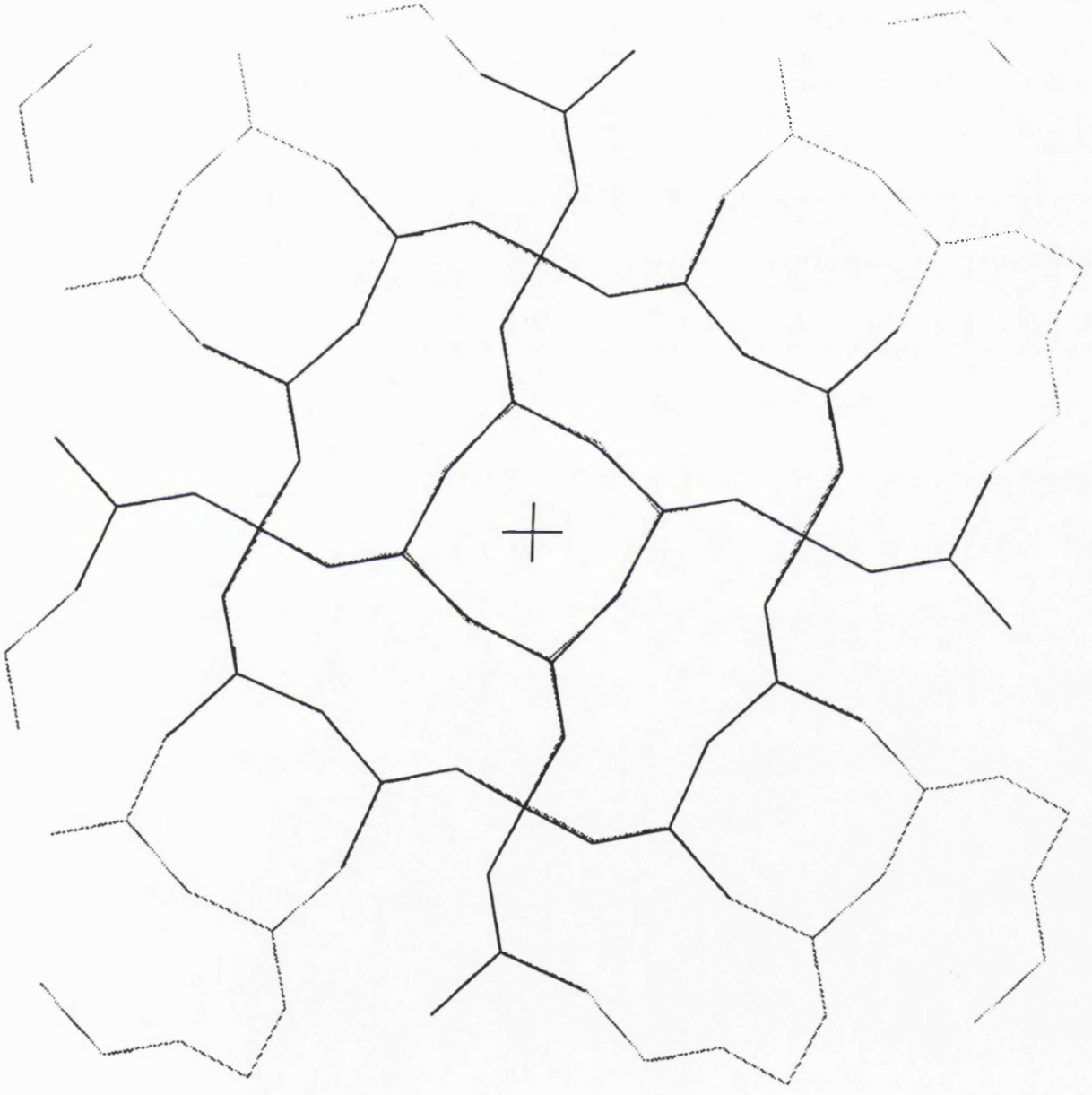

In the case of Li^+, the relaxation of the framework oxygen ions is extensive and as can be seen there is a large distortion of the O-Si-O tetrahedral bond angle from 112.6° to approximately 100.6° in the relaxed structure; whilst the Li^+-O nearest neighbour distance is reduced from 2.73Å to 2.08Å. The Na^+ perturbs the cage to a much lesser extent with little deviation in the overall shape and tetrahedral angles. However, the Na^+-O distance is reduced by a small amount to 2.56Å. We can, of course, relate these differences in relaxation to the effective ionic radii, $Li^+ \approx 0.68$Å; $Na^+ \approx 0.97$Å, though it must be stressed that using the latter concepts we could only achieve a qualitative and not a quantitative description as in the work presented here. The relaxations are very localised around the interstitial as emphasised by figure 7.1.4 which shows the variation in structure of around F^-, Na^+ and Ni^{2+} inserted into the D4R cage. The extensive relaxations although different for all three systems do not extend more than 2 or 3 tetrahedral units away from the defect.

Figure 7.1.4 : An overlay of the resulting relaxed geometries for the F^-, Na^+ and Ni^{2+} systems.

The frameworks are described in varying shades of grey; Black is F^-, Medium grey is the Na^+ system and the lightest shade represents the Ni^{2+} substituted system.

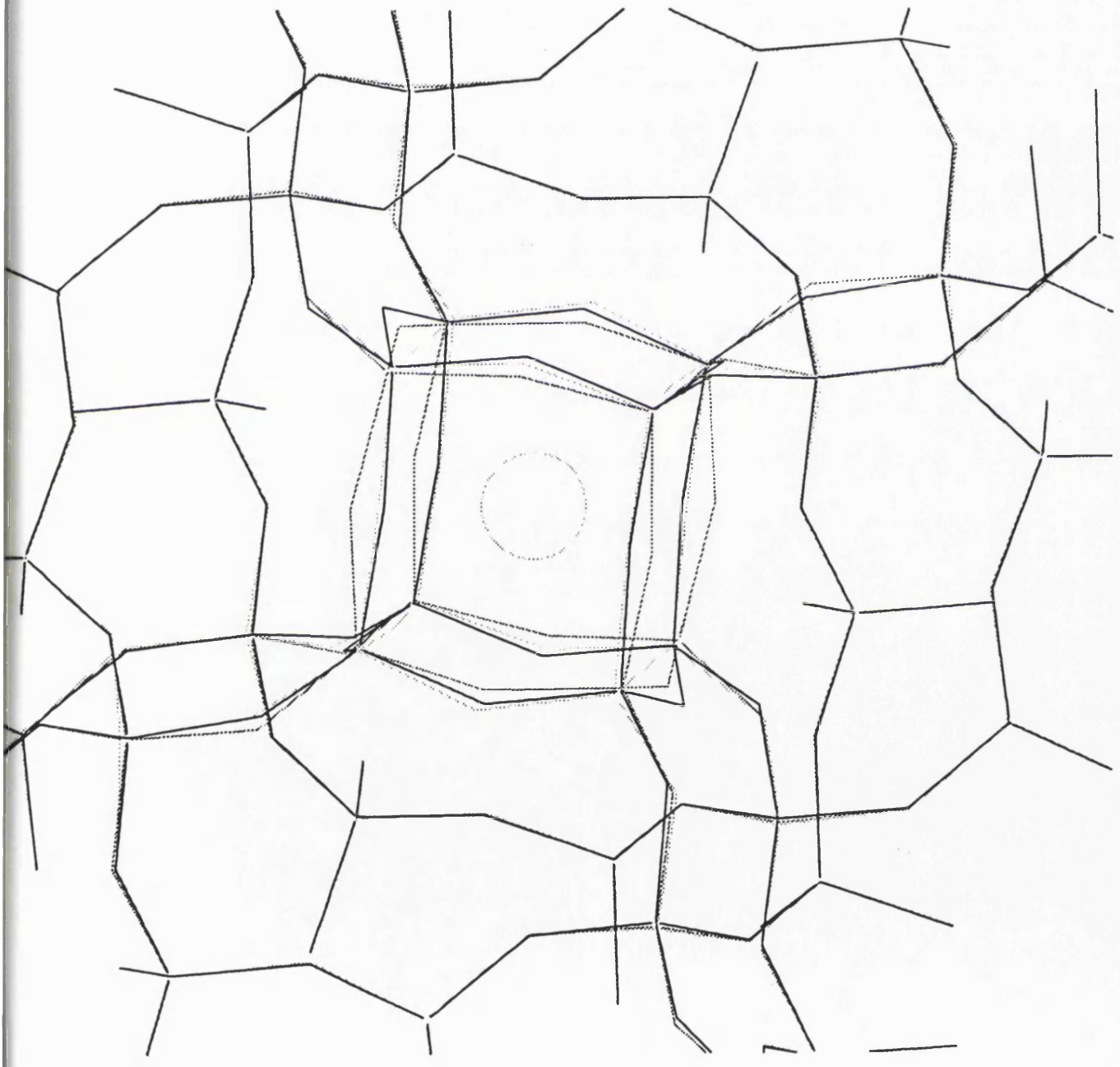

7.1.4 Ion Migration.

The catalytic processes within a zeolite depend not only on the shape selective topology of the framework[21] but also many applications rely on the availability of extraframework ions. An example is Ni^{2+} in Zeolite-Y which catalyses the trimerisation of acetylene to form benzene, (as investigated in chapter 4). Here, the cations must migrate out of the Double-6-ring, D6R and into the supercage before the reaction can occur[22]. Chapter 4 describes how the energetics of the process could be explored in detail. In general, however, to calculate the energies of activation, we identify likely saddle point configurations for the migrating ion. In the structures discussed in this chapter, a likely saddle point structure is in the 4-ring window, at the centre of the plane mapped out using the four corresponding T-atom sites. This point is termed the "saddle point" for future reference. We should note that it may not be the precise saddle point in all systems, as this will vary from system to system but it should be close to the energy maximum in all cases. We therefore repeated the calculations with the extraframework ion fixed at the saddle point and the surrounding framework was allowed to perturb to their presence. Table 7.1.4 reports the calculated energies and resulting activation energies for the migration process, and the effective ionic radii[23] for the different ions placed at the saddle point.

The calculations show that the migration energy barriers, $\Delta Energy$, can vary significantly from system to system. For F^- and OH^- located in the D4R, the calculations suggest that the F^- ion is located in a much deeper energy well, than for the OH^- defect within the D4R. This would have experimental repercussions in that the OH^- could be labile and could thus migrate out of the D4R, either thermally or by a ligand assisted process[24]. It will be far more difficult for the F^- ion residing in the much deeper minimum to migrate out and indeed, it could prove experimentally impossible to extract the F^- anion from the D4R of Octadecasil.

Table 7.1.4 : Calculated migration energy barriers for the systems under investigation.

Ion Inserted.	*Saddle Point Energy. (eV)*	*Δ Energy (eV)*	*Ionic Radius. Å*
F^-	-0.386	3.15	1.33
OH^-	-6.788	0.62	1.33*
Li^+	-3.13	0.06	0.68
Na^+	3.84	5.20	0.97
K^+	11.56	9.32	1.33
Rb^+	11.28	1.95	1.47
Ni^{2+}	-8.31	3.72	0.69

* We assign the same radius to OH^- as to the isostructural F- ion.

The calculated migration energies of the cations show a distinct trend which is attributable primarily to variation in the ionic radius, although more subtle effects are present. Progression down the alkali metal group, leads to an increase in the proposed migration energy with the barrier height increasing to 9.3eV, (≈930kJ/mol) for K^+ within the D4R. A dramatic reduction is calculated for the Rb^+ system, which is best explained by reference to the final relaxed geometries of the saddle point configurations for these systems, shown in figure 7.1.5.

Figure 7.1.5 : The relaxed geometries for the alkali metal ions. The view is aligned along the cavity axis and the D4R, with the extraframework ion placed at the centre of the 4-ring window.

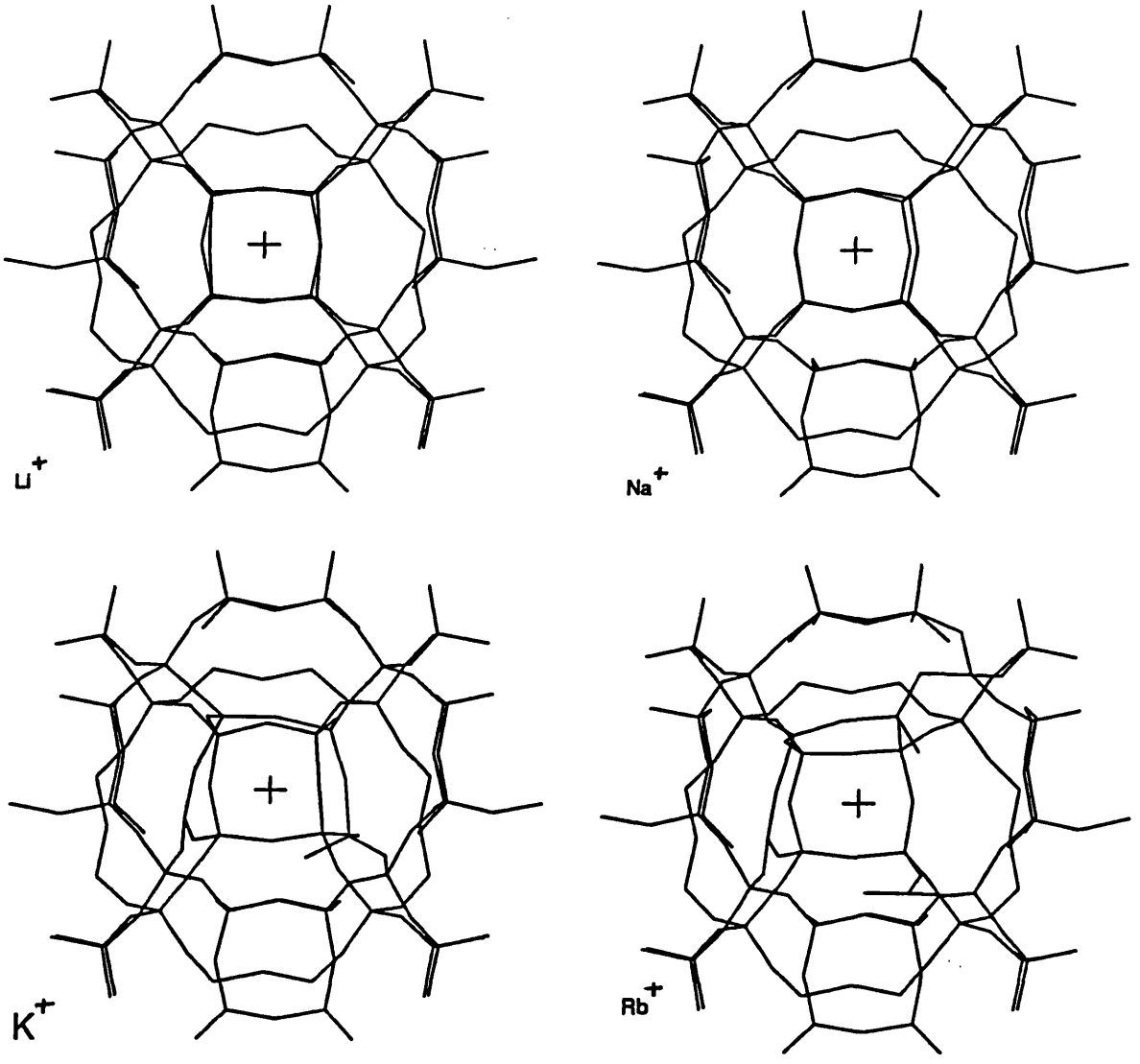

The Li^+ and Na^+ systems, show large relaxations around the ion, but these occur in such a way as to preserve the framework structure although as the size of the ion increases the ring cannot adjust in such a way as to prevent bond dissociation. (Bond dissociation is defined here to be the distance at which there is no overlap of covalent radii, although in the calculation, the two-body energy terms are still considered.) In the case of K^+ at the saddle point, one Si-O bond stretches to the distance defined as non-bonding; thus this process of ring breaking, serves to reduce some of the internal strains, but nevertheless there is a high activation barrier of approximately 9eV. When Rb^+ is placed at the saddle point the framework topology is altered beyond recognition; indeed, two Si-O bonds are observed to be broken and the ring is substantially altered, resulting in a substantial decrease in the migration energy; although we note that the high energy of insertion of the Rb^+ means that this cation is unlikely to be observed in the real system.

7.1.5 Conclusions.

The results reported in this chapter, agree well with the available experimental data, that is the F^- anion is stable within the D4R. However, this investigation has proceeded in-advance of experiment and predicted that the structure could exist without the need of extraframework ions, such as F^-, but the possible experimental removal of F^- from the D4R is unlikely, due to the large energy barrier for the migration out of the ring. The possible synthesis of a D4R containing an OH^- anion is predicted. This differs from the result of the F^- system in that the OH^- anion could be labile and thus migrate out of the D4R, perhaps leaving a structure that would be more suitable as a catalyst. It is possible for the D4R to contain other extraframework cations, such as alkali metal cations, though the energies and migration barriers vary considerably with the ion.

The flexibility of the framework is highlighted by several comparisons of the relaxed structures and dissociation is observed for some configurations.

The relaxations investigated in this section are the predominant structural implications of ion insertion into the D4R, but if one uses *ab-initio* techniques to probe the systems, the electronic effects of the insertion process can be calculated.

7.1.6 Appendix A : Potentials used in this study.

Atomic Parameters

	Core Charge. (|e|)	Shell Charge. (|e|)	Spring Constant. (eV/Å^2)
Silicon.	4.0	----------	----------
Oxygen.	0.86902	-2.86902	74.92
Aluminium.	3.0	----------	----------
O_h-H	-1.426	----------	----------
Hydrogen.	0.426	----------	----------
Fluorine.	0.34	-1.34	37.98
Lithium	1.0	----------	----------
Sodium.	1.0	----------	----------
Potassium	1.0	----------	----------
Rubidium.	-3.82	4.82	94.23
Nickel.	-1.344	3.344	93.7

Morse Potentials : $Energy = D*\left(1-\exp\left[-\alpha*\{r-r_o\}\right]\right)^2$

O_h - H D= 7.0525 eV α= 2.1986 Å^{-1} r_o= 0.9485 Å

Buckingham Potentials : $Energy = A_{ij} \exp\left\{\frac{-r_{ij}}{\rho_{ij}}\right\} - \frac{C_{ij}}{r_{ij}^6}$

		A_{ij} (eV)	ρ_{ij} (Å)	C_{ij} (eVÅ^2)
O(s)	O(s)	22764.0	0.149	27.88
"	Si	1283.907	0.32052	10.66158
"	O_h	22764.0	0.149	27.88
"	Al	1460.3	0.29912	0.0
"	H	311.97	0.35	0.0
"	F(s)	1440.21	0.3027	22.468
"	Li	816.309	0.26085	0.0
"	Na	5836.84	0.2387	0.0
"	K	1000.3	0.36198	10.569
"	Rb	962.184	0.37723	40.11
"	Ni(s)	1582.5	0.2882	0.0
O_h	Si	1283.907	0.32052	10.66185

Note : (s) denotes a shell interaction.

A short range cut-off of 10Å was implemented in all defect calculations.

Three-body terms : $Energy = k_{ijl}\left[\varphi_{ijl} - \varphi^o_{ijl}\right]^2$

O-Si-O k_{ijl}= 2.09724 eV rad^{-2} φ^o_{ijl}= 109.47°

O-Al-O k_{ijl}= 2.09724 eV rad^{-2} φ^o_{ijl}= 109.47°

7.2 An Investigation of the D4R by *Ab-initio* Computational techniques.

7.2.1 Introduction.

The calculations reported in the previous section showed how atomistic computer simulations, based on the experimentally reported structure[3] of Octadecasil gave useful results on the F^- anion in the D4R but also on a range of different ions, both anions and cations inside the cage. The lattice framework was subsequently observed to relax in a variety of ways, depending on the nature of the ion inserted. The present study continues the investigation of the structural relaxation of the framework around a charged defect but examines in detail the changes in electron density around the inserted ion. To investigate these charge distributions, one must return to *ab-initio* techniques, i.e. to solve the Schroedinger equation and to calculate the resulting electron density distributions. An investigation of this nature differs in many respects to much of the previous *ab-initio* work carried out in the field of zeolite chemistry. Previous work has mainly been concerned with modelling the catalytic nature of zeolites, using small or medium clusters; i.e. up to 5 tetrahedral units. However, with the recent development of both periodic Hartree-Fock and periodic LDF[25], larger more complex structures are tractable, although presently these calculations are restricted to high symmetry structures due to the constraints of computational resources. The work described here does not invoke symmetry operators, that is we introduce a defect into the structure and watch the subsequent perturbations, free from any symmetry constraints.

The D4R was investigated, along with several inserted ions namely F^-, OH^- and Na^+ which should allow us to assess how far the framework electron density responds to a charged ion and how such an excess or deficiency of electron density is distributed over the framework. This work is fundamentally different from the atomistic simulations where the charge is modelled as a discreet point entity, with electronic polarisability can be accounted for by the simple Shell model methodology.

7.2.2 Methodology.

The initial starting structure for the D4R was taken from the Rietveld refined structure (reference 3). The cluster investigated comprised of $Si_8O_{12}(OH)_8$, with 20 tetrahedral and bridging oxygen atoms, with termination by hydroxyl groups - a common method of cluster termination within zeolitic simulations as shown in figure 7.2.1. The cluster contains 289 electrons. The Local Density Function, LDF, *ab-initio* methodology was used in these calculations; details of the technique were described in Chapter 2.6. This methodology was chosen due to its inclusion of an approximation of the electron correlation energy, which may be important for this type of defective system. LDF may only calculate the properties of the electronic ground state which is acceptable for these types of system, as we do not require information on excited states. The basis sets used were atomic centred numerical basis set and are reported in Table 7.2.1. We note that this is a large scale calculation with the total number of orbitals used being in excess of 300 valence orbitals, since no orbitals were frozen. The code DMOL[26] was used to perform the calculations.

Table 7.2.1 : Numerical orbitals used for the Basis Set in this investigation.

Silicon	:	1s, 2s, 2p, 3s, 3s**, 3p, 3p**
Oxygen	:	1s, 2s, 2s**, 2p, 2p**
Hydrogen	:	1s, 1s**
Fluorine	:	1s, 2s, 2s**, 2p, 2p**
Sodium	:	1s, 2s, 2s**, 2p, 2p**, 3s, 3s**

Note: ** denotes a high exponential orbital.

In the calculations on F^-, OH^- or Na^+ the inserted ions were introduced into the centre of the D4R and a full geometry optimisation (using conjugate gradient techniques[27]) was performed on all the atoms in the system; the properties were then

calculated for the optimised geometry. The total Mulliken charge analysis and individual orbital occupancies were subsequently calculated; they provide valuable information on how the framework responds to the charged defects. The structural information gained after the geometry optimisation can also be compared to the results obtained from the atomistic simulations described previously, chapter 7.1. Finally, we note that the clusters although very large are not of sufficient size to extend beyond the range of framework deformation observed in the atomistic simulations, i.e. 2-3 tetrahedral units; but they do represent some of the largest reported *ab-initio* calculations of this nature.

Figure 7.2.1 : A ball and stick representation of the isolated D4R terminated by hydroxyl groups.

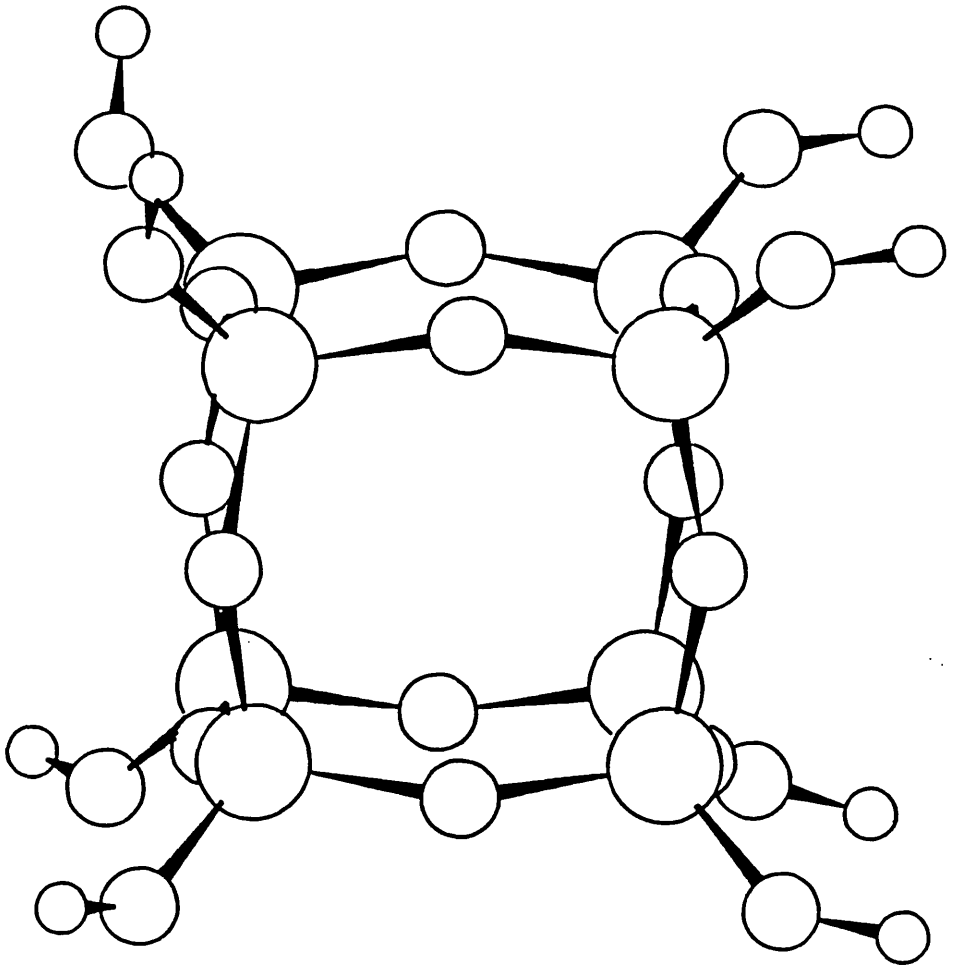

7.2.3 Results and discussions.

Table 7.2.2 reports the structural values for the most important bond lengths and angles for the optimised geometries and makes a comparison between the quantum mechanical calculations and the results obtained using the energy minimisation calculations based on effective potentials..

Table 7.2.2 : Some structural parameters obtained from the different types of calculation; *ab-initio* and energy minimisation using Born model potentials.

Property	***D4R***		***F^- in D4R***		***Na^+ in D4R***		***OH^- in D4R***			
	ab-initio	*atomistic*	*ab-initio*	*atomistic*	*ab-initio*	*atomistic*	*ab-initio*		*atomistic*	
							near O_h	near H_o	near O_h	near H_o
Ion - O_{br} (Å)			2.77	2.73	2.53 or 2.72	2.54 or 2.56	2.59	2.42 or 2.74	2.27	2.46 or 2.74
Ion - Si (Å)			2.78	2.61	2.84	2.74	2.5	2.56	2.07	2.58
Si-O_{br} (Å)	1.66	1.63	1.66	1.62	1.66	1.62	1.69	1.66	1.62	1.62
Si-O_{nbr} (Å)	1.64	1.63	1.68	1.62	1.61	1.57	1.675	1.675	1.615	1.615
Si- $\hat{O}_{br}$-Si (°)	155.03	136.73	143.39	136.75	151.85 or 166.07	158.35	130.37	152.19	128.77	146.4
O_{br}- Si - O_{br} (°)	106.86	112.6	111.54	114.45	102.84	104.36	115.33	108.39	113.29	111.25

Note: *br* denotes a bridging oxygen and *nbr* denotes an oxygen of the terminating hydroxyl group.

The *ab-initio* results for the isolated D4R, which has been terminated by hydroxyl groups, shows that the structure is indeed stable and is close to being nearly cubic, even though no symmetry operations were used in these calculations. The Si-O_{br} bond lengths, for oxygen ions within the ring, are 1.66Å with a value of 1.64Å obtained for the Si-O_{nbr} bond lengths outside the D4R. These bond lengths are longer than the experimental values but this is commonly found for this type of cluster

calculation Typical Si-O_{nbr} bond lengths is of the order of 1.62Å for Hartree-Fock calculations on orthosilicic acid with a very good basis set.[28] However, the calculated bond angles are in reasonable agreement with previous studies, both for structures calculated via periodic techniques[29] and for the structure of clusters[30].

We now address the calculated relaxations around the inserted ions, where there is a fair measure of agreement between the different techniques, although significant differences are noted.

The results for the F^- contained within the D4R show an increase in the F-O_{br} and F-Si distances in the quantum mechanical calculations compared with the simulations based on Born model potentials. This may in part be attributed to redistribution of electron density between the defect and the framework, but of greater significance is probably the fact that the cluster can expand in the quantum mechanical calculations, whereas in the atomistic simulations such expansion is reduced by the surrounding lattice. The perturbations and general relaxations observed in the framework are however similar in both approaches. In the F^- system, the Si-O_{br}-Si angle and O_{br}-Si-O_{br} angle are both within 4% of the atomistic results and the experimental structure.

In the Na^+ cation system, the framework defect distances have two values; the two sides of the D4R are drawn in equally and the edges eased slightly out. This results in 8 Na-O_{br} distances at 2.53Å and 4 at 2.72Å, (table 7.2.2); the average distance of 2.61Å is however, in good agreement with the values obtained for the atomistic simulations. Although a little of the asymmetrical distortion is calculated in the atomistic simulations it is not on the scale given by the *ab-initio* results. The effect of including a positively charged defect has reduced the Si-O_{br} interim bond length and at the same time spilt the Si-O_{br}-Si bond angles into two distinct groups, 151.85° and 166.07°; though only one value of 158.35° is calculated in the atomistic approach. The average of the *ab-initio* derived bond angles 158.96°, in excellent agreement with the atomistic simulation results. Another effect of the positive charge is to decrease substantially the value of the O_{br}-Si-O_{br} angle to 102.84° for quantum mechanical

calculations (or 104.36° from atomistic simulations) as compared to an initial value of approximately 112.0° for the unoccupied D4R. The differences between the two sets of calculations again probably reflect the greater constraints of the surrounding lattice in the simulations, although the use of spherically symmetrical potentials in the simulation may result in an underestimation of the asymmetric distortions.

In the cluster containing the OH^- ion, the D4R responds in a different way from that previously described, because the hydroxyl group is an asymmetric dipolar molecule. Indeed, from the structural data summarised in table 7.2.2, it is clear that the equilibrium structure is of low symmetry which serves to emphasise the importance of not using symmetry constraints in these *ab-initio* calculations. The framework-ion distances obviously depend on the orientation of the hydroxyl group. The Si-O_{br}-Si angles have a similar dependence on the OH^- orientation; the angles nearer to the oxygen end decrease, whilst those closer to the hydrogen end increase with respect to the unoccupied D4R. The same distribution of angles is observed for the O_{br}-Si-O_{br} angles, i.e. a reduction at the hydrogen end coupled with an increase near the oxygen end of the inserted OH^-.

Using the trends evident from these calculations, it is therefore clear that for a negatively charged inserted ion the Si-O_{br} distance increases, as does the Si-O_{br}-Si and O_{br}-Si-O_{br} intra-ring bond angles. As expected, for a positively charged ion the trend is reversed: the Si-O bond length decreases as do the O_{br}-Si-O_{br} bond angles. However, for a dipolar ion the result is more complex, as seen for OH^- with the relaxation depending on the orientation of the defect, although the response of the lattice is as expected for the different ends of the dipole.

The results so far described have only dealt with structural rather than electronic responses to the inserted ions. The latter are of course only available from an electronic structure method, which yield orbital occupations, charge densities and other electronic properties of the ground state.

The Mulliken populations can be calculated for all the structures involved in this study and their variations provide a measure of the transfer of electron density due

to the insertion of the ion. For the *ab-initio* calculation of the isolated D4R, it is important to relate these results to those of previous workers, although much of there work was predominantly concerned with smaller structures[31,32]. The average charge on the framework atoms of the isolated D4R is reported in table 7.2.3, as are some results from other workers employing either a cluster or periodic modelling technique. We must stress that the previous results cited here are not for calculations relating to the D4R but for clusters of 1-5 tetrahedral atoms.

Table 7.2.3 : Mulliken charges calculated for the D4R, as compared to previous work.

Property		*This Work*	*Cluster*[33]	*CRYSTAL*[34]
Total Mulliken Charge	Si	1.949	1.53	1.94
|e|	O *(br)*	-1.04	-0.84	-0.97
	O *(nbr)*	-0.855	-0.74	n/a
	H	0.464	0.38	n/a

Note: *br* denotes a bridging oxygen within the D4R and *nbr* denotes an oxygen atom in a cluster terminating OH group.

We find that our values are close to those obtained in the previous cited studies both for the Hartree-Fock cluster calculations and also from the periodic Hartree-Fock methodology, embodied within the CRYSTAL code[35]. However, the charges are approximately a factor of 2 less than those used in the Born model atomistic approach, where a formal charge model was employed. This might suggest inadequacies in the potentials use in the latter studies; but this is not necessarily so as the important factor is the total potential, i.e. the short range, three body and Coulombic interactions when coupled together; and an enhanced contribution from one particular interaction may be compensated by a reduction in other terms. As noted in chapter 2.1, this difference of approach has lead to the derivation of two types of potential model: those based on formal charges (as used in this study) and those derived from partial charges[36]. One

problem associated with the partial charge model is the transferability of potentials from one system to another; the charges or some other parameter must be consistent between the two potential sets but this is rarely the case. The atomic and overlap charge densities for the framework oxygen atoms are given in Table 7.2.4.

Table 7.2.4: Orbital occupations calculated for the framework of the D4R.

Oxygen Orbital Overlap |e|			
Orbital	Atomic Populations	Overlap Populations.	
1s	Self 2.00		
2s	Self 1.792	Si **3s**	0.054
$2p^{-1}$	Self 1.842	Si **$3p^{-1}$**	0.104
$2p^{0}$	Self 1.436	Si **3s**	0.064
		Si **$3p^{0}$**	0.120
$2p^{+1}$	Self 1.877	Si **$3p^{+1}$**	0.087

The majority of covalent bonding in the framework is via the oxygen **$2p^{0}$**, which overlaps with the both **3s** and **$3p^{0}$** of the adjacent silicon atoms; yet most of the electron density remains exclusively in the atomic orbitals.

We next consider how the ions inserted into the D4R cage alter the bonding by transferring density to and from the cage. Table 7.2.5 reports the populations for the isolated ions and for those inserted into the cage.

Table 7.2.5 : Electronic properties of the defect, both as an isolated entity and upon inclusion into the D4R. (Units in |e|).

Property		F^-		Na^+		OH^-			
		Isolated	*In D4R*	*Isolated*	*In D4R*	*Isolated*		*In D4R*	
						O_h	H_o	O_h	H_o
Mulliken Charge. |e|		-1.0	-0.68	+1.0	0.626	-1.177	0.177	-0.977	0.292
						Total -1.0		Total -0.685	
Orbital. Occupations |e|	**1s**	2.000	2.000	2.000	2.000	2.000	0.823	2.000	0.708
	2s	2.000	1.972	2.000	2.005	1.961		1.918	
	$2p^{-1}$	2.000	1.897	2.000	1.998	1.971		1.840	
	$2p^0$	2.000	1.897	2.000	1.998	1.971		1.857	
	$2p^{+1}$	2.000	1.897	2.000	1.998	1.249		1.399	
	3s			0.0	0.331				

In the case of the F^- anion inserted into the D4R, the Mulliken population is reduced from -1.0|e| in the isolated state, to -0.68|e| when inside the cage. The effect of the zeolite framework is to facilitate the transfer of electron density away from the charged anion and on to the surrounding lattice. It is clear from table 7.2.5 that, as expected, electron density has mainly been removed from the **2p** orbital with this transfer occurring equally from the **$2p^{-1}$**, **$2p^0$** and **$2p^{+1}$**. Again as expected owing to the cubic symmetry of the cage; a 4.4 % reduction in the electron density contribution is calculated for each of these orbitals. However, this reduction is higher for the high exponential **2p**** orbitals indicating that density is being drained from the more diffuse parts of the electron charge cloud.

On inserting the Na^+ cation, the change in the Mulliken population indicates a reduction of the cation charge from +1.0|e| to +0.636|e|. The effect of the zeolite framework is indeed the reverse of that observed for the F^- system, in that the electron density is transferred from the framework onto the sodium orbitals. All of the charge

is transferred into the previously unoccupied **3s** orbital, and there is an associated contraction of the lower orbitals as manifested in a total occupation of 6.037|e| in the **2p** orbital and 2.005|e| in the **2s** orbital. These latter values are larger than the Pauli allowed maximum occupancy of 6.0|e| and 2.0|e| because the effective size of the **2p** and **2s** orbitals contract, yet in the simple Mulliken approach the effective orbital size does not change and hence an over population is calculated. The increase in the effective ionic radius of the Na^+, due to the filling of the sodium **3s** orbitals, could be responsible for the increase in the calculated Na-O_{br} and Na-Si distances. In the atomistic calculations the effective ionic radius, which can be thought of as a function of the A and ρ parameters in the Buckingham potential is constant and thus the calculated framework relaxations do not include the effects of varying cation radius.

When an OH^- functional group is included within the D4R cage, the effects are a superposition of the two cases previously described. As reported in table 7.2.5, the oxygen has a Mulliken population of -1.177|e| and hydrogen +0.177|e| in the isolated molecule but when this is included into the D4R, the framework perturbs the electronic structure of each atom in a different way. The O_h once incorporated, has a Mulliken population of -0.977|e|, i.e. 0.2|e| of electron density has been removed; whilst the hydrogen of the group now has an electronic population of +0.292|e|, a change of 0.115|e|. The overall charge on the hydroxyl group once incorporated into the D4R is -0.685|e|, a value very similar to that calculated for the inserted F^- anion; the framework has responded so as to withdraw 0.2|e| from the oxygen orbitals and only 0.115|e| from the hydrogen orbitals, that is an symmetrical withdrawal of electron density. In the case of the hydrogen atom most of the electron density has as expected been removed from the **1s** orbital, though curiously an increase in density is observed for the higher exponent **1s** orbital. Whilst for the oxygen atom, splitting of the degeneracy of the orbitals is observed for the encapsulated compared with the isolated molecule, as can be seen from table 7.2.5. We see that the $2p^{+1}$ has substantially less density than the other **2p** orbitals, because the $2p^{+1}$ is involved in covalent bonding with the hydrogen atom. Indeed, there is 32% overlap of the total oxygen $2p^{+1}$ with

the hydrogen 1s orbital in the isolated state but this is reduced to 19% in the encapsulated form, although the percentage of electron contribution of the hydrogen 1s to the bonding is about the same, i.e. 45% of the total hydrogen electron density. The inserted hydroxyl group shows a reduction in the electron density of 5.7% in the $2p^{-1}$, $2p^{0}$ similar to the reduction calculated for the F^- system. There is a decrease in the electron density of the $2p^{+1}$ orbital overlapping with the hydrogen 1s and an associated increase in the electron density of the $2p^{+1}$ self orbital which implies that the bond has become more ionic.

The question arises as to where this extra electron density on the O_h $2p^{+1}$ originates: is it from the other oxygen 2p orbitals or from the framework?. From the three dimensional population matrix, the overlap population of the 2p oxygen framework orbitals is about the same but there is a little overlap from the 3s and 3p orbitals of the silicon atoms aligned in the direction of the $2p^{+1}$ O_h orbital. The question of the reduction in electron density of the O_h $2p^{-1}$, $2p^{0}$ can be explained by the slight overlap with the 3s orbitals of the other silicon atoms closest in the ring. Those silicon atoms are different from the ones involved in the oxygen $2p^{+1}$ bonding because the orientation of the $2p^{0}$ is approximately perpendicular to that of the $2p^{\pm1}$ orbitals.

To summarise the difference in the bonding of the OH^- isolated and encapsulated system: in the isolated system, the bonding is of a covalent/ionic nature with the bonding orbitals being those of the oxygen $2p^{+1}$ and hydrogen 1s; once incorporated into the D4R, the overlap between hydrogen 1s and oxygen $2p^{+1}$ is reduced but the atomic density of the $2p^{+1}$ orbital is increased, implying a decrease in the covalent nature of the bond and an increase the dipole moment of the molecule, i.e. increase the ionic character of the bond. One clear way of emphasising this deviation is in the bond length of the hydroxyl group: in an isolated state the bond length is 1.01Å, but once included inside the D4R, we calculate a reduction to 0.99Å for the quantum mechanical calculation and 0.97Å from the atomistic simulations.

The results reported so far have dealt with the effect of the framework on the inserted ion but we can examine the contrary effect, i.e. how the inserted ion affects the charge distribution of the framework. Table 7.2.6 reports the average Mulliken population for the atomic orbitals centred on the framework atoms for all the structures studied; also tabulated are the total Muliken charges on the atoms concerned.

The core electrons as expected do not participate in any of the bonding processes. However, the behaviour of the valence orbitals is markedly different and varies from structure to structure.

Table 7.2.6 : Average electronic properties of the framework.

Property			***D4R***	***F⁻***	***Na⁺***	***OH⁻***
				In D4R	*In D4R*	*In D4R*
Average		Si	1.949	1.848	1.972	1.848
Mulliken Charge.		O *(br)*	-1.040	-1.005	-1.039	-1.004
|e|		O *(nbr)*	-0.855	-0.812	-0.839	-0.819
		H	0.464	0.431	0.483	0.438
Orbital Occupations.	Silicon	1s	2.000	2.000	2.000	2.000
|e|		2s	2.000	2.000	2.000	2.000
		2p	6.000	6.000	6.000	6.000
		3s	0.619	0.653	0.587	0.656
		3p	1.433	1.499	1.443	1.497
	Oxygen *(br)*	1s	2.000	2.000	2.000	2.000
		2s	1.821	1.837	1.810	1.839
		2p	5.219	5.170	5.236	5.164

In the case of the F^- anion within the D4R, electron density is transferred from the anion on to the silicon atoms of the framework. The electron density is calculated to reside mainly in the Si **3p** and **3s** orbitals; indeed both of these orbitals show an increase of approximately 5% in their total electron density, i.e. 0.1|e| of additional electron density and the transfer of electron density is distributed equally among the 8

silicon atoms. This increase in electron density is responsible for the reduction in the total Mulliken charge on the Si atoms, from +1.949|e| to +1.848|e|; whereas on the surrounding oxygen atoms, (both bridging and non-bridging,) a decrease of 5% in the electron density is calculated; the hydrogen atoms also have a calculated increase of approximately 5%. The addition of the singly charged anion to the D4R has reduced the ionic nature of the framework.

For the Na^+ encapsulated into the D4R, the average Si charge increases from +1.949|e| to +1.972|e|; clearly electron density has been transferred from the framework onto the cation, with the high level Si **3s** orbitals undergoing a reduction in population of ≈5.2%. The oxygen atoms do not readily participate in this back-bonding process, with the average charge remaining constant, although there is a slight redistribution of the populations within the internal orbitals; the **2s** population decreases in electron density, whilst the **2p** increases by approximately the same density. However, there is a difference in the two types of bridging oxygen: those in the ring faces which are pulled nearer the Na^+ and those which are pushed away. The 8 oxygen atoms nearer to the Na^+ have a total charge of -1.059|e|, whereas those slightly away have a charge of -1.019|e|. This can be explained by a very slight increase in the orbital overlap between the **3s** centred on the sodium ion and the **2p** on the oxygen atoms nearest to the defect. The charges centred on the 8 oxygen atoms near the Na^+ have decreased due to the transfer of 0.02|e| in electron density, whereas an additional 0.02|e| resides on the 4 oxygen atoms which have been pushed away. Hence, the framework oxygen atoms add a total of 0.08|e| to the Na^+, with the other 0.374|e| reduction in the sodium ion charge coming from the 8 silicon atoms in the framework.

The hydroxyl group contained within the D4R can be considered to be a mixture of the above scenarios. Electron density is transferred from the OH^- group onto the framework and as in the F^- system, this density resides mainly on the orbitals of the framework Si atoms, although in this case it is predominantly redistributed to the silicon **3p** orbitals. The O_{br} atoms have the same total average charge as in the F^-

system, though the overall spread of orbital occupations is much larger than in the F^- case; -0.955|e| to -1.033|e| for the OH^- group and -0.994|e| to -1.018|e| for F^- in the D4R. Nonetheless, the average value is very similar to that for the encapulsation of a single anionic defect, although surprisingly, the oxygen atoms nearer the oxygen of the hydroxyl group respond as if close to a negative defect and the framework oxygen atoms nearer to the hydrogen atom, as if in close proximity to a positive charged defect.

The framework, as can be seen from the above discussion, responds to a charged defect in a variety of ways, yet in all cases, common features have been observed: the silicon atoms act as an electron density "sink" from which density can be withdrawn or enhanced.

The results so far have described the structural and the electronic properties of the systems, yet *ab-initio* calculations also of course yield energies.

Table 7.2.7 : The substitution defect energy calculated both via *ab-initio* and atomistic methods. The energies relate to the optimised structures.

Ion Defect	*Ab-initio Energy (eV)*	*Atomistic Simulation Energy (eV)*
F^-	-4.234	-3.53
Na^+	+0.493	-1.36
OH^-	-4.171	-7.41

The differences in the defect energies between the *ab-initio* and atomistic simulations are reported in table 7.2.7 and although the results for the F^- system are in reasonable agreement, there are appreciable differences in the energies of the other systems. These differences may reflect inadequacies in the ion-framework potentials used in the simulation, but the much more restricted polarisation field in the *ab-initio*

calculations is likely to contribute to the higher calculated energies. Nonetheless, the energies still reveal that F^- is stable within the D4R, as observed experimentally in the Octadecasil phase; the OH^- group is also stable but not in as deep a minimum as predicted by the atomistic approach to the system. However, the Na^+ within the D4R is calculated to be unstable with respect to the free ion and empty framework, although when entropy factors are taken into account the Na^+ within D4R cage could be found to be just stable.

7.2.4 Conclusion.

From the above large cluster and interstitial substituted cluster calculations we can draw the following conclusions :-

The D4R cage can exist in an isolated state, as a cluster and the bonding in such a zeolite fragment is semi ionic. The total Mulliken charges on the isolated D4R are in good agreement with previously reported values, derived from either calculations involving smaller clusters or via a periodic approach. The structure adopted by the D4R is also comparable to previous results from other workers.

Upon introduction of a charged particle into the centre of the D4R, the framework properties changed quite distinctly. For a singly charged anion, F^-, the framework induced transfer of electron density from the anion onto the silicon atoms; 0.32|e| was transferred in total. This transfer of electron density was found to build up on the **3s** and **3p** orbitals of the tetrahedral framework silicon atoms and in general to reduce the ionic nature of the zeolite fragment.

Upon inclusion of Na^+, the framework silicon atoms donated electron density, up to 0.374|e| onto the cation orbitals, partially filling a previously unoccupied **3s** orbital on the Na^+ ion. The structure was also observed to distort asymmetrically - a feature not observed in the atomistic calculations partly due to the spherical nature of the atomistic potentials and partially due to the less constrained nature of the cluster considered.

When an hydroxyl group was included, the framework perturbations varied depending on which part of the OH^- was closer to the framework. If the positively charge hydrogen atom was closer, then the framework responded as if a positive defect has been encapsulated and at the oxygen end of the hydroxyl group, the framework perturbed in the opposite way. The resulting structure deviated markedly from the symmetric starting structure and this observation serves to highlight the need to perform this type of calculation without any symmetry constraints. An interesting observation is that the bonding of the OH^- group once inside the D4R is predicted to

be more ionic or dipolar than in the isolated state; less electron density accumulates in the overlapping orbitals with more being placed in the atomic populations. This redistribution of electron density, once incorporated inside the D4R, manifests in a reduction in the bond length as compared to the isolated molecule.

The energies of the F^- and OH^- group showed that they were stable within the D4R, as observed experimentally, yet the Na^+ was calculated to be slightly thermodynamically unfavourable.

In summary, this work represents a new direction in the investigation of zeolite clusters via *ab-initio* techniques, allowing subtle aspects of structure and bonding to be investigated for systems of considerable complexity.

7.3 References.

1 Bibby D.M.; Dale M.P.; *Nature*, **317**, 157, (1985).

2 Bennett J.M.; Kirchner R.M.; *Zeolites*, **11**, 502, (1991).

3 Smith J.V.; Bennett J.M.; *Amr. Miner.* 66, 777, (1981).

4 Caullet P.; Guth J.L.; Hazm J.; Lamblin J.M.; Geis H.; *Eur. J. Solid State Inorg. Chem.*; **28**, 345, (1991).

5 Maxwell I.E.; "*New Perspectives in Catalysis*", Ed. Thomas J.M.; Zamaraev K.I.; IUPAC Oxford, Blackwell, (1990).

6 Haag W.; Lago R.M.; Weisz P.B.; *Nature*, **309**, 589, (1984).

7 Rietveld H.M.; *J. Appl. Crystallog.*, **2**, 65, (1969).

8 Dick B.G. and Overhauser A.W.; *Phys. Rev.* **112,** 90, (1958).

9 Jackson R.A.; Catlow C.R.A.; *Molec. Sim.*, **1**, 207, (1988).

10 Sanders M.J.; Leslie M.; Catlow C.R.A.; *J. Chem. Soc. Chem. Comm.*, 1273, (1984).

11 Lewis G.V.; Catlow C.R.A.; *J. Phys. C.*, **18**, 1149, (1985).

12 Catlow C.R.A.; Diller K.M.; Norgett M.J.; *J. Phys. C. Solid State Phys.*, **10**, 1395, (1979).

13 Leslie M.; Daresbury Laboratory, Report *In Press.*

14 Tosi M.P.; *Solid State Phys.*; **16**, 1, (1964).

15 Leslie M.; Daresbury Laboratory Report No. DL/SCI/TN31T, 1982.

16 Wyckoff, "*Crystal Structures*", **1**, 251, Interscience, J. Wlley & Sons. N York. (1965).

17 Flanigen E.M.; Bennett J.M.; Grose R.W.; Cohen J.P.; Patton R.L.; Kirchner R.M.; Smith J.V.; *Nature*, **271**, 512, (1978).

18 Gale J.D; Cheetham A.K.; *Zeolites*, **12**, 674, (1992).

19 Saul P.; Catlow C.R.A.; Kendrick J.; *J. Phil. Mag. B.*, **51**, 107, (1985).

20 Groenen E.J.J.; Kortbeek A.G.T.G.; Mackay M.; Sudmeijer O.; *Zeolites*, **6**, 403, (1986).

21 Barthomeuf D.; Derouane E.G.; Holderich W.F.; *NATO ASI Series*, **B 221**, 319, Plenum Press, N. York, (1990).

22 Couves J.W.; Jones R.H.; Thomas J.M.; Smith B.J., *Adv. Mater.*, **2**, 181, (1990).

23 CRC, Handbook of Chemistry and Physics, 66th Ed. CRC Press, Table F164.

24 George A.R.; Catlow C.R.A.; Nature, Submitted July 1993

25 d e Vita A.; Gillan M.J.; Lin J.S.; Payne M.C.; Stich I.; Clarke L.J.; *Phys. Rev. B.*, **46** (20), 12964, (1992).

26 DMOL; Biosym Technologies Inc.; 9685 Scranton Road; San Diego, CA, 92121, USA.

27 Press W.H.; Flannery B.P.; Teukolsky S. A.; Vetterling W.T.; "Numerical Recipes, "*The Art of Scientific Computing*"; Cambridge University Press; Cambridge, (1986).

28 Gibbs G.V.;'Arco P Boiser M.B.JR.; *J Phys.Chem,* 5347,(1987).

29 Dovesi R.; Pisai C.; Roetti C.; Silvi B.; *J. Chem. Phys.*, **86**, 6967, (1987).

30 O'Keeffee M.; Gibbs G. V.; *J. Phys.Chem.* ,**89**, 4574, (1985).

31 van Beest B.W.H.; Verbeek J.; van Santen R.A.; *Catal. Lett.*; **1**, 147, (1988).

32 Fripiat J.G.; Berger-Andre F.; Andre J.; Derouane E.G.; *Zeolites*, **3**, 306, (1988).

33 Gale J.D.; Private Comm.

34 Nada R.; Catlow C.R.A.; Dovesi R.; Pisani C.; *Phys. Chem. Miner.*, **1**, 353, (1990).

35 Dovesi R.; Pisani C.; Roetti C.; Causa M.; Saunders V.R.; "*Crystal88: An ab-initio all electron LCAO-Hartree-Fock Program for periodic systems*"; QCPE Program #577, Quantum Program Exchange; Indiana University; Bloomington; Indiania.

36 van Beest B.W.H.; Kramer G.J.; van Santen R.A.; *Phys. Rev. Lett.*, **64**, 1955, (1990).

Chapter 8

General Conclusions.

8.1 General Summary and Conclusions.

The results presented in the previous chapters show that both methods based on interatomic potentials and *ab-initio* calculations can be used to simulate various physical properties of zeolites and indeed, to aid determination of their structures, the interpretation of their vibrational spectroscopy and the understanding of the catalytic mechanisms.

In chapter 3, the relaxation of the zeolite framework around extraframework cations was investigated and several plausible models for aluminium distribution around the double six-ring were proposed. The resulting cation-oxygen distances for ions in the S_I sites were found to be in very good agreement with the EXAFS experiments[1] and the longer distances found by XRD were explained in terms of averaging over relaxed sites and unoccupied, unrelaxed sites. This line of investigation was continued with out study of the vibrational behaviour of such systems and indeed, only when several combinations of individual aluminium arrangements were coupled together, did the resultant calculated vibrational spectra begin to resemble the features observed in the experimental data. This is reasonable since the bulk sample contains many different aluminium arrangements and not just the ones proposed here. The study was extended to an investigation into the effects of different cation loadings and temperature on the zeolite motions, (details are reported in the Appendix to this thesis), indeed via Molecular Dynamics, (MD), oscillatory behaviour of the extraframework cations was observed. This vibrational behaviour has a distinct time period of approximately 0.35ps for the Ni^{2+} cations in the S_1 site and 0.45ps for the Na^+ cations in the less tightly bound S_2 site. Overall, the results presented in this chapter shows the need to employ several atomistic computational techniques to investigate the structural behaviour of a very complex catalytic system.

In chapter 4, the mechanistic steps involved in the cyclotrimerisation of acetylene to benzene were elucidated from the initial activation of the catalyst to the proposal of the detailed mechanism. In the dehydrated, unactivated form, the Ni^{2+}

cations are predominantly bound in the S_1 site, although some are entrapped inside the supercage via some residual water molecules. The process of activation of the catalyst entails migration of the Ni^{2+} ions from the S_1 site out into the supercage; as reported there is an energy barrier of approximately 2eV to this "unassisted migration", thus this barrier cannot be simply overcome via thermal means. Hence these systems are stable in the dehydrated form up to quite high temperatures. This "unassisted migration" is overcome by the reactant itself. Indeed, the *ab-initio* calculations showed that H_2O and NH_3 as well as acetylene interact sufficiently strongly with the migrating Ni^{2+} ion to overcome the barrier.

The migration of the cation out of the hexagonal S_1 site and into the supercage is only the first step of a very complex catalytic cycle. In section 4.2, we investigated how the acetylene molecules associate themselves around the cation in order to yield benzene. The investigation of the various stages of the molecule-Ni^{2+} interaction was performed in a number of different ways, firstly via a purely electrostatic approach and secondly via maximising the HOMO/LUMO orbital overlap, (an approach somewhat analogous to the Frontier Orbital type of approach in mechanistic studies.) The results showed that the approach of the first acetylene is dominated by purely electrostatic factors, the approach of the second molecule is influenced by both orbital overlap and electrostatic interaction, although the electrostatic one is probably dominant. It is important to note that these two acetylene molecules are not yet bonded to each other, but are acting as simple ligands. Only when the third molecule approaches with a specific orientation, do these previous two molecules bond. The product is <u>not</u> benzene but a stable intermediate, (which would not be expected from the classical Diels-Alder type of concerted ring formation). The third molecule dissociates, which is probably the rate determining step and the complex subsequently readjusts with the acetylene molecules still bonded. The third molecule now associates again but with a different topology for the orbital overlap and an open benzene molecule is formed; the benzene ring closes upon dissociation from the cation. We have therefore elucidated a very complex mechanism but moreover, we have not only

reported intermediates but also why and how these intermediates are aligned. This is somewhat more detailed than for many previously reported reaction mechanisms which only detail intermediates and give no indication of how or why they are oriented in such a way. Also reported was the redox reaction undergone by the Ni^{2+} cation, in which it was reduced effectively to a singly charged cation and then oxidised back to Ni^{2+} after the reaction.

Indeed, from the work reported in chapter 3 and 4, a comprehensive description of the Ni-Na-Zeolite-Y catalyst was elucidated. This involved a number of techniques which could now be applied to any number of other catalytically interesting systems, such as those tabulated in table 1.1.1 in chapter 1.

A distinct change of tack was described in chapter 5, whereby modelling was undertaken in advance of experiment, which is becoming increasingly possible with contemporary computational chemistry. Here a number of SiO_2/GeO_2 structures were studied and all were found to exist as solid solutions, though as the mole fraction of Ge was increased Vegard's Law was not necessarily obeyed. The variation in the physical properties was shown to be highly dependent on the position of the substitution of the larger Ge atoms in the framework and variations in structural properties of up to ±5% are reported. Moreover, a few of the Si/GeO_2 analogues studied and proposed in this section have since been made and are presently under characterisation. We also found as expected that the pure form of GeO_2 is more stable in the rutile than in the α-quartz structure. Yet in the structures previously reported, the pure GeO_2 remained in the α-quartz structure, thus the local minimum around the α-quartz phase was investigated and indeed, was found to be very well defined. By adjusting the unit cell angles from those appropriate for α-quartz to those for rutile, an activation barrier of +0.483 eV per T atom was calculated for the phase transition. Lattice energy minimisation and Molecular Dynamics were applied to the pure GeO_2 α-quartz structure but they could not fully model the phase transition. However, the techniques did locate other interesting local minima en-route, which may be worthy of further investigation.

The work reported so far and especially that in chapter 6, highlight the potential problem of local minima, which has caused difficulties in many computational investigations. These local minima are especially important when a highly flexible guest, such as an n-alkane, is included into a large structurally complex host, such as a zeolite; clearly this type of problem also applies to many other areas of chemistry, i.e. a target drug molecule and a complex flexible protein receptor. Chapter 6 reported work on "docking" of molecules within zeolites, using a technique which is designed to sample all important minima. the method was successfully applied to the inclusion of n-alkanes and 1-n-alkenes, into several zeolite structures, namely C_1-C_8 n-alkane, and 1-n-alkene into Chabazite and Silicalite-I. The results show that the interconnecting channel topology of Silicalite-I proved a more suitable host for the absorption of both types of hydrocarbon. However only the Chabazite structure showed any signs of possible use for the separation of alkanes from alkenes. We also investigated the problem of varying the loading or concentration of a particular guest, and in the second section, 6.2, methane molecules were successively docked into the Mordenite, Silicalite-I and Chabazite type structures. These systems showed very interesting behaviour whereby the methane molecules clustered together to form triads, especially if the interaction with the framework was not sufficiently favourable; and it is these triads that act as nuclei for the occupancy of less favourable parts of the zeolite, i.e. in the interconnecting channel intersections and large cavity voids. Indeed, the absorption of methane into the Chabazite structure typifies these observations.

In the search for new zeolite structures, several interesting novel synthetic routes have been proposed as viable alternatives for the common aqueous environment; one such route is via synthesis employing added F^- ions, but a fundamental problem arises, in that the F^- anion has been structurally located and appears "fixed" in the structure. The penultimate chapter, (chapter 7), investigates such a phenomenon by both atomistic and *ab-initio* techniques and an activation barrier of 3.15eV was found for the F^- migration out of the structure, as compared to the much lower barrier of 0.62eV for the OH^- migration. The F^- anion is calculated to

be thermodynamically stable in the double four-ring but as considered in chapter 4, an interaction with a suitable ligand can dramatically change this situation. The framework was also observed to perturb greatly the charge distribution and nature of the non-bonded extraframework species. Thus, for example, the encapulsation of OH^- inside the D4R increases the dipole moment of the OH^- ion.

As can be seen from these concluding remarks the field and area of application of computational chemistry is indeed widening, with many new and alternative explanations being proposed for yet experimentally unobservable phenomena. However, results of computational calculations must always be compared with experiment and thus the development of new techniques especially *in-situ* techniques in catalytic studies will greatly improve the communication between the computational and experimental chemist.

8.2 Future Pathways.

At the time of writing this thesis a new approach is being taken in computational chemistry, in that computer codes are becoming more applicable to a wider variety of systems and available for non-experts. Moreover, the rapidly advances in computer architecture and processor power mean that in a few years, the calculations of the type reported in this thesis will be entirely routine.

In addition, this increase in raw processing power is being matched by advances in graphical tools. And indeed, the theorist will soon be able to tackle macro-problems such as faults, crack propagation, stress and other engineering related phenomena that are observable on the macroscale. The advances in artificial intelligence, (AI), mainly in neural networks and virtual reality will also play an increasingly important rôle, (although our control over AI methodologies is less secure). What is certain is that computational tools will have an ever growing rôle in the study of complex phenomena.

8.3 References.

---

1 Dooryhee E.; Greaves G.N.; Steel A.T.; Townsend R.P.; Carr S.W.; Thomas J.M.; Catlow C.R.A.; *J. Chem. Soc. Farad. Trans.*, **89**, (1990).

Appendix.

Dynamical Behaviour of the Ni-zeolite-Y Catalyst.

A.1 The Dynamical Behaviour of the Dehydrated Ni-zeolite-Y Catalyst.

A.1.1 Introduction.

The structural investigations so far conducted into the Ni-zeolite-Y catalyst have involved static energy minimisation calculations, as typified by the results presented in section 3.1 and the subsequent investigation of the vibrational spectra based on the energy minimised configuration as described in section 3.2. The results of these simulations as previously demonstrated, are in good agreement with the available experimental data. However in calculations of this type, although we can demonstrate relaxation effects we cannot investigate the dynamical nature of the cation behaviour. In this section, we investigate the dynamical properties for varying temperatures, extraframework ion loading and for different possible aluminium arrangements, utilising the Molecular Dynamics, MD, technique.

A key feature of all these simulations, is the inclusion of flexibility in the zeolite framework. In the majority of previously reported MD simulations[1,2], the framework lattice was held rigid, which might be a suitable approximation for the simulation of organic molecules within zeolites where the lattice distortion is small, but for simulations involving highly polarising extraframework ions, such as Ni^{2+}, the framework lattice relaxation is very important, as shown in section 3.1 and as will be apparent from the results presented in this section.

A.1.2 Methodology.

In this investigation, the Molecular Dynamics, MD, technique was applied to several different models of the type discussed in section 3.1 for the Ni-zeolite-Y system.

The basic principles of the MD technique have already been discussed in chapter 2.5.1, so only the ensemble and simulation details will be reported here. An NPT ensemble, (constant pressure, constant temperature and constant number of molecules), was employed with the initial ion positions being derived from the resulting structures described in section 3.1. The potential parameters used are the same as those reported in section 3.1, except that a core-only representation has been used. In the MD simulation, the repeating unit cell was increased to a 2x2x1 super cell. Thus, 576 framework atoms were considered in each simulation with the number of extra framework ions being dependent on the system under investigation. A Boltzmann distribution of velocities was initially assigned to the atoms in accordance with the required thermal energies corresponding to, 300K, 600K, or 900K. Numerical integration of the velocities was performed over a time step of 1fs. Each system was allowed to evolve over 20ps, data acquisition for 5ps was subsequently undertaken. As we are primarily interested in structural and vibrational properties, such short simulation time are acceptable.

The nature of the framework vibrations are reported as both radial distribution functions, RDFs and as mean square displacements, MSD. The computer code FUNGUS[3] was used to perform the calculations, as it embodies all the desired features and uses the Verlet leapfrog algorithm[4] for the numerical integration. An Ewald summation[5] is also used for the calculation of the long range Coulombic interactions.

The systems to be investigated fall into broadly three categories:-

i) *Dynamical behaviour as a function of loading at 300K.*

In these systems the Ni^{2+} cations are introduced into the double hexagonal S_I prisms sites of the zeolite structure and the overall charge on the tetrahedral atoms is adjusted to retain charge neutrality. We recall that this was one of the models used in the previous section, 3.1, in investigating framework relaxations. The number of cations substituted can correspond to loadings of 25%, 50%, 75% or 100% substitution of the D6R. These different loadings can be thought of as models for the experimental system, which has been determined to exist with an approximate 66% loading of Ni^{2+} in the S_I sites in the dehydrated form. The percentages used are derived from the primitive F symmetry of the asymmetric unit cell of zeolite-Y.

ii) *Dynamical motion as a function of temperature.*

Each of the above models were simulated at 300K, 600K and 900K. This investigation into the behaviour of the zeolite at high temperatures is useful for investigating the calculated thermal Debye Waller factors from the simulations and for probing the extent of high temperature cation redistribution.

iii) *The effect of aluminium arrangements on the motions of the cations.*

In section 3.1, several plausible models were suggested for the possible arrangement of Al substitutions around the D6R and in section 3.2, we investigated the extent to which these could reproduce the experimental IR. spectra. In these MD simulations we used the same five aluminium arrangements, that were depicted in figure 3.1.1, and investigate the effect of the different arrangements on the motion of the cation. In these cases electroneutrality has been retained by placing two Na^+ ions at the S_{II} site and the motion and dynamics of these Na^+ extra framework cations is therefore investigated.

A.1.3 Results and Discussion.

i) Behaviour as a function of loading of extraframework cations into the lattice.

As described in the previous section, a series of cation loadings ranging from 25% to 100% substitution of the S_I site was investigated at 300K. The results are represented as time averaged radial distribution functions, RDFs, over the 5ps data acquisition period and the framework interactions are shown in figure A.1(a-c), which describe the O-Si, O-O and Si-Si RDFs respectively. The majority of O-Si bonds in the framework, (figure A.1(a)), retain the same length of 1.61Å, irrespective of the extraframework cation loading. However, the height of this peak decreases as a function of loading, and this redistribution is manifested by the formation of a second peak which increases in intensity as a function of loading. The second peak, with a maximum at 1.88Å, is involved with the extraframework cation location and upon closer inspection of the structure, the long O-Si bond is the bonded interaction contained within the D6R. This extension occurs because the inward oxygen relaxations towards the cation, increase the corresponding O-Si bond lengths, whilst the majority remain constant. The other features in the O-Si RDF are similar due to the vast majority of O-Si interactions being unaffected by the inclusion of the cations. For the non-bonded framework interactions, i.e. O-O and Si-Si, figures A.1(b,c) respectively, the peaks are very similar for all loadings and indeed any differences observed in the first peak can be attributed to the increased perturbation of larger numbers of the O-Si bonds around the D6R. The effect of increased extraframework cation loading on the Si-Si interaction is first to yield the second maximum after the first peak and then generally to smooth out and broaden the subsequent peaks.

Figure A.1(a-c) : The framework interaction RDFs grouped as a function of loading.

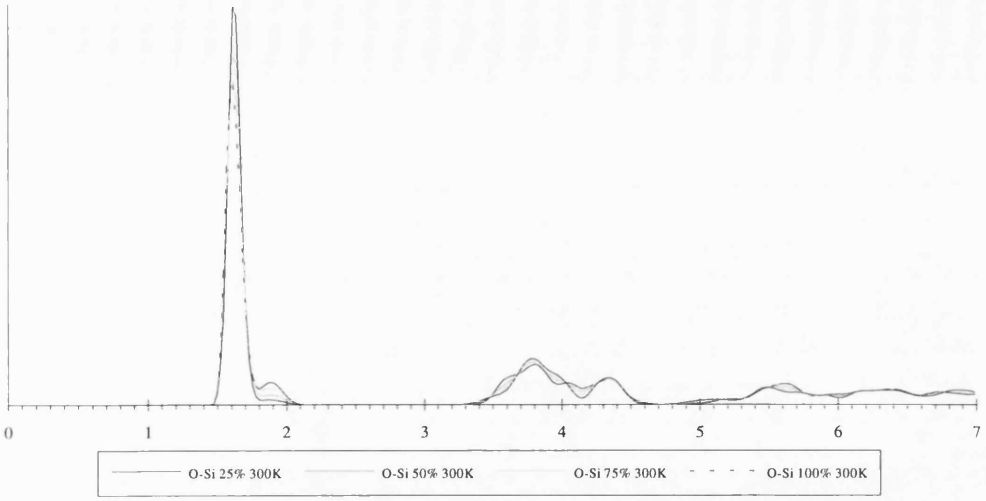

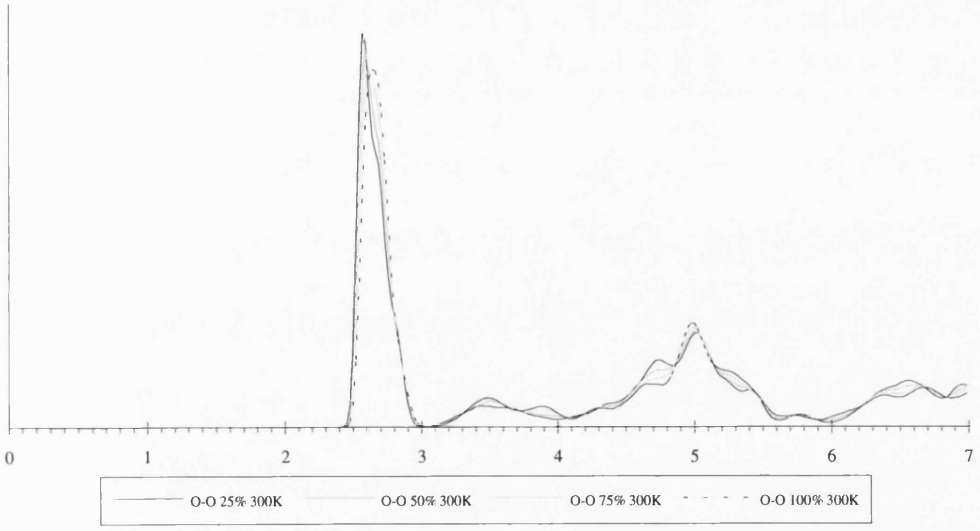

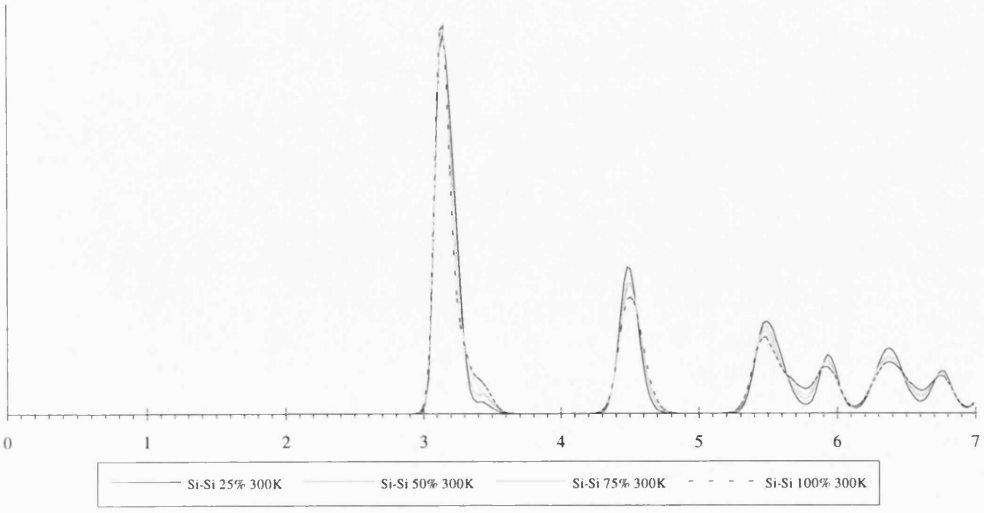

For the O-Ni interaction, (figure A.2(a)), the position of the first peak decreases slightly from 2.03Å (at 25% loading) to 1.99Å for 100% loading of the S_I site and the charge on the T atoms also decreases. Thus the first oxygen shell will not be bound as tightly to the T ions, due to the decrease in Coulombic energy between framework species. Interestingly, this interaction is not passed onto the second peak, centred around 3.0Å. These relaxations are thus very local. However, longer range effects do exist once higher loadings are simulated and this is due to the long range cation - cation interactions.

In the Si-Ni interaction, the first peak remains approximately constant at 3.31Å, implying that the effect of altering the T atom charge has little influence on this property. However, on closer investigation, the Si-Ni second shell shows a larger variation with loading, with this second shell Si-Ni distance decreasing as the loading of extraframework cations increases.

One feature the previously reported simulations could not investigate, concerns the perturbations and influences of the long range Ni-Ni electrostatic interactions. For loadings of 50% and higher, the cations are within 7Å of each other. As shown in figure A.2(c), the RDF is very ill defined because of insufficient data acquisition time, due to the constraints of the computational resources. However, one broad point is evident from this preliminary data. The 75% loading of extraframework cations shows a narrower spread of interaction distances, than is exhibited for the 50% or 100% loading. This is somewhat surprising as the 100% loading has the most symmetrical distribution of Ni^{2+} cations and might therefore be expected to have the best defined Ni-Ni separation. Clearly, Ni loading in the S_I site has a marked effect on the structural behaviour of the zeolite framework, especially at high loadings.

From the MD simulation it is possible to extract Mean Squared Displacements, MSD, and from this property the time evolution of the motion can be investigated. Figure A.3(a,b), reports the MSD values for the framework species, oxygen and silicon respectively. The displacements are measured from a fixed point of reference, usually the initial positions.

Figure A.2(a-c) : Non-bonded cation-framework RDFs.

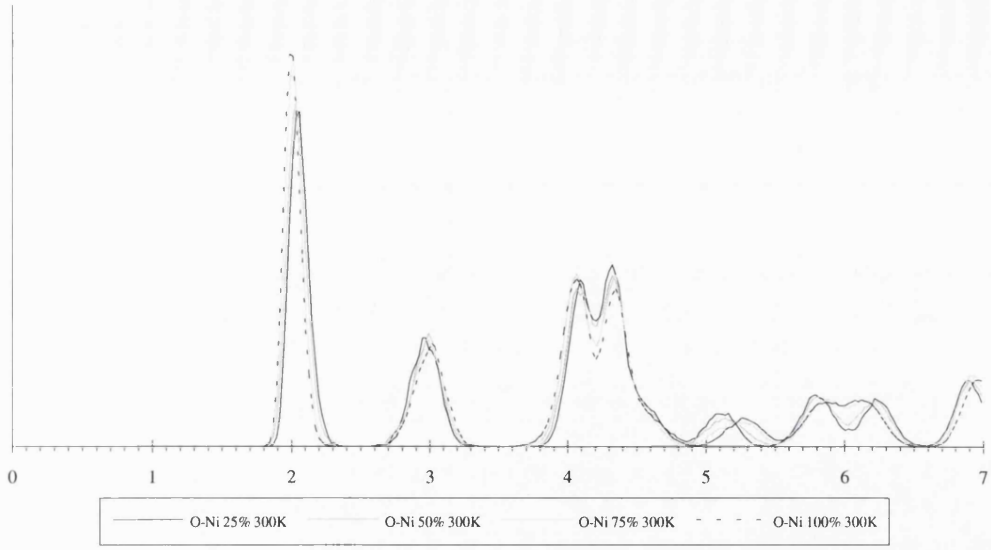

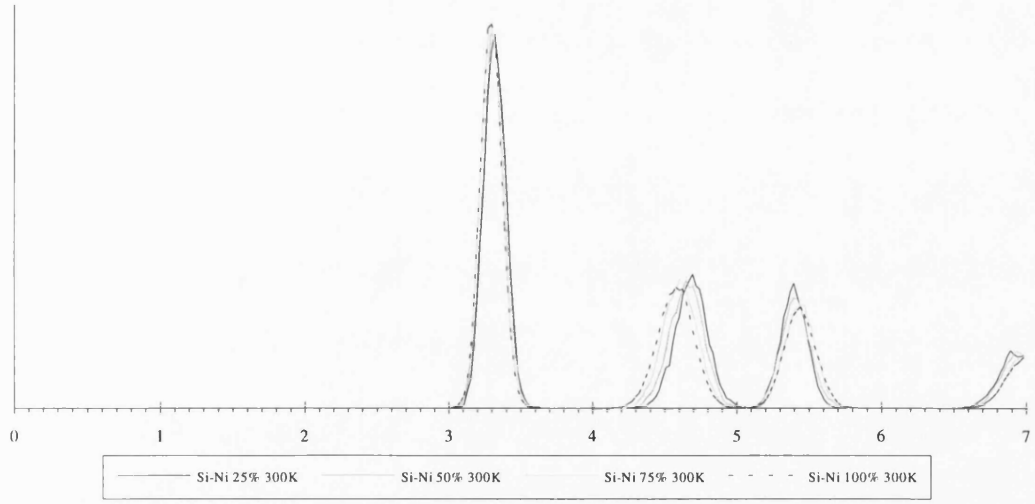

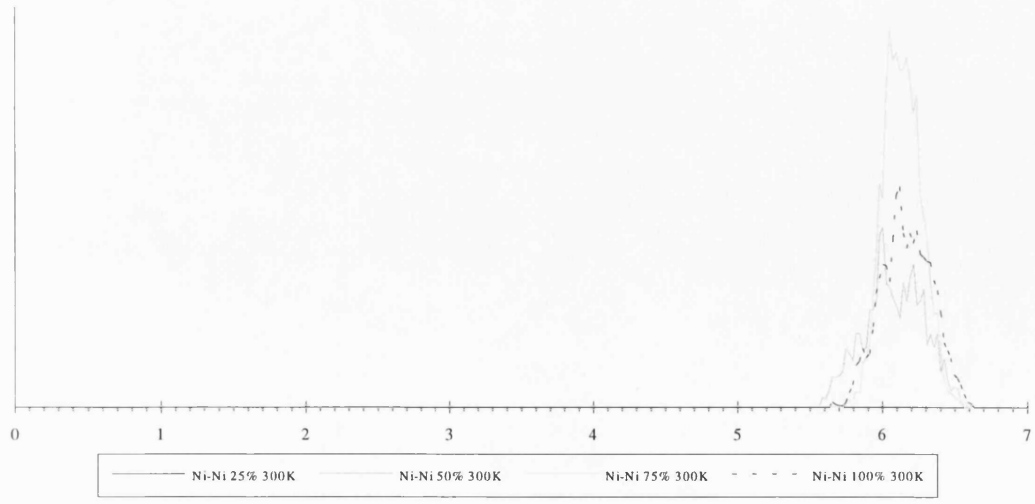

Figure A.3(a,b) : The MSD functions for the O and Si atoms at 300K. The various loadings have been shifted by 0.05 to allow clarification, with the units in $Å^2$.

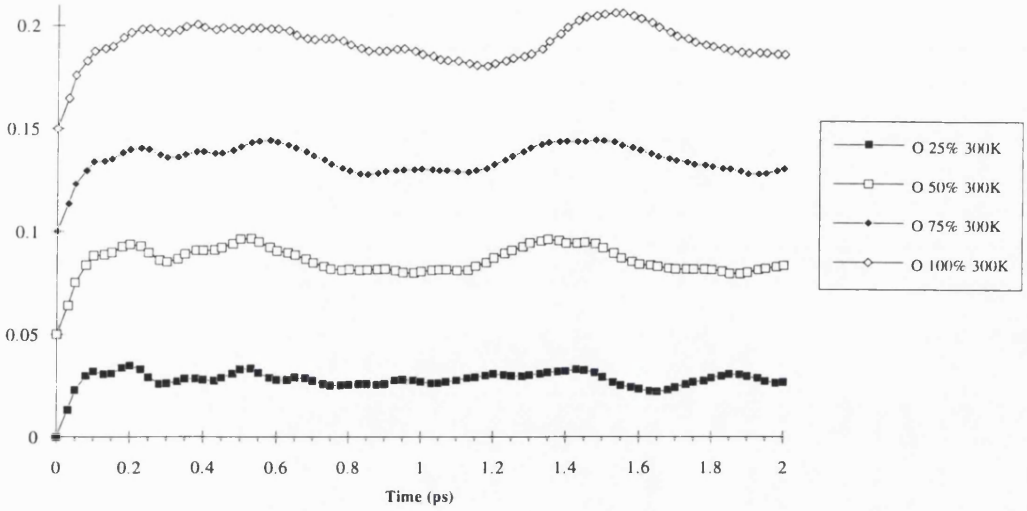

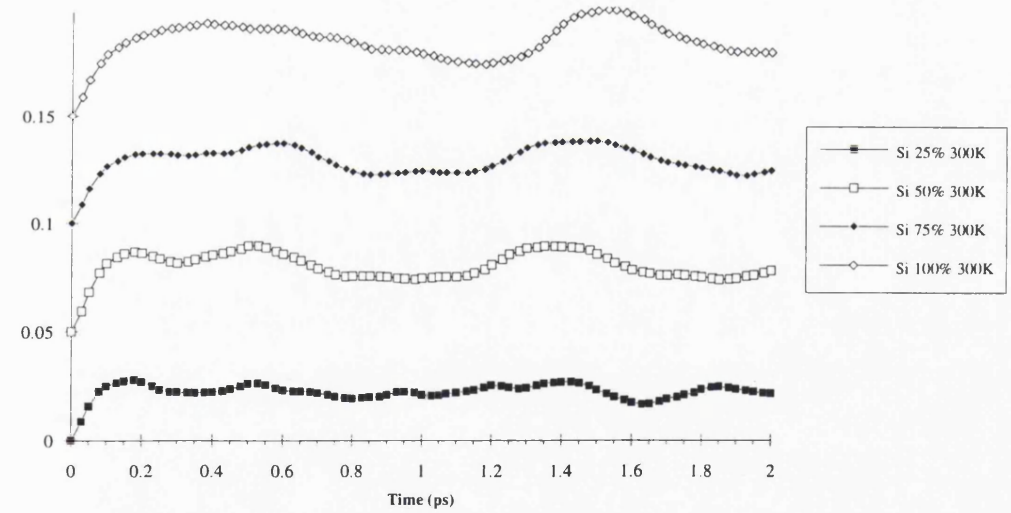

The effect of loading on the oxygen ion motions is marginal, in fact a number of features in the MSD curve have been smoothed out, i.e. the features around 0.25ps at 25% loading are better pronounced than for the 100% loading, but the reverse is true of the peaks around 1.45ps. The framework atoms are clearly, as expected, not diffusing but are simply oscillating in the framework structure.

The effect of loading of the cations is to increase slightly the motions of the framework atoms at 300K, i.e. approximately 0.18Å ±0.04Å for the O atoms and 0.17Å ±0.04Å for the Si atoms. Overall, the effect of cation loading on the framework motion is negligible at 300K, but very subtle perturbations have been observed that are worthy of further investigation.

So, as expected the framework species merely vibrate around their lattice sites. However, when the time evolution of the non-bonded cations are considered, a very complex process is observed. Figure A.4 reports the MSD of the nickel cations as a function of loading. Clearly, oscillatory behaviour is observed, with an amplitude much larger than previously reported for the framework species.

Figure A.4 : The MSD plots of the nonbonded Ni^{2+} cations.

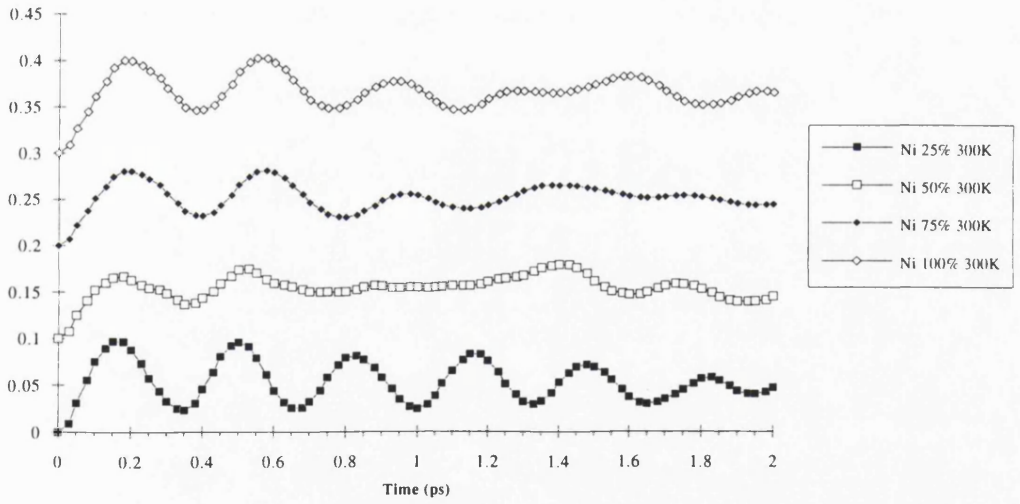

The motions of the 25% loading system at 300K, exhibit this periodic feature with the MSD only losing definition after 2ps; such a periodic oscillatory motion is indicative of vibrational motion, the coupling between which is as expected dependent on loading. For low loadings, the individual Ni^{2+} cations are weakly coupled and there is only a slow variation in the phase difference between the different oscillators. For higher loadings the high degree of coupling rapidly randomises the phase difference leading to a constant value of the MSD.

Table A.1 : The main MSD features of the various cation loadings at 300K.

		25% Ni	*50% Ni*	*75% Ni*	*100% Ni*
Nickel					
Average MSD	$Å^2$	0.229	0.233	0.225	0.256
Std Deviation MSD	$Å^2$	0.0219	0.0135	0.0153	0.0185
Periodicity	ps	0.325	0.375	0.325	0.375
Amplitude	Å	0.1566	0.1274	0.1106	0.1021

The periodicities of the oscillations, average MSD and amplitude of the first two cycles are reported in table A.1. The effect of loading on the cation motions is relatively similar because the average MSD and the associated standard deviation are approximately equal. Yet, the actual time-evolved motions are very different. The periodicity of the motions is essentially the same for all systems; thus, the cations motion within the D6R has a period of approximately 0.35ps and cover the allowed 3-dimensional space. The actual molecular motions of the cations is indeed very complex but by using the MD technique, these motions can be resolved.

ii) *Behaviour of systems as a function of temperature and loading.*

In this section, we will discuss results relating to variation of the temperature factors and loadings, as many of the catalytic cycles involving zeolites take place at higher temperatures. Figure A.5(a,b,c) report the **intra** framework separations O-Si, O-O and Si-Si for simulation at 900K. The results are grouped by loading so that a comparison can be easily made.

In the bonded framework vibrations, (O-Si figure A.5(a)), the influence of increasing temperature is as expected, as the peaks in the RDF become broader and smoother. The calculated Debye-Waller factors increase as the temperature is increased. Table A.2 reports the variations of the calculated O-Si Debye-Waller for all loadings. The Debye-Waller factors are approximately constant, within experimental error, for each loading at a particular temperature. Again this stresses the localised nature of the framework perturbations. As previously discussed, in the O-Si RDF, a second peak is observed to form at 1.88Å, as the loading of extraframework cations increases. However, this peak is only really well defined at around 300K, with the simulations at higher temperatures broadening it to such an extent that it coalesces with the first shell to form a weakly defined shoulder. The effect of thermal factors on the bonded O-Si framework interactions is to broaden the peaks and in doing this, the previously observed difference between the loadings is largely obscured.

Figure A.5(a-c) : Framework RDF interactions for the loadings investigated at 900K.

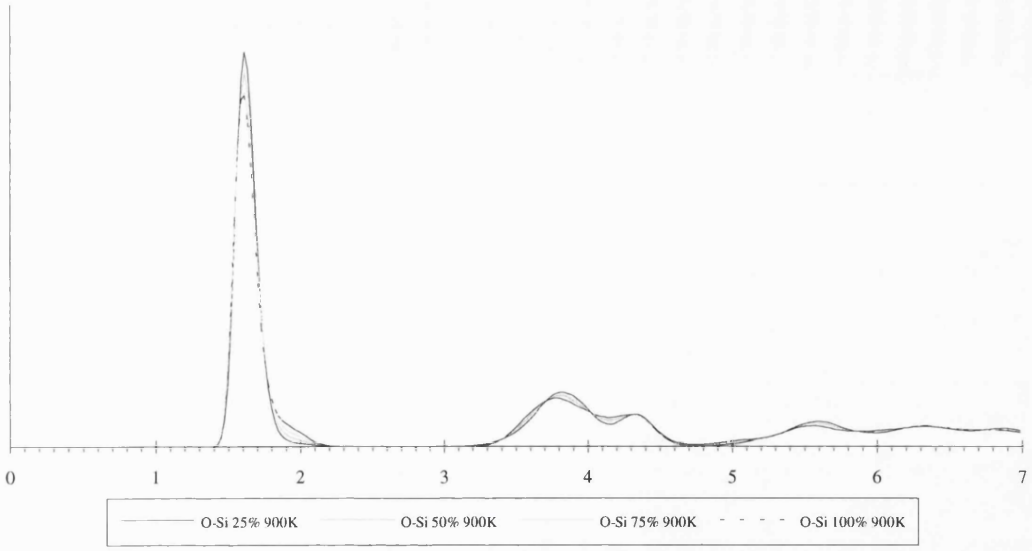

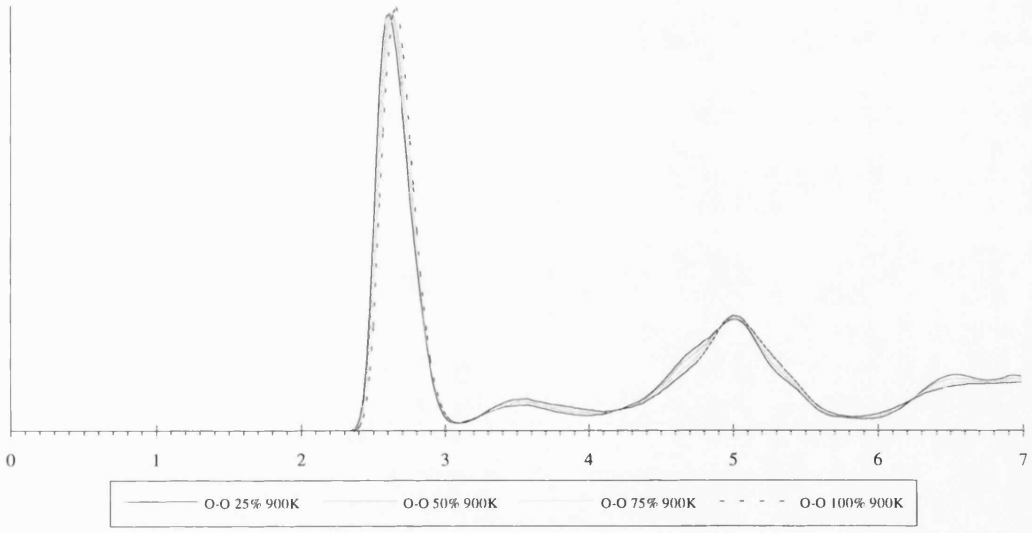

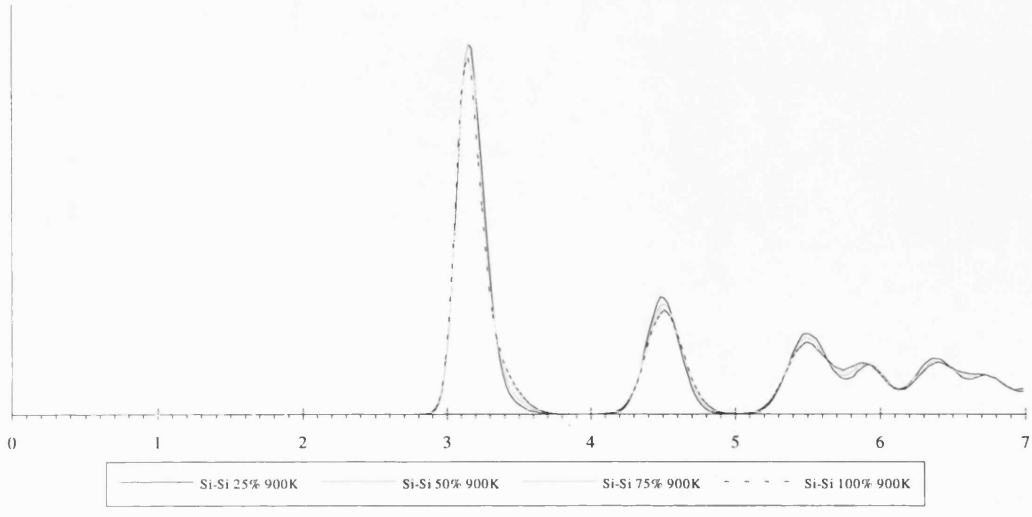

Table A.2 : Calculated thermal Debye-Waller factors, for the O-Si interaction at the different loadings and temperatures.

Loading	*Interaction*	*300K*		*600K*		*900K*	
		Debye-Waller	*Position*	*Debye-Waller*	*Position*	*Debye-Waller*	*Position*
		Å	Å	Å	Å	Å	Å
25%	O-Si 1st Shell	0.058	1.612	0.0686	1.612	0.076	1.612
50%	O-Si 1st Shell	0.059	1.612	0.067	1.612	0.0767	1.612
75%	O-Si 1st Shell	0.059	1.612	0.067	1.612	0.0759	1.612
100%	O-Si 1st Shell	0.055	1.612	0.0622	1.612	0.0708	1.612

The effect of raising the temperature on the O-O non-bonded framework interactions, is first to shift the maximum of the 25% and 50% systems and broaden the peak shape; while for the higher loadings, the temperature only acts so as to broaden the first shell interaction and does not shift the peak maximum. For the non-bonded Si-Si framework interactions, the effect of increasing the temperature is to broaden the peak shape and indeed, mask many previously discernible features.

Overall, the effect of increasing cation loading on the time-averaged framework structure becomes indistinguishable at elevated temperatures. Thus, the results presented here indicate that the effect of varying the cation loading from 25% to 100% on the behaviour of a purely siliceous framework is small once an elevated temperature has been reached. However, the effect on the framework of increased cation concentrations might be negligible at increased temperatures, but the effect of

the framework on the cation behaviour is markedly different. The results of the previous 300K simulation showed first that the first shell O-Ni distance decreased as a function of loading and this was attributed to the reduction in the tetrahedral charge and secondly that the long range doublet peak, ≈ 6Å, coalesced into a single peak. As the temperature is increased, the O-Ni first and second shell peaks broaden, (figure A.6(a)) and again the calculated Debye-Waller factors highlight this point, (table A.3). The effect of temperature is also to merge the doublet, (which occurs at ≈4.2Å in all systems), into a single peak centred in-between the previous doublet. The doublet observed in the 25% and 50% loadings around 6Å, now becomes a singlet mainly due to the thermal broadening of the peaks.

Table A.4 : Calculated Debye-Waller factors for the cation-framework interactions.

Loading	*Interaction*	***300K***		***600K***		***900K***	
		Debye-Waller	*Position*	*Debye-Waller*	*Position*	*Debye-Waller*	*Position*
		Å	Å	Å	Å	Å	Å
25%							
	O-Ni 1st Shell.	0.037	2.05	0.091	2.05	0.142	2.01
	O-Ni 2nd Shell.	0.110	2.99	0.169	2.99	0.151	2.94
	Si-Ni 1st Shell.	0.082	3.31	0.135	3.29	0.117	3.31
50%							
	O-Ni 1st Shell.	0.058	2.03	0.099	2.01	0.135	2.01
	O-Ni 2nd Shell.	0.085	2.99	0.149	2.99	0.186	2.97
	Si-Ni 1st Shell.	0.092	3.29	0.093	3.31	0.121	3.31
75%							
	O-Ni 1st Shell.	0.062	2.01	0.090	2.01	0.009	2.03
	O-Ni 2nd Shell.	0.105	2.99	0.153	2.99	0.209	2.99
	Si-Ni 1st Shell.	0.079	3.29	0.113	3.29	0.134	3.29
100%							
	O-Ni 1st Shell.	0.077	1.99	0.093	1.99	0.113	1.99
	O-Ni 2nd Shell.	0.089	3.01	0.140	3.01	0.229	2.99
	Si-Ni 1st Shell.	0.074	3.29	0.126	3.29	0.129	3.29

Figure A.6(a-c) : Cation-framework RDF plots for the various loadings at 900K.

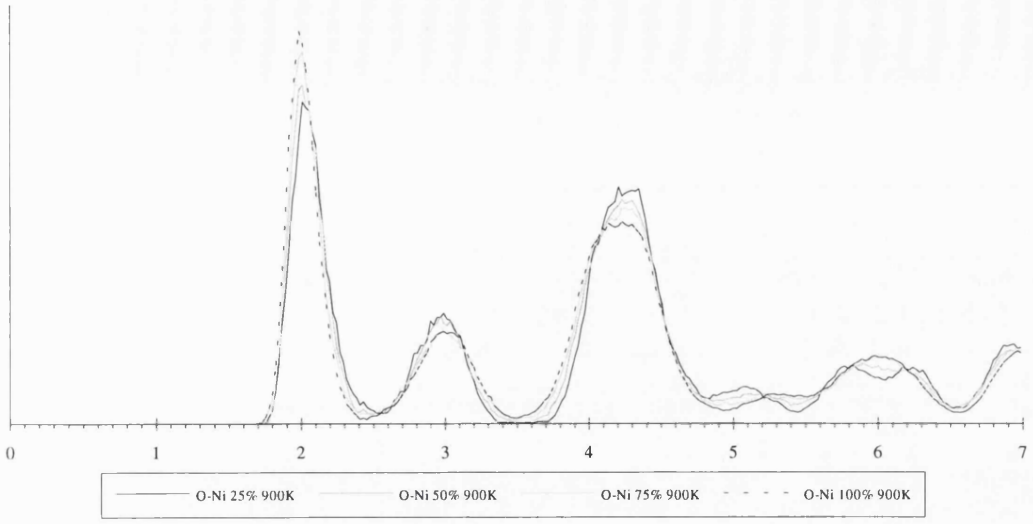

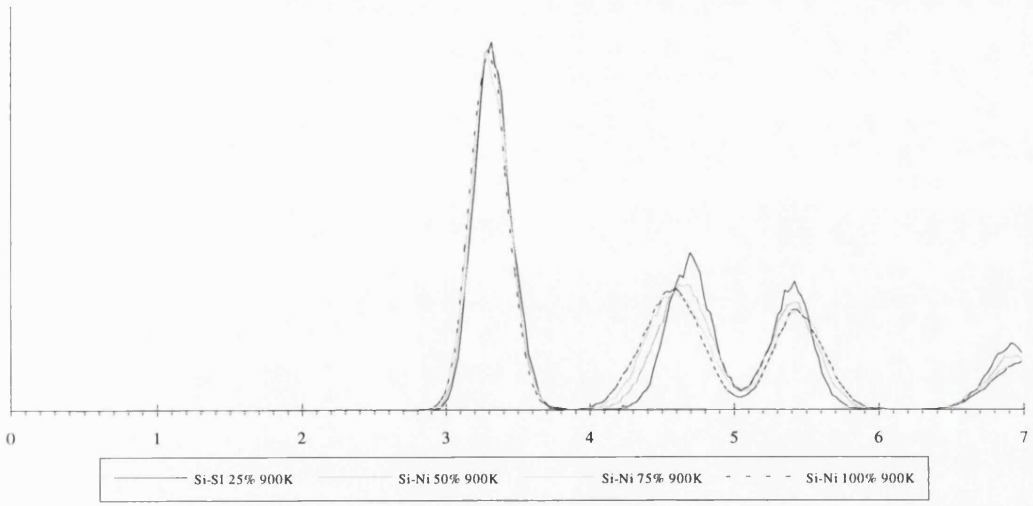

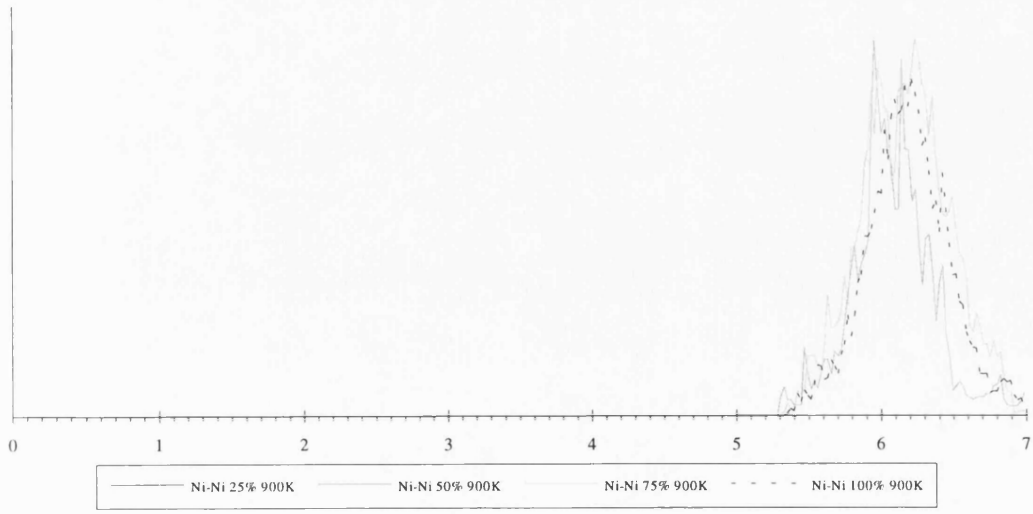

The effect of raising the temperature on the time averaged RDFs of the Si-Ni, (figure A.6(b)) and Ni-Ni, (figure A.6(c)) interactions is the expected broadening with increases in the calculated Debye-Waller factor, (table A.3). However, it is worth noting that the Ni-Ni interaction for the 600K, 25% loaded system is better defined more than either the 300K or 900K system, but due to the relatively short length of the simulation, 20ps, this cannot be investigated further.

The variation of the time averaged parameters has been discussed and resolved in detail, but this obscures any time evolution behaviour, which as described in the previous section showed an oscillatory motion of the Ni^{2+} cations. Indeed, figure A.7(a,b) reports the variation in MSD with temperature grouped as a function of the two extremes in loading. The effects observed are at first sight not as expected, one would envisage that an increase in thermal energy would; firstly, increase the average MSD and secondly, smooth out any of the underlying features previously reported for the 300K. Clearly, the increase in thermal energy has increased the average MSD, yet the features seem to be stronger and more pronounced than at 300K.

Figure A.7(a,b) : The MSD fluctuations for the 25% and 100% loadings and temperatures for all framework oxygen ions.

a)

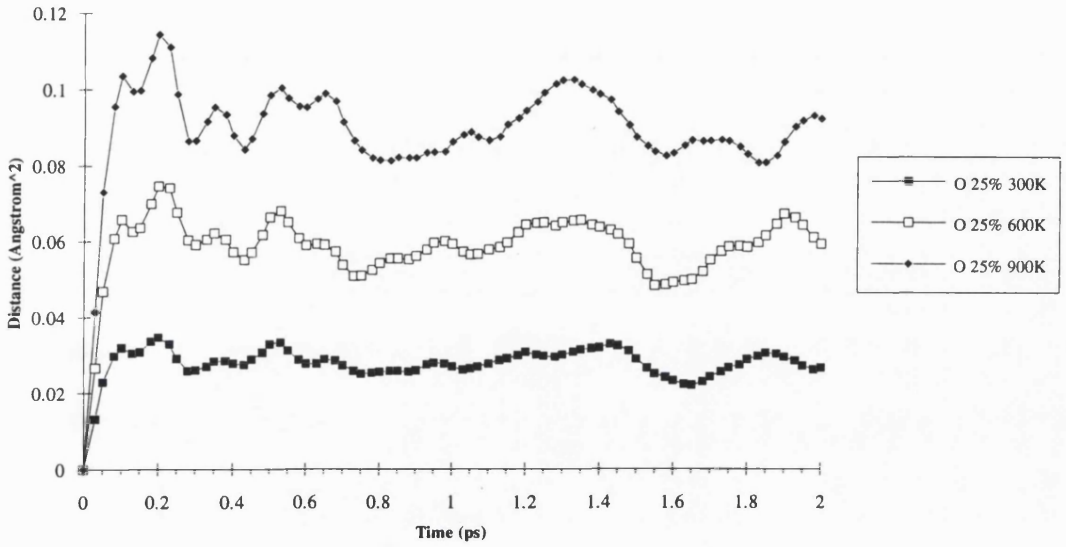

b)

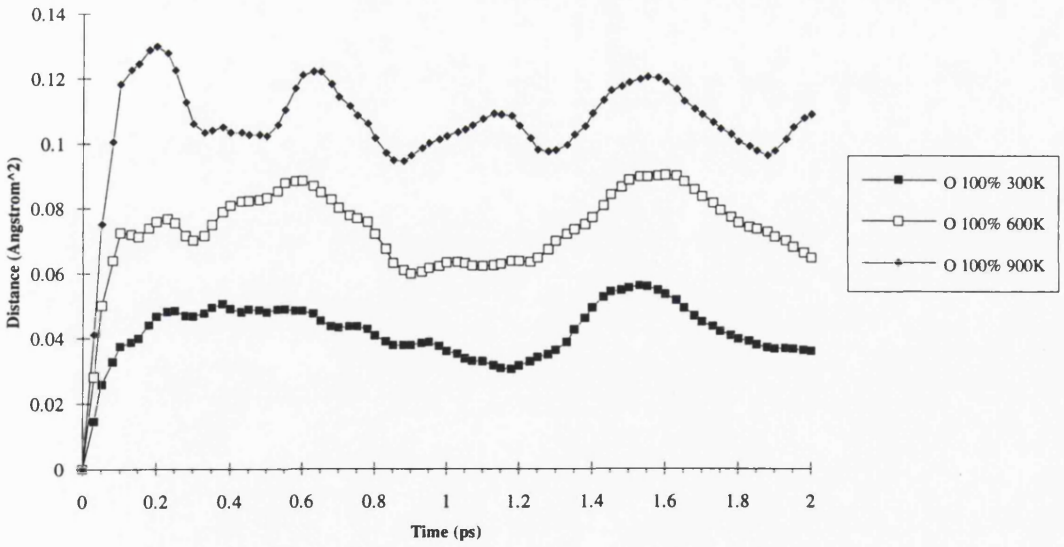

The averaged MSD for the O atoms, as expected increases with temperature, (table A.4). The same conclusions can be drawn from the MSD of the framework silicon atoms. Here the peaks show even more subtle changes which require a more in-depth investigation and longer simulations times to solve this highly complex motion.

Table A.4 : The average MSD, associated standard deviations and instantaneous velocities of all the framework ions at the different loadings and temperatures.

Loading		*Interaction*		*300K*	*600K*	*900K*
25%	Oxygen	Average MSD	Å^2	0.166	0.242	0.299
		Std Deviation MSD	Å^2	0.0044	0.00937	0.0138
	Silicon	Average MSD	Å^2	0.149	0.217	0.267
		Std Deviation MSD	Å^2	0.0039	0.0082	0.0123
50%	Oxygen	Average MSD	Å^2	0.189	0.25	0.321
		Std Deviation MSD	Å^2	0.0071	0.0118	0.0186
	Silicon	Average MSD	Å^2	0.173	0.235	0.291
		Std Deviation MSD	Å^2	0.0067	0.011	0.017
75%	Oxygen	Average MSD	Å^2	0.186	0.27	0.33
		Std Deviation MSD	Å^2	0.007	0.0129	0.0201
	Silicon	Average MSD	Å^2	0.17	0.244	0.298
		Std Deviation MSD	Å^2	0.0067	0.0119	0.0185
100%	Oxygen	Average MSD	Å^2	0.204	0.27	0.325
		Std Deviation MSD	Å^2	0.009	0.0135	0.0169
	Silicon	Average MSD	Å^2	0.186	0.243	0.292
		Std Deviation MSD	Å^2	0.0086	0.0125	0.0147

As reported in the previous section, the variations in the MSD of the non-bonded cations in the S_I site proved to be the most interesting, exhibiting oscillatory behaviour. The same MSD plots but grouped as a function of temperature are reported

in figure A.8(a-d). As expected the average MSD increases with temperature, (table A.5).

Table A.5 : The average MSD and standard deviation of the non-bonded Ni^{2+} cations.

Loading		*Property*		*300K*	*600K*	*900K*
25%	Nickel.	Average MSD	Å^2	0.229	0.295	0.344
		Std Deviation MSD	Å^2	0.0219	0.0251	0.0248
50%	Nickel.	Average MSD	Å^2	0.233	0.285	0.369
		Std Deviation MSD	Å^2	0.0135	0.0202	0.0016
75%	Nickel.	Average MSD	Å^2	0.225	0.288	0.404
		Std Deviation MSD	Å^2	0.0153	0.0181	0.0422
100%	Nickel.	Average MSD	Å^2	0.256	0.342	0.38
		Std Deviation MSD	Å^2	0.0185	0.0033	0.0349

In the 25% loaded system, the cation motion is highly correlated, i.e. the peaks are well defined and indeed, up to 600K the fluctuations are calculated to have the same periodicity, even though the cation velocities and overall motions are faster. However, at 900K, the motions appears to be de-correlated for a short time 0.4ps and then return in-phase, though at a different frequency from that previously observed.

For 50% loading, the oscillations are much more correlated at higher temperatures than for an intermediate temperature of 600K, but again after a few strong oscillations the motions de-correlate and then reform later at a different periodicity/frequency. However, for the 100% loading the effect of temperature really enhances the oscillations, increasing the amplitudes though not increasing the periodicity, the motions are decorrelated for 0.6ps and then reform at the same periodicity as before.

Figure A.8(a-d) : The time evolved MSD fluctuations of the non-bonded Ni^{2+} cations.

a) Ni cation MSD, 25% loading.

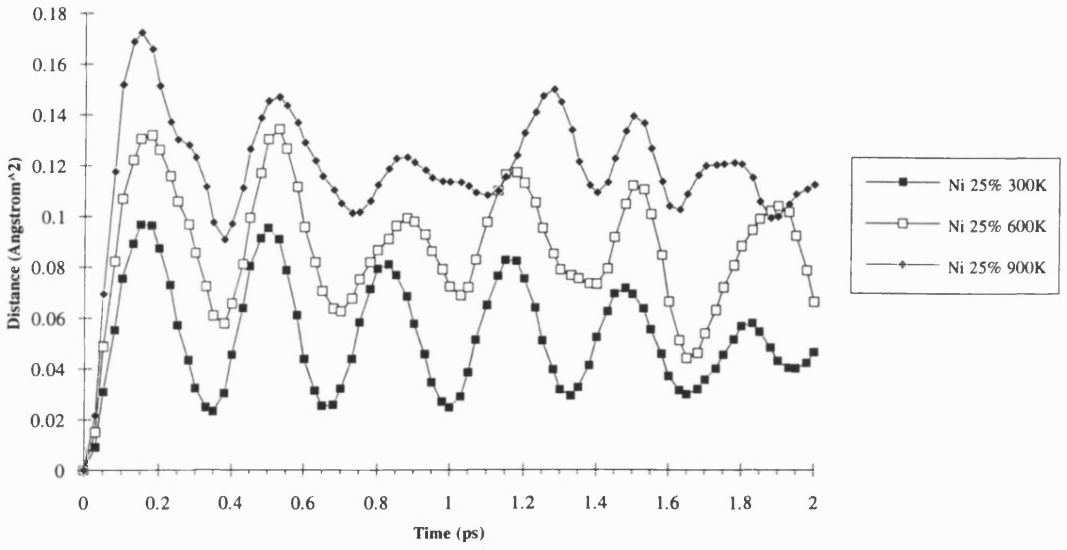

b) Ni cation MSD, 50% loading.

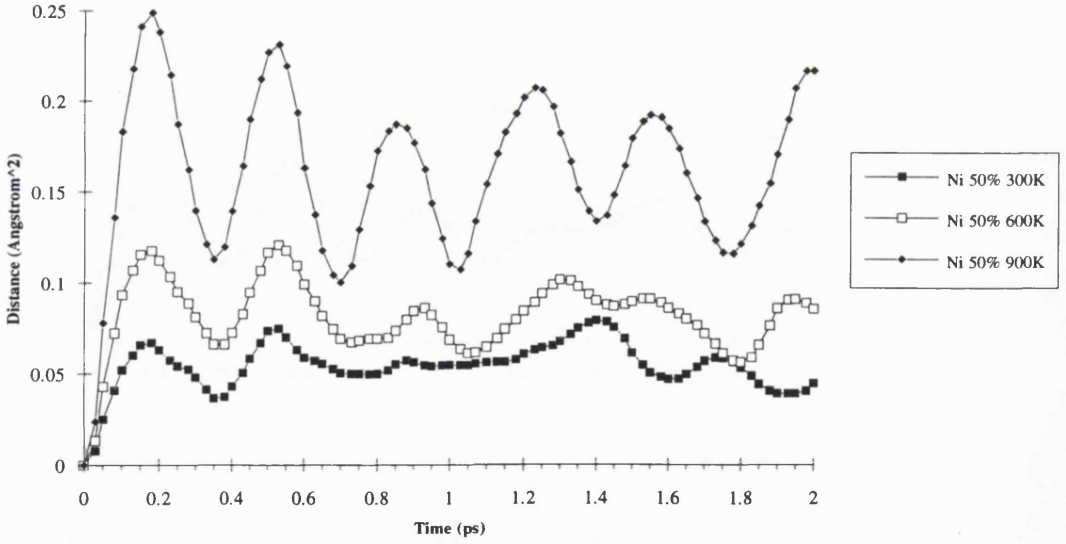

c) Ni cation MSD, 75% loading.

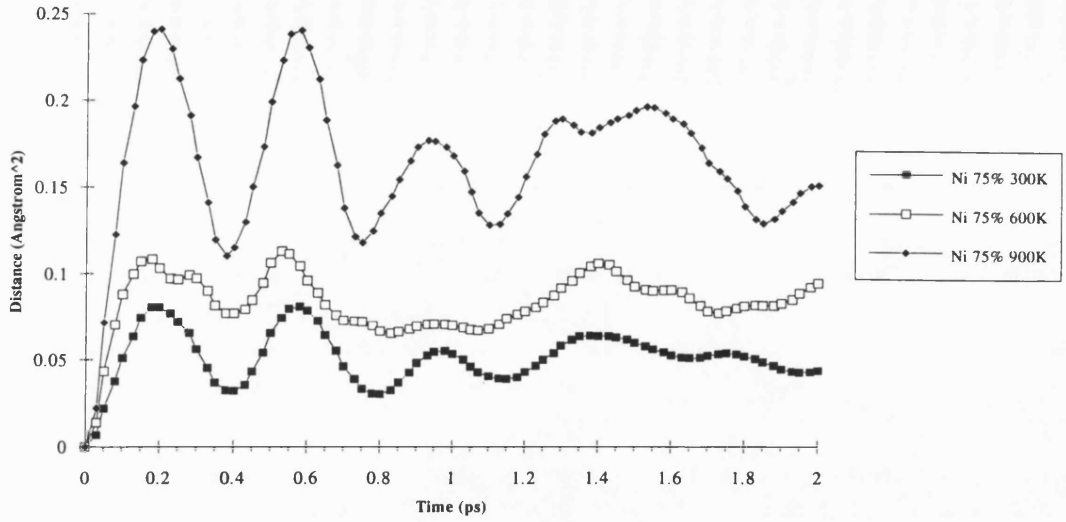

d) Ni cation MSD, 100% loading.

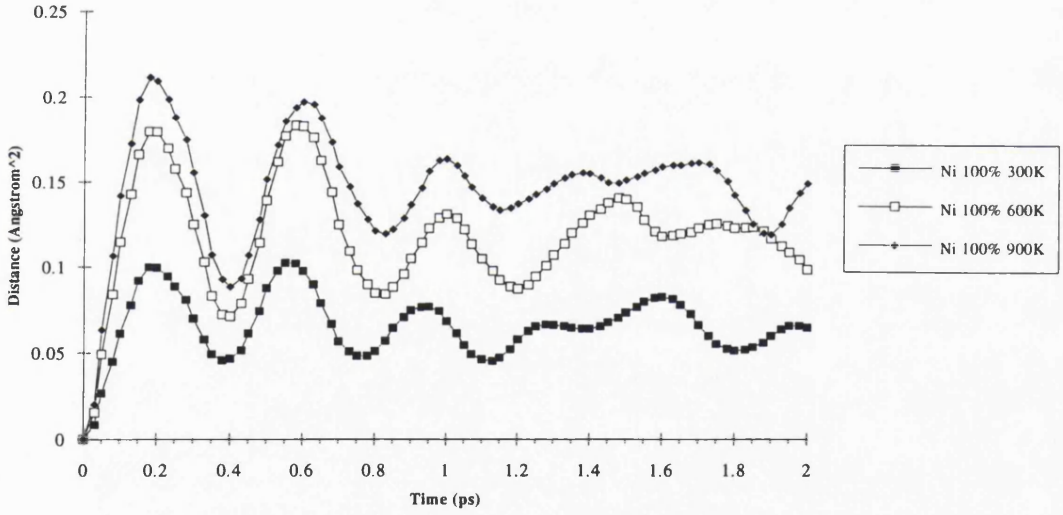

Clearly, these motions are highly coupled because varying the temperature has little effect on the periodicity, although the amplitudes are larger. There is some very interesting structural chemistry being observed in these simulations which requires longer simulation times than those performed within this thesis to give justice to the motions of the framework and extraframework species.

iii) *The kinetic behaviour of the models in several possible aluminium arrangement.*

As described in the previous section, 3.1 several plausible spatial arrangements of aluminium around the D6R have been investigated, using static lattice and harmonic lattice dynamical techniques, (section 3.2). These models yielded structures or frequencies closer to the experimental data than for the purely siliceous models. The aluminium distribution investigated are the same as those described in section 3.1 and are again reported here, (figure A.9).

Figure A.9 : The aluminium arrangements used to investigate the effect on the cation behaviour.

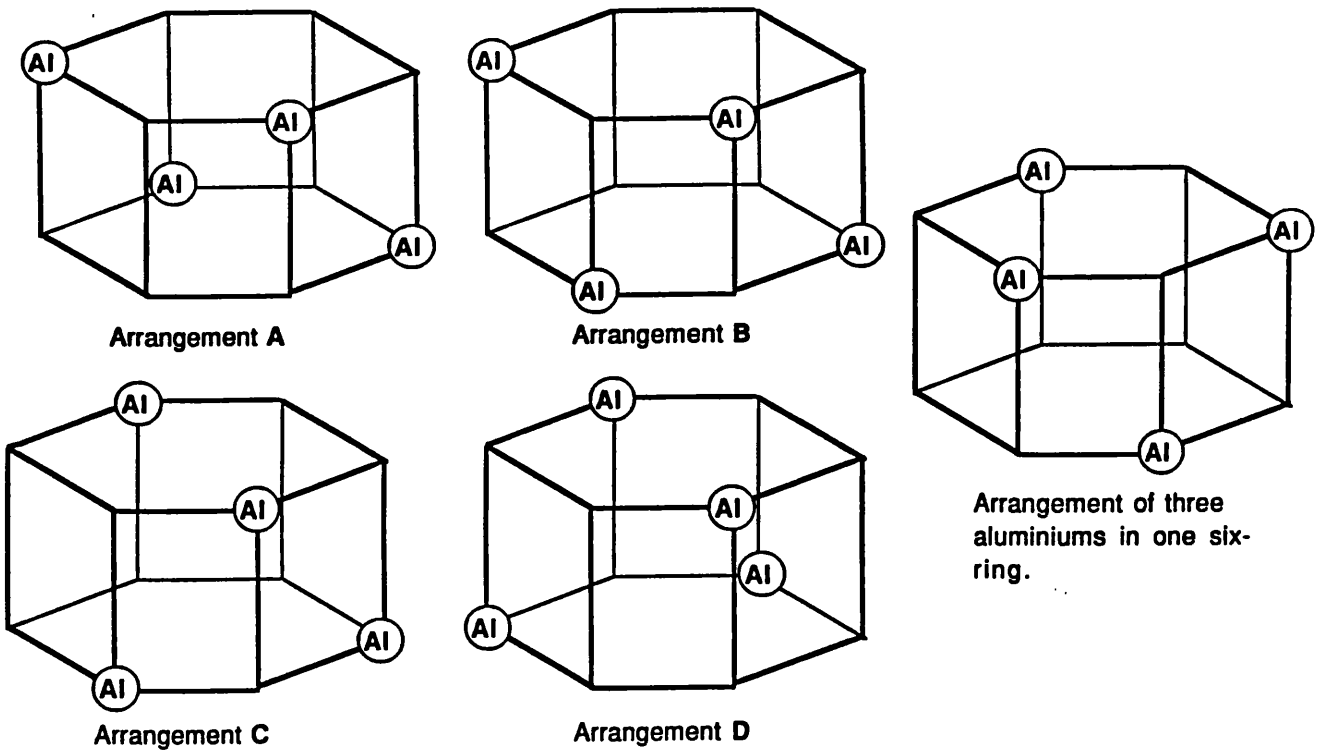

The effect of introducing aluminium into the D6R is to perturb the previously smooth Madelung field, which existed in the purely siliceous model, into a more uneven field with more distinct variations due to the replacement of Si^{4+} by Al^{3+}. Each proposed aluminium arrangement was investigated at a temperature of 300K. The effect of the aluminium substitution on the framework behaviour will be discussed prior to the effect on the more complex extraframework cation motions.

Figure A.10(a,b) shows the time averaged RDFs for all the bonded framework interactions, for the different Al distributions. The O-Si time averaged behaviour, again exhibits a single maximum at 1.61Å but no shoulder is observed around 1.88Å, because the effective loading is only 25% and the statistical number of longer O-Si bonds is not large enough to be observed above the thermal vibrations. Upon comparison with the 25% loading of the purely siliceous model around this distance, the intensity is even lower, suggesting that the oxygen relaxation has been fed into the O-Al bonds. The first O-Si shell in the Al arrangement models is more asymmetric than found with the purely siliceous model, and is strongly disimilar from a Gaussian distribution. This point has implications for experimental structural studies which rely on the use of Debye-Waller factors, which are generally assumed to have a Gaussian distribution, thus, slight inaccuracies will be incurred by such an approximation. The type of aluminium distribution has little effect on the time averaged behaviour when compared to the purely siliceous models.

The O-Al RDF, figure A.10(b), exhibits a first peak at 1.75Å and is clearly very asymmetric in nature. This asymmetric nature is due to the longer O-Al bonds influenced by the large inward oxygen ion relaxation toward the cations oscillating in the D6R. Again, when the instantaneous RDF is considered, i.e. that for a single conformation, the long O-Al bonds are visible and occur as a discreet group of peaks between 1.9Å and 2.1Å. This asymmetric first shell in the time averaged O-Al RDF is made up of the coalescence of two peaks, one predominant peak centred at 1.75Å and another less intense centred around 2.0Å. An interesting point is that the long O-T bonds are longer for the case of an Al distribution than for the purely siliceous case.

Clearly the inward relaxation of the oxygen ions is larger for the Al arrangements than for the purely siliceous arrangements - a result that is in close agreement with the defect calculations reported in section 3.1.

The non-bonded interactions between the framework oxygen ions in these models for the aluminium distribution shows very similar features to those described for the 25%-50% cation loading of the purely siliceous models at the same temperature, although the first peak is distinctly more asymmetric in shape. This asymmetric shape is obtained in the RDF and is due to a mixture of T atoms in the framework, and indeed once a full loading of aluminium is introduced into the framework, a more distorted first shell is expected.

The T atom non-bonded interactions, i.e. Si-Si, Si-Al and Al-Al show broadly the same features as described for the purely siliceous models. The Si-Si interaction shows a first peak at 3.17Å and is almost Gaussian in shape, yet lacks the shoulder observed for the purely siliceous models, whereas in the Si-Al, the first peak maximum is centred at 3.15Å, with a more asymmetric nature to the peak shape. In the case of the Al-Al time averaged RDF, there is no Al-Al interaction below 4Å, since all the arrangements obey Löwensteins rule.

Generally, the effect of limited aluminium distribution on the framework vibrations, does not perturb the time averaged motions in a definite well defined manner, yet, the instantaneous motions can reveal a more subtle behaviour. Indeed, such an observation partially validates the use of a purely siliceous structure in the majority of cases.

Figure A.10(a,b) : The bonded framework interaction RDFs for all the aluminium models investigated.

a) The RDF for the O-Si bond as a function of Al arrangement.

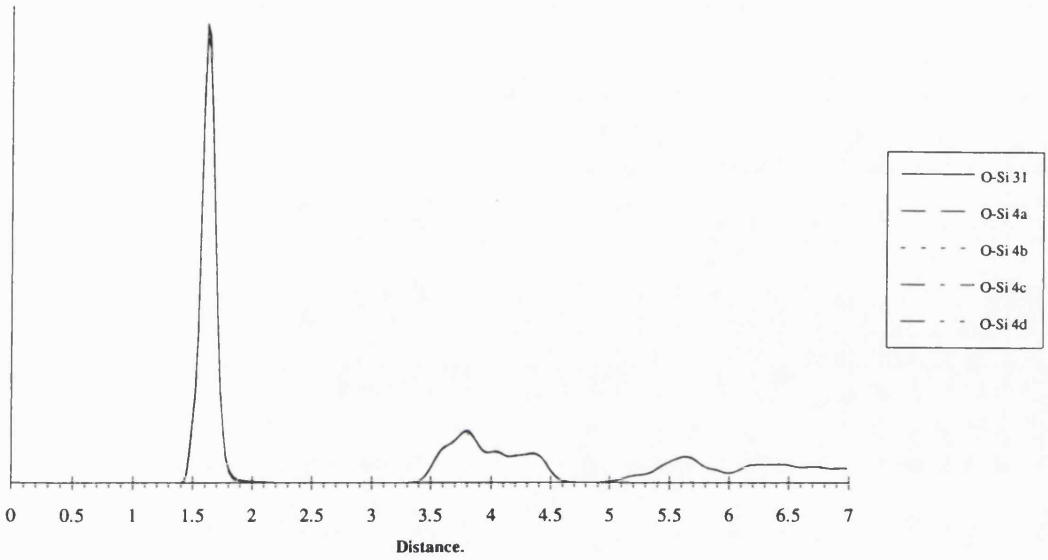

b) The RDF for the O-Al bond as a function of Al arrangement.

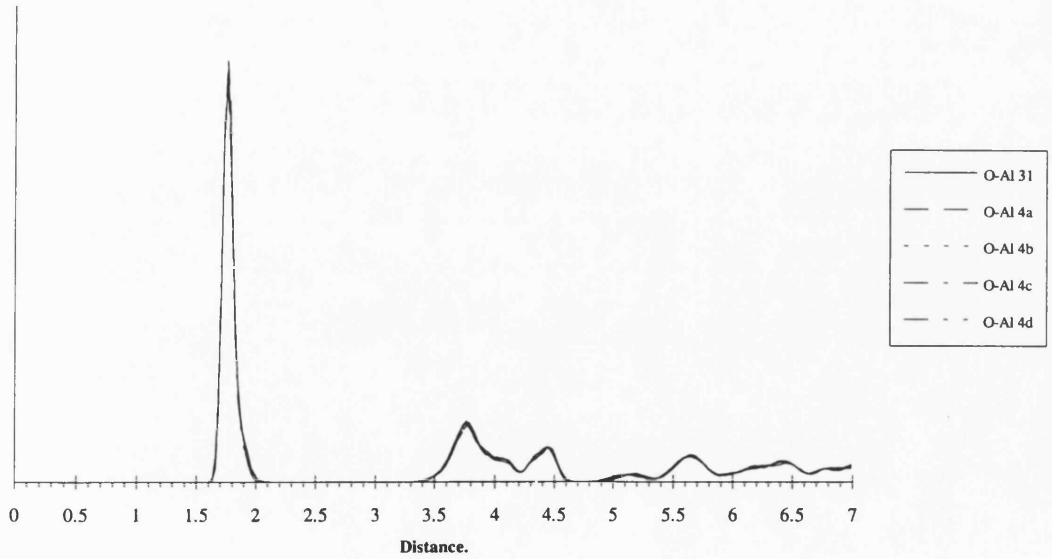

Figure A.11 (a,b,c) : The Ni^{2+}-framework interaction RDFs.

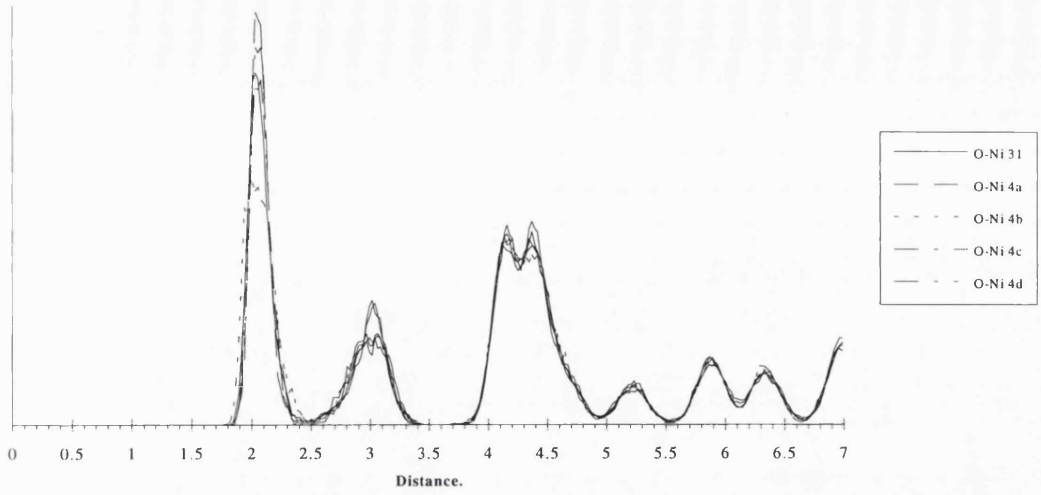

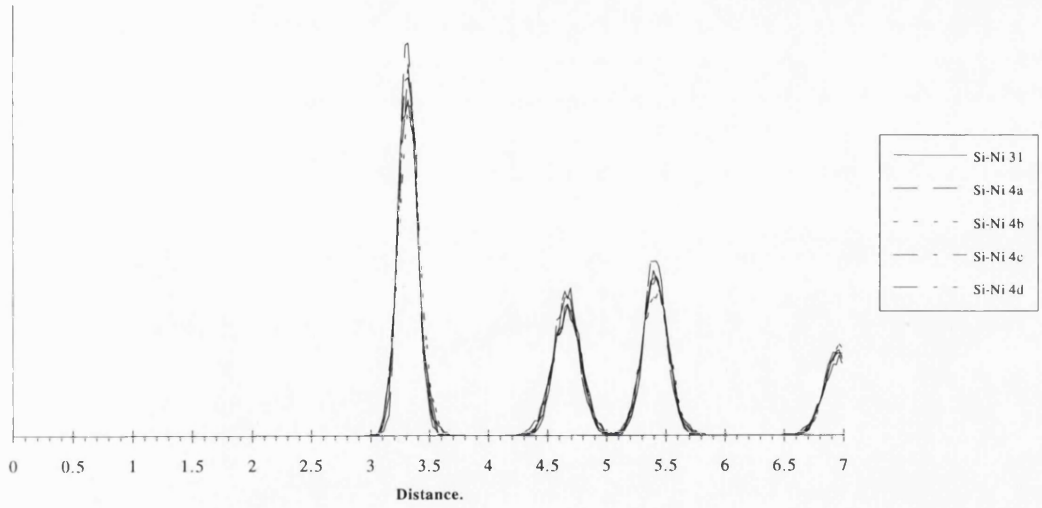

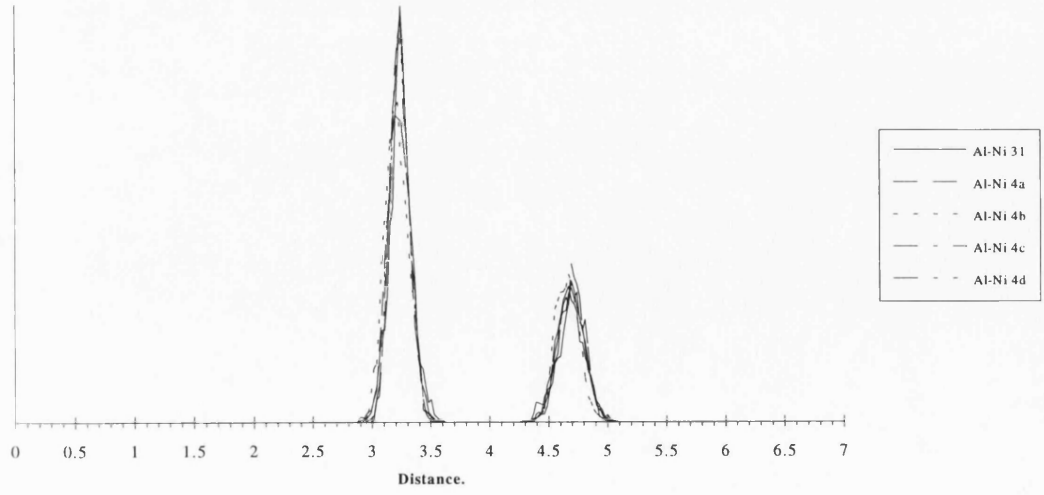

The time averaged cation behaviour inside an aluminated D6R, can be investigated by reference to the cation framework RDFs, figure A.11(a,b,c), which report the O-Ni, Si-Ni and Al-Ni separations. Table A.6, describes the calculated Debye-Waller factor and corresponding shell maxima positions for the Ni-framework behaviour.

The maximum of the first shell O-Ni interaction, ranges from 1.99Å for the **Al4_B** arrangement to 2.08Å for the **Al4_D** arrangement, yet the numerical average for all the arrangements is 2.03Å, which is in excellent agreement with the EXAFS first shell data of 2.02Å. Indeed, the O-Ni value is closer than that reported in the static lattice calculations, (section 3.1). For the second O-Ni shell there is a marked difference between the results for the symmetric and asymmetric distributions of aluminium in the D6R. The symmetric distributions reveal a more diffuse peak, whereas the asymmetric aluminium distributions show a well defined peak. This is partially reflected in the higher Debye-Waller factors for the symmetric arrangements. The third shell interaction, which was a well defined doublet in the purely siliceous models, is now less well defined and resembles a highly coalesced singlet.

Table A.6 : Calculated Debye-Waller factors for the Ni-framework interaction.

	O-Ni 1st Shell.		***O-Ni 2nd Shell.***		***Si-Ni 1st Shell.***		***Al-Ni 1st Shell.***	
	Debye-Waller	*Position*	*Debye-Waller*	*Position*	*Debye-Waller*	*Position*	*Debye-Waller*	*Position*
	Å	Å	Å	Å	Å	Å	Å	Å
Al3_1	0.096	2.03	0.100	3.04	0.082	3.31	0.059	3.25
AL4_A	0.102	2.03	0.105	3.01	0.071	3.32	0.061	3.25
AL4_B	0.181	1.99	0.106	3.06	0.098	3.32	0.078	3.23
Al4_C	0.066	2.08	0.1523	3.04	0.063	3.32	0.080	3.20
Al4_D	0.108	2.03	0.189	2.97	0.079	3.32	0.064	3.25

The T-Ni atom separations i.e. Si-Ni and Al-Ni show similar overall trends as described for the purely siliceous models and the first Al-Ni shell exhibits a shorter interaction distance of around 3.2Å whereas the first shell maxima for the Si-Ni distances is 3.32Å. These observations show that the Al containing framework is more flexible and is thus perturbed to a greater extent by cations inclusion than is the case for the purely siliceous models and that the non-bonded S_I cations prefer to reside near the Al^{3+} ions rather than the Si^{4+} ions, a feature which can be qualitatively explained on an electrostatic basis.

In the cases investigated above, charge neutrality was retained by initially locating Na^+ ions at the experimentally observed S_{II} site. The environment around such a site can be considered to be purely siliceous since only the D6R was substituted with aluminium ions in these models and the Al-Na interaction distance does not occur within the RDF maximum value of 7.0Å. Figure A.12 reports the time averaged RDFs for the O-Na nonbonded interaction. Clearly these vibrations are much broader than for the corresponding Ni-framework interactions, since the ions have a lower charge and the cations in the S_{II} sites are not so tightly bound, as for those located in the more restricted S_I site. In the O-Na interaction, the first peak is at 2.87Å, with a Debye-Waller factor of $0.158Å^2$, which is much longer and larger than the distance and Debye-Waller factor observed for the nickel cation. The width of the peak implies that the molecular motions of the Na cations are much larger, (a fact also derived from the MSD plots.) For the time averaged Si-Na interaction RDF, the first peak occurs at 3.51Å, which is very similar to the Si-Ni distances, again the calculated Debye-Waller factor is in excess of $0.14Å^2$ at 300K. Clearly, the Na^+ ions at the S_{II} site are more accessible than the Ni^{2+} cation at the more restricted S_I site.

Figure A.12 : The RDF for the Na^+-framework interaction.

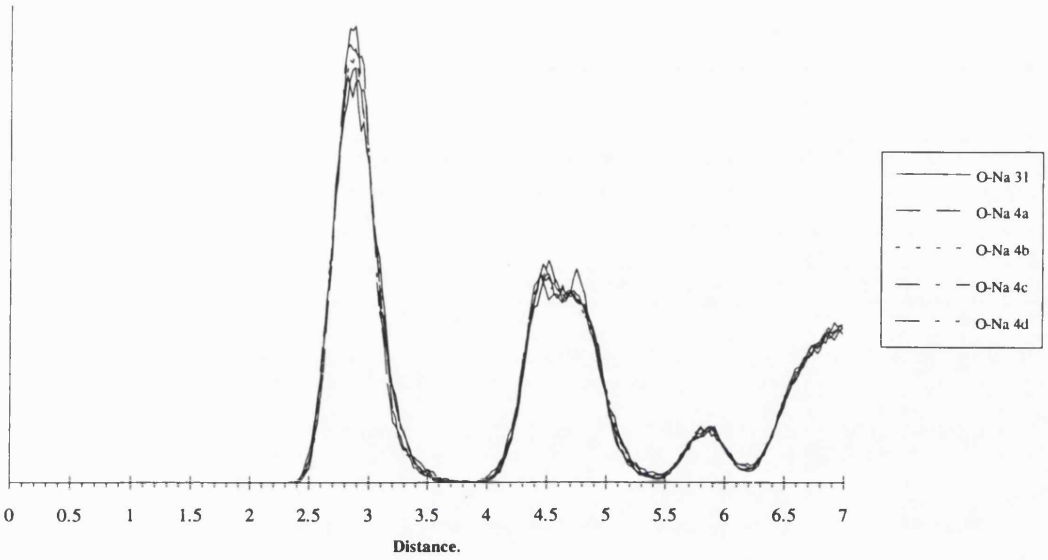

The results reported above relate to the time-averaged processes but it is possible to represent this as MSD plots and indeed, the previously described oscillatory behaviour is observed for both types of extra framework cation. Figure A.13(a-c) report the MSD plots for each species in the framework. In each case, the different aluminium arrangements have been overlaid since, as demonstrated in section 3.2, all could be present in the bulk sample.

Figure A.13(a-c) : The time evolved MSD plots for all the framework species in the aluminium arrangement models.

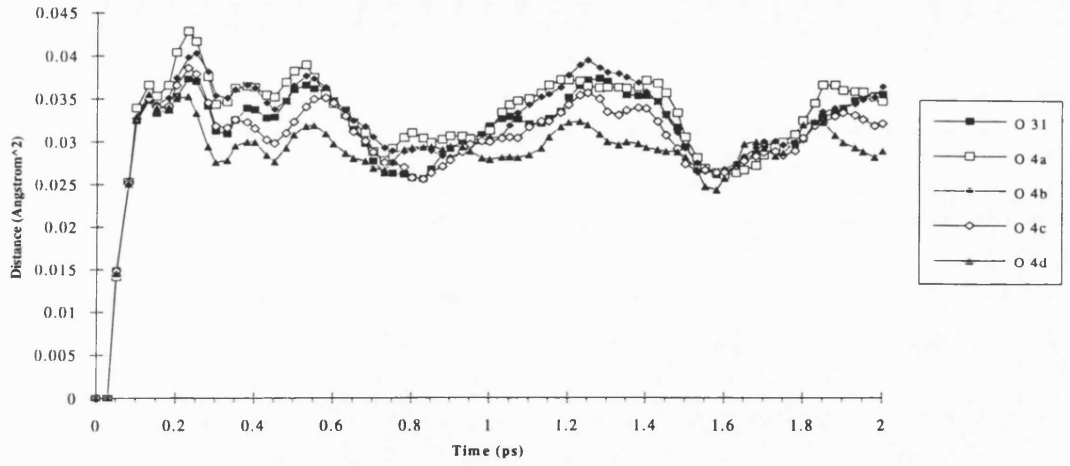

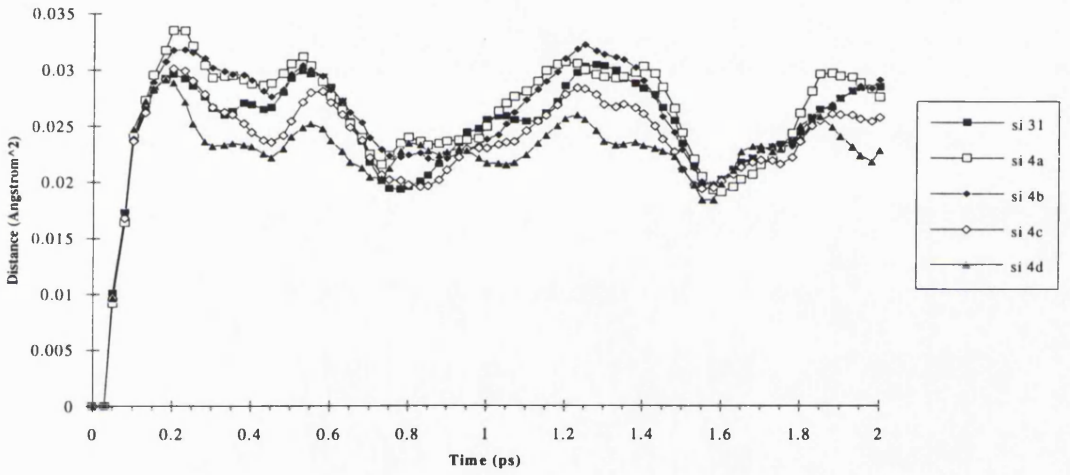

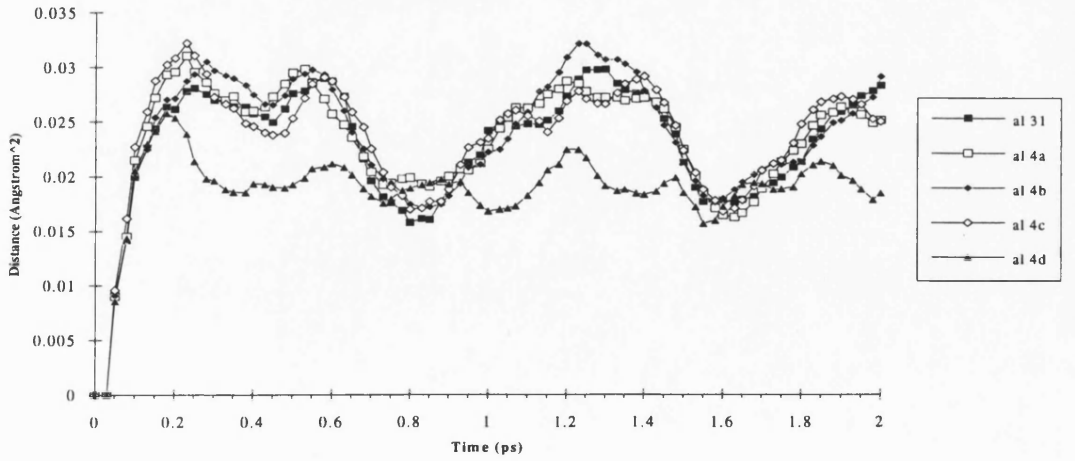

The oxygen ion MSD exhibits the same trends and the same features are observed at 0.3ps, 0.5ps and 1.5ps as for the 25% loading of the purely siliceous model at 300K. The effect of differing aluminium arrangements is to alter the instantaneous motions of the system but the overall features are still present. The MSD variation for the T atoms, again show very similar features to those observed in the purely siliceous models, most arrangements are similar, except for the **Al4_D** arrangement which exhibits a less well defined feature and indeed, there appears to be little correlation in this system. The average MSD values, the associated standard deviations and instantaneous velocities are reported in table A.7. The **Al4_D** arrangement, has a lower average MSD over the data acquisition period which implies that the motions are different from those previously simulated.

Table A.7 : The average MSD, associated standard deviations for the ions, (both framework and extra framework), in all the investigated aluminium arrangements.

Species	*Property*	*Units*	*Al3_1*	*Al4_A*	*Al4_B*	*Al4_C*	*Al4_D*
Oxygen	Average MSD	$Å^2$	0.178	0.182	0.18	0.175	0.171
	Std Deviation MSD	$Å^2$	0.0053	0.005	0.0056	0.0049	0.0043
Silicon	Average MSD	$Å^2$	0.158	0.161	0.16	0.154	0.151
	Std Deviation MSD	$Å^2$	0.0047	0.005	0.005	0.0043	0.0036
Aluminium	Average MSD	$Å^2$	0.153	0.154	0.155	0.155	0.138
	Std Deviation MSD	$Å^2$	0.0052	0.005	0.0055	0.005	0.0032
Nickel	Average MSD	$Å^2$	0.243	0.221	0.215	0.193	0.208
	Std Deviation MSD	$Å^2$	0.0198	0.0119	0.0116	0.008	0.014
Sodium	Average MSD	$Å^2$	0.255	0.226	0.151	0.167	0.172
	Std Deviation MSD	$Å^2$	0.0884	0.0784	0.0429	0.0607	0.0542

The behaviour of the non-bonded cations regarding the MSD fluctuations is described in figure A.14(a,b) which shows the same oscillatory behaviour as exhibited in the purely siliceous models, although the nature and frequency is strongly dependent on the aluminium arrangement. The MSDs for the Ni^{2+} cations emphasise this dependence on the aluminium arrangements because the Madelung field of the different arrangements is severely distorted and is highly dependant on the Al distributions. This differs from the purely siliceous case where all the T atoms had the same electrostatic characteristics and thus, the Madelung field was always smooth and well defined. The average Ni^{2+} cation MSD and its associated standard deviation is very similar to that previously reported for the purely siliceous models, yet as can be clearly seen the instantaneous motions are very different. This point highlights the potential use of a purely siliceous model to investigate time-averaged effects, yet the explicit inclusion of aluminium is required to investigate the precise local structural information and it's associated fluctuations.

Figure A.14(a,b) : The MSD plots for all the extraframework species in the aluminium distribution models.

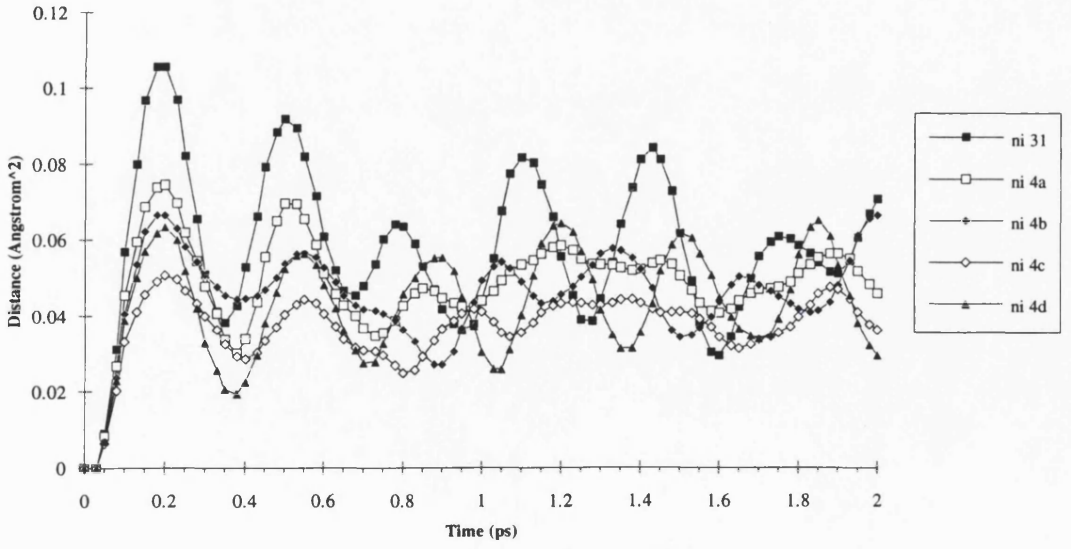

b) Na^+ MSD variations.

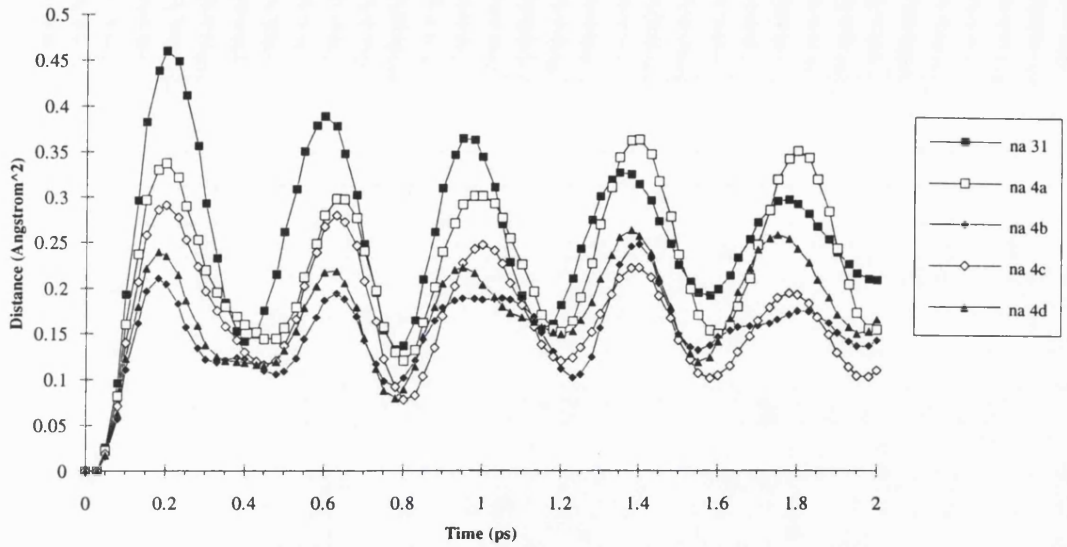

As discussed previously, charge compensating Na^+ cations were placed at the S_{II} sites, which are essentially purely siliceous in nature, and thus, the motions of these more loosely bound ions has been investigated. The RDFs reported in figure A.12 are broader and more asymmetric in shape, this is also supported by the average MSD values and an increased standard deviation in all the systems studied, (table A.8). The period of a Na^+ cation oscillating in the 6-ring window S_{II} site is in excess of 0.4ps with an associated amplitude of approximately 0.25Å. An interesting feature has been observed for the motions of the cation in the **Al4_B** arrangement, where unlike a simple oscillatory motion, there appears to be a single peak, followed by an extended peak, then returning to the single peak. Such a motion implies that even at long ranges the effect of the aluminium distribution and the oscillatory motion of the more polarising non-bonded cations can have a wide spread influence.

Overall the results presented in these sections highlight how the very detailed motions of a catalytic system can be studied by the MD technique.

A.1.4 Conclusion.

The results of this investigation into the dynamical motions of the complex Ni-Na-Zeolite-Y catalyst, show some remarkable behavioural patterns, which are exhibited by the oscillatory motion of the non-bonded cations either in the S_{II} site and to a lesser extent in the S_I site. The effect of increasing loading of the extra-framework cations is to perturb the local structure but at high loadings these local distortions begin to influence each other. The subtle effect of loading are obscured via peak broadening and coalescence as the temperature is increased up to 900K.

One effect of explicit aluminium inclusion around the D6R is that the instantaneous motions are less correlated, although the time-averaged properties are approximately independent of aluminium distribution.

The peak shapes for some of the systems deviate from Gaussian distributions being more asymmetric in shape. Such a peak shape has implications for the fundamental analysis of certain experimental techniques, most notably the Debye-Waller factor.

Overall, the results presented in this appendix serve to emphasise the complexity of the system and the dependence of the dynamics of the extraframework cations on the Al distribution in the framework.

A.2 References.

1 June R.L.; Bell A.T.; Theodorou D.N.; *J. Phy. Chem.;*, **94**, 8232, (1990).

2 Goodbody S.J.; Watanabe K.; MacGowan D.; Walton J.P.R.B.; Quirke N.; *J. Chem. Soc. Farad. Trans.*, **87**, 1951, (1992).

3 Vessel B.; Leslie M.; Catlow C.R.A.; *Molec. Sim.*, **3**, 123, (1989).

4 Verlet L.; *Phys. Rev.*, **159**, 98, (1967).

5 Ewald R.P.; *Ann. Physik.*, **64**, 253, (1921).